# Modelling Shocks using Molecular Dynamics


Nigel Park

Applied Science, Security and Resilience

Cranfield University

A thesis submitted for the degree of

*Doctor of Philosophy*

January 2010

This thesis is dedicated to
Derian
for her selfless support

# Acknowledgements

As with any work, the venture would be fruitless without assistance, particularly at crucial moments along the way.

Firstly I would like to thank Stephen White who originally gave me both the opportunity and the encouragement to set out along this research path. Furthermore, Stephen enabled me to spend time with a very active and fruitful group at the Lawrence Livermore National Laboratory in California. For this I would also like to thank Wayne King and Vasily Bulatov who facilitated my visit to the Laboratory, and both of whom have been encouraging of this and other research efforts in which I have been involved.

I would like to thank Eduardo Bringa and Alfredo Caro who have given me the most generous support throughout this project, and from whom I have learnt a great deal. I have also recieved encouragement and advice from Babak Sadigh, and Tom Arsenlis, as well as the rest of Tom's Computational Materials Science group. I would like to express my gratitude for how welcome they made me feel.

I have had generous support and encouragement from Justin Wark and his group at Oxford University, especially Andy Higginbotham, Will Murphy and Giles Kimminau. I would like to extend my gratitude to the rest of Justin's group for their welcome.

Further thanks go to Eduardo Bringa for introducing me to Giles Graham, and then to Anton Kearsley and Mark Burchell for their continued encouragement and support.

Within the AWE organisation I have received a great deal of help both in running simulations and in understanding the world of shock physics. In particular I would like to note the help of Duncan Harris for ensuring that the LAMMPS code was up-to-date and available, as well as adding some features which enhanced useability, and thus enabled a high-speed parallel

analysis code to be written. Neil Munday has been helpful by diagnosing issues which have arisen from time to time with the massively parallel supercomputers used for the simulations. Furthermore, I would like to thank Neil Bourne, Jeremy Millet, Steve Rothman and Chris Robinson for providing invaluable discussions regarding the nature of shocks.

I would also like to thank Mike Edwards for his encouragement, support and most of all for ensuring that I maintaned focus and momentum throughout this project.

# Abstract

The study of shocks in solid, crystalline metals has been ongoing since the early works of Rankine and Hugoniot in the latter half of the 19th century. However, the understanding of the behaviour of such materials under these extreme conditions remains an area of active research because of the paucity with which models can predict experimental observations. The modern era has seen a huge increase in the ability to solve many of the problems of this area of study by numerical, rather thatn analytic, means. One of these tools has been the use of computers to provide a numerical solution to the many–body problem posed by consideration of the medium as being composed of interacting atoms.

The issue, then, has been transferred from one of dealing with many particles (which remains a problem for some aspects) to one of being able to develop a model which correctly describes the atomic interactions. However, it has been found that approximately correct models provide sufficient fidelity to enable qualitative studies to be undertaken.

The study undertaken here has used this advantage to consider the behaviour of metallic materials under weak shock conditions. A comparison with some previous studies is given, which shows that, in order to avoid certain behaviours not observed experimentally, the simulation must contain thermal motion equivalent to at least room temperature. This thermal motion, and its resultant misalignment of the atoms, prevents spurious transfer of uni-directional momentum into rebounding translational supersonic waves. Further examination of the initial generation of dislocations indicates differences in the behaviour of not only the three high symmetry directions, but in the way that shear stress is relieved initially in low symmetry crystals as well. This behaviour gives some indication as to how the elastic precursor, commonly observed in weak shock experiments, decays from the level predicted by the Rankine–Hugoniot conservation relations to the much lower level observed experimentally. However, a very

large discrepancy exists between the amplitude of the elastic wave observed in these simulations and that of experiments. It is shown that the existence of defects within the crystal can account for at least some of this discrepancy. However, computational limitations not only prevent the creation of realistic sample sizes, but also prevent the simulation of realistic defect densities and microstructures. This computational limtation, then, means that it is not currently possible to recreate the low Hugoniot elastic limits observed experimentally.

The inability of atomistic simulations to recreate experimental data notwithstanding, useful analysis of shock behaviour is demonstrated. This fortuity is used to examine the behaviour of bicrystals under shock loading. It is shown that the difference in shock speed, together with the difference in response of the two crystal orientations leads to an interaction which modifies the behaviour from that observed in single crystal simulations.

Further use is made of the ability of modern simulation methods to recreate salient features of dynamic processes to examine the behaviour of metallic substrates under high–speed impact from nanometer sized particles. Here the plasticity of the substrate is shown to be vital to ensuring that the simulation results are faithful to experiment, and hence to space science work. In order to capture this behavioour correctly, issues of substrate size and boundary behaviour are seen to be key.

# Contents

# List of Figures

# Glossary

## B

**Bain path** Transformation of a BCC (FCC) lattice to a FCC (BCC) by means of a strain applied to the lattice.

**body centred cubic (BCC)** a cubic lattice in which atoms sit at the cube corners, with an additional atom at the cube centre. This causes the structure to have a lower packing density than the close packed structures.

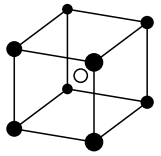

.

**Born stability criteria** The Born stability criteria are a set of inequalities which describe the onset of melting as the loss of shear strength. Melting onset is given by lattice instability which arises when inequalities between the elastic moduli are violated. In the original criteria,[21] only the elastic constants are included in the inequalities. More recently[153] it has been shown that the external stress must be included to match experimental data more accurately.

## C

**canonical ensemble (NVT)** A statistical collection of states such that the proportion of microstates within the macrostate follows the *Boltzmann* distribution. A system conforming to the *canonical* ensemble is more commonly known as the $NVT$ (constant number of particles, constant volume, constant temperature) ensemble.

**centrosymmetry (CSP)** Structural analysis parameter based on the comparison of opposing neighbours.

**cohesive energy** The difference between the average energy of atoms in a solid at minimum energy and that of the free atoms.

**common neighbour analysis (CNA)** A system for the identification of local crystal structure.

## D

**density functional theory (DFT)** A functional theory in which the contribution to the electric field due to bound electrons is approximated by a function.

## E

**embedded atom method (EAM)** A potential scheme which consists of a pair–repulsive term and a many–body attractive term.

**ensemble** A collection of particles, whose state variables match a statistically correct distribution. See *canonical*, *microcanonical* and *isthermal–isobaric* ensembles.

**Equation of State (EoS)** A relationship between pressure, $P$, volume, $V$, and energy, $E$, which can be used to describe the instantaneous thermodynamic state of the material.

**equipartition** A principle of statistical mechanics which states that the energy of the system is *on average* divided equally among all the degrees of freedom of that system. The principle fails at low temperature due to *quantum* effects.

**ergodic hypothesis** A hypothesis which states that the phase space ($p$,$q$) of a single particle averaged over an infinite number of steps is equivalent to the ensemble average phase space encompassed by a single snapshot of an infinitely large ensemble.

## F

**face centred cubic (FCC)** a close–packed cubic lattice which consists of layers of hexagonally packed atoms. The atoms of a layer sit in one of three possible

configurations, relative to the other layers, forming a repeating pattern of

**ABCABCABC** . 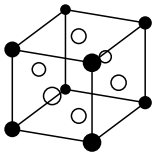 .

## H

**Hamiltonian** A description of the energy of a system based on the application of the *principle of least action* to the Lagrangian. The Hamiltonian is given as the sum of the potential and kinetic energies for a system of interacting particles.

**hexagonal close packed (HCP)** a hexagonal lattice in which the atoms lie in close–packed planes in a hexagonal structure, with the planes layered one above the other, forming a repeating pattern of **ABABAB** . 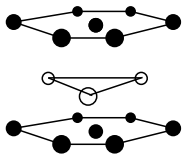 .

**Hugoniot** Locus of points in the pressure–volume plane accessed via a shock.

**Hugoniot Elastic Limit (HEL)** Maximum stress supportable by the material without undergoing plastic deformation, under shock loading.

## I

**isothermal-isobaric ensemble (NPT)** A statistical collection of states in which both the temperature and pressure are controlled. Over time the distribution of both the temperature and the pressure follow the *Boltzmann* distribution. A system conforming to the *isothermal-isobaric* ensemble is more commonly known as the *NPT* (constant number of particles, constant pressure, constant temperature) ensemble.

## L

**Large scale Atomistic Molecular Massively Parallel Simulator (LAMMPS)** Highly optimised code for carrying out a range of atomistic and molecular dynamics simulations. Developed by S.Plimpton *et al*[124] at Sandia National Laboratory in the US.

## M

**Markov chain** A series of states of a system connected via a Markov process. That is, each state is connected only to the immediately previous state, by some random change in the state variables.

**microcanonical ensemble (NVE)** A statistical collection of states such that each microstates within the macrostate has the same energy. A system conforming to the *microcanonical* ensemble is more commonly known as the *NVE* (constant number of particles, constant volume, constant energy) ensemble.

**modified embedded atom method (MEAM)** A modification to the embedded atom method scheme to account for angular depencies. (See appendix A.).

**molecular dynamics (MD)** A computational system for solving the equations of motion of a number of interacting particles.

## N

**non equilibrium molecular dynamics (NEMD)** simulation technique in which the atoms are allowed to respond freely to the motions of neighbouring atoms.

**nudged elastic band method (NEBM)** A means of finding the lowest energy pathway between two minima on a potential landscape.

## Q

**quantum** A description of matter where the properties are not continuously variable, but rather occupy descrete values separated by integer multiples of some minimum amount.

## R

**radial distribution function (RDF)** a description of the density of neighbours at increasing distance from the central atom.

## S

**Schmid factor** The effective stress on a slip system due to the angle that the slip system makes to the loading axis. (see appendix C.).

**stacking fault energy ($\gamma_{\mathbf{SFE}}$)** In FCC crystals it is possible for dislocations to dissociate into a pair of *partial* dislocations, with Burger's vectors whose sum is equivalent to a full dislocation. Due to elasticity considerations, these partial dislocations will push away from each other. The region between the partial dislocations has a modified order of the atomic planes, i.e. the stacking sequence has a fault. This planar defect, then, has an associated surface energy, $\gamma_{\mathrm{SFE}}$.

**symplectic** A description of a manifold (mathematical space) in which the *wedge product* ($\partial p \wedge \partial q$) is conserved.

## T

**twinning** Deformation of a crystal lattice by small movements of the atoms, resulting in a new lattice orientation which appears to be mirrored when compared to the original lattice.

## V

**virial** A theorem which relates the kinetic energy to the forces between particles.

## Symbols

| | |
|---|---|
| $a_0$ | equilibrium lattice spacing. |
| $B$ | bulk modulus. |
| $\partial$ | partial derivative. |
| $E$ | energy. |
| $G$ | shear modulus. |
| $m$ | mass. |
| $P$ | pressure. |
| $p$ | momentum. |

| | |
|---|---|
| $q$ | position. |
| $U_p$ | particle velocity. |
| $U_s$ | shock velocity. |
| $r$ | distance; separation between nucleii. |
| $t$ | time. |
| $V$ | potential energy. |
| $v$ | specific volume. |
| $\mathtt{v}$ | velocity. |

# Chapter 1

# Introduction

## 1.1 Research Context

The study of shock wave behaviour is of vital importance in the modern world. Whilst most of the fundamental theoretical research is connected with gas dynamics, fluids and fuel combustion, the application of strong shock effects is associated with planetary impacts[102] and other astronomical phenomena such as gamma-ray bursts,[106] geophysics, nuclear physics such as the thermal shock due to neutron spallation,[145] fusion energy research,[120] aviation counter–terrorism,[7] as well as in the areas of defence and armaments.

The study of shocks in solid, crystalline metals has been ongoing since the early works of Rankine and Hugoniot in the latter half of the 19th century. However, the understanding of the behaviour of such materials under these extreme conditions remains an area of active research because of the paucity with which models can predict experimental observations. The modern era has seen a huge increase in the ability to solve many of the problems of this area of study by numerical, rather than analytic, means. One of these tools has been the use of computers to provide a numerical solution to the many–body problem posed by consideration of the medium as being composed of interacting atoms.

This work is associated with shocks in metallic materials. The methods developed to deal with such situations are based on the simpler models used to understand gas dynamics. This derives from the assumption that in understanding deformation driven by pressures which are substantially larger than the known yield strengths of metals, the strength of the material can be ignored. Unfortunately this simplification cannot be valid for solid materials, since experimental results show that the assumption of purely hydrodynamic flow leads to poor models which inadequately recreate those results. The effects of strength, then, need to be included in order to produce

higher fidelity modelling. However, accounting for the mechanisms enabling plastic flow in crystals into models of high strain–rate pressure driven deformation has proven to be a very difficult task, and shows that the difficulties associated with understanding the complexities of shock behaviour in condensed, especially solid, media cannot easily be translated from the arena of fluid flow.

In order to make the problems tractable, certain assumptions have been included in both the models and the theoretical frameworks upon which those models are based. Continuum modelling suffers greatly due to the use of these assumptions. Where the flow is caused by very high pressures, such as exist behind shocks, the resultant flow is determined by the momentum fluxes calculated without explicitly including any resistive forces due to the viscous nature of the solid medium. It has been understood for more than a century that an increase in strength in metals can be brought about by introducing microscopic variations in the underlying microstructure (features such as the size of the constituent crystals or grains; the degree to which those grains are randomly oriented, or the texture; the nature of microstructural defects, both intrinsic such as dislocations, interstitials, vacancies and extrinsic such as second phases), and that the strengthening effect is due to the interaction of dislocations with those inhomogeneities. However, continuum modelling assumes that any small region of material has the same physical properties as any other small, or large, region of material. That is, the material is assumed to be homogeneous. Similarly, continuum modelling assumes that the response behaviour of solid materials is independent of any orientation of the small region of material in relation to the applied forces. That is, the material is assumed to be isotropic. This latter point has been addressed in the modelling of low–rate deformation, such as in metal forming processes,[154] and work is starting to apply these techniques to high–rate deformation and shocks.[103]

The furtherance of shock modelling in metals is assisted greatly by the application of multiscale modelling.[122] Multiscale modelling follows the successful understanding of how the behaviours observed at the macroscale (that is, those responses of materials which are familiar to everyday life; for metals this means material samples which are greater than a millimetre in any dimension) are determined by the microstructure of the material and in turn these microstructural features are predicated on the behaviours of the constituent atoms.

The issue, then, has been transferred from one of dealing with many particles (which remains a problem for some aspects) to one of being able to develop a model which correctly describes the atomic interactions. However, it has been found that

approximately correct models provide sufficient fidelity to enable qualitative studies to be undertaken.

Hence there is a need to understand how the atoms behave. The studies undertaken here set out to understand the atomic interactions themselves – how the atoms act collectively under the rapidly rising pressure of a shock wave.

## 1.2 Thesis Layout

Chapter 2 provides some background in order to put this work into context. Section 2.1 introduces the reader to some basic concepts in shock behaviour, including shock compression and the resultant development of shear stresses and how materials might respond to the pressures and shear stresses so produced. Also described is the *Hugoniot* curve and how elastic behaviour leads to the *Hugoniot Elastic Limit* as well as some basic formulae used to describe the shock state.

Section 2.2 describes some modern modelling techniques used at length scales appropriate to atomic behaviour. This section compares some of the more prominent methods used for simulations in this arena. The bases of the methods are briefly described, and the relationship between the schemes is noted. The basis of the molecular dynamics (MD) method are described in more detail. From this, the formulae for some principal quantities are given.

The empirical atomic methods described are predicated on accurate and transferable potentials which are used to calculate the energies of the atoms. In this context *transferable* means that the calibration of the potential by fitting to the known properties in one physical arena (for example the elastic moduli) will also reproduce the material properties in an area (for example sublimation energy) where fitting procedures have not been used. It is the loss of accuracy of the description of the potential field which, as a consequence, reduces the level of transferability of that potential scheme. As is shown, it is the energies given by the potential scheme in use which gives the atoms their particular behaviour. Hence a brief outline of some of the better known potentials is described in section 2.3.

These simulations contain large numbers of atoms; on their own it is difficult to determine what is happening within the simulation. In order to examine the behaviour either as local regional values, averaged over some small space or by isolating those atoms with some property which is significantly different from their neighbours requires some form of analysis. Analysis methods ranging from the relatively sim-

ple, e.g. plotting local average velocity, to more complex, e.g. determination of local structure, are outline in section 2.4.

The main work of this thesis is given in chapters 3 and 4. This work describes the simulation of some situations in solid state condensed metals which lead to shocks. Section 3.1 covers simple piston–driven shocks in single crystals. The main thrust of this section is to describe the differences in behaviour of the crystals which observed when the crystal lattice is oriented with different lattice directions parallel to the direction of shock travel. This is taken further in section 3.2 which examines the effect of having adjoining crystals of differing orientation. Section 3.2.2 shows simple bicrystal interaction. These bicrystal simulations have been undertaken specifically to compare the expected behaviour as observed in this work with experiments being undertaken as part of an effort to develop a physics based understanding of the mictrustructural effects of shocks. Section 3.2.3, therefore, shows some simulations of nanocrystalline materials. This latter work is aimed at examining the circular effect which arises due to the polycrystal nature of engineering metals. That is to say that, the fact that an engineering metal is comprised of a large number of randomly oriented crystals (or grains) means that each crystal presents a different orientation to the oncoming shock. This, then, will have an effect on the shock front itself, and therefore a different (even if only subtely different) shock will now be passing through the material.

Section 4.1 finally considers a situation which is more practically driven; the simulation of the impact of nano–particles onto metallic substrates. This situation is of interest in space research. Whilst such work can help in leading toward more robust space vehicles, the focus here is to help understand the nature of comets. In particular, the work is aimed at improving the understanding of particulate matter found in space, diagnosed through examination of the impact craters recovered from space vehicles.

As was mentioned in the acknowledgements, during the undertaking of this project work was carried out as part of collaborative efforts in understanding the behaviour of crystals in experimental conditions. Appendix E presents a series of papers in which this author provided simulation output which was used by the main authors of those papers to carry out their work. Appendix E.1 presents some analysis of the spread in wavefront caused by the crystal orientation variation which occurs in polycrystalline metals. The work presented in this paper lead into the analysis of naocrystalline samples carried out in section 3.2.2. Appendix E.2 presents work which is part of a larger programme to develop novel experimental diagnostics for

shocked metals. Appendix E.3 presents work which was undertaken, like that shown in appendix E.2, to examine shocked crystals experimentally. Whereas appendix E.2 presents a theroetical analysis of how the atomic behaviour can be understood in terms of the effect observed in x-ray diffraction signals, appendix E.3 shows how such signals can be compared to simulated diffraction signals derived from MD, which would then enable the additional analysis of the MD to aid the understanding of the experimental results, and hence the response of real crystals to shocks.

# Chapter 2

# Background

## 2.1 Shock Physics.

The fundamental understanding of the behaviour of materials under shock conditions is due to the efforts of Rankine[127] and Hugoniot.[79] Salas[133] provides a narrative on the historical context of their work. The modern era of research into the response of materials to shock compression was led by the work carried out in Los Alamos as part of the Manhattan Project.[10,23,67,114,151]

Descriptions of the physics of shock are given in many texts. The interested reader is referred to [1, 44, 46, 111, 130, 139]. This section attempts to give a brief precis of the physics for completeness.

The development of shocks is predicated on the increase in sound speed as the pressure is increased. At very low pressures sound waves are propagated at a fixed velocity, but when the pressure is sufficient cause a noticeable increase in density, the sound speed also increases. It is this effect which causes a compression wave with a positive pressure gradient (pressure increases with time) to steepen up, because the higher pressure region of the pulse (currently later in time) travels faster than the lower pressure region ahead of it. Ultimately, then, as the highest pressure point catches up with the front of the wave, the slope of the front increases.

It is this near–instantaneous rise in density, and the accompanying rise in pressure and energy (temperature), which causes the material to respond in many and varied ways. This effect is exacerbated by the nature of the compression. That is to say that the wave, travelling in some direction, causes the immediate change in density to be focussed in that direction, *i.e.* the compression is one–dimensional (1-D). This causes the material to be placed in a state of high shear stress (see figure 2.4). The material is unable to support this stress, and atomic rearrangement is required to reduce it. This rearrangement can take one or more of several forms, and the processes

associated with these rearrangements are not well understood. The most common, and predominant mechanism is plasticity. Here, dislocations are the mediating agent, both via the movement of existing as well as the generation of new dislocations (see figure 2.1). There are two other processes which can occur to bring about the relaxation of the generated shear stresses. The first of these is twinning. This is an alternative plasticity mechanism, in which the atoms shuffle coherently, such that the lattice is rotated by a small degree relative to its original orientation (see figure 2.2). The second mechanism which can occur to reduce the shear stress within the distorted crystal is a phase change. This is a whole–scale rearrangement of the atomic structure into a new lattice structure[a]. The new structure has a lower atomic volume, and it is this reduced volume, combined with the atomic reorganisation itself, which creates an undistorted atomic arrangement. A scientifically important shock–driven phase change occurs in iron. The pressure–temperature phase diagram is given in figure 2.3 (from [111]). A shock will increase the temperature as well as the pressure. However, the temperature rise due to a shock where the sample is initially at room temperature is insufficient to reach the FCC region of the diagram. The early history of the investigation of this diagram under shock conditions, which was undertaken at Los Alamos between the 1940s and 1970, determined the crystal structure by relating the wave splitting observed dynamically to x-ray diffraction results from static high-pressure diamond anvil cell experiments. However, confirmation of the shocked high pressure phase by the determination of the structure *in situ* during shock compression was only determined recently.[86]

The increased density, coupled with increased internal energy also enables other changes to occur. For sufficiently large shock pressures the increase in temperature causes the material to melt. Due to the importance of this transition, the pressures at which most elements melt under shock loading has been determined (see table 2.1).

Included in this group of responses is the possiblity of chemical reaction. The huge increase in internal energy, particularly in the form of entropy, provided by the shock enables very large thermodynamic barriers to be overcome, enabling reactions which would otherwise not be possible. This enables both shock synthesis (including polymerisation) as well as decomposition.[111]

The study here examines the behaviour exhibited by copper, a simple FCC metal. Since this system comprises only a single element, clearly chemical reactions will not occur. Furthermore, phase changes have not been observed in the experimental shock

[a]There are some phase changes which are *isostructural* in which the two structures have the same crystal structure, symmetry etc, but different volumes. However, these are rare.

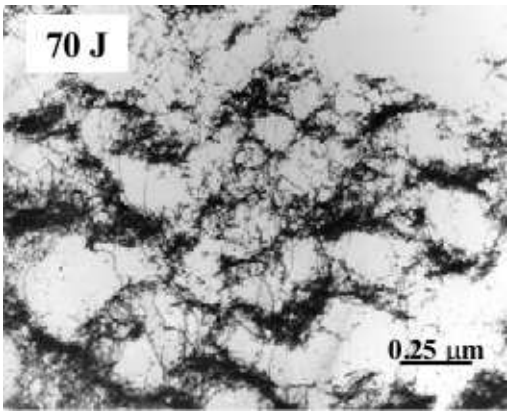


Figure 2.1: Transmission electron microscope image of dislocations in single crystal copper. The sample is oriented with $\langle 100 \rangle$ aligned with the shock direction. The sample was shocked by laser to 70GPa. From [134].

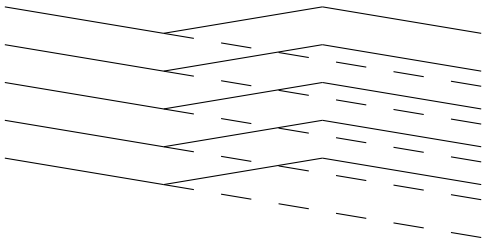

Figure 2.2: Schematic showing twinning deformation. The portions of crystal on the left and right are in the original configuration; that in the centre has been deformed such that the lattice planes lie in a mirror (twin) configuration to the original (parent) material. The dashed lines show the original (undeformed) confuguration, and the crystal region on the right can be seen to have moved (sheared) relative to its original position.

| Element | Melt Pressure (GPa) |
|---|---|
| Pb | 28 |
| Zn | 44 |
| Sn | 28 |
| Al | 103 |
| Fe | 184 |
| Ce | 43 |

Table 2.1: Pressures at which melt occurs under shock loading for a selection of elements (from [111])

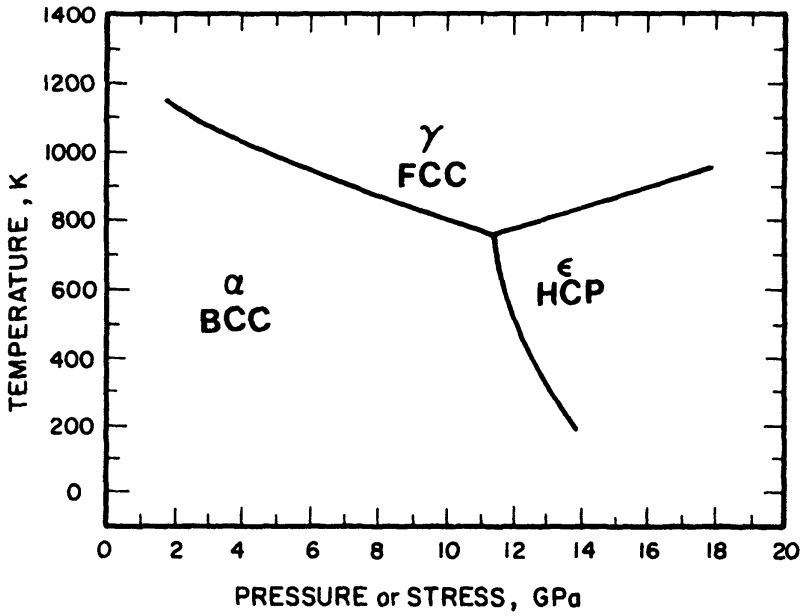


Figure 2.3: Phase diagram of iron. From [111].

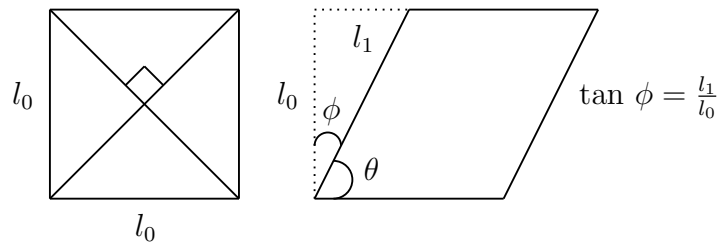


(a) simple shear

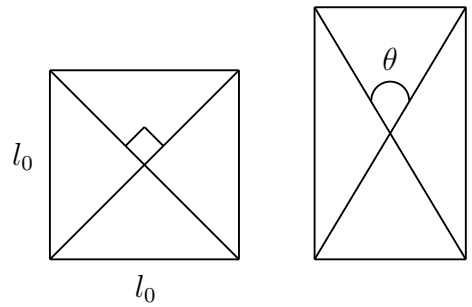


(b) pure shear

Figure 2.4: Shear stresses are generated when an originally orthogonal pair of directions in some representative volume element of material are deformed such that they are no longer orthogonal. For simple shear the amount of shear strain is given by the angle $\phi$, which relates the degree of deformation ($l_1$ in (a) above) to the original length $l_0$. For area preserving deformations, the angles, $\theta$ in (a) and (b) are identical.

| Element | Transition Pressure (GPa) |
|---|---|
| Fe | 13 |
| Bi | ∼2.5 |
| C | 23 |
| Ti | 9.4 |
| Zr | 23 |
| U | 50 |
| Pu | 0.6 |
| Sb | 7 |

Table 2.2: Pressures at which phase tranformations occur under shock loading for a selection of elements (from [111])

loading of this metal, so this type of behaviour would not be exhibited by a realistic model of copper. However, twin deformation has been observed in copper.[117,135]

Schematics of a simple piston–driven shock are shown in figures 2.5 and 2.6. Figure 2.5 shows how the shock front moves faster than the piston. From this a set of jump conditions are established to describe the transformation of variables from rest to the shocked state (see figure 2.7), and laws of conservation are then used to develop equations to relate the variables between the initial and final states.

From the considerations of the conservation of mass, momentum and energy a set of equations can be derived. These are known as the Rankine–Hugoniot relations, and are fundamental in any analysis of shock propagation.

Consider a continuous block of material of constant cross-section $A$ (figure 2.8). A piston drives into the material with a velocity $U_p$. In the situation being considered here, the piston is travelling at a constant velocity. Therefore the material behind the shock is travelling at the same velocity as the piston[b]. From figure 2.5 it can be seen that the motion of the piston causes an increase in the density of the material ahead of it, as the material is 'gathered up'. An analogy commonly used (see Meyers[111] p 98) is that of a snowplough. The action of the piston, which causes the material to begin moving, and the resultant increase in density causes a shock to travel forward at velocity $U_s$.

After some time $\triangle t$ the shock will have travelled $U_s \triangle t$ (distance $L_2$ in figure 2.8). The material behind the shock, now travelling at $U_p$, will have been compressed. The

[b]In our simple case there is a single shock which takes the material from its initial state (rest) to its final state (fully dense for that shock, and travelling at the piston velocity) instantaneously. In reality, for solids, strength and other dissipative effects modify the behaviour observed at the shock front itself, so that the material asymptotes toward the piston velocity.

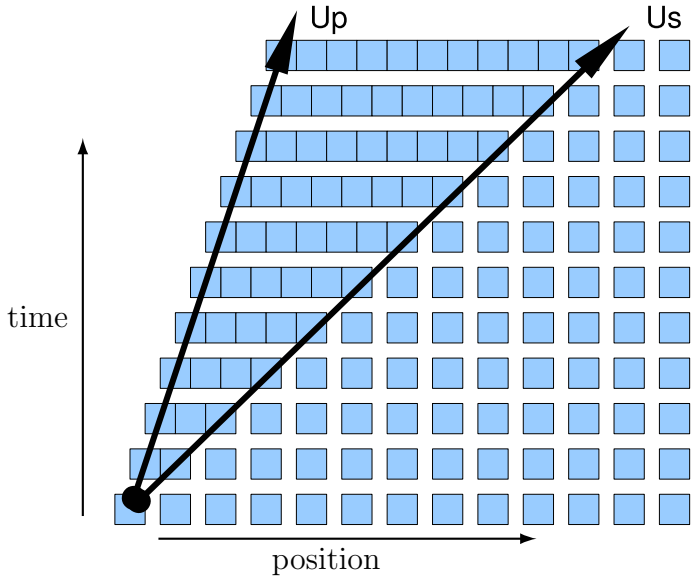


Figure 2.5: Schematic of a simple piston driven shock. The piston drives into the material from the left. Each horizontal row is a snapshot of the system at some time. The initial state is at the bottom of the figure, and time increases up the figure. Thus it can be seen that the slope of the arrow labelled $U_p$ gives the velocity of the piston, and that labelled $U_s$ gives the velocity of the shock front running ahead into the material at rest.

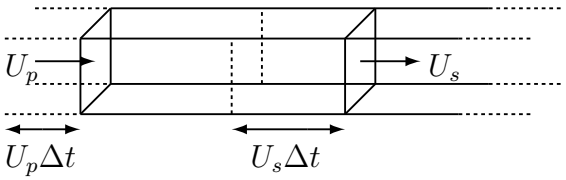


Figure 2.6: Schematic of shock propagation

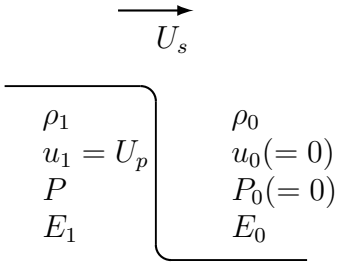


Figure 2.7: Schematic showing the state variables on either side of a shock

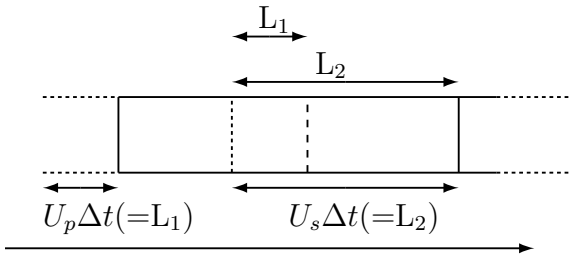


Figure 2.8: Schematic of shock propagation

piston will have moved $U_p \triangle t$ (distance $L_1$ in figure 2.8), so the material behind the shock which originally occupied a length $U_s \triangle t$, now occupies a length $(U_s - U_p)\triangle t$ (=$L_2$−$L_1$ in figure 2.8). The mass of the material in a length $U_s \triangle t$ is (density × area × length) $\rho_0 A U_s \triangle t$ . Since this is compressed into a length $(U_s - U_p)\triangle t$, then

$$\rho_0 A U_s \triangle t = \rho A (U_s - U_p) \triangle t \tag{2.1}$$

Since the specific volume $v = 1/\rho$,

$$\begin{aligned} \frac{U_s}{v_0} &= \frac{U_s - U_p}{v} \\ \frac{v}{v_0} &= \frac{U_s - U_p}{U_s} \end{aligned} \tag{2.2}$$

Equation 2.2 indicates that the change in volume (compression) is given by the two velocities, $U_p$ and $U_s$.

The pressure can be obtained from the conservation of momentum. Now Force = mass × acceleration = rate of momentum gain

$$P = m\frac{d\mathtt{v}}{dt} = \frac{d(m\mathtt{v})}{dt} \tag{2.3}$$

hence pressure = momentum gain ÷ area = mass accelerated in $\triangle t$ × acceleration ÷ area.

Since the mass accelerated is that swept by $U_s \triangle t$,

$$m = \rho_0 A U_s \triangle t \tag{2.4}$$

and the acceleration is

$$U_P \div \triangle t. \tag{2.5}$$

Together with the area, $A$, this gives

$$\begin{aligned} P &= \frac{\rho_0 U_s A U_s \triangle t U_p}{A \triangle t} \\ &= \rho_0 U_s U_p \end{aligned} \tag{2.6}$$

Equation 2.6 indicates that the pressure, like the compression above, is given by the two velocities, $U_p$ and $U_s$.

The energy consideration follows similarly. The total energy gain is the sum of the internal energy gain and the kinetic energy gain. The gain in internal energy is expressed as the mass crossed by $U_s$ times the change in specific internal energy $\triangle E$; the kinetic energy gain is $^1/_2\, mU_p^2$

Now work done is the force times distance moved, $W = PA \times U_p \triangle t$. From this

$$\underbrace{PAU_p\triangle t}_{\text{work}} = \underbrace{\rho_0 U_s A \triangle t \triangle E}_{\text{internal energy}} + \underbrace{^1/_2\, \rho_0 U_s A \triangle t U_p^2}_{\text{kinetic energy}}$$

rearranging

$$\triangle E = \frac{PU_p}{\rho_0 U_s} - \frac{1}{2}U_p^2 \tag{2.7}$$

Rearranging equations 2.2, 2.6, and 2.7 can yield a further seven relationships,[164] given here for completeness. (Note that the initial pressure is assumed to be zero. Where this is not the case, an alternative derivation of these relationships [using $P - P_0$ instead of $P$] can be used to obtain a set of similar equations)

$$\frac{v}{v_0} + \frac{U_p}{U_s} = 1 \tag{2.8a}$$
$$U_p^2 = P(v_0 - v) \tag{2.8b}$$
$$P = \rho_0^2 U_s^2 (v_0 - v) \tag{2.8c}$$
$$\triangle E = ^1/_2\, P(v_0 - v) \tag{2.8d}$$
$$\triangle E = \frac{P^2}{2\rho_0^2 U_p^2} \tag{2.8e}$$
$$\triangle E = ^1/_2\, U_p^2 + (v_0 - v) \tag{2.8f}$$
$$\triangle E = ^1/_2\, U_s^2 \left(1 - \frac{v}{v_0}\right)^2 + (v_0 - v) \tag{2.8g}$$

### 2.1.1 Hugoniot Curve

There are six primary variables associated with the material under consideration; whereas the original density, $\rho_0$ (or specific volume, $v_0$) is known, and the particle velocity, $U_p$, is specified by the piston velocity, the remaining four variables remain to be determined. As is shown above from the equations 2.2, 2.6, and 2.7, the jump

conditions provide three equations which relate the shock velocity, $U_s$, the pressure, $P$, compressed density, $\rho$ (or specific volume, $v$) and the energy gain due to the shock, $\triangle E$.

Clearly, then, the system is under specified and some further relationship is required in order to determine the values of the material state variables behind the shock. This relationship is colloquially referred to as the Equation of State (EoS). For shocks, the jump conditions given above are related to jumps within the EoS space.

We can see from figure 2.5 that the piston motion leads to a shock travelling with a higher velocity. We may describe this relationship through some polynomial

$$U_s = C_0 + SU_p + AU_p^2 + BU_p^3 \dots \tag{2.9}$$

It has been shown experimentally that for most materials, particularly metals, the non–linear terms are very small contributors to this relationship. This means that the shock velocity is related to the particle velocity through a linear relationship

$$U_s = C_0 + SU_p \tag{2.10}$$

Combining equations 2.10 and 2.6 yields a curve relating the pressure to the piston velocity for a shock

$$P = \rho_0(C_0U_p + SU_p^2) \tag{2.11}$$

This relationship is known as the *Hugoniot curve*. It should be noted that, since a shock is an instantaneous jump in thermodynamic states, then the Hugoniot curve describes the *locus of states* which are accessed via the shock process. That is, the material state does not pass *along* the Hugoniot curve, rather, for some given shock, the curve can be used to determine the endpoint value of the shock process.

For single shocks from an initial condition where the material is at zero pressure and room temperature, the Hugoniot is known as the *principal Hugoniot*. Figures 2.9 show the Hugoniots of copper in the $P$–$U_p$ and $P$–$v$ planes. Figure 2.9a is a plot of equation 2.11 with parameters from [27]. Figure 2.9b is made by using equation 2.2 to give a range of compressions against piston (particle) velocity for the abscissa, and equation 2.11 (over the same range of particle velocities) for the ordinate.

### 2.1.2 Hugoniot Elastic Limit

The shock process so far decribed is predicated upon a change in sound speed as the material is compressed. However, for very low amplitude compression waves (sound

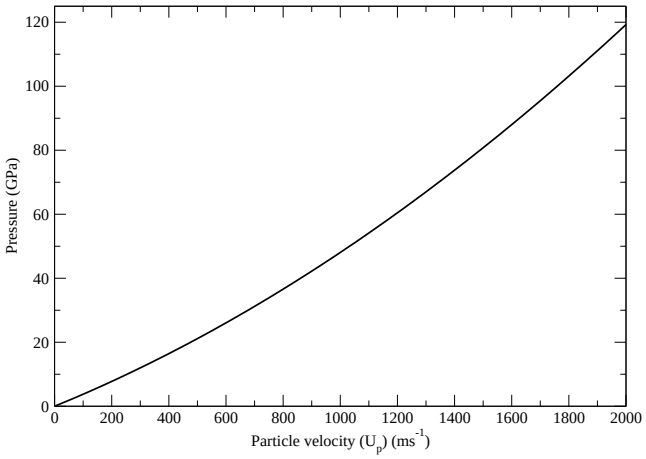


(a) $P$–$U_p$ plane.

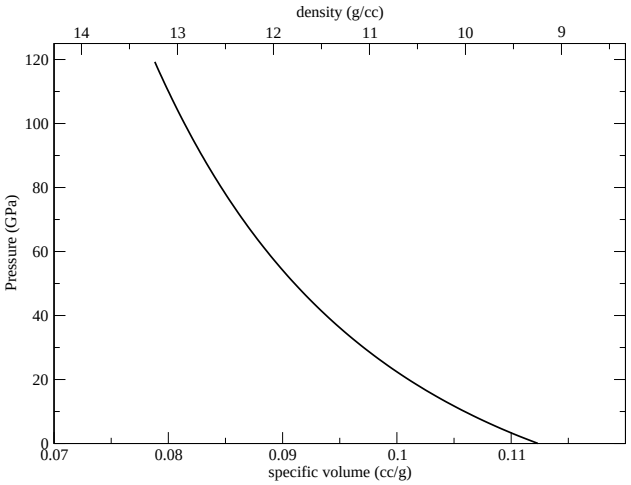


(b) $P$–$v$ plane.

Figure 2.9: Hugoniot for copper shown in the pressure – particle velocity and pressure – volume planes. See text for details of how these are produced.

waves) the speed of sound is constant. Furthermore, for solid, and especially crystalline, materials, such low amplitude compression waves cause no structural change in the material through which the sound wave passes. That is to say that the material is compressed elastically, and will return to its original state after the wave has passed. However, the compression induces shear stresses in the material. As the magnitude of the compression increases, so the amplitude of the shear stress increases. At some point, the material cannot support these shear stresses, and the material deforms plastically. This point is known as the *Hugoniot Elastic Limit* (HEL). Since the speed of sound of such elastic waves is constant, then the $U_s - U_p$ relation described earlier is not valid.

The Hugoniot curve described above gives the locus of the endpoints of the shock process. This process is assumed to be instantaneous, *i.e.* the material does not pass through any thermodynamic states during the shock. However, by combining equations 2.2 and 2.6, the slope of a line connecting the starting points and endpoints of the shock can be found,

$$\begin{aligned} \frac{P - P_0}{v_0 - v} &= \frac{\Delta P}{-\Delta v} = \frac{U_s^2}{v_0} \\ \frac{\Delta P}{\Delta v} &= -\frac{U_s^2}{v_0} \end{aligned} \tag{2.12}$$

where the subscript 0 indicates the initial state. This line is known as the *Rayleigh line*. A Rayleigh line for a 0.5 GPa shock is shown in figure 2.10. Note that the slope of the Rayleigh line is a function of the shock speed. This means that faster shocks are described by a steeper Rayleigh line.

We can use the relationship between the Rayleigh line and the Hugoniot to investigate what might happen where a material exhibits some change in behaviour at a fixed shock pressure. Such effects are shown by materials which exhibit phase changes, chemical reactions and strength.

Figure 2.11 shows a hypothetical Hugoniot for a material which exhibits a different behaviour above pressure $P_1$, as compared to shock pressures below that level. A Rayleigh line for a shock at a pressure below $P_1$ is shown at I. Here a single shock is observed. As the shock pressure is increased, the shock state is described by the Hugoniot, until the state at A is reached. Above this point, the Rayleigh line is described by two separate lines; a shock up to pressure $P_1$, and then a slower shock up to a higher pressure, as described by II in figure 2.11. The shock wave is thus caused to *split* into a precursor and a main shock. The precursor drives the material

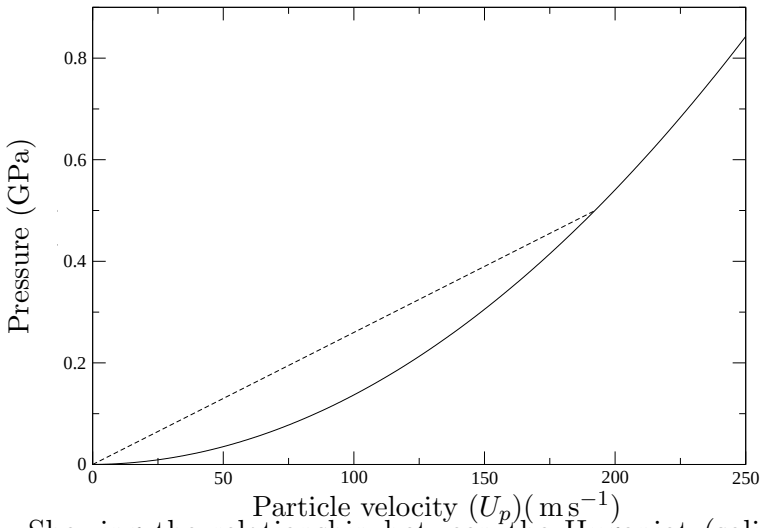

Figure 2.10: Showing the relationship between the Hugoniot (solid curve) and the Rayleigh line (dashed curve) for a 0.5GPa shock.

to the state described by A in figure 2.11 and the main shock increases the pressure (and associated parameters e.g. density, entropy) still further. As the shock pressure is increased, the shock speed of the precursor remains constant (because the state A is fixed), but that of the main shock increases up to B, at which point the shock speed of the main shock is the same as that of the precursor. At this point, then, the two shocks are indistinguishable. For shocks of a still higher pressure, for example that shown at III, only a single shock is observed.

Now, since the longitudinal sound speed $C_L$ is a constant, then a point exists in the $P - U_p$ plane where $U_s = C_L$. This can be found from the relations 2.6 and 2.10,

$$\begin{aligned} P^{\mathrm{HEL}} &= \rho_0 C_L U_p \\ U_p^{\mathrm{HEL}} &= \frac{C_L - C_0}{S}. \end{aligned} \tag{2.13}$$

This causes the Hugoniot curve (figure 2.9a) to be offset, such that it starts at $P = P^{\mathrm{HEL}}$ and $U_p = U_p^{\mathrm{HEL}}$. Figure 2.12 shows this offset for a hypothetical material. The offset corresponds with the *Hugoniot Elastic Limit* described above.

It should be noted that whereas the amplitude of an elastic precursor may be very small, since the precursor is travelling at the longitudinal sound speed, the main shock may have to be quite substantial in order to outrun it.

It has been observed that for some materials the HEL, given by the magnitude of the elastic precursor, is not constant, but decays over time as the shock travels through the sample. A description of the elastic precursor decay by Jones[80] attributes the phenomenon to rate dependent effects. In contrast Gilman, in a review[66] of the

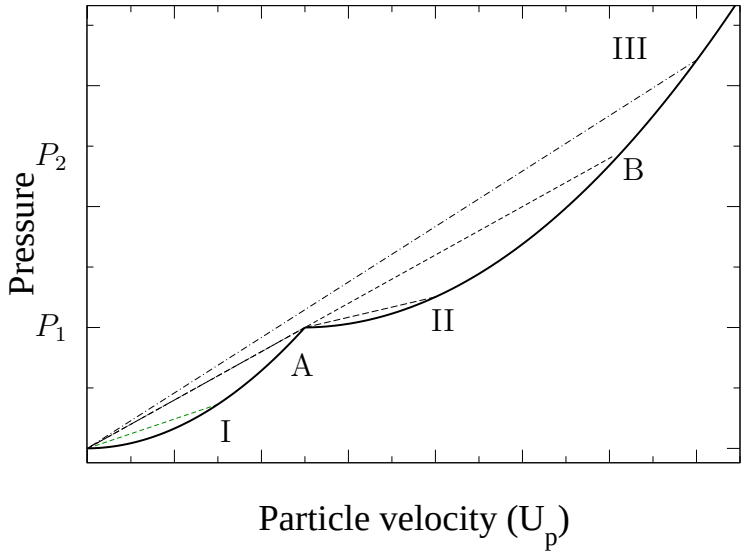


Figure 2.11: Showing the how the relationship between the Hugoniot (solid curve) and the Rayleigh line (dashed curves) can be used to investigate the *wave splitting* phenomenon.

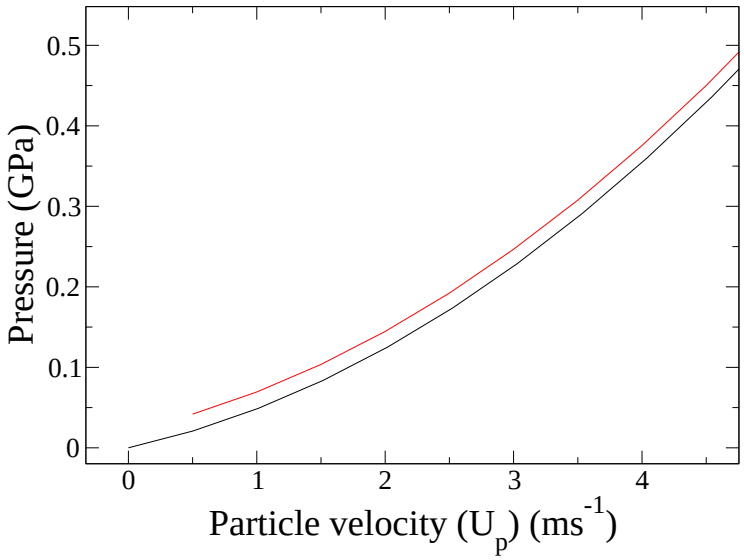


Figure 2.12: A comparison between a Hugoniot for a material with no strength (black curve) and a material with strength (red curve). The red curve is offset by a yield strength of 41 MPa corresponding to a particle velocity of 0.5 $\mathrm{m\,s^{-1}}$

assumptions used in analyses of impact experiments, describes how the realisation that impacts in solids are not a hydrodynamic[c] process leads to the development of an elastic precursor. Gilman shows that when the shear stress $\tau$ exceeds some critical value then some plasticity mechanism will convert elastic shear strain into heat. Due to this conversion, the shear stress at the front decays to a lower limiting level. The form of the decay curve follows that of the reduction in upper yield stress in iron with increasing specimen thickness. In another analysis the decay has been attributed to the damping of dislocation motion by viscous forces.[95]

## 2.2 Computer Simulation

The modelling of materials has been attempted for many years. Due to the advancement of computers, which enables the ready computation of the large numbers of calculations involved in the simulation of material at the scale of the atom, simulation has become synonymous with computer simulation. Furthermore, a consequence of this advancement is that there is a plethora of books available covering the range of modelling techniques available. However, it is often useful to consider a simpler text, such as that of Barber[13] which gives a very quick overview of many types of numerical modelling techniques.

The purpose of material modelling is to calculate the body forces which are experienced by a material, and then to work out how the material will respond to the applied forces. Atomistic modelling calculates the forces which are experienced by individual atoms and then modifies the motion of the atoms in response to those forces. The concerted response of large numbers of atoms observed in the atomistic model is used to understand macroscopic material behaviour. There are a variety of methods which have been developed to provide insight into the physical processes observed in materials. These methods range in the scale of the material being studied, but this distinction is driven primarily by the cost of each method together with the number of computational units which need to be followed within that method. Thus a scale emerges in which mathematical complexity, physical accuracy and problem size are related.

The most accurate methods, and the most mathematically complex, therefore apply to the smallest physical scale. These methods fall under the general name of *ab-initio*, which means "from the beginning". This name is given because the

[c] A material which exhibits purely hydrodynamic behaviour has no strength; it will deform immediately upon loading to a state in which the stresses in all directions are uniform.

mathematical basis does not include parameters derived from experimental data, rather the scheme is built up from an understanding of the way that atomic nuclei and electrons interact. Thus the forces on the nuclei are described explicitly in response to the instantaneous electronic configuration.

Methods which treat atoms individually, but do not consider electrons as distinct particles use models which derive from the results of ab-initio calculations and experimental data. Therefore these models describe the forces experienced by charged ions. Functional forms are used to describe the forces on the ions and therefore the forces are considerably easier to calculate in such schemes. There are two main types of method in common use; the Monte-Carlo method uses random numbers to generate possible configurations, and criteria can be set to decide whether the new configuration is adopted. Molecular dynamics, on the other hand, calculates the forces in order to update positions based on Newton's laws of motion. Changes in the configuration are driven by these laws, in that the forces local to each ion are aligned with the direction of a reduction in the potential energy. However, the total energy of the system is conserved, so any reduction in potential energy arises as an increase in the kinetic energy.

There are difficulties with the above approaches which arise from computational cost. Here computational cost refers to either memory or time limitations. This means that the numbers of separate particles which can be represented is limited. In the *ab-initio* scheme this is both a memory issue in that the memory required to store the information necessary to build up the correct configuration is prohibitive as well as a time issue since the complex interaction between the electrons means that the computational cost scales as the cube of the number of atoms. For this reason such calculations are usually limited to providing calibration data for more empirical schemes. In the ion models the computational limit is driven by the time taken to calculate the potential energy (and forces) on each particle. Therefore, although far more atoms can be simulated in the atomistic method[d] compared to *ab-initio* schemes, the volume of material being simulated is still rather small. This means that there is a trade-off between the numbers of atoms being simulated, and the time (real time and hence simulated time) over which the simulation is run. In the 10 billion atom example given in the footnote (d) it takes ∼24hrs to calculate 1ps of simulated time. But since the block of material is quite large (in MD terms) any physical process takes

[d]The current limit is one trillion ($10^{12}$) atoms,[65] which represents a cube of approximately 2.5 $\mu$m on an edge. Even a modest high performance computer, say of 2048 processors, each having 4Gb memory can handle quite large numbers ($\sim 10^{10}$) of atoms.

some significant time, and so the simulated time is necessarily large. A strong shock in copper driven by a piston velocity of $1750\,\mathrm{m\,s^{-1}}$ will send a shock at $2630\,\mathrm{m\,s^{-1}}$ (see section 2.1) and produce a pressure of $\sim$1 Mbar. If the material sample being simulated is $0.5\mu$m across, the shock will take 100ps to traverse the sample, which from before will take 100 days to calculate.

A major issue arises from defects. Extrinsic defects present difficulties at this scale because it is not fully understood how they should be treated. The physics of the interaction of the base material with defects within the lattice is not sufficiently understood and this difficulty is compounded by the size of problem necessary to represent extrinsic defects at the correct density. This latter point applies less so to intrinsic point defects such as interstitials and vacancies but the treatment of dislocations falls into both camps. That is to say that the simulation of a single dislocation is relatively simple whereas simulating multiple dislocations and dislocation inclusion interaction is more difficult.

In order to overcome these difficulties it is necessary to treat the problem in a different way. At longer length scales it is solved by considering the material as a continuous region of space, with its properties based on concepts of mechanics. However, many other difficulties arise from such treatments. Many of these are due to the anisotropic nature of crystals. In continuum modeling there is an assumption that the large number of crystals covered by each representative region implies that the region is isotropic in its response. In reality not only do real metals demonstrate some degree of intrinsic anisotropy, but also such behaviour is amplified by processes of mechanical work due to the grain reorienting, which causes the metal to develop 'texture'. There have been attempts by several workers, most notably Hill,[73] to address this through modifications to the yield surface.

A different model paradigm has been devised to address these issues. This framework considers the material at a lower length scale than continuum without considering each particle individually. Such schemes are known as *mesoscale* methods, indicating their 'in-between' scale. These techniques address the anisotropic and crystalline nature of metals without describing the agents of that behaviour explicitly. These models are parameterised by consideration of specific experiments, but also by numerical experiments undertaken by lower length scale methods, such as dislocation dynamics and molecular dynamics.

### Ab-Initio

In atomistic modelling the *ab-initio* technique holds a unique position amongst modelling methods. This is because it is used to underpin more emprical modelling methods. Since the forces on the nuclei are calculated, it is possible to use this information to update the positions of those nuclei, and carry out *quantum molecular dynamics* (QMD). This technique is used where the errors or uncertainties observed in longer length scale models are large, such as crack propagation. However, the main work carried out with these methods is to calculate properties of matter, against which other models can be assessed or calibrated. Such data include elastic constants and phonon spectra, lowest energy structures and phase boundaries. By carrying out a number of calculations covering a large portion of configuration space, a database of forces for a range of atomic arrangements can be built up. A comparison between the forces predicted by empirical schemes, such as the embedded atom method (EAM) scheme (see section 2.3.3) and those in the database can then be made. The parameters within the EAM scheme can be varied, and the comparison against the database repeated. A method which undertakes this comparison by minimising an objective function has been developed by Ercolessi and Adams.[53] This *force matching method* includes both experimental data in the databases, as well as weighting parameters. By choosing configurations which cover various situations, e.g. interstitials, next to vacancies, surfaces and defects, then the EAM scheme can be developed to have a wide *transferability*.

The *ab-initio* technique covers a range of calculational methods in which the quantum description of the wave-particle duality of electrons is used to determine the forces acting on the atomic nuclei. At its most fundamental level this description requires one to solve Schrödinger's equation for each of the electrons in the system. Because of the intensely complex nature of finding such solutions for even modest sized problems, alternative methods have been developed. The most widely used technique is density functional theory (DFT). In this case the function at the heart of the method is the electronic density. In DFT the electrons are replaced with non-interacting particles moving in an effective potential. However, this leaves two difficulties, namely the interaction of the electrons caused by the antisymmetric nature of the electronic wavefunction, and the Coulombic interaction between the electrons. These are the

*exchange*[e] and *correlation*[f] terms. One solution, based on the concept of a uniform electronic gas, is the *local density approximation*(LDA) in which the electronic density is described by a spatially varying functional. A modification to the LDA is given by the *generalised gradient approximation* (GGA). Whereas in LDA the electronic density is considered, in the GGA the gradient of the electronic density is included, as well as the density itself, in the functional description.

### Static Calculations

The variables associated with each particle are its position and its momentum. The mathematical space encompassed by these variables is known as the phase space. This concept is important because we can use this space to ensure that our calculation is consistent with the real world, whose behaviour we are trying to examine. Thus by ensuring that the phase space encompassed by the model has the same extents as the phase space covered by the system then we get valid results. Suppose we were to set up a simulation containing a single particle which is not at rest, or in the ground state, and then run the simulation for an infinite length of time. In the simulation that particle would pass through every position and be possessed of every value of momentum which the model will allow. Similarly, if the simulation was set up with an infinite number of particles with suitable positions and momenta such that the system was in equilibrium, then at any instant every value of position and momentum allowed by the model would be contained within the simulation. Clearly these two extremes are not possible. However, it can be seen that the location in phase space of the single particle, averaged over the whole of the (infinitely long) simulation is the same as the instantaneous location in phase space of the infinitely large simulation, averaged over all the particles. This is known as the ergodic hypothesis. This hypothesis is used to describe the phase space encompassed by the model by simulating a finite number of particles, and averaging their individual phase locations over a finite number of simulation steps.

Another mathematically defined constraint which is used in order to relate the behaviour of the small system of the simulation to macroscopic observable behaviours is related to the ergodic hypothesis described above. This is Louiville's Theorem which

[e]The electrons are *fermions*, that is the *Pauli excusion principle* states that no two fermions can occupy the same quantum state. Therefore when one electron is exchanged (labels swapped) with an otherwise identical electron the sign of the wavefunction is reversed.

[f]In a system of interacting particles subject to quantum mechanics, the description of each of the particles includes terms from the other particles. This makes the problem a more difficult form of the n-body problem in classical mechanics.

states that any of the microstates which can be accessed have an equal probability of being sampled. This is accomplished by showing that the density of states close to the current state is uniformly distributed, and that this density of states does not vary over time.

In order to utilise the results of the phase space averages these numbers must be converted into useful thermodynamic quantities. The averages over some system are known as ensemble averages, and a variety of ensembles are used, depending on which quantities are conserved. In standard statistical mechanics there is no issue regarding the numbers of particles, whereas there is difficulty accessing more fundamental quantities such as energy. Consequently most of those ideas are cast using the canonical ensemble (NVT), in which the number of particles, $N$, the volume, $V$, and the temperature, $T$, are held fixed. However the concept of temperature is difficult to associate with a single particle. On the other hand, since in molecular dynamics we have a closed system and all the energy derives from the initial conditions, the energy of each particle is defined. In this case, we make use of the microcanonical ensemble (NVE) in which $N$, $V$, and energy, $E$, are held constant.

The macroscopic quantities derived using statistical mechanics make the assumption that the proportion of the system which differs by any significant amount from the average value is very small and can be discounted. This assumption can be shown mathematically to be correct.[70,128] Further, in comparing the variances observed over the full phase space trajectory with the phase space sampled by a finite simulation, the precision is independent of the size of the full trajectory sample. What this means, is that the ensemble average $\langle X \rangle$ is approximately the same as a snapshot average $\langle x \rangle$, but the standard deviation of that average will depend on the number of samples in the snapshot.

### Thermodynamic Quantities

In order to relate our simulation to real experiments, we need to measure similar properties. Derivation of these formulae is given in [70, 128], so the results only are given here. The function for the temperature starts by relating the entropy, $S$, to the number of microstates, $\Omega$, as

$$S = k_B \ln \Omega \qquad \text{and} \qquad \frac{1}{T} = \left( \frac{\partial S}{\partial E} \right)_{Nv} \tag{2.14}$$

where $k_B$ is Boltzmann's constant. From this an expression for $k_BT$ as an ensemble average of the kinetic energy, $\langle E_k \rangle$, can be derived, which reduces to

$$k_BT = \frac{2}{3N}\langle E_k \rangle \tag{2.15}$$

Since the kinetic energy of each particle is $\frac{1}{2}m\mathtt{v}^2$, then the ensemble average kinetic energy is $\frac{1}{2N}\sum m_i\mathtt{v}_i^2$. If the masses are uniform, temperature is now

$$T = \frac{1}{3mNk_B}\sum \mathtt{v}_i^2 \tag{2.16}$$

Similarly pressure, which derives from the virial theorem, is obtained using a measure of the momentum flux across a plane. In general the momentum flux comes from two contributions; the particles which cross the plane and the change in momentum of the particles near the plane due to the forces which exist between particles on either side of the plane. From the definition $P = \frac{F}{A}$, the pressure is

$$\langle P \rangle = \frac{2N}{3v}\langle E_k \rangle + \frac{1}{3v}\langle \sum\sum F \cdot q \rangle \tag{2.17}$$

Since the forces and positions are vectors, this expression for the pressure can be expressed as a tensor. Consider a stress tensor

$$J_{\alpha\beta} = \begin{pmatrix} J_{xx} & J_{xy} & J_{xz} \\ J_{yx} & J_{yy} & J_{yz} \\ J_{zx} & J_{zy} & J_{zz} \end{pmatrix} \tag{2.18}$$

Then this tensor can be written as

$$J_{\alpha\beta} = m\sum \mathtt{v}_\alpha \mathtt{v}_\beta + \frac{1}{2}\sum_{i\neq j} q_{ij\beta}F_{ij\alpha} \tag{2.19}$$

The hydrostatic pressure is given by the ensemble average of the trace of this tensor

$$P = \frac{1}{3v}\left\langle \sum_{\alpha=x,y,z} J_{\alpha\alpha} \right\rangle \tag{2.20}$$

Notice that this formula has a volume component. This means that although the pressure for the whole simulation can be obtained from this expression, the stress on each atom is given as a stress–volume term, the volume of an atom being difficult to calculate.

### 2.2.1 Monte-Carlo

The *Monte Carlo* (MC) method is based on sampling phase space by the judicious use of random numbers. It is this part of the algorithm from which the name derives. In this simulation method the positions of the particles are set up at random and the new state is compared in some way to the previous state. Because the acceptance or otherwise of the new state depends only on the previous state, and on no other, the sequence of states sets up a sequence known as a Markov chain. The method was originally devised by Ulam, Fermi, von Neumann and Metropolis at Los Alamos during the 1940s to study neutron transport in nuclear explosions.

The reasoning behind the method is based on the difference between position and momentum in the formulation of ensemble averages. It can be shown that many fundamental properties of materials depend only on positions, and not on the atomic momenta. Therefore it is only necessary to set up a random array of positions, and then measure the quantities needed. After many such samplings, the ensemble average can be calculated. However, the number of random states is large compared to the number of states which are close to the true average. If we give the probability of finding a sample of material in a particular state as $\rho(\mathrm{s})$, then the ensemble average is given by the integral of $\rho(\mathrm{s})$ over all s. But the fraction of states, s, actually contributing to the integral is small, approximately $e^{-N}$, where $N$ is the number of particles. So for even a small system of, say, 100 particles, the ratio of states of relevance (i.e. $\rho(\mathrm{s})>\approx 0$) is $e^{-100}$, or $10^{-44}$. To get the correct average, then, would require $10^{44}$ samples, clearly an unfeasible task. Metropolis *et al*[109] developed an algorithm to deal with this, in which any possible state is compared to the current state. If the energy of the new state is lower than the current state then the new state is accepted. If, however, the new state has a higher energy than the current state, then the new state is only accepted with a probability which diminishes exponentially as the energy difference increases. This probability is given by

$$\exp\left(-\frac{1}{k_B T}(E_b - E_a)\right), \tag{2.21}$$

where $E_a$ is the energy of state $a$, and $E_b$ is the energy of state $b$. This means that the system will converge asymptotically towards sampling the correct $\rho(\mathrm{s})$ states, and a number of steps must be discarded during this converging process. After the converging process all states sampled will have a significant $\rho(\mathrm{s})$.

There is one further point of note from this acceptance probability criterion (equation 2.21). Now since the connection between the states is a Markov chain, which

requires that the sum of probabilities over all states (in equilibrium) is unity, the inclusion of the $-1/k_BT$ term within the exponential leads the Metropolis Monte Carlo method to naturally sample states with a Boltzmann distribution. Therefore the method will sample from the canonical, or NVT, ensemble.

Monte Carlo methods are used in a large number of problems, from the original neutron transport and related sub-atomic particle behaviour, through atomistic, ionic and molecular to mesoscale and granular behaviour and also to study financial market behaviour, disease spreading, population growth, animal migration and seismology among many others.

### 2.2.2 Molecular Dynamics

Molecular Dynamics is a mature technique, having been applied early on in the development of computers. There are a number of texts available which describe the molecular dynamics method and the interested reader is referred to [2, 59, 70, 128]. However, due to the importance of understanding the physics which underpins the modelling which is utilised within this thesis, an explanation is given here.

#### Physical Basis

The understanding of the behaviour of many-body systems derives from Newton's equations of motion. However, these principles are intimately linked with the underlying concept of energy conservation and minimisation. In the molecular dynamics scheme, assumptions and simplifications are made about the nature and behaviour of interacting particles. The most fundamental simplification is the replacement of electronic structure and behaviour with a model based on the concept of jellium[g]. In this model, the metallic ions, and their bound electrons, are represented as a point in space. The interaction between these particles is given by a mathematical description of the electric field which exists due to the charged nature of the electrons surrounding the nucleus. Thus the atomic behaviour is given as that of a point object moving within some potential field.

A simple analogy for this empirical atomic behaviour would be a ball on a track which is curved upwards at each side of some central point. When the ball is placed on the track, away from the central point, it has some potential energy due to its position in the gravitational field. On release, that potential energy is converted to kinetic

[g]In quantum mechanical modelling the *jellium* model smears out the positive charge of the ions and their bound electrons to a uniform gas. This enables the model to concentrate on the behaviour of the valence electrons, which are free to move through the resultant positive background.

energy as the ball travels down the track. After passing through the central point, the kinetic energy acquired during descent is converted back to potential energy as the ball rises through the gravitational field again. At some point, all of the kinetic energy is returned to potential energy (dissipative effects such as friction are ignored here), and the ball begins to fall again. Thus the total energy of this system is conserved.

An extension of this model then is to replace the track with a curved bowl-like surface. This bowl is certainly not circular but rather has smooth indentations created by the neighbouring atoms. Consequently as the atom descends towards the central minimum it may feel forces normal to its horizontal direction of travel. Thus it will not usually pass through that minimum point, but will pass by to one side. This causes the motion of the atom to be asymmetric within its own environment. This asymmetry has an effect on the potential field in which the atom moves. The effect then of such movement is to change the shape of the bowl itself. Similar motions of the neighbouring atoms will also affect the shape of the bowl surrounding the atom. After some time the motion of the atom can appear to be chaotic as the atom moves back and forth about some imaginary central point. In this framework, the total energy of the system is the additive sum of the disparate energies attributed to the processes affecting the system. In the simplest case, then, the total energy is the sum of the potential energy and the kinetic energy,

$$E = V + KE. \tag{2.22}$$

Now, work is given by the force on a body, multiplied by the distance which the body moves in response to that force

$$W = f\Delta r, \tag{2.23a}$$

and work done is given by the reduction in energy as a body moves through a potential field. Now

$$W = -\Delta V \tag{2.23b}$$

hence

$$f\Delta r = -\Delta V \tag{2.23c}$$

and

$$f = -\frac{\Delta V}{\Delta r} \qquad \left(= -\frac{\partial V}{\partial q}\right). \tag{2.23d}$$

From Newton's second law ($f = ma$), we can see that the acceleration is proportional to the gradient of the potential $\left(-\frac{\partial V}{\partial q}\right)$.

So the force is given by the gradient of the potential field, and the kinetic energy is given by the form

$$KE = {}^1\!/_2\, m\mathtt{v}^2. \tag{2.24}$$

The mathematical basis used to calculate the positions of particles interacting in this way follows Hamilton's variational principle. There are two equivalent descriptions of the many–body problem. In a system where energy is conserved, where all forces derive from some potential energy function $U$, then the Lagrangian, a function of the atomic positions, velocities and time,

$$\mathcal{L} = \mathcal{L}(q_i, \dot{q}_i, t), \qquad \dot{q} \equiv \frac{\partial q}{\partial t} \tag{2.25}$$

satisfies the Lagrange equations

$$\frac{d}{dt}\frac{\partial \mathcal{L}}{\partial \dot{q}_i} - \frac{\partial \mathcal{L}}{\partial q_i} = 0. \tag{2.26}$$

From this description derive the equations of motion,

$$\mathcal{L} = \sum_i \frac{1}{2} m\dot{q}^2 - V(q_i) \quad \text{and} \tag{2.27a}$$

$$-\frac{\partial V}{\partial q_i} = f_i = m\ddot{q}_i, \qquad \ddot{q}_i \equiv \frac{\partial^2 q}{\partial t^2} \tag{2.27b}$$

where $f$ is the force on particle i.

Of course, the potential energy and kinetic energy terms are intimately linked; the potential energy is a function of the atomic positions, the kinetic energy is a function of the velocity, the velocity is modified by the acceleration, the acceleration is a function of the force and the force is a function of the slope of the potential at the position of the atom. Mathematically this is described as

$$\text{Potential energy} = V(q) \tag{2.28}$$

$$\text{Kinetic energy} = \frac{1}{2}mv^2 = \frac{1}{2}m\dot{q}^2 \tag{2.29}$$

$$\text{Force} = ma = m\ddot{q} = -\frac{\partial V}{\partial r}. \tag{2.30}$$

The minus sign in the last equation indicates that the force tends to reduce the potential energy.

Alternatively the system may be described using the Hamiltonian rather than the Lagrangian. If the velocities are replaced by momenta ($p_i = m\dot{q}_i$), then the Hamiltonian is

$$\mathcal{H} = \sum_i \dot{q}_i p_i - \mathcal{L}_i \tag{2.31}$$

where $\mathcal{L}$ is the Lagrangian described above. Whilst both the Lagrangian and Hamiltonian are time dependent functions, the Hamiltonian is more readily observed to relate to the simplistic description given above when it is recast in the time-invariant form

$$\mathcal{H} = \frac{1}{2}\sum_i \frac{p_i^2}{m} + V(q_i) = E. \tag{2.32}$$

Whereas the Lagrangian is the difference between the kinetic and potential energies (equation 2.27a), the Hamiltonian is the sum of these two parts. Consequently in a closed system, where energy must be conserved, the Hamiltonian remains constant. This fact can be used to ensure that the integration algorithm is behaving as expected. Taking the time derivatives of this form gives the differential equations

$$\dot{q}_i = \frac{\partial \mathcal{H}}{\partial p_i} \text{ and } \dot{p}_i = -\frac{\partial \mathcal{H}}{\partial q_i} \tag{2.33}$$

which can be used to calculate the trajectories of the particles.

### Algorithms

The purpose of any code used in molecular dynamics studies is to calculate the positions of and forces on the particles being investigated. These quantities are then used to derive a range of other quantities used in order to examine some physical behaviour. As can be seen from equation 2.33, there is a cyclic nature to the set of equations of motion. So the code is required to work out the gradient of the potential, and then use that to update the velocities and positions of the atoms, and then to repeat that exercise for the time required for the simulation.

There have been many schemes devised for carrying out this kind of time integration. The purpose of examining different ways to carry out these integrations is to increase the time step used, and hence reduce the computational cost in carrying out the required simulation. However, in molecular dynamics, the potential function used to describe the atomic interaction actually derives from the quantum mechanical description of electronic structure. This quantum mechanical description includes the repulsive forces arising from the Pauli Exclusion Principle. Consequently the gradient of the potential function rises rapidly as the separation of the atoms is

reduced. Therefore any calculation which makes an estimate of the gradient of the potential at some distance from the current atomic position based on the current gradient will have an increasing error as the atomic separation is reduced. This puts a limit on the time step which can be used in the calculation, and negates the gains which may be obtained from more complex, higher order schemes. Two of the most popular for molecular dynamics are the leap-frog and predictor–corrector. Schemes of the latter kind have been devised by Gear,[62] Beeman and Berendsen.[2] Whilst predictor–corrector schemes can be used, the more commonly used scheme is that due to Verlet[150] which is a leap–frog scheme. The preference for this particular method is that it yields better energy conservation than the predictor–corrector methods. The basic algorithm derives from the Taylor expansion of position

$$q(t+\triangle t) = q(t) + \triangle t\dot{q}(t) + \frac{\triangle t^2}{2}.\ddot{q}(t) + \frac{\triangle t^3}{3!}.\frac{d^3q}{dt^3}(t) + \mathcal{O}(\triangle t^4). \tag{2.34}$$

An advantage can be had by adding the equivalent expression for $r(t-\triangle t)$ (which eliminates odd-ordered terms) and rearranging to get

$$q(t+\triangle t) = 2q(t) - q(t-\triangle t) + \triangle t^2\ddot{q} + \mathcal{O}(\triangle t^4). \tag{2.35}$$

Notice that the term with the velocity has dropped out as this is an odd-powered term. This means that an estimate of the velocities must be made, if this quantity is needed for another calculation. Estimates for this can be made at both the half-step

$$\dot{q}(t+\frac{1}{2}\triangle t) \approx \frac{q(t+\triangle t) - q(t)}{\triangle t} \tag{2.36}$$

or via a central difference estimate

$$\dot{q}(t) \approx \frac{q(t+\triangle t) - q(t-\triangle t)}{2\triangle t} \tag{2.37}$$

An improvement which explicitely includes the velocities is the *velocity–Verlet* scheme

$$q(t+\triangle t) = q(t) + \dot{q}(t)\triangle t + \frac{1}{2}\ddot{q}(t)\triangle t^2 \tag{2.38a}$$

$$\dot{q}(t+\frac{\triangle t}{2}) = \dot{q}(t) + \frac{1}{2}\ddot{q}(t)\triangle t \tag{2.38b}$$

$$\ddot{q}(t+\triangle t) = -\frac{1}{m}\nabla V(q(t+\triangle t)) \tag{2.38c}$$

$$\dot{q}(t+\triangle t) = \dot{q}(t+\frac{\triangle t}{2}) + \frac{1}{2}\ddot{q}(t+\triangle t)\triangle t \tag{2.38d}$$

used in the LAMMPS code and hence in the work described here.

### Ensemble Simulations

Many of the quantities calculated by molecular dynamics are either calibrated against or used to compare to quantities obtained from experiments. In contrast, experiments are not able to maintain the ensemble constants used in the microcanonical ensemble (NVE), other than that of the number of particles. Rather, experimentally the pressure, $P$, and temperature, $T$, are held fixed. In order to simulate such experiments a method has to be devised to hold these derived quantities at some fixed value. This problem is solved by considering which fundamental variables are related to the derived quantities, and then artificially modifying the fundamental quantities in order to maintain the system at the desired state. The temperature (equation 2.16) is related to the atomic velocities by

$$T = \frac{1}{3mNk_b} \sum \mathrm{v}_i^2 \tag{2.39}$$

so it can be seen that to change the temperature from its calculated value, $T$, to the desired value, $T'$, the velocities need to be scaled by a factor $\lambda$

$$\lambda = \sqrt{\left(\frac{T'}{T}\right)} \tag{2.40}$$

An issue arises in that such scaling, if performed directly, does not allow the system to evolve naturally across phase space, and the trajectory described is not the correct one. This fact is caused by the relationship between the Hamiltonian, which describes the energy of the system, and the velocities, or rather momenta, which contribute to the energy. Thus if the velocities are modified without taking account in the other terms within the Hamiltonian then energy is not conserved and the trajectories will not be followed correctly. Consequently the phase space traversed by such a scheme does not follow that of a canonical ensemble.

Several schemes have been proposed which are based on some form of velocity rescaling. A simple rescaling method is that due to Berendsen.[17] Here the value of the rescaling parameter is calculated so that the desired temperature is reached after some number of timesteps. The Andersen thermostat[6] mimics a heat bath by selecting a number of particles and rescaling their velocities to those of a Boltzmann distribution centred about the desired temperature. The Langevin thermostat adds a random quantity to each velocity term. This is sometimes described as 'white noise'. However, this can lead to some atoms having an excessive velocity, and a 'frictional' force, proportional to the atomic velocity is used to reduce such effects. The size of

the random distribution and the frictional force are balanced to maintain a constant temperature.

Dissipative Particle Dynamics considers the separation and relative velocities of pairs of particles. The force calculation for each particle is modified as a result to add random and dissipative forces. The advantage of this scheme is that rotational and translational momenta are maintained. This means that processes which utilise transport properties will be observed, rather than being damped out as occurs with most thermostats.

Care has to be taken with velocity rescaling schemes, however. The modification to the velocities can cause the energy in the high frequency modes (spread in particle velocities) to be transferred to low energy modes, such as the rotational and translational whole body motion. This results in the temperature of the system falling towards absolute zero, even though the kinetic energy matches the desired value, due to the absolute (not accounting for whole–body motion) average velocity matching the target value. This phenomenon is known as the *flying ice cube*.[72] Ultimately, then, this issue causes a violation of the *equipartition* principle.

In order to ensure that the system follows that of a statistical ensemble, one has to return to the original expression for the energy of the system, the Hamiltonian. This problem was discussed by Nosé,[121] who realised that the velocities are directly related to the timescale of the simulation. Thus, by rescaling time, the requisite rescaling of velocities was achieved. This was accomplished by adding a dummy particle to the Hamiltonian function thus forming what is known as an *extended Hamiltonian*. The new particle, being part of the Hamiltonian function, is effectively connected to every particle in the system, thus acting as a bath. In order to control the behaviour, the mass of the dummy particle is set by the user and thus governs the responsiveness of the system. The kinetic energy of the particle is altered at each step, depending on how far the calculated temperature is from the desired value. The effect, then, of the new particle is to either add or remove energy from the system in order to bring it towards the user defined value.

In the Nosé formulation the time separation of the calculational step is now non-uniform. This adds complexity to the output which is a hindrance to understanding. This latter problem was addressed by Hoover,[77] who considered the derivation of the equations of motion from the extended Hamiltonian and was able to recast those equations in a form which now had a uniform time base. For most purposes this new formulation is adequate. However, the Nosé-Hoover equations of motion are

no longer directly connected to the Hamiltonian and the symplectic[h] nature of the scheme is lost. This issue only causes a problem when the simulation is run for very large numbers of timesteps, where the energy may tend to drift away from its correct value. More recently this problem has been examined by Laird and Leimkuhler.[18] They went back to the description of an extended Hamiltonian, and performed the necessary timescaling within the Hamiltonian by use of a Poincaré transformation. Now the equations of motion can be derived directly from the Hamiltonian and the system maintains its symplectic nature.

The concept of the extended Hamiltonian as a means of adjusting the temperature can be utilised to control the pressure.[6] Now, however, there is no property of the individual particles which is directly related to the pressure, and so can be modified. Rather, the pressure is a property of the density. Since the number of particles is fixed, the density can be modified by changing the simulation box volume. Clearly, modifying the volume alone is insufficient, as the particles will take some time to respond to the new box size, and stress waves will reverberate through the system as part of that process. Instead, the entire box is rescaled to the new volume. This is accomplished by using the volume itself as the extended Hamiltonian variable. Together with the volume is a representation of the mass and kinetic energy of the volume. As with the temperature scheme, the mass controls the responsiveness, and the kinetic energy is varied via a feedback mechanism from the pressure. By combining the Hamiltonian extended variable for temperature with that for pressure gives an ensemble in which both the pressure and temperature are held fixed, This is known as the isothermal-isobaric ensemble (NPT).[59]

### Dynamic Calculations

In many situations one wishes to understand the response of one group of atoms due to a change in the configuration of another group of atoms. For example, one might wish to examine the frictional behaviour of an interface, and the forces would be set up by imposing average motion onto atoms at some distance from the interface. One of the consequences of the relative motion of atoms is a resultant change in the kinetic energy of those atoms. This, then, causes a change in the temperature of the affected atoms. Over time, of course, the collisional nature of the simulation will cause the variations in kinetic energy to be averaged out. This dispersion of kinetic energy, driving the system towards equilibrium, is a function of the heat capacity of the material. This, however, highlights one of the failings of the molecular

[h] A simplectic manifold is a mathematic description of the phase space.

dynamics method. The model considers only the motion of the charged ions; the behaviour of the electrons is assumed to reach equilibrium so quickly that variations in electron temperatures does not affect the behaviour of the ions on the timescale considered (*cf.* section 2.3.1). This assumption is reasonable at high temperatures, but at not at low temperatures. This is because the heat capacity, and thermal behaviour, has two main contributions; that due to ions where the description is given by phonon behaviour, and that due to electrons which requires a quantum mechanical description. The balance over which term dominates changes as the temperature changes. At low temperatures there is little ionic motion, and the behaviour of the electrons is important. At higher temperatures the amplitude of ionic motion is considerably higher, and consequently phonon behaviour dominates.

### 2.2.3 Comparison of Molecular Dynamics and Monte Carlo methods

It is useful to briefly compare Monte Carlo and molecular dynamics methods. The most obvious difference between the methods is in the area of transport processes. Clearly the MD method, since it calculates momenta, can track the movement of particles explicitly and therefore examine properties involving the movement of atoms. In order to examine these processes using MC, a technique called *kinetic Monte Carlo* is used to modify the probability function. In this method events which would normally be excluded can have an increased likelihood based on some separately defined criteria. Whilst this makes it possible to study transport phenomena such as viscous effects, studying such behaviour is difficult. However, use of the probability modification does enable the study of rare events, which is much more difficult in MD. Thus it becomes possible to investigate phenomena such as chemical reactions, diffusion, grain growth, thermally driven phase transitions and dislocation motion[49] where the timescale is large. The behaviours which trigger the rare events have to be known beforehand, and some awareness of their likelihood is also required, in order to develop the probability functions. This severely limits the predictive capability of these methods. If the system configurations involved in transitioning from one state to another via the rare event are known, then it is possible to investigate these processes directly using either MC or MD, using a method known as the *nudged elastic band method*. Other schemes for preselecting events on order to reduce the simulation time have been developed, including *parallel replica* and *temperature–accelerated dynamics*.[147]

The MD method is naturally adapted to the microcanonical ensemble. In this statistically–based mathematical environment, the quantities describing the number

of particles, $N$, the volume of the simulation cell, $V$, and the total energy, $E$, of the system are held fixed (NVE). However, this set of predetermined quantities is not easily translated to the behaviour of real-world experimentation. In order to simulate different conditions, and to examine different behaviours, a range of statistically significant ensembles can be set up. The most commonly seen is that in which the temperature is held constant. This is known as the canonical ensemble (NVT). Setting up such a system in MD is quite difficult (see section 2.2.2), but in MC this ensemble falls naturally into the Metropolis algorithm. The use of ensembles other than the canonical can also be treated in a similar way but require more computational effort.

MC methods are also ideal for modelling systems where the timestep is not easy to know, or is non-uniform. An example of this is the study of magnetism. In the MC formulation it is possible to setup magnetic domains as the particles of interest; such a simulation is not possible in MD. Similarly, when examining regions of phase space with local minima, whereas MD may get stuck in one of the minima, it is easy to move MC from that situation by providing an unphysical push.

However a scheme for dealing with this issue has been devised. Simulated Annealing is a derivative of the Monte Carlo method, used to find energy minima of a system. In this scheme the phase space is described by some function $S$ and some potential new phase state $S'$. The probability that the system can transfer from state $S$ to state $S'$ is given by a probability function $\mathrm{P}(E, E', T)$ where $E$ and $E'$ are the energies of the states $S$ and $S'$ respectively. $T$ is a temperature descriptor, which describes the difference between two states $S$ and $S'$. As the calculation proceeds, the temperature value is reduced. An analogy used to describe simulated annealing is that of a ball bouncing into valleys between hills. The probability function P will indicate whether a particular bounce event is accepted. Initially the temperature descriptor, $T$, is very large. Thus the distance in phase space between $S$ and $S'$ is large, or the bounces of the ball are very high. As the temperature is reduced so the system will settle into a minimum (the ball will restrict its movement to a single valley). But since large regions of phase space have already been sparsely sampled, there is a higher probability that the minimum being sampled is the global minimum (deepest valley).

### 2.2.4 Mesoscale methods

The term *mesoscale* is used to cover a large range of modelling techniques in which the characteristic length scale (and therefore timescale) falls between that of atomistic and continuum methods. The aim, as with the the atomistic methods, is to capture

the behaviour of the material due to the motion of lower length scale elements, but without having to explicitly track those elements. In atomistic methods, it is the electrons which are described collectively via functional forms. In mesoscale methods it is the collective behaviour of individual atoms which is described via functions. There are, consequently, two varieties of mesoscale modelling which are used in the simulation of metallic response.

The first method considers the generally accepted mediators of plastic deformation as the computational element. Dislocation dynamics is a computational method in which individual dislocations are tracked as a series of connected line segments moving in an elastic medium. The two primary difficulties encountered are the multiplication of dislocations, leading to a large number of segments which need to be stored, and the calculation of dislocation–dislocation interaction (Peach-Koehler forces[123]). These forces are computationally expensive because they are long range in nature. Consequently this technique is primarily applicable to small numbers of grains and over small degrees of strain. However the method is ideal for understanding the interaction of dislocations both with each other[32] and with obstacles such as precipitates and grain boundaries. This modelling technique yields rates of dislocation multiplication and crystal hardening.

The second method for mesoscale modelling of the strength response of metals to stress is known as *crystal plasticity*. This scheme is based on the concept that slip occurs on slip systems, comprised of a slip plane and a slip direction. The active slip system in any particular crystal is determined by *Schmid factors* and the resolved shear stress for the system. In crystal plasticity calculations the Schmid factors for all possible slip systems are calculated. A degree of plastic deformation is then allowed on the system with the highest Schmid factor. One consequence of the slip allowed is that the crystal rotates relative to the loading axis. This changes the Schmid factors for all the systems, reducing the stress on the active system and increasing it on other systems. When the Schmid factors on more than one system are equivalent (and the highest) then both systems are activated and *multiple slip* occurs. In order to correctly model the change in response for each slip system, it is necessary to input hardening rules to the crystal plasticity model. These hardening rules can be obtained from either dislocation dynamics or from molecular dynamics calculations.

## 2.3 Potentials

The earliest description of interatomic forces came from developments in quantum chemistry during the 1920's. Many workers were considering the nature of molecular bonding and amongst them were Lennard-Jones, Morse, Rydberg and Buckingham. It was already accepted that the nature of interatomic interaction consisted of two prominent features; the sharply repulsive force at small separations due to the Pauli exclusion principle, and the attraction at long range due to Van der Waals' forces. The debate at that time concerned the increased attraction which occurs in molecular bonding. Lennard-Jones developed the idea of starting with the closed–shell structure of the inert gases and then removing electrons from the outer atomic orbitals and placing them in molecular orbitals of simple diatomic gases. The closed–shell structure should (apart from long ranged, transitory Van der Waals' forces known as London forces) be purely repulsive. By removing electrons from the outer shells to molecular orbitals, an attractive force is set up between the ions which becomes dominant at larger separations.

### 2.3.1 Born-Oppenheimer Approximation

The ability to describe the behaviour of atoms without explicitly following and calculating the wavefunctions of the individual electrons is due to a timescale separation known as the Born–Oppenheimer approximation.[20]

The complete atomic description is given by the Schrödinger equation for a particle in a potential field,

$$E\Psi = \mathcal{H}\Psi \tag{2.41}$$

where the Hamiltonian, $\mathcal{H}$, is given by the contributions from the various energy interactions and $\Psi$ is a wavefunction of the system. The Hamiltonian is given by

$$\mathcal{H} = -\frac{h}{2m} \bigtriangledown^2 \Psi(q) + V(q)\Psi(q). \tag{2.42}$$

Here $q$ describes the positions of the particles, the $\bigtriangledown^2\Psi(q)$ term is a kinetic energy term including Plank's constant, $h$ and the particle mass, $m$, and the $V(q)\Psi(q)$ term describes the potential field (*cf.* equation 2.22). The potential term, $V$, contains a sum of interparticle interactions, describing the relationships between the ions, $R$, and the electrons, $r$,

$$\underbrace{\sum_{\alpha,\beta} \frac{Z_\alpha Z_\beta}{R_\alpha - R_\beta}}_{\text{ion–ion}} + \underbrace{\sum_{i,j} \frac{Z_j}{r_i - R_j}}_{\text{ion–electron}} + \underbrace{\sum_{k,l} \frac{1}{r_k - r_l}}_{\text{electron–electron}} . \tag{2.43}$$

Here this sum expressed in *atomic units* (a.u.)[i] for clarity; otherwise we would have to include Planck's constant, the dielectric constant of the vacuum, electronic charge, and electronic mass.

The timescale associated with the electrons is about three orders of magnitude shorter than that of the ions. As a consequence, when considering electronic motion, the ions are effectively static. Conversely, the electronic behaviour is so rapid that the electrons can be assumed to be in local equilibrium when considering ionic motion. Therefore the electron–electron and ion–electron interactions can be taken as fixed when focussing on the ion–ion interaction. This second assumption then enables the use of empirical potentials to describe the atomic behaviour in molecular dynamics.

Computationally the total potential energy is given by a sum over all the atoms

$$V(q) = \sum_i E_i \tag{2.44}$$

In this sum the energy contribution from each atom is independent of the other atoms. This assumes, then, that the energy derived from bonded electronic orbitals can be divided uniformly between the bonded atoms. When modelling purely metallic bonding, the *jellium* model is invoked. In this model, the valence electrons are effectively 'shared' between all the atoms in the system.

It should be noted that the assumption within the approximation, i.e. that the mass and timescales of the electrons, when compared to the ions, means that the electronic structure is in local equilibrium, is not truly valid.[136] At low temperatures (below the Debye temperature, which for many metals is above room temperature) quantum effects are not negligible. At high temperatures, the contribution to the thermodynamic behaviour by the electrons, both in terms of the electron temperature (the thermal kinetic energy stored within the electronic structure), as well as the electron–electron and the electron–ion conduction becomes significant. These effects have been investigated by Koči *et al*[94] who studied the shock–induced melting of Ni using a two–temperature model. Their model separated the temperature of the electrons from that of the ions, which allowed the electronic structure to conduct heat faster than that allowed for by ionic motion alone. The effect of this was to conduct heat away from the shock front into the cold material ahead of the shock, and therefore the temperature behind the shock is reduced, for a given pressure, and consequently the shock pressure at which melting is observed is increased when compared to the regular MD simulation.

[i] In the system of atomic units, length is in units of the Bohr radius of the hydrogen atom; energy is the Hartree energy; time is given by $\hbar/E_H$ where $E_H$ is the Hartree energy.

### 2.3.2 Pair Potentials

The simplest scheme to describe the interaction of atoms is to consider, for each atom–neighbour pair, how the energy, $E_i$, varies with separation, $r$. The total energy for each atom is then given by summing the calculated energy over all of the neighbours Such models fall into the category of *pair potentials* which consider each host–neighbour pair independently of any other atoms.

#### Lennard-Jones

The Lennard-Jones potential[61] is probably the most widely used interatomic potential. Its simple description is easy to appreciate and is readily implemented in computer codes. A very accessible assessment of the paper is given by [71].

The model itself is a mathematical form which mimics both the short–range repulsion and the long–range attraction between atoms.

$$V(r) = 4\epsilon \left[ \left(\frac{\sigma}{r}\right)^{12} - \left(\frac{\sigma}{r}\right)^{6} \right] \tag{2.45}$$

where $r$ is the interatomic separation distance, and $\sigma$ and $\epsilon$ are parameters. The $(\frac{1}{r})^{12}$ term dominates at short distances, whereas the $(\frac{1}{r})^6$ becomes prominent as $r$ increases (see figure 2.13). Significantly, the main features of the interaction are readily apparent from the equation. The function evaluates to zero at $r = \sigma$, the well depth is given by $\epsilon$ and the function minimum occurs at $r = 2^{\frac{1}{6}}\sigma$. This enables the units used in the simulation to be rescaled readily to the natural units of the potential form, further simplifying the computations required. If distance is given by $\sigma$ and energy by $\epsilon$, then time is in units of $\sqrt{\frac{m}{\sigma^2}}$. From this, then, the units of other required parameters (pressure, velocity etc) can be determined.

It should be noted that there are a large number of alternative pair potentials which have been developed. Two, which are based on an exponential function, are given here as examples.

**Morse**[118]

$$V(r) = D_e(1 - e^{1-a(r-r_e)})^2 - D_e \tag{2.46}$$

**Buckingham**[31]

$$V(r) = Ae^{-Br} - \frac{C}{r^6} \tag{2.47}$$

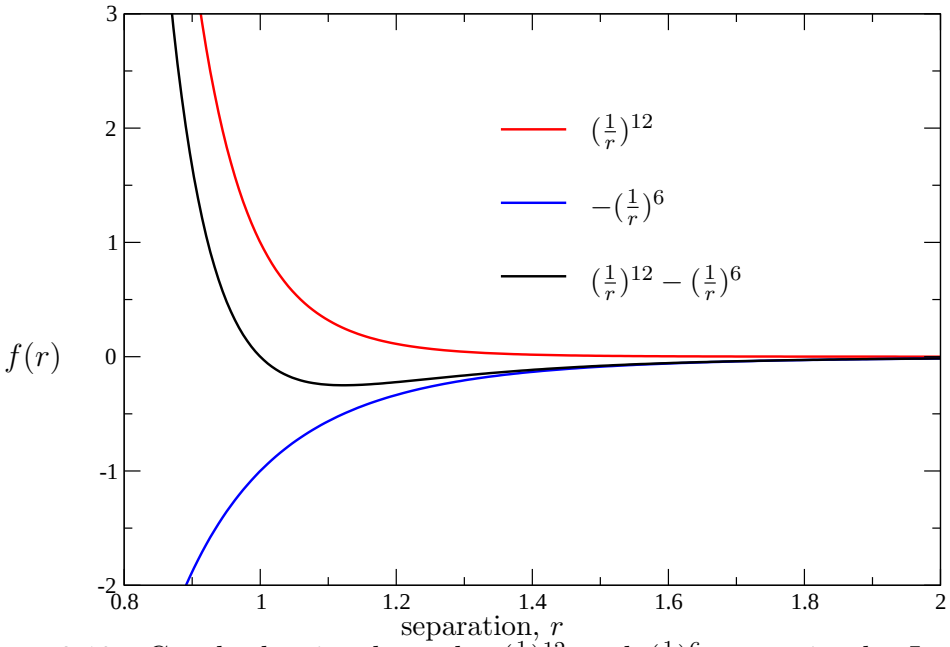


Figure 2.13: Graph showing how the $(\frac{1}{r})^{12}$ and $(\frac{1}{r})^{6}$ terms in the Lennard-Jones potential combine to form the repulsive core and attractive tail

### Issues

There are several issues which arise with the above schemes simply because they are pair potentials.[54] That is, the fact that the total energy is given by a simple sum over the each of the neighbours with no consideration of the other neighbours in each calculation leads to some non–physical results.

The first issue is that the solid structure resulting from pair potentials is a close packed structure. Therefore more open structures such as BCC or the diamond structure are not reproduced. Indeed, although the FCC structure is readily formed, the HCP structure is more energetically favourable.[137,149]

Pair potentials predict a vacancy formation energy equivalent to the sublimation energy whereas experimentally the vacancy formation energy is about one third of the sublimation energy.[54,126]

However the most well-known issue, when dealing with shear and plasticity, that pair potentials predict is related to the elastic constants [j]. Specifically, pair potentials predict the elastic constant equality $C_{12} = C_{44}$. This relation does not hold for transition metals.[59] Indeed, the ratio $C_{12}/C_{44}$ is around 2 for most metals, and is 3.7 for gold.[54] This issue in particular is important when trying to understand the mechanical behaviour of the metal being simulated, since these shear moduli govern the nature

[j] The elastic constants relate the stress tensor to the strain tensor under infinitessimal strains (see section 2.4.2).

of shear stress development, and hence dislocation formation. Consequently pair potentials are not ideal for the work being undertaken here.

### 2.3.3 Many-body Potentials

In order more realistically to reproduce the known behaviours of most elements in the solid crystalline state requires that the presence of many neighbours be accounted for within the potential scheme. This applies especially to the elements with more complex electronic structures and which exhibit allotropes with lower packing densities and lower symmetries than the close–packed FCC structure. But even the FCC metals are not simple to model, and many schemes have been developed to deal with the problem.

In one of the earliest attempts a three–body term is added to an underlying two–body (pair) function in order to reproduce the solid and liquid structures of silicon.[140] A more generic system, however, is based on the concept of the valence electrons forming a background negatively charged 'jellium' into which the positively charged ions are embedded. This system, known generically as the embedded atom method (EAM), is the system upon which the potential used in the simulations presented here is based. Consequently a description of the mathematical scheme is presented below.

#### Embedded Atom Method

The EAM scheme as a generic potential method was developed by Daw and Baskes.[47,48] The general concept encompasses the idea (like that in the Lennard-Jones scheme above) that the total energy of each ion (atom) is the sum of a repulsive term and an attractive part. The repulsive part arises from the ion cores and the Pauli exclusion principle. The attractive part, on the other hand, arises due to the consideration of metallic bonding. The metallic bond can be conceived of as a sharing of valence electrons between all the atoms in the metal. Therefore, if an ion is removed from its lattice site, the atom is positively ionised, and the remaining lattice is negatively charged. Therefore the embedding energy is the reduction in energy as the positively charged ion core is placed into the background 'sea' of electrons.

In the EAM scheme whereas the repulsion between ions is a pairwise (i.e. independent of the other neighbouring ions) interaction, the attractive (embedding) term is dependent upon the electron density at the atom site. This, then, requires knowledge of all the neighbouring atoms, both numbers and distances.

The potential energy of the system is given by the following expression.

$$V(q) = \sum_i F_i(\bar{\rho}_i) + \frac{1}{2}\sum_i \sum_{j \neq i} \phi_{ij}(r_{ij}) \tag{2.48}$$

where $r_{ij}$ is the distance between the atom $i$ and its $j^{\text{th}}$ neighbour. This expression can be rewritten as a sum over the atoms.

$$V_{tot} = \sum_i \left( F_i(\bar{\rho}_i) + \frac{1}{2}\sum_{j \neq i} \phi_{ij}(r_{ij}) \right) \tag{2.49}$$

The calculation for each atom consists of two parts

$$V_i = \underbrace{F_i(\bar{\rho}_i)}_{\substack{\text{embedding} \\ \text{term}}} + \underbrace{\frac{1}{2}\sum_{j \neq i} \phi_{ij}(r_{ij})}_{\text{pair term}} \tag{2.50}$$

The embedding function, $F(\bar{\rho}_i)$ is associated with the electron density at the site of atom $i$, and $\phi_{ij}(r_{ij})$ is the repulsion associated with the ion cores.

The embedding function is comprised of a sum over the neighbours of $i$

$$\bar{\rho}_i = \sum_{j \neq i} \rho_j^a(r_{ij}) \tag{2.51}$$

where $\rho_j^a(r_{ij})$ is the contribution made by the $j^{\text{th}}$ neighbour at a separation of $r_{ij}$ to the electron density at $i$.

The repulsive term, $\phi_{ij}$ is a description of the ionic interaction. Consequently the expression for $\phi$ can be given in terms of the effective charges

$$\phi(r) = \frac{(Z(r))^2}{r} \tag{2.52}$$

It is noted within the papers describing the system that the embedding function, $F(\rho)$ depends only on the element at $i$, and that the repulsive function $\phi_{ij}$ is a function only of the two elements $i$ and $j$. So for different element types, $A$ and $B$, the repulsive term is given by

$$\phi_{AB}(r_{ij}) = \frac{Z_A(r_{ij}) Z_B(r_{ij})}{r_{ij}} \tag{2.53}$$

This means that the scheme is readily adapted to the modelling of alloys, thus showing the versatility of the scheme. However, in general those workers who have derived EAM potentials for alloy systems have produced forms which are noticeably different from those developed for pure elemental studies.

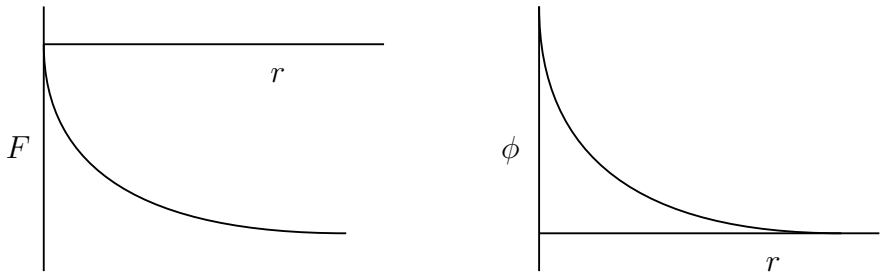


(a) EAM $F(\rho)$ (b) EAM $\phi(r)$

Figure 2.14: Form of EAM functions as described in Foiles *et al.*[60]

The development of a potential model using this scheme requires functional forms for the embedding energy, repulsive energy and electronic density. In general codes are built which take these three functions as tables of data and operate a look-up and interpolation algorithm to determine the values to be used. Foiles *et al*[60] gives guidance on these functions from an understanding of the general behaviours seen in *ab–initio* calculations. The embedding energy (relative to the free–atom energy) must be zero for zero electron density, have a negative slope and positive curvature. This is shown schematically in figure 2.14a. The pair term, $\phi(r)$, is repulsive and the effective charge, $Z(r)$, must be positive and decrease with increasing separation, $r$ (see figure 2.14b).

The exact form of these functions can be varied in order to describe differing degrees of subtlety in the model, and for illustration two examples are given here.

A scheme derived from *ab–initio*, given in [60], uses knowledge of functions for the electronic density and pair repulsion to lead to the function for the embedding energy by comparing the total energy given by equation 2.48 to the Rose universal equation of state[131] given by

$$E(a) = -E_{sub}(1 + a^*)e^{-a^*} \tag{2.54}$$

Here $E_{sub}$ is the sublimation energy at zero temperature and pressure and $a^*$ is a measure of the volume deviation from equilibrium given by

$$a^* = \frac{\left(\frac{a}{a_0 - 1}\right)}{\sqrt{\frac{E_{sub}}{9B\Omega_0}}} \tag{2.55}$$

where $a$ is the FCC lattice constant at the current volume, $a_0$ is the equilibrium lattice constant, B is the bulk modulus, and $\Omega_0$ is the atomic volume at equilibrium.

The form for the electron density function, $\rho^a$, can be taken from *ab–initio* calculations. Using Hartree–Fock wave functions, the densities are given by

$$\rho^a(r) = n_s\rho_s(r) + n_d\rho_d(r) \tag{2.56}$$

where the subscripts $s$ and $d$ refer to the outer s and d electrons; $n$ and $\rho$ are the corresponding number of electrons and density due to the orbital wavefunctions respectively.

the $n$s are the numbers of electrons, and the $\rho$s are densities due to the orbital wavefunctions.

The pair repulsion is a function of $Z(r)$

$$Z(r) = Z_0(1 + \beta r^\nu)e^{-\alpha r} \tag{2.57}$$

$\alpha$, $\beta$, and $\nu$ are parameters. $Z_0$ is taken as the number of outer electrons of the atom and hence follows the group in the periodic table. That is, $Z_0$ would be 10 for Ni, Pd and Pt and 11 for Cu, Ag and Au. The parameters are adjusted to provide a fit to known elastic constants and vacancy energy. Then the repulsion function, $\phi(r)$ is given by inserting equation 2.57 into equation 2.52. As stated above, the values for the electron density (equation 2.56) and pair repulsion (equation 2.57) are taken together and then compared to the Rose universal equation of state (equation 2.54) to give the embedding term. This, then, enables the potential scheme to be used in high pressure simulations.

In contrast, Doyama and Kogure[50] have developed a simple model based on equation 2.49. The embedding function $F(\rho)$ is given by

$$F(\rho_i) = D\rho_i \ln \rho_i \qquad \text{where} \qquad \rho_i = \sum_{j\neq i} f(r_{ij}) \tag{2.58}$$

Consequently, two functions are needed, the pair repulsion, $\phi(r_{ij})$ and the density, $f(r_{ij})$.

$$\phi(r_{ij}) = A_1(r_{c1} - r_{ij})^2 e^{(1-c_1 r_{ij})} \tag{2.59}$$

$$f(r_{ij}) = A_2(r_{c2} - r_{ij})^2 e^{(1-c_2 r_{ij})} \tag{2.60}$$

The parameters, $A_1$, $A_2$, $c_1$, $c_2$ and $D$ are selected so as to reproduce the Born stability criteria stability, cohesive energy energy, energy of vacancy formation, stacking fault energy stacking fault energy and elastic constants, $C_{11}$, $C_{12}$ and $C_{44}$.

Doyama and Kogure simulated the generation of dislocations through bending and tensile deformation, and did not assess any pressure dependent properties.

Since the EAM describes a framework potential scheme, many workers have developed forms for the embedding energy, repulsive energy and electronic density. A scheme by Finnis and Sinclair[58] was developed at the same time as the EAM. Other workers who had developed parameters for this model have consequently described their potentials as being 'Finnis–Sinclair' form. However, this method can be seen as falling within the general EAM framework, but having a square root function for the embedding term.[92] Furthermore, the Sutton–Chen[141] form is described as an alternative implementation of the Finnis–Sinclair.[92] Other EAM forms have been developed including those by Ercolessi and Adams[53] and Mei and Davenport.[108]

The work presented in Chapter 3 uses the potential developed by Mishin *et al*[116] for copper, and labelled within that work as 'EAM1'. This potential was parameterised by use of the force-matching method,[53] with modifications as described in an earlier paper by Mishin.[115] The forms for the pair interaction, electron density descriptor and embedding function, together with the parameters, are given in appendix B. The parameters for the potential have been optimised by comparison to both experimental data as well as results from *ab initio* calculations. The fitting procedure ensures a match to the lattice constant, $a_0$, the cohesive energy, $E_0$, and the bulk modulus, $B$. Furthermore, included in the set of experimental data used in the fitting procedure is the intrinsic stacking fault energy, $\gamma_{\mathrm{SFE}}$. Importantly for this application, the short range portion of the potential was fit in a separate procedure, following a similar methodology to the equilibrium $r$, through the parameters $\{r_s^{(n)}, S_n\}_{n=1,2,3}$ and $Q$, to *ab initio* calculations of the energies of the FCC structure and a dimer (two–atom system) under strong compression.

### Comparisons

Erhart *et al*[55] compared different EAM potentials for aluminium. That paper mentions previous reports of weakness in available EAM Al potentials, but that shock simulations that have been carried out with, for example, iron potentials not fitted to high pressure data have enabled insight to be gained. However, the authors do point out that although the experimental Hugoniot is matched reasonably well, the development of plasticity (dislocation generation) in the models studied is very poor, with two potentials displaying a double–elastic behaviour, and the material remains elastic up to shock melting. Even for those potentials which do exhibit dislocation

generation under shock loading, this behaviour is observed to occur at anomalously high pressures.

Bringa *et al*[27] carried out a comparison of some EAM potentials for copper. They describe the different behaviours observed when single crystals are shocked along the three principal (high symmetry) crystal directions. The purpose of this work was to determine the suitability and transferability of these potentials in non equilibrium molecular dynamics (NEMD) shock simulations.

It should be noted that although the above discourse shows that the EAM has shown significant improvement over the pair potential schemes, this method is also spherically symmetric in its description. This, then, provides limitations for many of the transition metals. These metallic elements posess incomplete $d$ shells within their electronic structure, and these incomplete shells lead to a loss of spherical symmetry in their interatomic potentials. Comparisons of Cu and Al EAM potentials against *ab initio* calculations carried out by Boyer *et al*[22] and Černý *et al*[39] highlight some of the resulting difficulties. These papers show that the EAM scheme produced by Mishin produced a better match to the *ab initio* calculations than that of Ercolessi but Boyer *et al*[22] note that 'Aluminium presents a greater challenge to empirical potential description because of the directional nature of its interatomic bonding.' This bonding is a result of the anisotropic electronic densities exhibited by Al. Further work on Al potential schemes has been attempted by Schultz *et al*,[136] whilst Ni potentials have been developed by Kum.[97,98] In contrast, then, the more spherical nature of the electronic structure of copper lends itself to fitting by this method.

The difficulties shown for those transition metals exhibiting a highly symmetric FCC structure are considerably worse for those crystal structures with lower symmetry. There are EAM potentials available for bcc metals such as Ta,[152] Mo[156] and Fe[82,83] but low symmetry structures such as those exhibited by, for example, Pu cannot be modelled within this framework. An attempt to improve the EAM scheme to include angular terms has been developed by Baskes *et al*[15] (see appendix A). The modified embedded atom method(MEAM) scheme breaks down the embedding term into a set of angularly dependent terms through the use of Legendre polynomials.

## 2.4 Analysis Methods

Atomistic simulations can be considered to be experiments carried out in a computer. This has the big advantage that not only can the diagnostics which are used experi-

mentally be emulated, but the properties of the bulk of the material can be examined at the same time, thus enabling a test of the assumptions used.

Analysis of the simulation output is the most vital part of carrying out the simulation experiment, as it is the means by which physical insight is enabled. Of course, the type of analysis carried out, like the type of experimental diagnostic deployed depends upon the nature of the simulation, which in turn depends upon the information sought.

Analysis of atomistic calculations is also used as part of the development of new potentials. Often this work is used to compare the behaviour of the simulation with predictions from *ab-initio* calculations, and measured quantities, for example elastic constants, from experiments. The background to such calculations is given in many texts and papers, see for example Finnis,[59] Gülseren and Cohen.[68]

### 2.4.1 Velocity

The velocities of the atoms are quantities carried by the MD calculation. Consequently using velocities as part of the analysis of shock simulations is a natural and simple task. Experimentally, however, only the velocity of the free surface is known, except where magnetic gauges are used. Note that in both of these cases, the velocities are known only in the direction of the shock. In the calculation the velocities at all positions, both at the surface and in the bulk are known, simultaneously for any time during the simulation.

### 2.4.2 Stress

In section 2.2 the stress tensor on an atom was given by equation 2.19. This formula can be used to evaluate the pressure, as given by the trace of the stress tensor, equation 2.20. As noted, this tensor is written in a stress-volume form. Since the volume of each atom is not known, an average for a small region can be calculated by taking an average over some small volume, then dividing by that volume.

Furthermore, since the full stress tensor is available, estimates of the shear stress can be calculated. The hydrostatic pressure is given by the trace of the stress tensor

$$P = \frac{1}{3}\left(\sigma_x + \sigma_y + \sigma_z\right) \tag{2.61}$$

The von Mises stress is given by

$$9\sigma_{vm}^2 = (\sigma_{11} - \sigma_{22})^2 + (\sigma_{22} - \sigma_{33})^2 + (\sigma_{11} - \sigma_{33})^2 + 6(\sigma_{12}^2 + \sigma_{13}^2 + \sigma_{23}^2) \tag{2.62}$$

where $\sigma_1, \sigma_2$ and $\sigma_3$ are the principal stresses. As a simple estimate, since the off-diagonal terms are usually much smaller than the diagonal terms, equation 2.62 can be approximated by

$$\sigma_{shear} = \frac{1}{2}\left(\sigma_1 - \frac{1}{2}(\sigma_2 + \sigma_3)\right) \tag{2.63}$$

Since the stress measure is a fundamental part of the analysis of shock, this calculation is used frequently in shock simulations. The measure of pressure behind the shock is used as a means of checking the calculation against experimental data.

The measure of stress is of vital importance in the modelling of shock deformation. However, it is impossible to measure stress experimentally in a dynamic experiment. An answer to this problem is brought about by relating the strain, which is readily measurable, to the stress through the elastic constants. Hooke's law gives a linear relationship between the stress and strain for a body. For a body under arbitrary elastic strain, represented by a 3x3 tensor $\epsilon_{kl}$ the stress ($\sigma_{ij}$ or *Cauchy stress tensor*) is given by (making use of Einstein's summation notation)

$$\sigma_{ij} = C_{ijkl}\,\epsilon_{kl}. \tag{2.64}$$

Since the volume stress state of the element is unaltered either by bulk motion or rotations (the volume element is in equilibrium), the stress tensor must be symmetric, *i.e.*

$$\sigma_{ij} = \sigma_{ji}. \tag{2.65}$$

This implies that

$$C_{ijkl} = C_{jikl} = C_{ijlk} \tag{2.66}$$

If the stress and strain are represented in matrix notation, they can be simplified to *Voigt* notation. Here

$$[\sigma] = \begin{bmatrix}\sigma_{11}\\ \sigma_{22}\\ \sigma_{33}\\ \sigma_{23}\\ \sigma_{31}\\ \sigma_{12}\end{bmatrix} = \begin{bmatrix}\sigma_1\\ \sigma_2\\ \sigma_3\\ \sigma_4\\ \sigma_5\\ \sigma_6\end{bmatrix} \text{ and } \quad [\epsilon] = \begin{bmatrix}\epsilon_{11}\\ \epsilon_{22}\\ \epsilon_{33}\\ 2\epsilon_{23}\\ 2\epsilon_{31}\\ 2\epsilon_{12}\end{bmatrix} = \begin{bmatrix}\epsilon_1\\ \epsilon_2\\ \epsilon_3\\ \epsilon_4\\ \epsilon_5\\ \epsilon_6\end{bmatrix}. \tag{2.67}$$

From this the stiffness tensor $C$ becomes

$$[C] = \begin{bmatrix} C_{1111} & C_{1122} & C_{1133} & C_{1123} & C_{1131} & C_{1112} \\ C_{2211} & C_{2222} & C_{2233} & C_{2223} & C_{2231} & C_{2212} \\ C_{3311} & C_{3322} & C_{3333} & C_{3323} & C_{3331} & C_{3312} \\ C_{2311} & C_{2322} & C_{2333} & C_{2323} & C_{2331} & C_{2312} \\ C_{3111} & C_{3122} & C_{3133} & C_{3123} & C_{3131} & C_{3112} \\ C_{1211} & C_{1222} & C_{1233} & C_{1223} & C_{1231} & C_{1212} \end{bmatrix} = \begin{bmatrix} C_{11} & C_{12} & C_{13} & C_{14} & C_{15} & C_{16} \\ C_{12} & C_{22} & C_{23} & C_{24} & C_{25} & C_{26} \\ C_{13} & C_{22} & C_{33} & C_{34} & C_{35} & C_{36} \\ C_{14} & C_{22} & C_{33} & C_{44} & C_{45} & C_{46} \\ C_{15} & C_{22} & C_{33} & C_{44} & C_{55} & C_{56} \\ C_{16} & C_{22} & C_{33} & C_{44} & C_{55} & C_{66} \end{bmatrix} \tag{2.68}$$

Now Hooke's law is written as

$$\sigma_i = C_{ij}\,\epsilon_j \tag{2.69}$$

For isotropic materials, symmetry enables the strain to be split into a *hydrostatic* (volumetric) term and a *deviatoric* term

$$\epsilon_{ij} = \left(\frac{1}{3}\epsilon_{kk}\delta_{ij}\right) + \left(\epsilon_{ij} - \frac{1}{3}\epsilon_{kk}\delta_{ij}\right) \tag{2.70}$$

where the volumetric term (the trace of the strain tensor $\epsilon_{ij}$) represents a pure change in size, and the deviatoric part represents a change in shape. Now the stress may be written as

$$\sigma_{ij} = 3B\left(\frac{1}{3}\epsilon_{kk}\delta_{ij}\right) + 2G\left(\epsilon_{ij} - \frac{1}{3}\epsilon_{kk}\delta_{ij}\right) \tag{2.71}$$

where $B$ is the *bulk modulus* and G is the *shear modulus*. The bulk modulus can be determined from

$$B = \frac{1}{3}\left(C_{11} + 2C_{12}\right) \tag{2.72}$$

The bulk modulus, $B$, relates the response of the material (pressure, $P$) to a change in volume ($v$). Thermodynamically the bulk modulus is given by

$$B = -v\left.\frac{\partial P}{\partial v}\right|_T \tag{2.73}$$

but since the pressure, $P$, is related to the change in energy with volume, $v$

$$P = \left.\frac{\partial E}{\partial v}\right|_T \tag{2.74}$$

then

$$B = \left.\frac{\partial^2 E}{\partial v^2}\right|_T \tag{2.75}$$

This last relationship can be used in the calculation of the bulk modulus. By fitting a polynomial function to calculations of the energy at a range of volumes about the minimum, the second derivative can be determined readily. The shear modulus $(C_{11} - C_{12})$ can be determined from the second derivative of energy with lattice strain[107] by using a volume conserving strain

$$\epsilon = \begin{pmatrix} \delta & 0 & 0 \\ 0 & -\delta & 0 \\ 0 & 0 & \frac{\delta^2}{1-\delta^2} \end{pmatrix} \tag{2.76}$$

with an energy function

$$E(\delta) = E(-\delta) = E(0) + \left(C_{11} - C_{12}\right) v_0\,\delta^2 + \mathcal{O}(\delta^4) \tag{2.77}$$

where $v_0$ is the equilibrium volume.

Similarly, the modulus $C_{44}$ can be determined from the volume conserving monoclinic strain[107]

$$\begin{pmatrix} 0 & {}^1\!/_2\,\delta & 0 \\ {}^1\!/_2\,\delta & 0 & 0 \\ 0 & 0 & \frac{\delta^2}{4-\delta^2} \end{pmatrix} \tag{2.78}$$

with a corresponding energy function

$$E(\delta) = E(-\delta) = E(0) + {}^1\!/_2\, C_{44}\, v_0\, \delta^2 + \mathcal{O}(\delta^4) \tag{2.79}$$

The advantage of using the volume conserving strains (equations 2.76 and 2.78) is that $\Delta v = 0$, and appears only as a constant in the energy functions (equations 2.77 and 2.79) which means that there is neither a pressure nor a stress term in these functions.

### 2.4.3 Spatial Variations

The calculations described above are given for the entire simulation cell by taking the average values over the atoms. This methodology allows one to establish the spatial variation of those same quantities. This approach is not uncommon, and has been described by Kubota.[96] The premise is simple; the simulation cell is divided into a series of small regions. The variables associated with each atom within each small region is averaged and, where necessary, the volume of the small region is used in place of the entire simulation cell volume. In the simplest case, the small regions are created by dividing the cell dimension in the shock direction uniformly. This then gives a series of slabs, which enables a graph of value against position to be drawn. By further dividing each slab into smaller regions, one can determine a spread of values for each spatial coordinate; an error bar as it were.

The regions are usually created by subdividing the simulation cell uniformly into small boxes aligned with the cell axes. There is a drawback with this technique, which gets worse with smaller boxes, in the analysis of simulations where the crystal axes are aligned with the simulation cell, and hence the calculation. If the spacing of the small boxes is not an exact multiple of the crystal lattice spacing, then a situation can occur in which the number of atoms in a cell changes dramatically from neighbouring cells. The problem is due to an aliasing or Moiré effect. But the volume of the box is calculated to be identical to that of the neighbours. The consequence is that any average calculation which includes some density element (*i.e.* some quantity summed over the atoms and hence is a function of $N$, divided by the cell volume) will display sudden jumps in the calculated quantity.

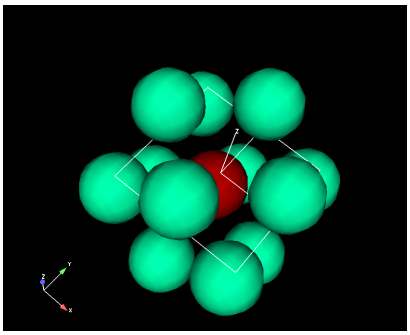

Figure 2.15: An atom in the fcc structure showing only its nearest neighbours. The face of the cube, of which the atom of interest is in the central position (the *face centred* atom) is marked.

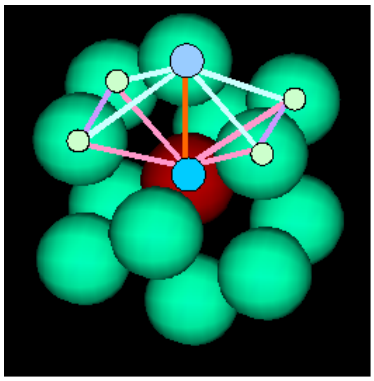

Figure 2.16: An atom in the fcc structure showing only its nearest neighbours. The bonded atoms making up the links in a common neighbour analysis of one of the *i,j* pairs are shown. Here the {421} (4 common neighbours, 2 bonds between those neighbours and longest chain (from neighbour to neighbour) of 1) can be seen to be produced by a pair of opposing tetrahedra.

### 2.4.4 Structural Analysis

#### Common Neighbour Analysis

One of the more difficult visualisation tasks is the identification of local structure. This is particularly important for those systems which display allotropy. The determination of crystal structure by observation of atomic positions by eye alone is almost impossible (see figure 2.15). However, the application of graph theory to local structure has enabled the separation of atomic neighbourhoods into a few classes. The common neighbour analysis[57] (CNA) derives from the radial distribution function. The method identifies different local symmetries by comparing the local neighbour lists of the first (closest) neighbours of the atom under consideration. So for each $i, j$ pair a primary distinction identified is made between face centred cubic (see fig 2.16), hexagonal close packed, body centred cubic and an *icosahedral* structure.

### Centrosymmetry

The centrosymmetry parameter[91] is a simple parametrisation of the atoms based on their local symmetry. The method compares the distance to each neighbour with that to an opposing neighbour. These differences are then summed over 12 neighbours.

$$\mathrm{CSP} = \sum_{i=1}^{6} |\vec{R}_i - \vec{R}_{i+6}|^2 \tag{2.80}$$

For an ideal centrosymmetric structure, the sum is zero. Any number above zero, then, is to some degree out of ideal.

The CSP sum depends upon knowing the diametrically opposing neighbours among the 12 nearest. The algorithm within the LAMMPS code accomplishes this by producing a list of vectors which are the sum of the position vectors of each neighbour of the central atom with every other neighbour of the central atom. It can be seen that for diametrically opposite neighbours, the central atom is located mid-way between those opposing neighbours. Therefore, for any pair of neighbours, if one subtracts twice the position vector of the central atom from the sum of the respective neighbour position vectors, then the vector with the smallest resultant length will arise from diametrically opposing neighbours. In an ideal centrosymmetric lattice the length of this vector will be zero (which leads to a sum of zero from equation 2.80). Hence the lengths of the vectors resulting from the aforementioned subtractions are stored, and the sum of the 6 smallest values from the list of evaluations gives the value of the CSP.

In this code snippet the array 'nearest[]' contains the identities of the 12 nearest neighbours of the central atom $i$ and the arrays 'x[]', 'y[]' and 'z[]' contain the positions of the atoms in each dimension of the simulation cell axes.

```
For (j=0; j<12; j++) {
  jj = nearest[j]
  for (k=j+1; k<12; k++) {
    kk = nearest[k]
    dx = x[jj] + x[kk] - 2*x[i]
    dy = y[jj] + y[kk] - 2*y[i]
    dz = z[jj] + z[kk] - 2*z[i]
    pair[n++] = dx*dx + dy*dy + dz*dz
  }
}
```

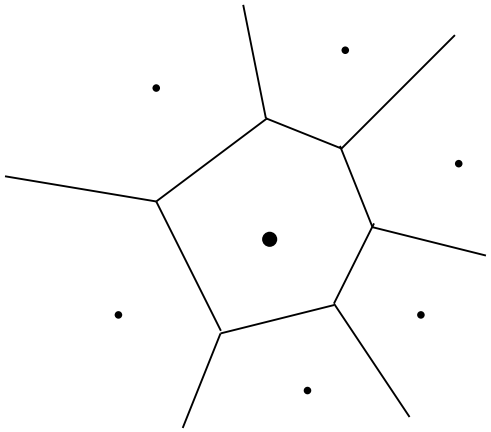

Figure 2.17: Schematic showing how space is divided in a Voronoi diagram.

Hence the 6 smallest values in the array 'pair[]' are the values $|R_j + R_{j+6}|^2$ to be summed.

The values generated under various defect circumstances are dependent upon the lattice parameter of the material being simulated. For copper with a lattice paramter of 3.615Å, partial dislocations give a value of $\sim 3$Å$^2$ and stacking faults $\sim 6.5$Å$^2$. Consequently this scheme highlights the defect structure readily observed in the simulations of shocked FCC metals.

### Voronoi Analysis

The Voronoi (or Dirichlet) tessellation is a means of dividing space up into regions according to the proximity to a set of points within that space. This analysis method is extremely powerful for understanding the spatial relationships existing in the data at hand. This technique has been used for a range of situations, from analysing football games[93] to nerve growth.[113] The application to crystals[8,41] is now a common tool enabling the analysis of coordination number and the identification of crystal structures. However, the calculation of the Voronoi polyhedra is a complex and time–consuming task, and whilst many algorithms exist,[29,99,144] their robustness is variable. The most common algorithm is that of [11] (*Qhull*), which has been implemented into several commercial packages, e.g. *mathematica*[155] and visualisation suites e.g. *ensight*.[38]

### Comparison

It is interesting to compare the centrosymmetry, CNA and Voronoi analyses. Whilst the centrosymmetry is by far the easiest and quickest parameter to calculate, it suffers

from variations from ideal lattice spacings, particularly in high thermal noise environments. The Voronoi analysis is often difficult to translate into a computer algorithm, and the more efficient schemes utilise assumptions which cause the method to fail when analysing degenerate structures. In order to overcome this, small perturbations to the atomic positions are made, mimicking thermal noise. However, excessive perturbations cause the scheme to identify additional neighbours, faces and edges. These additional features lead to erroneous analyses. The method of [29] attempts to deal with this by applying contractions under a set of rules, thereby eliminating falsely identified neighbours.

The CNA, in contrast, requires the identification of the nearest (coordinating) neighbours beforehand. This is usually achieved by identifying neighbours within a spherical shell. The analysis itself is based solely on neighbour lists, and as such utilises only integers within the algorithm. Consequently, specific atomic positions are not included in the scheme, and, provided that the neighbour lists are correctly identified, thermal noise is not an issue.

### Visualisation

A major advantage which MD has over experiments is the ability to freeze the simulation at any desired time and examine the state of all of the atoms. Not only can subsequent calculations be carried out (post–processing) to yield, for example, spatial variations of quantities (see section 2.4.3), but also the positions of the atoms can be visualised using appropriate software. Furthermore, the atoms themselves can be separated out, visually, by either colouring by some quantity being examined, or alternatively a threshold mechanism can be applied. This enables atoms with some range of quantity to be included in (or excluded from) an image, with the remainder excluded from (or included in) the image.

In the following sections both of these methods have been combined to create illustrative images. In order to show the shock position, the simulation is sectioned to give a thin slab which is narrow in the plane of the page, but extends to the limits of the simulation laterally (i.e. in the shock direction and one normal direction). The atoms in this slab are coloured according to their velocity in the shock direction, using blue for zero, through green and yellow for intermediate velcities to red for atoms with the highest velocity. In this way, a background is created which is mostly blue in stationary (unshocked) regions and has a different colour otherwise. One consequence of displaying large numbers of atoms in this way is that, when the image is shown at low magnification, a moiré fringe effect can be seen where the lattice

planes are well aligned with the simulation axes (and hence the viewer). This effect can be seen even in the images used in this document, when shown electronically.

In order to show dislocations and stacking faults, the CSP has been used in combination with a threshold routine, to show only those atoms with a CSP value greater than 3.0. Additionally these atoms are represented as small spheres, so that they stand out clearly against the background velocity colouring. It should be noted that, due to the temperature of the simulations, there is a degree of thermal noise in the CSP quantity and a number of atoms are shown which are clearly not part of any plasticity. In this case the viewer is required to exercise some judgement in ignoring this effect.

## 2.5 Conclusions

The MD can be seen then as an appropriate tool to examine the behaviour of metals at a scale below the grain size, even though the technique is currently not as accurate as the *ab initio* method. Furthermore, the Rankine–Hugoniot relations indicate that shocks can be seen to occur over very small spatial scales since, in theory, the shock front should have no measureable width. However, one might expect that the manner in which the shock compression is passed from on discrete atom to the next would cause some variation from that idealised view.

From the descriptions given in sections 2.2 and 2.1, then we can see that MD is a suitable tool for studying the rapid processes occuring during shock compression. Therefore one can use this tool to examine how these processes interact with crystals found in metallic materials.

The chosen potential, that of Mishin *et al*,[116] has been widely used study a range of properties and behaviours of copper. The scheme used to develop the potential has been designed to provide both accurate high pressure properties, as well as being widely transferable. This is further suported by the absence of reports of unexpected stable crystal structures which are not observed experimentally. Such a feature would cause incorrect behaviour to be seen in shock simulations. In contrast, it has been shown[27,28] that simulations of shocks exhibit defect generation through the production of dislocations and stacking faults, as might be expected experimentally.

In the next part of this work, these interactions will be examined in a range of circumstances, both as single entities, in pairs and as agglomerations as would be found in polycrystalline experimental samples. Finally, the MD method will be

used to examine a situation which relevant to space science research; the impact of nanometer size particles onto metallic surfaces.

# Chapter 3

# Simple Shock Simulations

## 3.1 Single Crystals

### 3.1.1 Introduction

#### Context

The advantage which MD has as a simulation tool lends NEMD ideally to the study of shocks. The difficulty in dealing with this area of physics experimentally derives from the timescales involved. The risetimes for shock waves, that is the timescale over which the state variables such as pressure and particle velocity rise, is of the order of picoseconds to nanoseconds, $10^{-12}$ – $10^{-9}$ s. Such timescales are difficult to deal with experimentally, and so diagnostic devices have large errors in that part of the signal associated with the shock rise. This issue applies especially to in-situ gauges, such as pressure gauges which require an equilibration time due to the package design of the gauge.

By contrast, then, the very fact that shock fronts occur over such short time scales (and space scales, even though the associated velocities are very high) enables simulations to be realised within modern computers. This was recognised very early on in the development of computational techniques for the understanding of shock behaviour. With the development of readily–available high performance computing, coupled with the increasing sophistication of freely–available MD codes the variation of material types studied under shock loading is quite substantial. As a result, this technique is being used to examine explosives, gases and liquids, as well as crystalline elemental solids such as metals.

Holian and Straub[76] examined the conclusions drawn by earlier workers. The previous workers had carried out MD simulations which showed that shocks do not develop to steady conditions in their simulations. However, the results of [76] show

that the transition to steady shocks occurs invariably for simulations where the initial temperature is above zero. Furthermore, [76] shows that unsteady shocks are themselves unstable, and perturbations, such as slippage defects, will cause the one–dimensional nature of the unsteady shock to produce relaxation mechanisms.

This work is taken further by Holian[74] to show the transition from elastic compression through weak plastic shocks to over–driven strong shock conditions. Holian shows that for ideal perfect crystals, plasticity occurs when the stress exceeds the theoretical shear strength. This paper also shows that the plasticity observed in MD simulations, where the shock strength is considerably above the threshold for inducing plasticity, is relatively insensitive to initial defects. It should be noted that this insensitivity does not imply that the initial defect density does not modify the shock behaviour; only that it has a secondary order effect.

The extension of the MD method to very large simulations[75] shows how rich the defected microstructure can become. It is an interesting feature of this work to describe the unusual initial defect nucleation mechanism in such perfect crystals. Holian[75] shows that the shock travels elastically as an unsteady one–dimensional (i.e. with no relative lateral motion of atoms) compression wave for some distance, before stacking faults are generated in the compressed material. These defects then travel back towards the piston, as well as forward towards the receding shock front, thus making that front non–planar.

### Simulation Techniques

There are several methods commonly used in MD to simulate the passage of shocks through material. The primary goal is to cause the dramatic change of state described in section 2.1. Such changes are associated with a large strain imposed upon the material in question. Whilst it is possible to arbitrarily relocate the atoms individually in order to impose the required strain, such immediate gross changes do not enable the correct microstructural changes to develop. This can been seen by considering the Hugoniot relations described in section 2.1. The increase in energy derives in part from the increase in potential energy, but also there is a large contribution from the increase in kinetic energy associated with the acceleration of the material. In simulations where the atoms are moved in a non–physical way in order to increase the density, only the potential energy contribution to the energy increase is applied.

In the earliest work,[76] two shocks were created by reducing the length of the simulation cell in one dimension. This was achieved by changing the position of the periodic boundaries. The effect on the atoms at each end was as if the material with

which it is connected via the periodic boundary was being driven into the sample. Because this behaviour occurs at both boundaries, two shocks are created which move towards the centre of the sample. This means that the simulation is, in effect, mirrored and only half the sample being simulated will yield productive results.

In the simplistic description of a shock given in section 2.1 no account is taken of the physics associated with driving some large mass at the high velocities required in order to develop the shock phenomena of interest here. The large mass is required since the material being compressed (even a gas) will respond, due to Newton's third law, to decelerate the piston. In reality, then, shocks are set up in solid media by either explosive means, or by accelerating a flyer (a thin flat plate) to a high velocity[a] prior to that flyer impacting upon the sample.

In a MD simulation it is possible to recreate the flyer experiment by superimposing an additional uniform velocity upon a subset of the atoms within the simulation. This method is attractive in that it enables a *prima facie* faithful representation of the experimental conditions. However, there is a severe drawback. Since, as in the experiment, a shock is set up at the flyer–sample interface, two shock fronts are observed; one travelling forward into the sample and another travelling back into the flyer. Now the shock travelling into the flyer reaches the free surface at the rear of the simulation and, as in the experiment, is reflected back into the material as a release wave. Since the release wave is moving into compressed material, the sound speed is high and this wave will catch up with the shock travelling forward into the sample, after which time the amplitude of that shock is eroded. Consequently there is a relationship between the amount of material included in the flyer and the run length of the shock within the sample. Therefore, if one wishes to observe relaxation effects behind the shock, it will be necessary to include a large flyer. This section of the simulation, *viz* the flyer, is being carried as nugatory calculational expense, and will count towards the maximum size of simulation which can be accommodated by the compute resource to hand.

However, it is also possible to override the physical constraints associated with a piston–driven experiment. In this case, the atoms at one end of the simulation region have conditions placed upon them within the integration scheme. Their velocities are replaced by $U_p$ in the direction in which the shock is to be applied, and zero in orthogonal directions. Furthermore, any change in velocities due to interactions with atoms in the main part of the simulation are ignored. The region comprising the

[a]If the flyer is composed of the same material as the sample, then the flyer velocity will be twice the particle velocity, $U_p$, of the experiment.

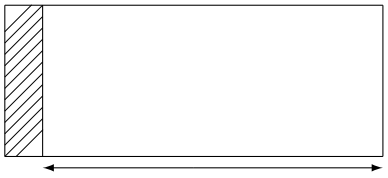

Figure 3.1: Schematic of piston driven simulation. The entire box is filled with atoms, but those in the shaded region do not have their forces calculated, or their velocities modified by the integration scheme. These atoms are initialised with a velocity $U_p$ in the shock direction and zero otherwise. The region denoted by the arrow, then, comprises the simulated crystal and evolves under NVE conditions.

piston extends as far as the extent of the simulation orthogonal to the shock direction, but only 4 or 5 planes of atoms into the simulation cell in the shock direction. In this way a rigid wall, or piston, is created, which drives into the simulation cell at a velocity of $U_p$.

An alternative scheme utilises the boundaries of the simulation cell. Here a test is carried out on the motion of the atoms near to the boundary on one side of the cell. The test examines whether, during the time covered by that timestep, any atom will pass across the boundary. For any atom where such a motion is predicted, then its position is not updated, and its velocity towards the wall is reversed. In this way, the momentum associated with the atoms crossing the boundary is reversed, thus creating a *momentum mirror* on one side of the simulation cell. The entire set of atoms in the simulation is then given a superimposed additional velocity of $-U_p$ in the direction of the momentum mirror. This causes the atoms to compress up against that mirror, and a shock then propagates at a velocity of $U_s - U_p$ away from the mirror boundary. It should be noted that, in this case, the atoms in the compressed region ('behind the shock') are stationary, and the atoms in the uncompressed region ('ahead of the shock') are in motion. This is the reverse of the usual situation, and is in reverse to that assumed in the analysis described in section 2.1. Account should be taken of this fact, which necessitates a change in variables to account for the different frame of reference.

Among the studies of shock behaviour one may wish to understand behaviours observed some significant time after the shock front has passed the region in question. Alternatively, one may wish to examine the evolution of the shock front over a significant period of time. A difficulty arises in that, in order to allow the necessary time to pass within the shock simulation, the size of simulation needed is prohibitive. Although such studies do not form part of this work, it is worth noting that two

methods have been developed to examine these situations. The Hugoniostat[105] uses the concepts described in section 2.2.2 to create a simulation in which the shock front is maintained within the simulation cell. For studying regions far behind the shock front, the method of *matched pistons* captures a subregion of the simulation cell, after the shock has compressed the material. The subregion is then allowed to evolve naturally to the long time state desired. This is achieved by utilising a piston to create the shock in a simulation cell considerably larger than the subregion to be studied, and then, after the shock has passed, a slab of atoms on the other side (in the sense of the shock direction) of that subregion is fixed in an identical fashion to the piston used to set up the shock. In this way the subregion is held clamped at the density and energy state created by the passage of the shock.

### Orientation Effects

It is clear that due to the nature of crystals, and the fact that the shock process is dominated by uniaxial motion, there will be some difference in the observed behaviour of single crystals when oriented differently with respect to the shock direction. Furthermore, since the primary slip system in FCC crystals is by slip in a $\langle 110 \rangle$ direction on $\{111\}$ planes, it can be seen that there are different slip systems which may operate depending on the orientation of the crystal relative to the shock direction. Where there are multiple systems which are oriented equally to the shock direction the orientation is said to be *degenerate*. Now, for crystals loaded along $\langle 100 \rangle$ or $\langle 110 \rangle$, there are eight suitable systems oriented for slip.[81] In contrast, loading along $\langle 111 \rangle$ is oriented for slip on only 6 systems, along two different $\langle 110 \rangle$ directions on each of three $\{111\}$ planes; $(11\bar{1})$, $(1\bar{1}1)$ and $(\bar{1}11)$.

In order to relate the results of simulations to those of macroscopic experiments, it is necessary to understand these differences. Thus an appreciation of the different behaviours observed in shock simulations under different crystallographic orientations is necessary as part of that translation from atomic–scale simulation to macroscopic experiment. In this section simulations in which the three principal directions of the FCC cube are aligned with the shock direction are compared.

That this difference exists was appreciated by Germann *et al*[64] who examined the high symmetry directions $\langle 110 \rangle$ and $\langle 111 \rangle$ and compared the observed behaviour with that of the $\langle 100 \rangle$ oriented simulations reported previously. Here the operation of the expected slip systems is observed in the $\langle 100 \rangle$ and $\langle 111 \rangle$ oriented simulations, but the $\langle 110 \rangle$ orientation is shown to behave is a more complicated way. In this case the operation of slip on four $\{111\}$ planes is observed. One consequence of slippage

occurring on these other {111} planes is that the shear is not fully relaxed, and the slippage occurs in two components; in the [001] direction and in the $[1\bar{1}1]$ direction. Simulations using a momentum mirror show unusual behaviour which they describe as *martensiticlike*, and in order to elucidate the processes operating, Germann *et al*[64] used shrinking periodic boundaries to ensure that only the behaviour of bulk material is observed.

### 3.1.2 Current Simulation Setup

In this work, the piston method described in section 3.1.1 was used to generate a single shock in the sample, which was a single crystal of copper. This work was carried out in order to improve the understanding of the shock behaviours observed by other workers in the field (see section 3.1.1 above), and furthermore to examine the microstructures generated by a single shock process.

In order to simulate the behaviour of bulk material, the lateral extents of the simulation cell were set up with periodic boundaries. By this is meant that the atoms on one side of the simulation cell have, as computational neighbours, i.e. included within the calculation of the energy and derivatives, the atoms on the other side of the cell. The effect of this behaviour is that the simulation cell is repeated periodically, as if to fill space. Clearly such a computational scheme is inappropriate in the shock direction; firstly the forces on the atoms which comprise the piston are set to zero and secondly as the piston moves into the sample, those atoms move at the piston (particle) velocity away from the atoms at the free end of the sample.

When the crystal lattice is initially created, the atoms sit on the ideal lattice sites at a spacing specified by the user (usually the equilibrium lattice spacing). The atoms have no associated velocity and the simulated temperature is 0K. However, this is not the situation which is exists in reality; nor is it the state one wishes to examine under shock. Such a condition would lead to erroneous results, as pointed out by Holian.[76] The temperature can be specified by randomly associating a velocity to each atom, such that a histogram of the velocities displays some desired distribution. The velocity histogram for a given temperature should follow a Boltzmann distribution.[70] What is found is that when atoms, sited at ideal lattice positions, are given velocities (kinetic energy), after a short time, when simulated in the NVE ensemble, the mean potential energy has risen and the mean kinetic energy has fallen. This is the operation of the Hamiltonian with the *equipartition principle*, which states that the total energy is spread equally across the different degrees of freedom. What is happening here is that as soon as the simulation starts then the atoms will move (since they have been

given velocities) and hence will no longer be on ideal lattice sites. As each individual atom moves, its potential energy increases, and its kinetic energy falls, whilst the total energy for the whole sample has remained constant. Subsequently, as it moves about across the phase space its time averaged kinetic energy becomes constant, as does its time–averaged potential energy. However, the system will take some time before all the atoms achieve the state in which any one time–average is the same as any other. At this point, the system is said to be equilibrated.

In this work the simulation cell was equilibrated by initially reducing the potential energy via a conjugate gradient minimisation, followed by equilibration under NVE for 20 ps. The reason for the minimisation is related to the temperature of the simulation. For this work, the simulated temperature was set at 300 K. Now the ideal lattice spacing for this potential is 3.615 Å. But this spacing is defined at 0 K; at 300 K the system will be under a positive pressure when at the density specified by a lattice spacing of 3.615 Å. To rectify this short runs were undertaken with varying lattice spacings, and it was found the the pressure was zero when a lattice spacing of 3.63188 Å was defined. However, the initial transient behaviour during equilibration was found, by trial and error, to be damped out more quickly by use of a minimisation, especially for those simulations which were not aligned with the $\langle 100 \rangle$ directions along the simulation axes, even though this caused the system to be initially under a large negative pressure. Following equilibration the simulations were carried out under NVE conditions, allowing the temperature in the shocked region to rise to its natural value.

The simulations in this work were carried out to investigate the behaviour of copper crystal shocked to a level which produces plasticity. Here we mean that some crystal defect has been produced within the simulation where there has been some form of atomic rearrangement. Therefore such plasticity would be readily observed by examination of the CSP. One of the consequences of such plastic deformation is the relaxation of the shear stresses produced by the shock compression. Bringa[27] states that a transverse size of 25x25 cells will show the relaxation effects of much larger cross-sections. However, in other work Bringa[25] also states that a sample size of 200x200 cells is required where pre-existing defects are placed in the simulation, to ensure that the defects are far enough way from their periodic images so as to prevent cross-talk. Whilst the work presented in this thesis examines the relaxation effects, there is also a requirement to examine the behaviour and interaction of the dislocations and stacking faults themselves. Hence a cross-section has been chosen which is slightly larger than that used for the bulk of the work in [27]. Similarly the

| Orientation | Dimensions | | | | | | No. of atoms |
|---|---|---|---|---|---|---|---|
| | X | | Y | | Z | | |
| | nm | repeats | nm | repeats | nm | repeats | |
| 100 | 21.8 | 60 | 21.8 | 60 | 109.0 | 300 | $4.32\times10^6$ |
| 110 | 21.8 | 60 | 20.6 | 40 | 102.8 | 200 | $3.84\times10^6$ |
| 111 | 20.6 | 40 | 23.1 | 26 | 114.0 | 180 | $4.50\times10^6$ |
| 311 | 23.0 | 60 | 22.9 | 60 | 120.4 | 100 | $5.20\times10^6$ |
| 134 | 1264 | 10 | 239 | 5 | 2324 | 300 | $46.2\times10^6$ |

Table 3.1: Setup parameters for the simulation cells used in the single crystal studies. Note that the repeat numbers given here are not lattice cells, but rather numbers of repeat vectors. Only the 100 orientation has its lattice vectors aligned with the simulation cell, and so in this case the number of repeats is equal to the number of lattice cells. For the 134 orientation, the repeat vector is very long, which means that even the smallest periodically repeating cell is very large.

length of the simulation is slightly longer than that of [27] to allow relaxation effects sufficient time to mainfest themselves. The details of the cells are given in table 3.1.

### 3.1.3 $\langle 100 \rangle$ Shock Direction

The conventional, and most common,[27] orientation of shock simulations is for the FCC lattice to be aligned with the simulation cell. This arises because the atomic positions within the FCC cell are most easily described in relation to the simulation cell axes as being at $(0,0,0)a_0$, $(\frac{1}{2},0,0)a_0$, $(0,\frac{1}{2},0)a_0$, $(0,0,\frac{1}{2})a_0$ where $a_0$ is the equilibrium lattice parameter. This leads to the shock direction falling along the $\langle 100 \rangle$ crystallographic direction. It is reported that for shocks along $\langle 100 \rangle$ the lowest observable plastic front has a velocity which is very similar to the elastic wave velocity.[4,27] This means that a velocity profile will not show a clear distinction between the elastically compressed material and that which exhibits plasticity. Also, since in the shocked region the pressure is related to the particle velocity then the pressure profile will similarly not show a clear distinction between the elastically compressed and plastically deformed material.

In [27], the plastic front was described as being slightly behind the elastic wave front position, as determined by visual examination of the simulations. This behaviour was also observed in this work, as is shown in figure 3.2. The transition from the elastically compressed to over–driven states can be observed by fine–scale incremental variation of the piston velocity over the range from $600\,\mathrm{m\,s^{-1}}$ to $750\,\mathrm{m\,s^{-1}}$ (see figure 3.3). Figure 3.4 shows clearly the increase in plasticity as the stress level increases. It should be noted that the stress levels in both the elastically compressed

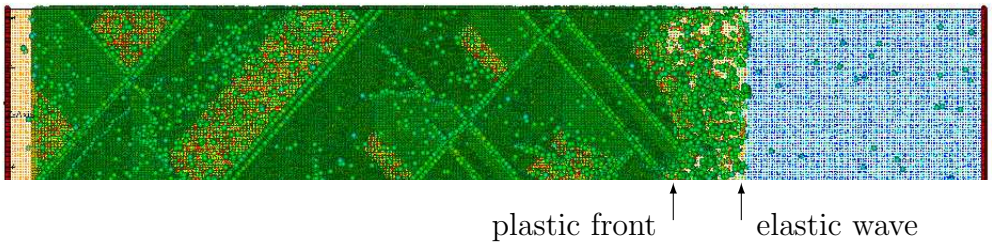


Figure 3.2: $660\,\mathrm{m\,s^{-1}}$ simulation of shock along $\langle 100 \rangle$. Thresholding with the centrosymmetry parameter enables the stacking faults caused by plasticity to be seen clearly. The background colours are shown by a thin slice of atoms coloured by their velocity in the shock direction. See section 2.4.4 for more explanation.

and plastically deformed regions are very close, and no difference can be seen in either the velocity or pressure profiles (see figure 3.3a), as expected. However, the relief of the shear stress by the activity of the dislocations can clearly be seen in figure 3.3b.

It can be seen in figure 3.3 that there is a distinct sawtooth form to the profiles, particularly for those traces from the lower piston velocity simulations. This 'jagged' feature can also be seen in some of the other profiles in this work (e.g. figure 3.10). This issue arises due to the subdividing method used to calculate spatial profiles. This scheme was described earlier (see section 2.4.3). Fortunately, this problem does not exist where the distortions in the lattice cause the atomic planes to be no longer aligned with the simulation cell axes. This latter situation occurs where there is plasticity in the lattice. The plasticity not only causes distortions in the immediate vicinity (i.e. atoms associated with dilocation cores), but also elastic distortions in the surrounding crystal. Consequently this numerical artifact is not seen in regions of the profiles where plasticity has occurred. Although these regions show noise in the signal, as may be expected, they do not show the sawtooth features of the uncompressed and elastically compressed parts of the profile.

Figures 3.5 and 3.6 show the increase in plastic activity within the sample with an increase in piston velocity of only $10\,\mathrm{m\,s^{-1}}$. At $650\,\mathrm{m\,s^{-1}}$, the system remains elastically compressed for a substantial time before any plasticity is observed. As described by Holian,[75] the stacking fault is observed to initiate at a small distance behind the shock front, before propagating both backwards towards the piston and forwards, with the shock front. At this stress level, only a single slip system is activated. However, at $660\,\mathrm{m\,s^{-1}}$, not only is plastic behaviour observed to begin earlier in the simulation (12 ps for $650\,\mathrm{m\,s^{-1}}$ *cf.* 8 ps for $660\,\mathrm{m\,s^{-1}}$), but a different slip system (albeit crystallographically equivalent) initiates first. Furthermore, at this higher stress level, again a single slip system operates initially, but a second system

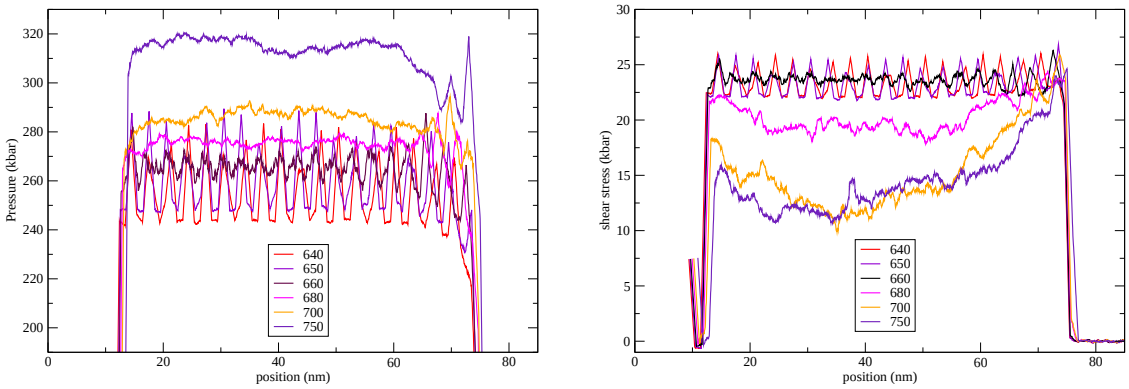


(a) Pressure (b) Shear stress

Figure 3.3: Shear stress profiles of shock along ⟨100⟩. Snapshots taken at 14ps. The piston velocities (shown in the legend) are given in $\mathrm{m\,s^{-1}}$, and correlate to the images shown in figure 3.4. The oscillations seen in some of the lower velocity curves relate to the aliasing effect which arises due to the slices taken in order to calculate the average values along one dimension of the simulation (see section 2.4.3).

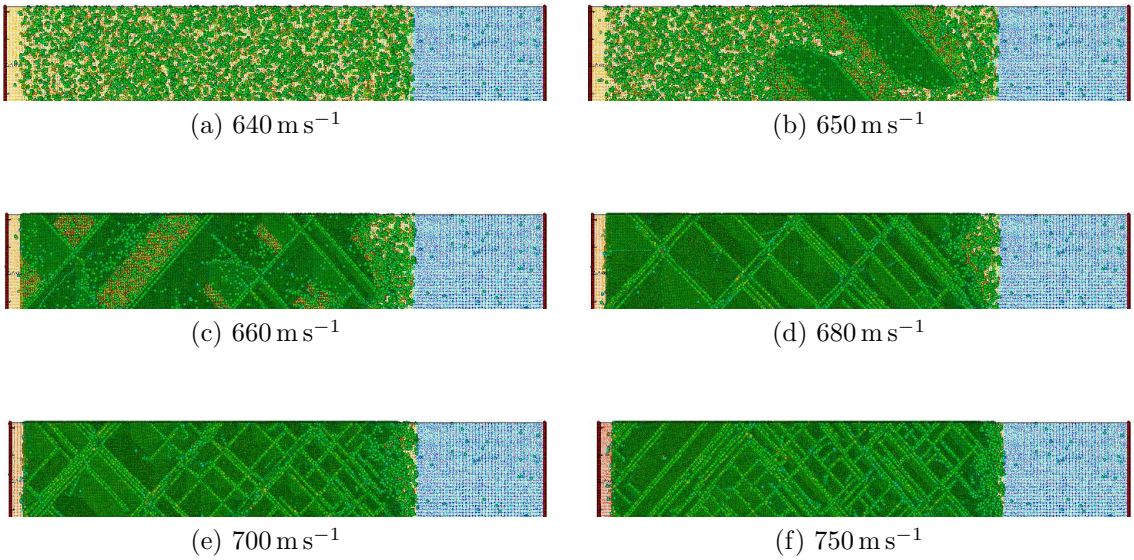

(a) $640\,\mathrm{m\,s^{-1}}$ (b) $650\,\mathrm{m\,s^{-1}}$

(c) $660\,\mathrm{m\,s^{-1}}$ (d) $680\,\mathrm{m\,s^{-1}}$

(e) $700\,\mathrm{m\,s^{-1}}$ (f) $750\,\mathrm{m\,s^{-1}}$

Figure 3.4: Simulation of shock along ⟨100⟩. The images show atoms with a centrosymmetry parameter greater than 3, on a background coloured by velocity along the z (shock) axis, in order to show the elastic wave position. All snapshots taken at 16 ps from the start of the simulation.

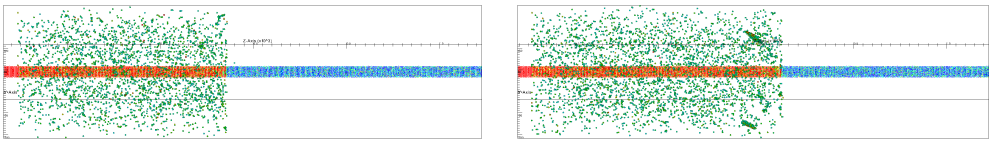

(a) 10ps



(b) 12ps

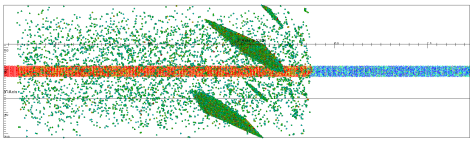

(c) 14ps

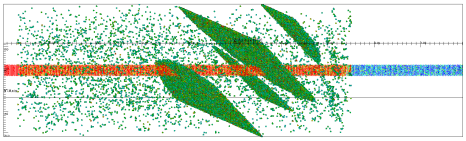

(d) 16ps

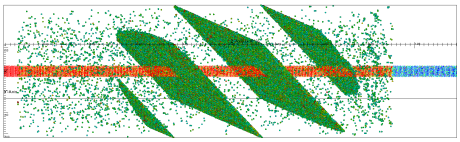

(e) 18ps

Figure 3.5: $650\,\mathrm{m\,s^{-1}}$ simulation of shock along $\langle 100 \rangle$. All views are rotated so the viewer is looking along $[\bar{1}10]$ . The images show atoms with a centrosymmetry[91] parameter greater than 3. The central bar additionally shows atoms coloured by velocity along the z (shock) axis, in order to show the elastic wave position. [See animation F1.1 in the electronic appendix.]

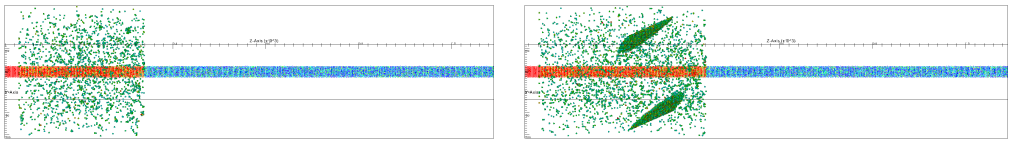

(a) 6ps



(b) 8ps

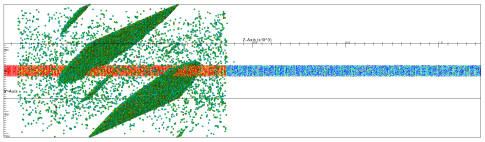

(c) 10ps

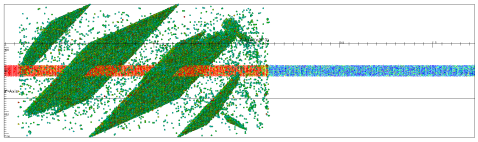

(d) 12ps

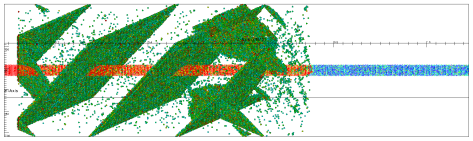

(e) 14ps

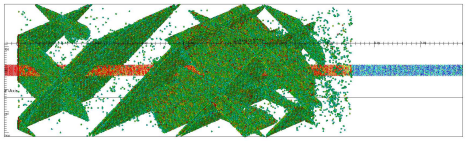

(f) 16ps

Figure 3.6: $660\,\mathrm{m\,s^{-1}}$ simulation of shock along $\langle 100 \rangle$. All views are rotated so the viewer is looking along $\langle \bar{1}10 \rangle$ . The images show atoms with a centrosymmetry[91] parameter greater than 3. The central bar additionally shows atoms coloured by velocity along the z (shock) axis, in order to show the elastic wave position. [See animation F1.2 in the electronic appendix.]

comes into play after a further 4 ps, indicating that although some stress must have been relieved by the operation of the first system, this did not reduce the stress level below that required to generate further stacking faults.

It can also be seen that the number of stacking faults within the shocked material increases with increasing shock pressure. This point leads one to examine how much the activity observed contributes towards the relief of stress. Examination of figure 3.4b shows that plastic deformation occurs for shocks driven by a piston velocity of $650\,\mathrm{m\,s^{-1}}$ or greater. However, it can be seen in figure 3.3b that relief of the shear stress only occurs for shocks driven above $680\,\mathrm{m\,s^{-1}}$. Returning to figure 3.4, one can see that this means that a significant degree of multiple slip is required before noticeable stress relief takes place. That is to say that the action of an individual dislocation (and its associated stacking fault) makes only a small contribution to the total change in stress. Even so, there must be some level at which the stress relief from a single stacking fault will affect the behaviour of the remaining system. Cao *et al*[35] examined shocks along $\langle 100 \rangle$ and found that the differing slip systems operated some competing mechanism, which in their work accounted for the change in stacking fault density with shock strength.

### 3.1.4 $\langle 110 \rangle$ Shock Direction

When the crystal is rotated such that the shock direction lies along the $\langle 110 \rangle$ crystallographic axis, the elastic shock behaviour is noticeably different to that described for $\langle 100 \rangle$ above, as clearly described by Bringa *et al*[27] and in Germann *et al.*[64] In those papers, the elastically compressed region is preceded by large variations in velocity. These are brought about by the way in which the atoms are lined up with the direction of closest packing parallel to the shock direction. This means that the force is transferred from one atom to the next in the most efficient way. This in turn causes the atoms at the very leading edge of the shock wave to 'overshoot' and approach the next atom at too close a distance. Consequently, when that atom moves forward, the first atom 'bounces' off the second, and its velocity is reduced, before being driven forward again by the atoms behind. This motion is efficiently transferred forwards at a high velocity, creating an isolated spike in velocity. Figure 3.7a shows how a train of these isolated waves are set up ahead of the elastic wave.

However, the simulations carried out as part of this work do not exhibit this behaviour. As can be seen in figure 3.8, the $\langle 110 \rangle$ simulation behaves in a more simplistic fashion, displaying a classic elastic–plastic two wave structure.

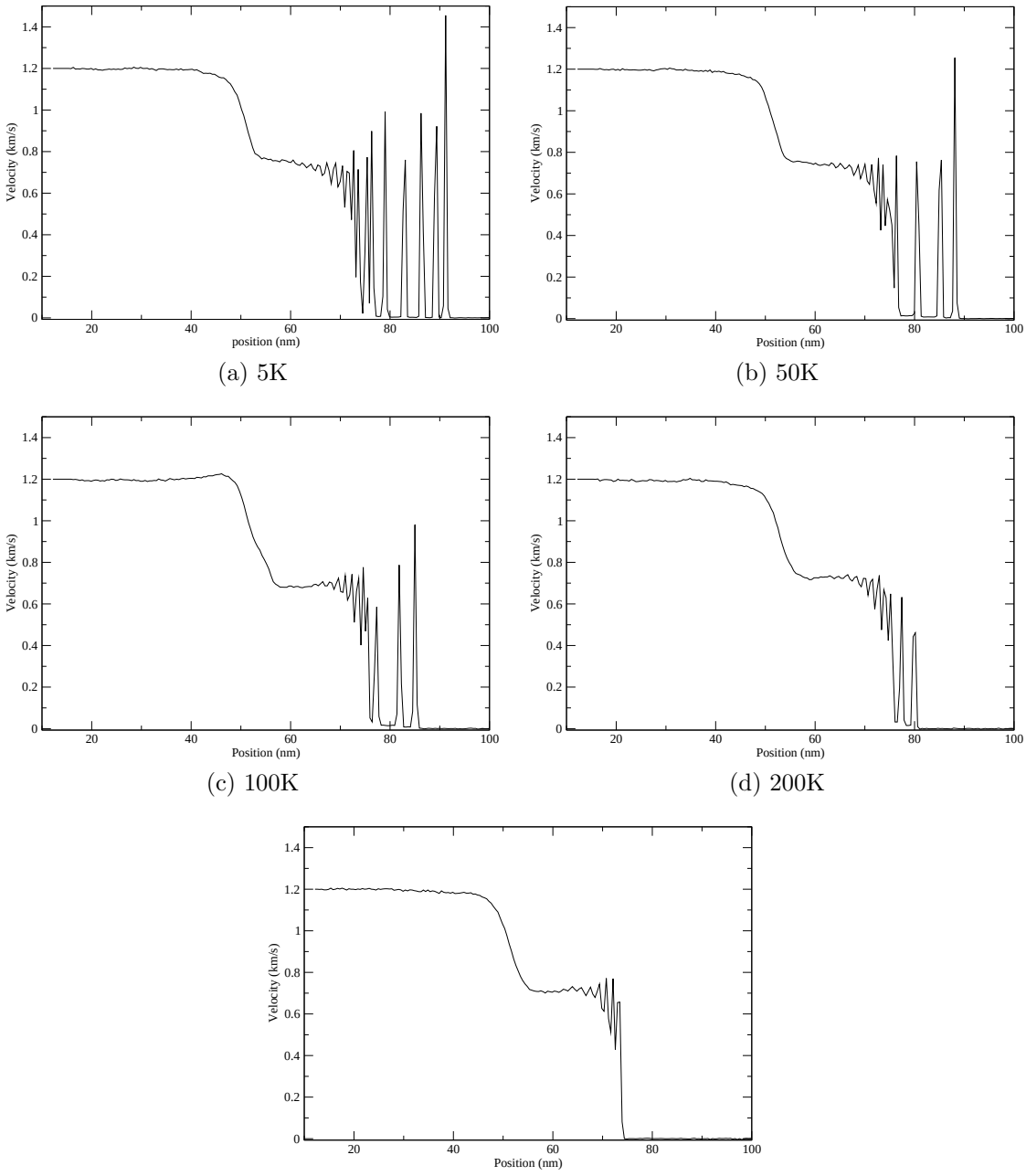


(a) 5K

(b) 50K

(c) 100K

(d) 200K

(e) 300K

Figure 3.7: Velocity profiles in ⟨110⟩ showing the soliton precursor behaviour ahead of the elastic precursor. The extent of the solitons is reduced as the temperature is raised from 5K (a) to 300K (e).

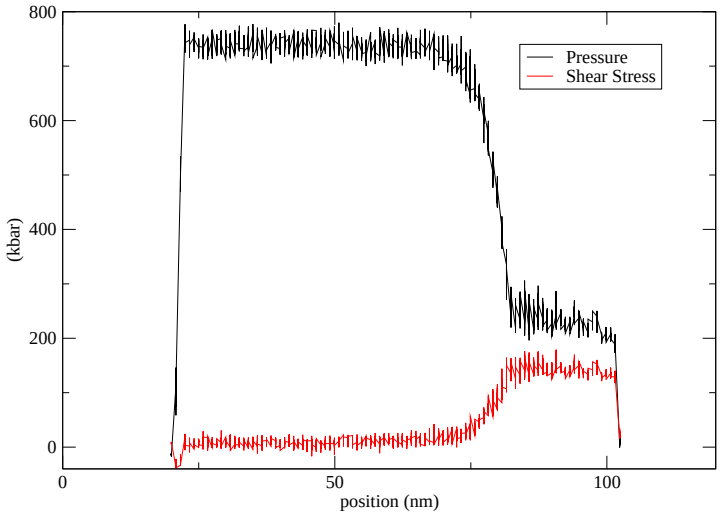


Figure 3.8: $\langle 110 \rangle$ pressure profile showing the elastic precursor ahead of the main shock. Piston velocity is $1400\,\mathrm{m\,s^{-1}}$. Snapshot at 14ps. The red curve shows how the action of the dislocations relieves the shear stress within the plastically deformed part of the shock wave.

The reason for the difference lies in the temperature at which the simulations were run. In order to reduce thermal noise effects, and thus show the plasticity more clearly when using the centrosymmetry parameter for analysis (see section 2.4.4), Bringa *et al*[27] ran their simulations at 1.5 K. Figure 3.7 shows the velocity profiles for a series of simulations run with a piston velocity of $1200\,\mathrm{m\,s^{-1}}$, in which the initial temperature of the simulation is varied between 5 and 300 K. Germann *et al*[64] describe how these solitary waves remain stable up to $T_0 \simeq T_m/10$, where $T_0$ is the temperature at the start of the simulation and $T_m$ is the melting temperature. For this work that would imply soliton behaviour up to $T_0 \simeq 160$ K. In the work presented here (figure 3.7) the soliton behaviour is reduced with increasing temperature, as opposed to dropping off suddenly as implied by Germann *et al*,[64] although some oscillations are evident even up to 300 K.

The main reason for the reduction in this behaviour is due to the degree of idealism within the single crystal. At very low temperatures the atoms sit very close to their ideal positions, and rows of atoms are well aligned, leading to a system which can transfer momentum efficiently down the row. As the temperature is increased, the atoms become increasingly displaced from their ideal positions, due to the increased kinetic energy driving the atoms further from the location of the minimum in the potential well. Consequently the alignment of the atoms atoms within the row is reduced, reducing the efficiency of the single–atom momentum transfer process.

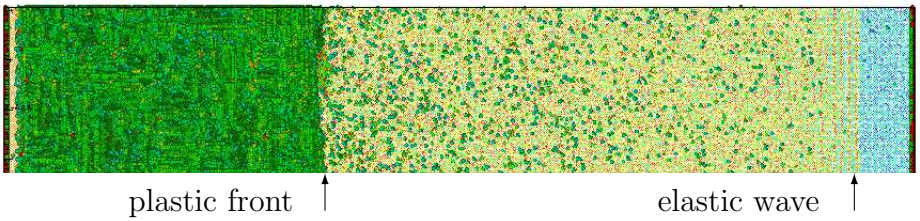


Figure 3.9: $\langle 110 \rangle$ showing the plastically compressed region immediately ahead of the piston. The elastic wave is indicated, ahead of the plastic front. $U_p = 800\,\mathrm{m\,s^{-1}}$. Snapshot at 14ps.

In these $\langle 110 \rangle$ shock simulations, in contrast to those along $\langle 100 \rangle$ described above, the initial dislocation activity occurs just ahead of the piston, as shown in figure 3.9, rather than just behind the shock front. Furthermore, the plasticity very quickly develops into multiple slip.

### 3.1.5 $\langle 111 \rangle$ Shock Direction

By orienting the crystal so that the $\langle 111 \rangle$ direction is parallel to the shock direction, and since the slip planes are $\{111\}$, there are three planes all at equal angles to the the vector describing the shock direction. Furthermore, each slip plane contains two $\langle 110 \rangle$ directions, each being also at equal angles to the shock axis described. Therefore the simulation presents six different, albeit crystallographically equivalent, slip systems to the shock. This places this system in contrast to the $\langle 100 \rangle$ and the $\langle 110 \rangle$ (with 8 stressed systems). Now, the Schmid factor is nearly the same for the primary slip systems for all three high symmetry orientations,[81] so one may inquire as to whether this degeneracy means that the single–slip observed in the $\langle 100 \rangle$ simulations above is also seen here, or rather the material goes directly to the multiple slip condition as observed in the $\langle 110 \rangle$ simulations. Now, not only does the material go directly to multiple slip, but unexpectedly, the pressure profile is very different to that observed in either the $\langle 100 \rangle$ or $\langle 110 \rangle$ orientations.

In this orientation the nucleation of dislocations causes a relief in the observed pressure in the region surrounding the newly generated dislocations (see figure 3.10). This reduction in pressure is observed to form what appears to be a release wave on either side of the slipped region. Toward the piston the velocity, and hence pressure, is maintained by the piston, and the slope of the velocity curve increases towards a maximum level. Towards the leading edge of the compression, however, this release

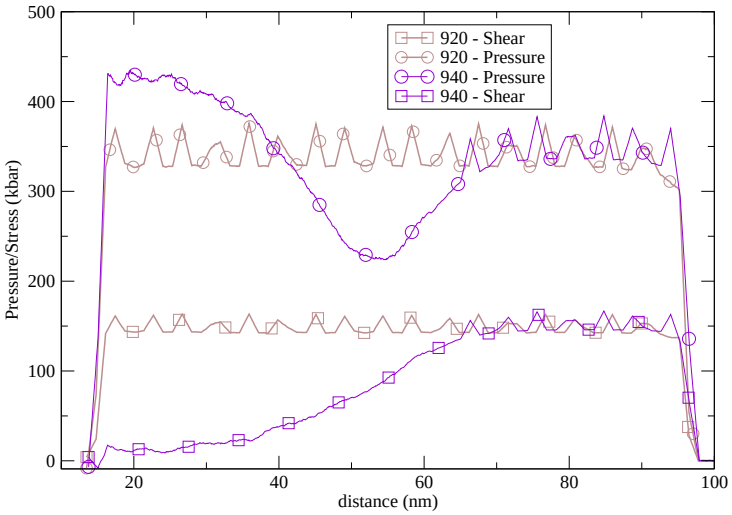


Figure 3.10: ⟨111⟩ simulation showing early pressure and shear stress profiles for shocks just below ($920\,\mathrm{m\,s^{-1}}$) and just above ($940\,\mathrm{m\,s^{-1}}$) the threshold for plasticity. Snapshot taken at 14ps from start of simulation.[See animation F1.3 in the electronic appendix.]

attenuates the pressure. The amplitude in the elastically–compressed region then decays, as the wave progresses forwards, to some new, lower value.

The question arises as to why the profiles show the dip at the point of dislocation nucleation. The conventional analysis of stresses indicates that the material cannot support shear stresses at a higher level than the yield strength. Therefore, when the material plastically deforms, the pressure should subsequently rise. Clearly, then, the shear stress required for homogeneous nucleation of dislocations is above the yield stress of material with an existing defect structure (that is, material containing pre-existing dislocations). Once dislocations are formed, the stresses both in the shock direction, and normal to that direction are reduced to a level which the material can support even in the presence of dislocations. Indeed, the entirety of the material behind the shock front would be reduced to this level, but for the continuing action of the piston, acting to maintain the compression and particle velocity. The front of the elastic wave continues to travel forward at the longitudinal sound speed, whereas the front of the plastically deformed region moves at the velocity of shear waves. Comparisons with the experimental Hugoniot[27] indicates that the longitudinal sound speed for bulk polycrystalline copper is $3.96\,\mathrm{km\,s^{-1}}$. Examination of figure 3.10 shows that the elastic wave in this simulation is travelling at $6.93\,\mathrm{km\,s^{-1}}$. This velocity is excessive for elastic waves in this material, and reflects the fact that the material is compressed to a higher pressure than the material can normally support elastically.

The operation of these two processes (*viz.* the piston maintaining the pressure at the back of the shock, and plasticity reducing the shear stress which can be supported by undeformed material at the front of the shock) work together to develop the classic two–wave structure observed in all weak–shock experiments (see figure 3.11).

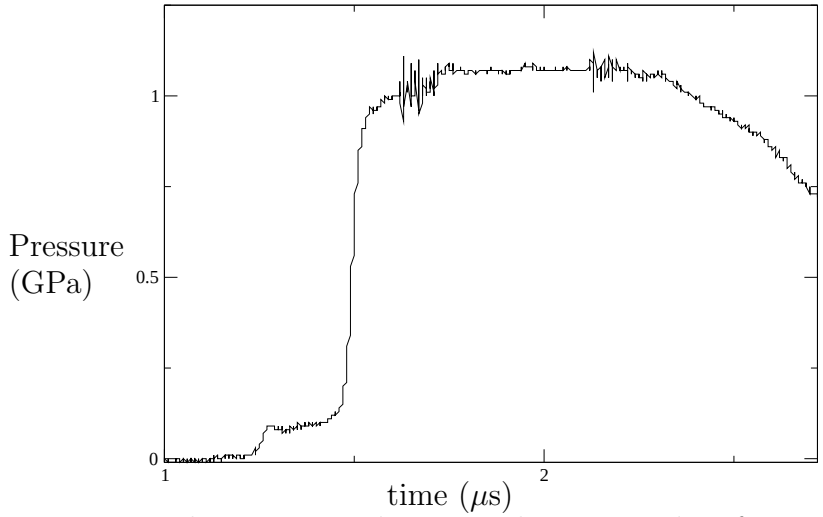


Figure 3.11: Typical experimental trace. This trace taken from the rear surface of a sample of $Ni_3Al$ impacted by Al at $569\,\mathrm{m\,s^{-1}}$. The trace is derived from a manganin gauge sandwiched between the rear surface of the target and 5mm of PMMA. (Courtesy of J. Millett)

### 3.1.6 Low Symmetry

Most work to date has been carried using crystals set up with one of the high symmetry directions oriented parallel to the direction of deformation (or shock). Indeed, when comparisons are made in order to describe orientation effects, it is the main high symmetry directions which are compared (see, for example [27, 64]). However, in reality the probability of finding any grain oriented in this way is almost zero.

Understanding low symmetry is important due to the way in which material responds to shock compression. Along the high symmetry directions the crystal is degenerate with respect to the available slip systems. That is to say, that the crystal is oriented so that crystallographically equivalent slip systems are at the same angle to the compression axis, and hence have the same Schmid factor. Thus, upon arrival of the plastic front, many slip systems are activated, and the crystal is driven immediately into a regime of multiple slip. Such behaviour is very different to the expected initial single slip regime.[3]

In contrast, then, a crystal oriented so that there is a definite single slip system with a maximal Schmid factor will exhibit single slip deformation readily. For this

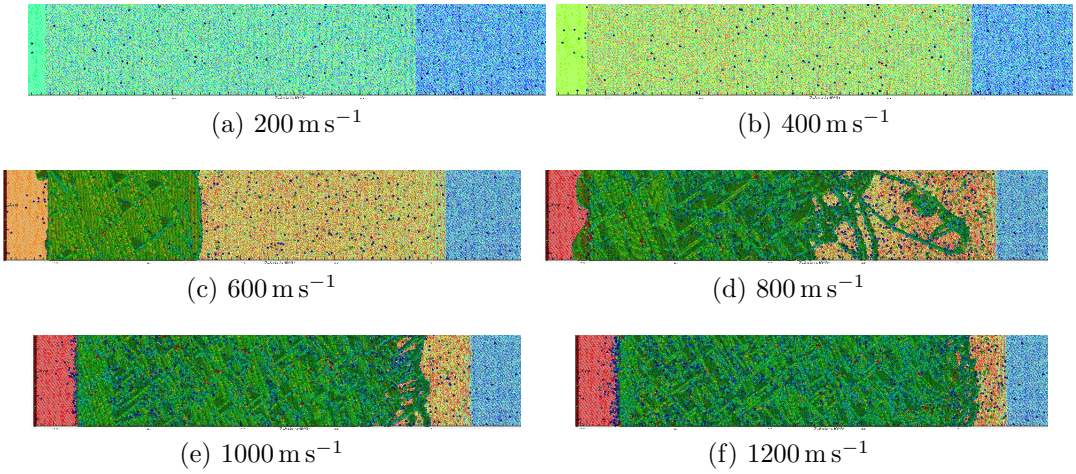

(a) $200\,\mathrm{m\,s^{-1}}$ (b) $400\,\mathrm{m\,s^{-1}}$

(c) $600\,\mathrm{m\,s^{-1}}$ (d) $800\,\mathrm{m\,s^{-1}}$

(e) $1000\,\mathrm{m\,s^{-1}}$ (f) $1200\,\mathrm{m\,s^{-1}}$

Figure 3.12: Shocks in [311] crystal. All snapshots at 16ps. The shock moves from left to right. The background colour indicates the velocity in the shock direction; the elastic front can be seen at the right hand end where the stationary (blue) transitions to moving (red).

work two similar orientations were examined. The [311] orientation is a vector which lies close to being at equal angles to all three high symmetry directions. Figure 3.12 shows the effect of increasing piston velocity. In contrast to the high symmetry orientations described above, there is clearly a region of few dislocations at the leading edge of the plastically deformed region. This is especially noticeable in figure 3.12d. These dislocations are full dislocations, rather than the partial dislocations which form a stacking fault behind, as observed in the high symmetry simulations. This direction, however, is not ideally oriented for single slip as there are two systems with identical Schmid factor, namely $[101]/(11\bar{1})$ and $[110]/(1\bar{1}1)$.

Experimental work is being carried out to examine the behaviour of shocks in polycrystals. In order to produce the highest contrast between the high symmetry and the lowest symmetry, the stereographic triangle was examined. Although the [311] vector is equi-angle to the three high symmetry directions, the centre of the stereographic triangle is occupied by a vector close to [134]. For this loading direction, the slip system with the highest Schmid factor is $[101]/(\bar{1}11)$. Hence, as part of this experimental work a copper single crystal was manufactured in the form of a cylinder with a vector close to [134] lying along the cylinder axis. This enabled gas gun samples to be manufactured with the shock direction close to [134]. As part of the work to determine the expected behaviour of crystals of this orientation, simulations were run in which a simulation cell was built with the [134] direction of the crystal parallel to the z–axis of the computational cell. The cell dimensions are given in table 3.1. The

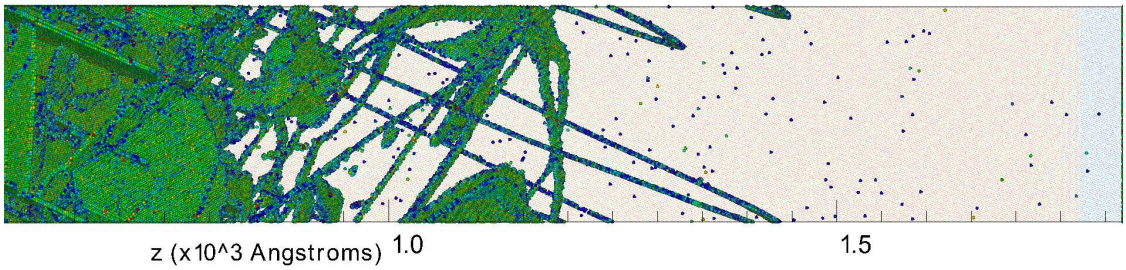


Figure 3.13: $500\,\mathrm{m\,s^{-1}}$ shock in [134] crystal. The shock moves from left to right. The background colour indicates the velocity in the shock direction; the elastic front can be seen at the right hand end where the stationary (blue) transitions to moving (red). [See animation F1.4 in the electronic appendix.]

cell was necessarily large in order to ensure that the boundaries were periodic.

Figure 3.13 shows the dislocations produced by a $500\,\mathrm{m\,s^{-1}}$ shock. The plastic deformation can be partitioned into three zones. At the leading edge is a region characterised by one or two full dislocations. Behind this is a region of multiple slip, but still characterised by a few full dislocations. Towards the piston is a region where there is a large number of stacking faults occupying many slip systems.

### 3.1.7 Effect of Defects

In the preceding section, the generation of stacking faults and dislocations occurs above some threshold stress, or piston velocity. For those simulations where the piston velocity is close to the threshold, the simulation runs for some time before the dislocation activity is initiated. This means that in order to carry out a simulation in which the steady state (i.e. self–similar) behaviour is to be examined then it is necessary to create a large simulation cell.

Now it is expected that where there is some pre–existing dislocation structure within the simulation then not only would the generation of further plasticity require lower stress levels, but also the observed reduction in stress level within the elastic zone would occur at earlier times.

It is possible to include single dislocations within a MD simulation, but the generation of a defect microstructure is more complex. A simple way to cause the simulation to generate dislocations at low stresses is to create a small void some distance ahead of the piston. As the shock wave passes over the void, it collapses readily, and in so doing dislocations are emitted into the surrounding material.[45]

In order to test this behaviour the simulation cells described in section 3.1.2 were re–used, but with some atoms removed. The effect of the removal is to create a 2nm

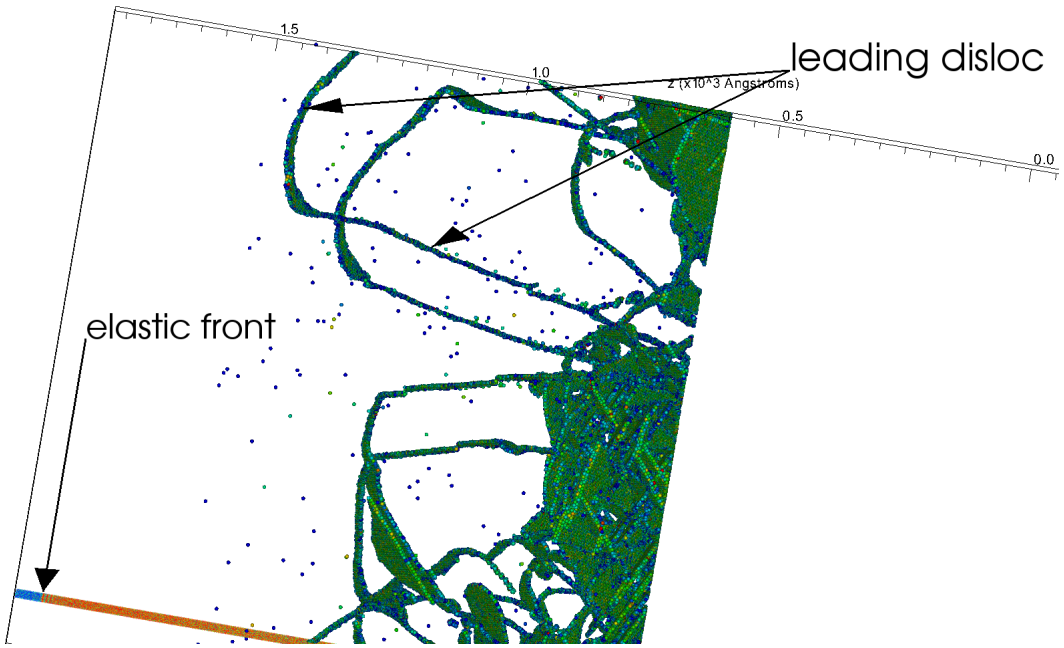


Figure 3.14: Image from figure 3.13 rotated to show the leading dislocation. The shock moves from right to left. The coloured bar in the lower part of the image indicates the velocity in the shock direction; the elastic front is indicated where the stationary (blue) transitions to moving (red).

diameter void placed 20nm ahead of the piston (see figure 3.15).

Since the dislocations are nucleated by the collapse of the void, the effect seen in figures 3.5 and 3.6, where the dislocation activity is observed to start spontaneously just behind the shock front, does not occur. That is, the dislocation activity in the defected simulations starts as the shock front passes over the void (see figure 3.16). The stacking faults lie on the $\{111\}$ planes (the primary slip planes of the FCC lattice), generating a cross pattern. The dislocations continue to expand away from the void, wrapping around the periodic boundaries thus creating what appears to be a network of stacking faults.

For the simulation oriented with $\langle 100 \rangle$ parallel to the shock direction it was found that dislocations were generated for piston velocities as low as $200\,\mathrm{m\,s^{-1}}$. However, examination of the pressure and shear stress profiles were similar in shape to those for a piston velocity of $700\,\mathrm{m\,s^{-1}}$ (see figure 3.3) in perfect crystals. That is to say that the dislocations are initiated as the elastic wave passes over the void, and the front of the plastic region continues to grow forward at a similar velocity to the elastic wave. Due to the time required for the dislocations to be emitted from the void and pass across to the simulation cell walls, thereby generating the front of the plastic zone, there is a time lag between the elastic wave and the plastic front. These two parts of

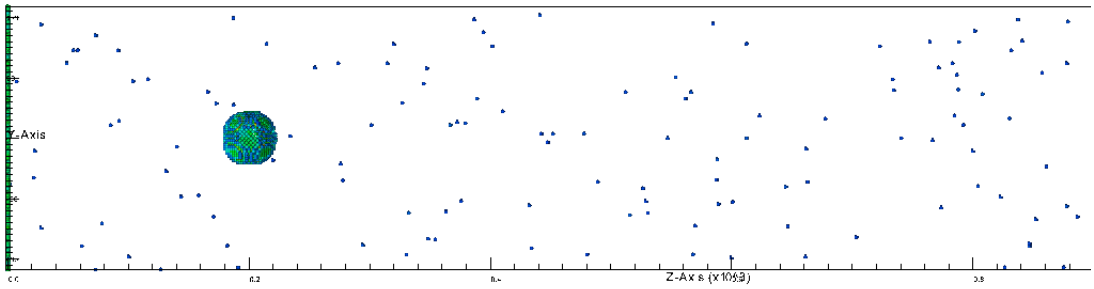

Figure 3.15: Image of ⟨100⟩ simulation with a void created by deleting the atoms from a spherical region. The void is highlighted by the atoms immediately surrounding the void, which appear (using CSP) to be defected since they have no neighbours on the void side.

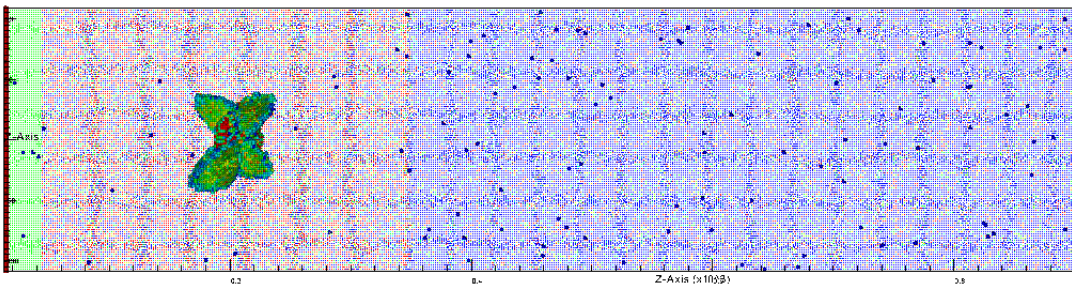

Figure 3.16: Image of ⟨100⟩ simulation with a void created by deleting the atoms from a spherical region. The shock has passed over the void (shown by the background unshocked (blue) and shocked (red) regions). The piston (and hence shock) travels from left to right. [See animation F1.5 in the electronic appendix.]

the shock profile are travelling at similar velocities, and travel forward together.

A similar process occurs in the ⟨111⟩ orientation. Here the generation of dislocations, which occurs when the elastic wave passes over the void as previously described, causes a reduction in pressure and velocity in the same way as occurs in the undefected crystals described above. Similarly to that described for the ⟨100⟩ case, there is a time/distance gap between the elastic wave and the plastic front. However, in contrast to the ⟨100⟩ orientation, and as described for the undefected samples above, the elastic wave travels faster than the plastic front. Now the elastic wave is reduced in amplitude as it moves forward, due to the release from the plasticity occurring behind, and the two parts of the shock wave move apart due to the differing velocities.

This last aspect raises another issue. That is to say that the elastic wave may be reduced in amplitude in comparison to that in a shock wave with no dislocation activity, but its magnitude is still very large in comparison to the experimentally determined value. One possible explanation for the failure of the dislocation activity to reduce the elastic wave to the expected value is due to the time lag which appears between the arrival of the elastic wave and the formation of the plastic front. It can be seen in figure 3.10 that the relief of the shear stress due to the action of dislocations takes some time (or travel distance, since the figure is given in space at a fixed time). This means that the minimum of the pressure profile, from which the release travels forward to reduce the amplitude of the elastic wave, is not at the low level expected from experimental results. This is due to that minimum being supported by the higher pressure of the elastic wave ahead, and the continued compression leading to higher pressures due to the piston behind.

Since the amplitude of the elastic wave in these simulations remains above the threshold for dislocation generation in the presence of voids, it may be possible to enable further reduction of the elastic wave amplitude by causing the wave to pass over more voids. Figure 3.19 shows the velocity profiles for a simulation in which three voids were placed along the shock path. Furthermore, the simulation was started with a piston velocity of $200\,\mathrm{m\,s^{-1}}$, corresponding to a level just able to produce dislocations in the presence of a void. However, the stronger pulse of $920\,\mathrm{m\,s^{-1}}$, which is at a level just below that which will produce nucleation of dislocations without voids being present causes an elastic wave to be produced which has a far higher amplitude than that of the $200\,\mathrm{m\,s^{-1}}$ pulse. This faster elastic wave, then, overtakes the lower amplitude, slower, elastic wave, and the latter's effect is negated. However, the main part of this simulation, *viz* to examine the reduction in amplitude of the elastic wave due to the heterogeneous nucleation of dislocations, can be clearly seen.

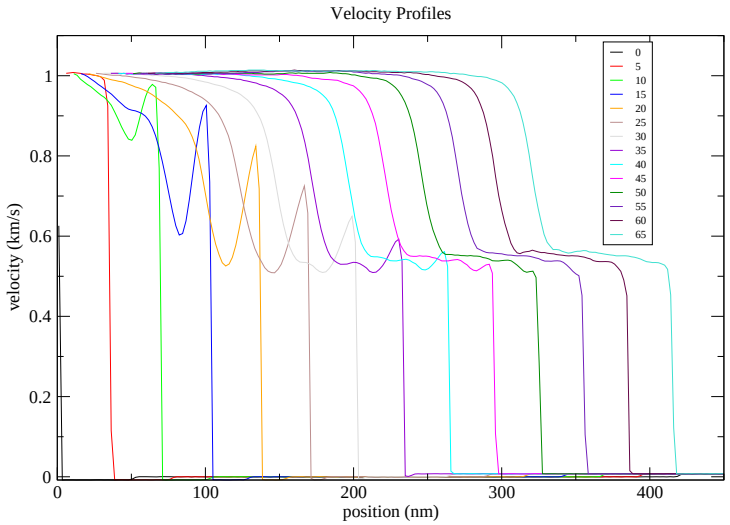


Figure 3.17: Graph of velocity profiles in ⟨111⟩ simulation showing how the production of dislocations causes a reduction in the particle velocity, which then causes the particle velocity associated with the elastic wave ahead to decay to some steady lower level. The legend gives the time associated with each snapshot.

Although such reduction occurs, the reduction in amplitude caused by the second void is considerably less than that from the first interaction event. Subsequent interaction events, then, have a diminishing returns effect and the elastic wave can be seen to asymptote to a level between 300 and 400 $\mathrm{m\,s^{-1}}$.

Now the level of this elastic wave in the presence of multiple voids is still very high when compared to the experimentally observed value. Indeed, from equation 2.6, the pressure can be estimated to be ∼210 kbar, considerably above the experimental HEL for single copper crystals of between 1.3 and 2.0 kbar determined by Jones and Mote.[81] Bringa *et al*[27] estimated the HEL for this potential to be 320±20 kbar, which compares well to that shown in figure 3.10. So the effect of the voids is seen to reduce the amplitude of the elastic wave considerably, but not sufficiently to account for the experimental observations. One reason for this may be the behaviour of this particular potential. Both Mishin *et al*[116] and Boyer *et al*[22] describe this potential as supporting considerably more stress than that estimated by DFT, and that the ideal shear strength is calculated to be ∼29 kbar compared to ∼22 kbar for DFT.[22]

### 3.1.8 Analysis of Velocity Profile

It is useful to understand the slope of the plastic front, as this enables comparison to experimental data. This latter point is valuable as the experimental data are not taken from the bulk of the material, rather they are either free surface measurements

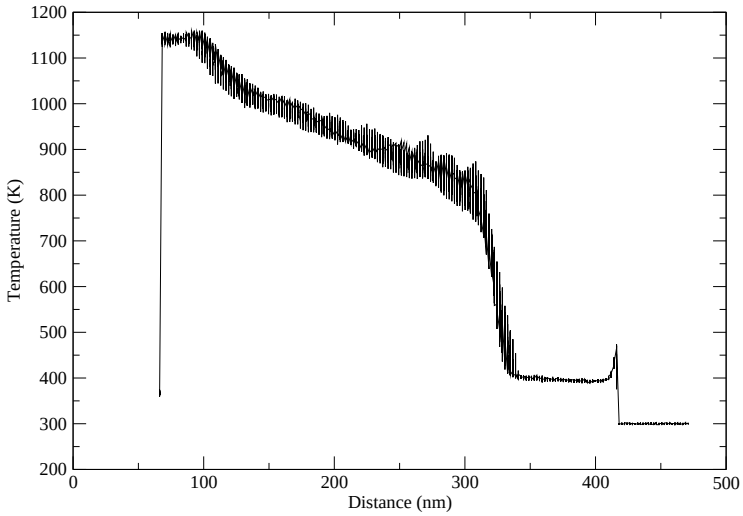


Figure 3.18: Graph of ⟨111⟩ simulation showing how the production of dislocations causes an increase in temperature. Snapshot time (65ps) corresponds to the last curve in figure 3.17

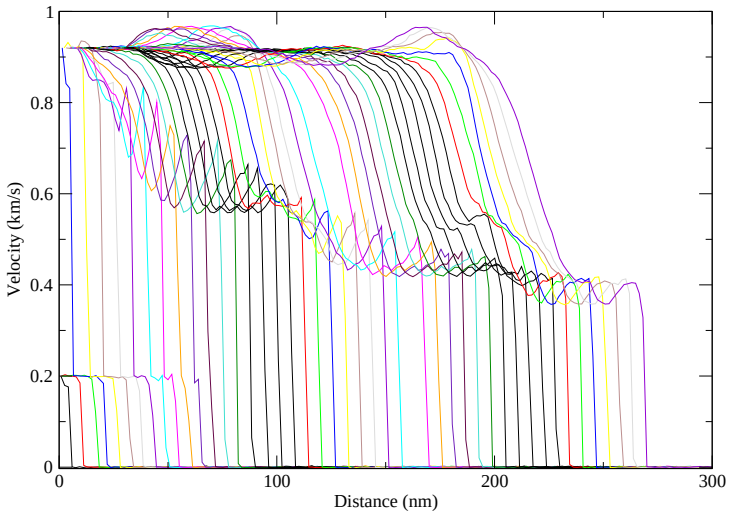


Figure 3.19: Graph of particle velocity in ⟨111⟩ simulation as the shock passes over multiple voids. The effect of each successive void on the elastic precursor is seen.[See animation F1.9 in the electronic appendix.

or else taken from embedded gauges. Understanding the behaviour of shock waves in crystalline materials using MD simulations enables better understanding, and hence interpretation, of experimental data.

As is shown above, in a MD simulation of perfect crystals, the dislocations evident at the leading edge of the plastic front are not nucleated at the very instant that a shock simulation is started. Rather, after a short amount of the travel of the compressive disturbance, dislocations are nucleated homogeneously in the compressed region. The dislocations are then observed to travel away from the central nucleation zone. For shocks travelling along the $\langle 111 \rangle$ direction, the relief of stress caused by the action of the dislocations acts as a release wave on the over–stressed elastic region. This relief causes a decay in the elastic precursor. Figure 3.17 shows the decay of the precursor.

The decay of the elastic precursor shown in figure 3.17 shows the same form as the precursor decay described by Gilman.[66] Figure 3.18 shows the temperature profile of the simulation at 65ps. A distinct rise in temperature can be seen at the same point as the rise in pressure associated with the front of the plastically deformed region. The action of the dislocations causes a temperature rise in the shocked material. Furthermore the shear stress can be seen to fall dramatically over the same spatial region as the temperature rise (cf. figures 3.17 and 3.18(last trace)). This shows that the elastic strain energy is being converted into thermal energy. Furthermore, the continued rise in temperature in the region between the plastic front and the piston (figure 3.18) shows that dislocation activity continues behind the plastic front, i.e. the stress state continues to move towards the hydrostat within the shocked material. This aspect is in contradiction to the shock analysis given in section 2.1. In that analysis it is assumed that the change in thermodynamic state, due to the action of the shock, is instantaneous, or at least occurs to completion prior to the equilibrium condition which would be taken as the shocked state.

### Comparison to Experimental data

Embedded gauges have relatively long response times because of the need to 'ring up' to the ambient pressure. That is, an embedded gauge needs to be electrically isolated from the metallic sample material. This is achieved by encapsulating the gauge material between thin (2 or 3 $\mu$m) layers of insulating material. Even though the layer of insulating material is very thin, the large difference in shock impedance means that the pressure seen by the gauge itself is much lower than that of the incoming wave. The low pressure wave travels through the gauge until it reaches the

sample material on the other side. Due to the higher impedance there is a reflected shock back into the gauge, raising the pressure in the gauge package. The reflected shock travels back and forth across the gauge, the pressure rising each time, until the pressure in the gauge matches that of the surrounding sample. It is believed that at least three passages of the wave are required before this occurs. For a shock to transit 20 $\mu$m (the typical thickness of the thinnest gauges) of copper takes approximately 3.6 ns. So the ring–up time is certainly longer than 10 ns.

So there is some interest in determining what is the true rise of the shock front. This latter question relates the empirically–determined relation between the fastest rate of compression (strain rate, $\dot{\epsilon}$) and the pressure behind the shock. Swegle and Grady[142] examined a large range of shock data. They showed that when plotted as log(strain rate) against log(pressure), the data for any particular material fit on a straight line. Moreover, *all* the data could be fit by lines with a slope of 4, with varying offsets. From this they deduced the so–called Swegle–Grady relation

$$\dot{\epsilon} = \kappa P^4. \tag{3.1}$$

Here $\kappa$ is a constant of proportionality which varies from material to material. In order to examine this relationship in these simulations, some measure of the slope of the plastic rise of the is needed. A simple method is to fit the data, using a least squares method, with a function in which the slope is related to a single parameter. Here a function is derived based on the error function.

$$y = a0 - a1 * erf(a2 * (x - a3)) \tag{3.2}$$

In this function, the value $a2$ governs the slope (see figure 3.21).

Two simulations were run with the unit cell oriented so that the $\langle 111 \rangle$ direction was parallel to the shock direction. The first used a piston velocity of $1.0\,\mathrm{km\,s^{-1}}$ and the second used a piston velocity of $1.2\,\mathrm{km\,s^{-1}}$. A comparison of the pressure profiles is shown in figure 3.22. Notably, it can be seen that the amplitude of the elastic wave varies between the simulations, being 155 vs. 230 kbar for the 1.0 and $1.2\,\mathrm{km\,s^{-1}}$ piston velocities respectively. This is in contrast to the expected behaviour, observed experimentally, where the elastic wave would be at the amplitude of the yield stress under dynamic conditions, known as the *Hugoniot elastic limit* (HEL). However it is observed that the elastic waves both travel at the same velocity, $6.42\,\mathrm{km\,s^{-1}}$.

The main shocks travel at 4.88 and $5.3\,\mathrm{km\,s^{-1}}$. Estimation of the pressure behind the shock is made difficult because, for both simulations, the pressure continues to rise from the end of the main shock back towards the piston. For the $1.0\,\mathrm{km\,s^{-1}}$

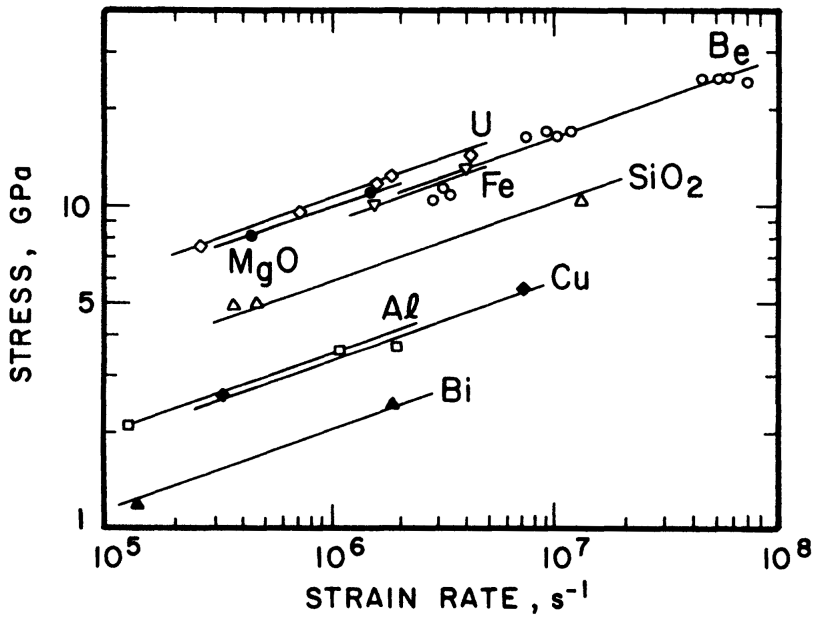


Figure 3.20: Graph of peak stress vs. strain rate for a range of materials. From [111]

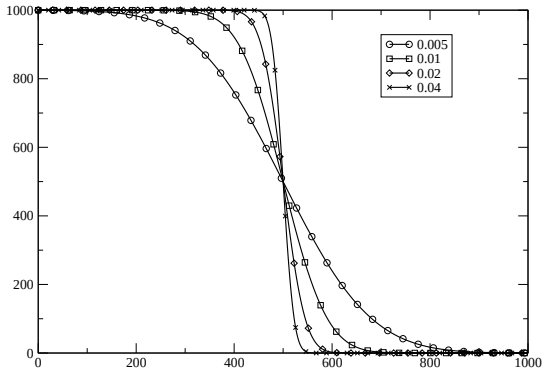


Figure 3.21: Graph of equation 3.2 showing the effect of the parameter a2. For all curves, $a0 = 500$, $a1 = 500$ and $a3 = 500$. $a2$ is as given in the legend.

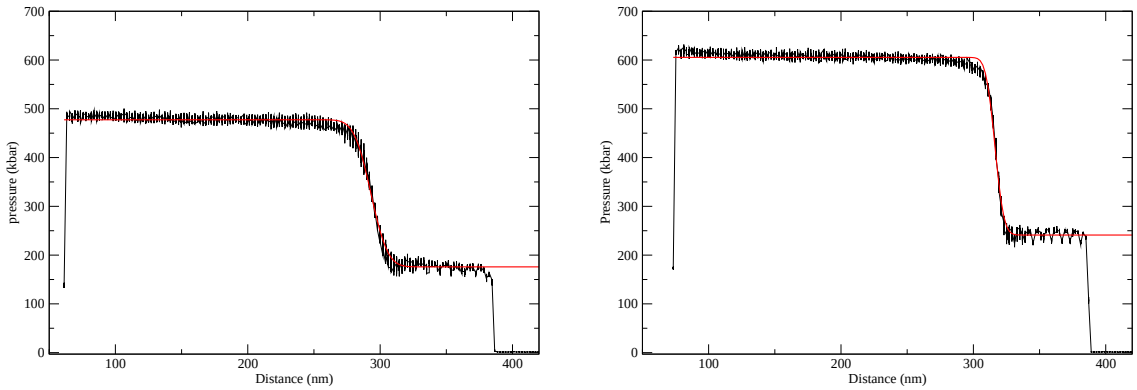


(a) $1000\,\mathrm{m\,s^{-1}}$ (b) $1200\,\mathrm{m\,s^{-1}}$

Figure 3.22: Shocks in $\langle 111 \rangle$ crystal. Snapshots at 60ps. The shock moves from left to right. The black curve shows the measured pressure profile; the red curve is the fit to equation 3.2 (Parameters are given in table 3.2).

| | $1000\,\mathrm{m\,s^{-1}}$ | $1200\,\mathrm{m\,s^{-1}}$ |
|---|---|---|
| a0 | 326.7 | 390.63 |
| a1 | 150.9 | 182.0 |
| a2 | 0.071 | 0.133 |
| a3 | 293.0 | 316.3 |

Table 3.2: Comparison of the parameters fit to equation 3.2 for two different piston velocities.

simulation, the pressure rises from ∼468 to ∼487 kbar. In the $1.2\,\mathrm{km\,s^{-1}}$ simulation, the pressure rises from ∼595 to ∼617 kbar. From equation 2.6 the pressure can be calculated as 43.5 and 56.6 GPa (∼435 and ∼566 kbar) which is slightly lower than the respective lower values estimated from the profiles in figure 3.22. This discrepancy may be due to the nature of the shock in the simulation. That is to say, the Rankine–Hugoniot relations (section 2.1) assume a single shock transition from an initial state to some final, steady, state. Clearly these simulations show that the material behind the shock is not steady, but continues to relax the shear stress developed during the shock compression. This is shown in figure 5.6f, where the shear stress can be seen to continue to fall behind the initial sharp relaxation of the plastic front, and also in figure 3.17 where the temperature continues to rise, indicating that motion and interaction of dislocations continues across the entire region between the plastic front and the piston.

Figure 3.22 shows that the slope of the main plastic front varies with the increase in piston velocity. Table 3.2 shows the difference in the fits to equation 3.2 of the main plastic shock front. The profiles shown here are not set up ideally for a comparison

with the Swegle–Grady relation given in equation 3.1. However, since the prime aspect of the relation is the slope of the log-log plot, a comparison with the data available here is possible. Using this data, the slope of the log(pressure rise with distance) against log(pressure) has a slope of 4.3, close to the Swegle–Grady value of 4. This dataset includes only two points, and therefore conclusions drawn from this work must be treated with caution. Furthermore, examination of this data using the tools shown here (in–material pressure and velocity plots) does not give an adequate explanation of why this particular relation should exist.

### 3.1.9 Conclusions

The studies shown here have examined the simulation of ideal and near–ideal crystals under piston–driven shock loading. In contrast to previous work,[27,64,76] these simulations show a behaviour more closely resembling the experimental traces. This has enabled comparison with observations made in those experimental studies, such as elastic precursor decay[66] and shock steepening.[142] However, simulations are not yet able to create many of the experimentally observed features of real materials, such as initial dislocation density.[81] This fact, taken with the errors described for this potential,[22,116] shows that these simulations cannot be used for detailed quantitative analysis. That having been said, there is much which can be learned from the behaviours exhibited by the material simulated, such as the way in which dislocation production occurs under a range of circumstances.

## 3.2 Polycrystal Behaviour

### 3.2.1 Introduction

Real metals are made of of a very large number of small crystals, all oriented randomly with respect to each other. There are exceptions to this situation including single crystals used in jet turbines due to the low creep properties afforded by not having grain boundaries or amorphous metals, which have no crystalline structure, which are finding increasing technological use, such as in retail store security systems where advantage is taken of the unusual magnetic properties of some nickel–iron alloys. Furthermore, metals processing, such as rolling, drawing and forging produce deformed grain shapes. As a consequence, the statistical measure of the number of grains against orientation does not show a truly uniform random distribution, rather there is preference for some particular orientation. This situation is known as *texture*.

Therefore, there is some interest in understanding how grain boundaries between crystals of differing orientation affects the bulk material behaviour. This situation arises at two scales; the finest scale relates to the action of a boundary itself – how the energies of grain boundaries affect the behaviour of atoms and plasticity agents (dislocations, twins) and how the existence of a boundary affects those agents, acting as a barrier to motion or continued plasticity. The longer scale considers how the existence of a large number of grains randomly oriented affects the macroscale behaviour of the sample. This can be seen, for example, in the way in which the heterogeneous mechanical response to stress is averaged over the sample either in the Voigt limit, where the strains are assumed to be constant, or the Reuss limit in which the stresses are assumed to be constant across all of the constituent grains.

When considering shocks, since the shock velocities and behaviours are different along different crystallographic orientations, one may expect that shock waves will respond in some way to the two situations described above. That is, for the case where there is a grain boundary between two grains, one might expect that there will be some effect due to the differing grain orientations, and some effect due to the grain boundary itself. This section describes briefly some work carried out to examine these situations.

### 3.2.2 Bicrystals

Cao *et al*[36] examined the behaviour of a $[100]/[01\bar{1}]$ copper bicrystal experimentally, via a shock recovery technique. They found that twinning was present in the [100], but not the $[01\bar{1}]$ crystal, for the shock pressures they examined. They describe this difference as being attributed to the different behaviour of dislocations, which enable the twinning process. Although twinning was not observed in the single crystal work carried out here (see section 3.1), differing dislocation behaviour was observed, which supports the results of Cao *et al.*[36] It should be noted that, although the recovery method used ensures that all the stress waves within the sample travel only in the shock direction, that is to say that the sample is retained in a one dimensional strain state, the sample nevertheless undergoes a release phase during the recovery process. Therefore one should be mindful of the effect upon the shock–generated microstructure of that release phase. Even so, the release phase will, like the shock wave, behave differently between the two orientations within the bicrystal, making such experimental work extremely valuable in bringing insight to the effect of orientation within the understanding of shock processes.

Dremov and Bringa[51] examined the effect of a grain boundary on shock waves. They compared how the angle of the grain boundary to the shock direction affected the shock wave. Their work showed that the energy of the atoms in the grain boundary region was higher than in the bulk crystals, and the additional energy supplied by the shock wave could cause the grain boundary region to melt preferentially at a shock pressure lower than that predicted by examination of the phase diagram.

For this work, in order to examine the effect of one grain upon another, pairs of crystals have been set up such that the grain boundary lies parallel to the direction of the shock. Thus the shock is set up in each grain independently at the start of the simulation, and the effects observed are related to the shock properties of one crystal affecting the behaviour of its neighbour. That work was presented at the *Plasticity 2005* conference, see Appendix D.1.

A simulation was set up utilising a nickel potential, with the MEAM model[15] (see Appendix A). The simulation cell occupied a space of 29.1 nm in $X$, 28.3 nm in $Y$ and 66.4 nm in $Z$. The $Y$ extents of the cell were from $-14.55$ nm to $+14.55$ nm. Schematically, then, the cell was split along the plane $Y = 0$. The top half was filled with atoms oriented with $\langle 100 \rangle$ parallel to the $Z$ axis. The lower half was filled with atoms oriented with $\langle 111 \rangle$ parallel to the $Z$ axis. These orientations were used to maximise the difference in shock velocities between the two crystals. The shock was created by superimposing a velocity of $2\,\mathrm{km\,s^{-1}}$ onto the leftmost ($Z \leq 0$) 13.3 nm of both crystals. In this way, the setup of a gas-gun flyer experiment is simulated (see section 3.1.1). Because both the flyer material and the sample material are the same, the simulation recreates a symmetric shock. In this arrangement a shock travels at the same speed away from the interface (in the frame of reference of that interface) into both the flyer and the sample material. Because of this, the particle velocity behind the shock is half that of the initial flyer velocity. Hence figure 3.23 shows an initial maximum particle velocity of $1\,\mathrm{km\,s^{-1}}$. The second aspect of this type of simulation is that the shock travelling backwards into the flyer, upon encountering the free surface, returns then into the simulation cell as a release wave. Examination of the particle velocity at some fixed point over time, as is shown in figure 3.23 provides the time for the shock to transit twice the thickness of the flyer, and hence the shock velocity. For the two crystals simulated, from figure 3.23, this value is 5.5 and $8.5\,\mathrm{km\,s^{-1}}$ for the $\langle 100 \rangle$ and $\langle 111 \rangle$ crystals respectively.

From figure 3.23 it is clear that not only is the shock velocity very different between the two crystals, but the response of the material to the shock compression is also very different. This is further shown in figure 3.24, where the difference in plastic

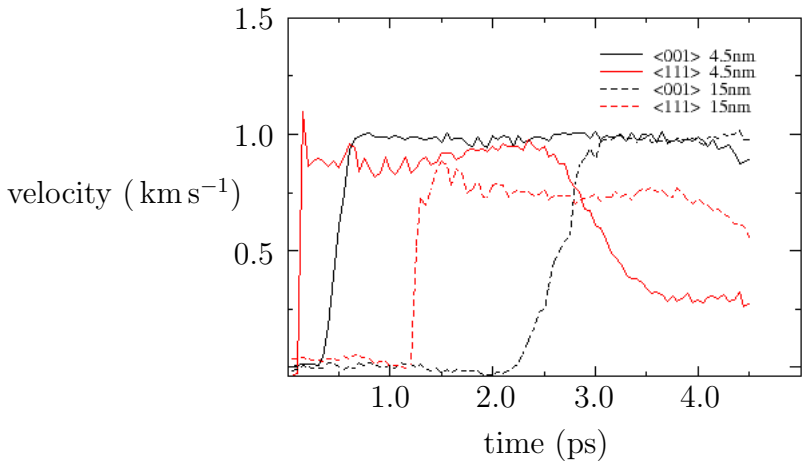


Figure 3.23: Flyer shock in [100](black curves)–[111](red curves) crystal. Traces taken by examining the velocity at the centre of each crystal at some fixed position (4.5 and 15 nm from the flyer–sample interface) over the whole time of the simulation.[See animation F2.1 in the electronic appendix.]

response can be seen. Furthermore, both crystals respond in a different way to that described for the copper single crystals in section 3.1. For this nickel potential, the ⟨111⟩ crystal is over–driven, i.e. the shock is of a strength that the plastic front travels faster than the elastic wave. Consequently the elastic wave is not seen. In the copper results shown in section 3.1 the shock is not over–driven until a particle velocity of 2000 m s$^{-1}$ (see figure 5.1).

The ⟨100⟩ crystal, in contrast, displays little or no plasticity. The reason for this is that the shock is driven such that the crystal passes through the *Bain path*. This process occurs because both the FCC and BCC are high symmetry instances of the body centred tetragonal lattice[b]. As a consequence, compression of the FCC lattice along ⟨100⟩ by $^1/_{\sqrt{2}}$ transforms the structure to a BCC lattice (see figure 3.25). Whilst for this uniaxial compression the volume is not conserved (that would require a compensating expansion orthogonal to the compression direction[9]), volume conserving transitions along the Bain path were examined by Mishin *et al* for copper[116] and nickel.[115] These works were both aimed at developing EAM models for copper and nickel respectively, but examination of the *ab initio* calculations shown in those papers is useful. For both of these models, there is a local maximum at $^c/_a = {}^1/_{\sqrt{2}}$,

[b]A tetragonal cell is one where the crystal axes are orthogonal, but one side differs in length from the other two, those being the same length as each other. The two identical axes are conventionally designated $a$ whereas the other (different length) axes is designated $c$. Thus the degree of tetragonality is given by the ratio $^c/_a$

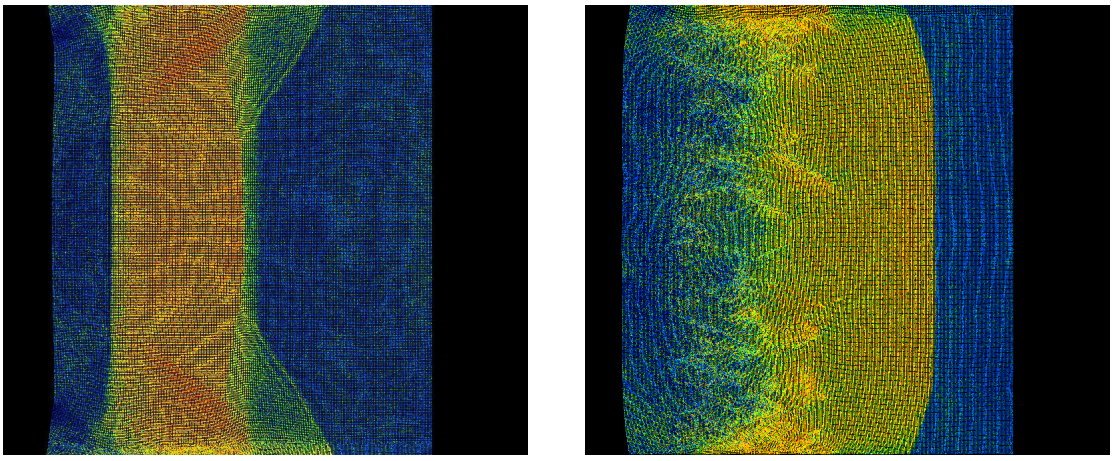

(a) 001 (b) 111

Figure 3.24: Comparison of shocked regions in ⟨100⟩ and ⟨111⟩ crystals. Atoms are coloured by velocity component parallel to the $Z$ axis of the simulation cell (i.e. in the direction of the shock). The image has been split along $Y = 0$, so that the top of 3.24b matches the bottom of 3.24a. Thus the extent of the interaction, particularly of the ⟨111⟩ upon the ⟨100⟩ can be seen.[See animation F2.2 in the electronic appendix.]

but in the copper case the local minimum at $^{c}/_{a} < {}^{1}/_{\sqrt{2}}$ is very small. In contrast, for nickel, the local minimum at $^{c}/_{a} < {}^{1}/_{\sqrt{2}}$ is quite significant, amounting to nearly 0.2 eV/atom. It is noted in the copper paper[116] that the maximum at $^{c}/_{a} = {}^{1}/_{\sqrt{2}}$ indicates that the BCC structure is unstable against the volume–conserving tetragonal distortion applied in that work, but the minimum at $^{c}/_{a} < {}^{1}/_{\sqrt{2}}$ is a form of body centred tetragonal lattice with the designation $A_a$ and is metastable in some metals under compression.

Further comparisons between the crystals studied in this bicrystal shock simulation can be made by use of the common neighbour analysis (CNA) (see section 2.4.4). Compression of the ⟨100⟩ crystal towards the BCC structure is shown in figure 3.26. Here it can be seen that the ⟨100⟩ crystal is composed of layers of BCC and unstructured material. This output from the CNA procedure is due to a small mismatch in the stacking of the atoms. Closer examination of the ⟨100⟩ crystal reveals that the $^{c}/_{a}$ ratio is slightly less than 0.8. This shows that the material is being compressed towards the BCC maximum at $^{c}/_{a} = {}^{1}/_{\sqrt{2}}$, $\sim 0.71$, but is not sufficiently compressed to be truly BCC.

It is possible that this difference in behaviour between nickel and copper is related to a difference in available deformation paths. In copper, there is a metastable structure which is described as the *9R*.[116] This structure can be described as the

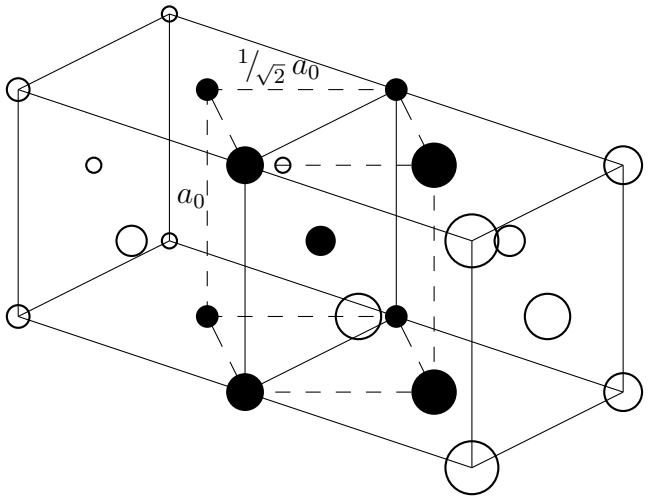


Figure 3.25: Schematic showing the relationship between the FCC and BCT lattices. The FCC lattice is shown by solid lines; the BCT by dashed lines. The original FCC lattice parameter is $a_0$. Therefore the $a$ lattice parameter of the BCT lattice is $^{\sqrt{2}}/_2 = {}^1/_{\sqrt{2}}$. It can be seen, then, that compression along [001] will produce a BCC lattice.

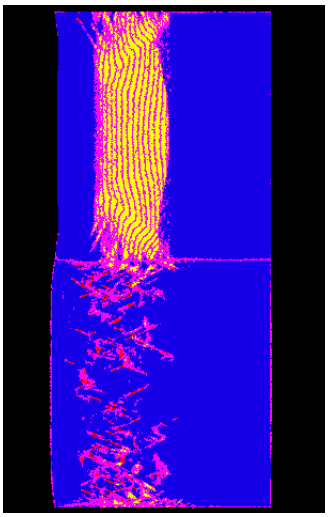

Figure 3.26: Common neighbour analysis of shocked Ni bicrystal. In this image, atoms identified as being in the FCC structure are coloured blue, those as BCC, yellow, HCP, red, and those of no identified order are coloured purple. The top half of the image is the $\langle 100 \rangle$ crystal, the bottom, $\langle 111 \rangle$.

FCC structure with a stacking fault on every third plane.[56] This structure has been observed for several metals under varying conditions such as copper precipitates in Fe alloys,[69] in ultrafine particulates[85] and at grain boundaries.[56] However, this structure does not appear to be commonplace in nickel. This feature, in turn, may be due to a difference in the stacking fault energies. For copper, this value is reported as $\sim 50$ mJ/m$^2$ for the stable stacking fault and $\sim 150$ mJ/m$^2$ for the unstable stacking fault.[116] In contrast, the nickel values are $\sim 125$ and $\sim 375$ mJ/m$^2$ for the stable and unstable stacking fault energies respectively.[115] Now, in these types of simulations, particularly for shocks along the high symmetry directions, the predominant mode of shear relaxation is by production of stacking faults, as shown in section 3.1. Therefore one can surmise that for nickel a higher uniaxial compression along the $\langle 100 \rangle$ direction may be achieved without the homogeneous production of dislocations, which then enables alternative means of energy reduction, such as a transformation along the Bain path.

It can also be seen from figures 3.24 and 3.27 that there is strong lateral interaction between the $\langle 100 \rangle$ and $\langle 111 \rangle$ crystals. The higher shock velocity in the lower, $\langle 111 \rangle$, crystal means that there is compressed material adjacent to uncompressed material. As a consequence the $\langle 100 \rangle$ crystal is compressed laterally (i.e. in the direction of the the $Y$ axis) before the arrival of the shock. It should be noted that, due to the periodic boundaries, which are applied to the lateral extents of the simulation cell, each crystal appears to have a grain boundary on both sides, *viz.* in the centre of the simulation cell, and at the outside boundaries of the cell. This, then, causes the symmetric behaviour observed in each crystal. It may be expected that, since the shock wave in the $\langle 111 \rangle$ crystal causes the atoms to move at a velocity $U_p$, there may be some interfacial friction effects observable at the grain boundary in the $\langle 100 \rangle$ crystal. Whilst such effects can be seen upon close inspection, these effects are small and affect only a few layers of atoms near to the boundary. Therefore the friction effects do not modify the bulk behaviour of the grains, which is dominated by the pressure pulse induced by the neighbouring compressed material.

It is important to understand this grain-to-grain interaction fully in order to gain a better understanding of the nature of shocks in polycrystal materials. This work is being undertaken both computationally and experimentally (both within the author's organisation and elsewhere[112]) in order to improve the mesoscale modelling of material behaviour. In order to investigate the grain-on-grain behaviour for mesoscale studies, a set of bicrystals were manufactured, from which gas gun samples were

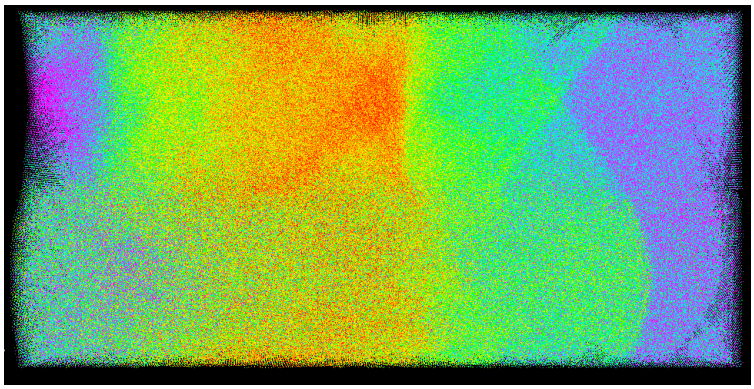

Figure 3.27: Shocked Ni bicrystal. The top half of the image is the ⟨100⟩ crystal, the bottom, ⟨111⟩. Snapshot at 5 ps. Atoms coloured by velocity component in the shock direction.

made. Simulations of the manufactured bicrystals were undertaken in order to gain some understanding of the expected experimental results.

In order to determine the crystal orientations precisely the samples were analysed using electron backscatter diffraction (EBSD). These then gave pole figures, from which Euler angles were determined. This information was then used in the simulation to set up two crystals side-by-side. The nominally ⟨100⟩ crystal was set up with lattice vectors shown in table 3.3 and the nominally [134] crystal was set up with lattice vectors shown in table 3.4. In the single crystal work described in section 3.1.6 the ⟨100⟩ crystal was oriented in the natural way, that is to say that the [100] direction was parallel to the $x$-axis of the simulation cell, [010] parallel to the $y$-axis and [001] parallel to the $z$-axis. Due to crystallographic symmetry, each of these directions is equivalent. The ⟨100⟩ crystal created here is set up with [010] parallel to the $x$-axis, $[\bar{1}00]$ parallel to the $y$-axis, and [001] parallel to the $z$-axis. This should produce a crystal which is crystallographically equivalent, but rotated around the $z$ axis of the simulation cell. However, it can be seen from table 3.3 that the crystal is not set up perfectly, but is slightly under-rotated around that axis, and is rotated to some small degree away from having the [001] direction parallel to the $z$ axis. Similarly, the [134] crystal is closer to having the [124] direction parallel to the shock axis. For simplicity, and in line with previous discussions, these latter orientations will be referred to (*stricto sensu* incorrectly) as ⟨100⟩ and [134].

The misalignment of the [134] crystal is expected to make only a small difference to the behaviour observed. In the simulation, there is one slip system which is more favourably oriented to the shock axis. The experimental orientation, similarly, will have one slip system most favourably oriented. Consequently some difference in the

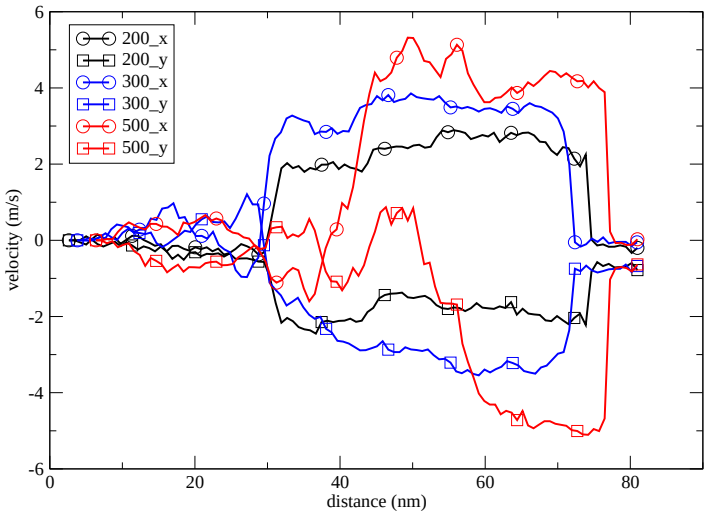


Figure 3.28: Shock in [134] crystal. Velocities normal to the shock direction. Piston velocities are shown in the legend.

stress at which the slip occurs may be observed, but the general behaviour will be the same.

In contrast one might expect that the ⟨100⟩ crystal will behave very differently if there is some degree of misalignment. True degeneracy of the available slip systems will only exist if the alignment is perfect. In theory, even a small misalignment will cause one slip system to be favoured over the others. But in practice, especially under shock loading, all of the degenerate slip systems will experience shear at a level above the critical resolved shear stress necessary for slip. Consequently there will be multiple slip in the same way as has been shown for the ⟨100⟩ single crystal (section 3.1.3). However, in contrast to the [134] crystal, as the degree of misalignment increases, rather than a simple change in stress amplitude determining the slip behaviour, one expects to see a change in the ratio of the activity on each of the slip systems, with one system at work more than the others.

Prior to the experiments, simulations were carried out to determine if there might be any unexpected effects which may invalidate the experiments. One such effect would be lateral motion of one crystal relative to the other, causing the two crystals to move apart during the experiment.

It is well known that elastic waves travelling along crystal vectors other than the high symmetry directions will be split into longitudinal and shear components.[19] One consequence of this is that the elastic wave generated by the shock front will induce lateral motion of the atoms. The behaviour, then, of the [134] crystal as the piston velocity is increased is of interest. In order to understand this effect, the single

[134] crystal simulations from section 3.1.6 were analysed to determine the extent of such motion. Figure 3.28 shows the normal particle velocity profiles (i.e. the velocity profiles of the components of velocity parallel to the $X$ and $Y$ axes of the simulation cell) at three piston velocities. Firstly it can be seen that the amplitude of the lateral motion increases with increasing piston velocity. The $X$ component is positive, i.e. to the right, and the $Y$ component is negative, i.e. out of the page.

This may imply, then, that the very effect one wishes to avoid, *viz.* the separation of the crystals, is being generated here. However, closer examination of figure 3.28 shows that, for the 500 $\mathrm{m\,s^{-1}}$ shock, where plasticity is observed, the curves show almost no lateral motion. That is to say, behind the plastic front, which is where any significant bulk motion may be expected to occur, the lateral motion of the atoms is seen to be negligible. Therefore, the stress on the grain boundary, i.e. whether it is under tension or compression, should be dominated by the pressure of the main shock, and so it will remain under compression.

| | | | |
|---|---|---|---|
| $X$ | $-0.258$ | $0.965$ | $0.045$ |
| $Y$ | $-0.965$ | $-0.259$ | $0.026$ |
| $Z$ | $0.037$ | $-0.037$ | $0.999$ |

Table 3.3: Orientation of $\langle 100 \rangle$ crystal. Crystallographic vectors along each of the simulation cell axes.

| | | | |
|---|---|---|---|
| $X$ | $-0.328$ | $0.840$ | $-0.433$ |
| $Y$ | $-0.851$ | $-0.461$ | $-0.25$ |
| $Z$ | $-0.410$ | $0.287$ | $0.866$ |

Table 3.4: Orientation of [134] crystal. Crystallographic vectors along each of the simulation cell axes.

The shock was set up by creating a piston along the boundary where $Z$ is a maximum, with a velocity of $500\,\mathrm{m\,s^{-1}}$ in the direction of $-Z$. This setup was used to recreate the shock experiments, in relation to the crystal axes as given in tables 3.3 and 3.4. Figure 3.29 shows the simulation after 21 ps. The difference in the elastic wave velocities is clearly seen. Furthermore, the effect of the faster wave in the [134] crystal can be seen in the $\langle 100 \rangle$ crystal, where the shock front is curved. It should be noted that this simulation was set up with periodic boundary conditions along its lateral extents. This condition is necessary to ensure that the material does not escape from the simulation under the action of the shock pressure. Such behaviour would lead to unphysical release waves entering the simulation cell, thus modifying

the observed behaviour. However, the effect of these boundary conditions is to create two grain boundaries; the centre boundary, which is clearly seen, and an additional grain boundary between the leftmost edge of the ⟨100⟩ crystal and the rightmost edge of the [134] crystal.

From this it can be seen that whereas the shock front in the ⟨100⟩ crystal is nearly symmetric, left to right, the front in the [134] crystal behaves differently depending on whether the neighbouring ⟨100⟩ crystal is on its left or right hand side. Where the slow neighbour is on the left, the front runs at nearly full speed, and the front itself appears flat. In contrast, where the neighbour is to the right, there is a noticeable drag effect, causing a curvature in the shock front profile.

The effect of the lateral motion is shown in figure 3.30. It is useful to compare this image to the graph shown in figure 3.28. Whereas figure 3.28 shows the average behaviour for a single [134] crystal with no grain boundary, figure 3.30 shows the [134] crystal with a grain boundary present. In this latter figure, there is noticeable chirality in both the ⟨100⟩ and [134] crystals. If one takes into account the periodic boundaries, then the lateral motion which figure 3.30 appears to show in both crystals has no discontinuity at either grain boundary (i.e. the centre or the lateral (wrapped) grain boundary). This supports the conclusion drawn earlier that any lateral motion will be small in amplitude, and the grains will hold together under pressure.

Figure 3.30 further supports the conclusion drawn that the lateral motion all but disappears with the onset of plasticity. Comparison of figures 3.30 and 3.29 (particularly the far right portion of both figures) shows the lateral motion ceasing abruptly where the stacking faults indicate the plastic front.

### 3.2.3 Polycrystals

In contrast to the two–crystal situation described above, the desire to simulate real materials leads one to consider a sample which is comprised of many small randomly oriented crystallites.

Bringa *et al*[24] examined the shock hardening of nanocrystalline materials. This work examined slip processes which dominate at very small grain sizes. For grain sizes which are found in regular engineering materials, the well known Hall–Petch relationship describes the increase in strength as grain size is reduced. However, it is found that for ultra-small grain sizes, this relationship is reversed.[37] Bringa *et al*[24] showed that, whilst the crystal strength increases with pressure due to the pressure–dependence of the shear modulus, the increase in pressure also suppresses the ability

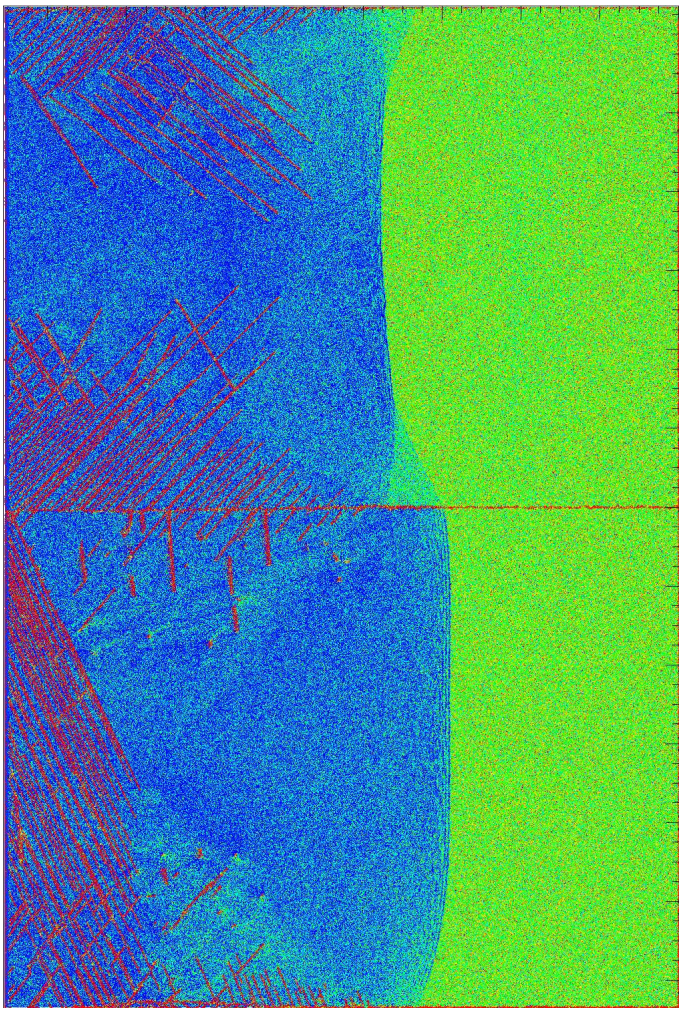

Figure 3.29: 500 m/s shock in ⟨100⟩ (top)–[134](bottom) crystal. The shock moves from left to right. The background colour indicates the velocity in the shock direction; the elastic front can be seen where the stationary (green) transitions to moving (blue). Dislocations and stacking faults are shown as bright red linear features. [See animation F2.10 in the electronic appendix.]

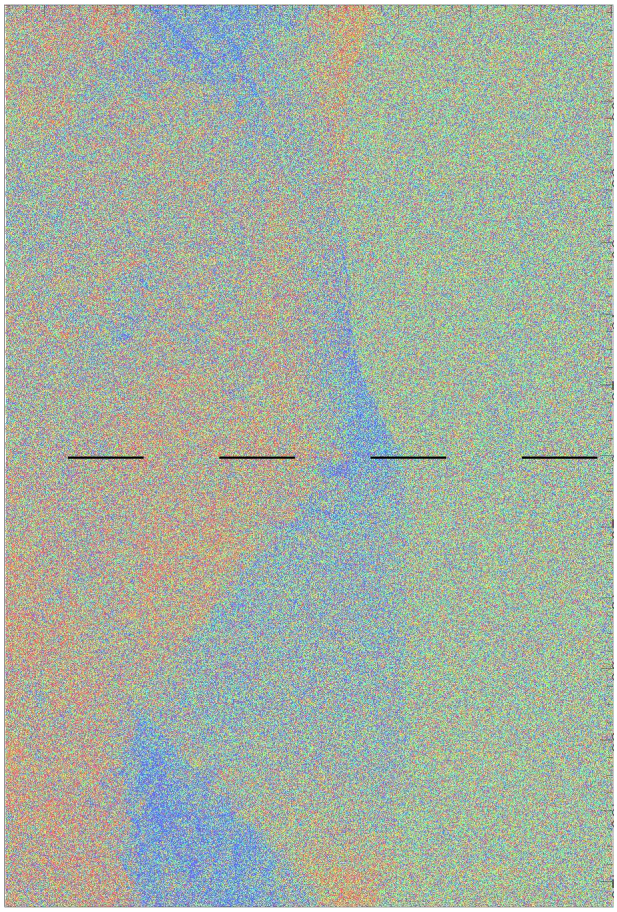

Figure 3.30: 500 m/s shock in $\langle 100 \rangle$ (top)–[134](bottom) crystal (boundary indicated by dashed line). The shock moves from left to right. Colour indicates the velocity in the $X$ (lateral) direction; red indicates material moving to the bottom; blue indicates material moving to the top.

of the grain boundaries to slide. These two features, then, lead to a regime in which ultra-hard materials may exist.

More pertinent to shock behaviour itself, several workers have considered what effect the randomly oriented grains have on the shock front. Bringa *et al*[26] considered how the interaction of the varying wave velocities in the different grains may cause a broadening of the wave front. This work examined the assumptions used in the model derived by Meyers *et al.*[110] Both Bringa *et al*[26] and Meyers *et al*[110] show that the shock width increases as the $^1/_2$ power of grain size.

Barber and Kadau[12] further examine the models for shock front broadening, adding a model of their own. In similarity to the Meyers[110] and Bringa[26] models, the Barber and Kadau[12] model predicts that the width of the shock front increases with the $^1/_2$ power of distance travelled into the sample.

In order to examine this behaviour, a simulation cell was created as a nanocrystalline material. The algorithm for creating such a material follows the Voronoi based method of Van Swygenhoven.[143] Here the grains are formed by creating a set of grain centres which are randomly spaced throughout the simulation cell volume. Each centre is then surrounded by atoms oriented to form a crystal of some random orientation. Atoms which are outside the Voronoi cell associated with the centre forming that grain are deleted. The number of centres is calculated from the ratio of grain volume to simulation cell volume. In this simulation the grain size (diameter) was approximately 5 nm. The material was then shocked by driving a piston from one end. The variation of the shock front due to the presence of grains is clearly seen in figure 3.31.

The shock front position was measured at several locations (on a unifiorm grid) across the sample cross-section for each snapshot. The standard deviation of the front positions then provides a measure of the shock front dispersion, or width, against time. Figure 3.32 shows the variation of this standard deviation measure over time for three piston velocities. Clearly the width of the shock front increases, but only to some limiting value. The mean value for the measure, taken over the region for which the measure is not increasing, is 1.24, 0.78 and 0.72 for the 500, 750 and 950 $\mathrm{m\,s^{-1}}$ piston velocities respectively. This indicates, then, that stronger shocks will display narrower front widths. Furthermore, figure 3.32 shows that the steady state is reached earlier for the stronger shocks.

This behaviour, however, will be dependent on the size of the grains in the sample. This point highlights one of the issues still facing workers in this field. The creation of a molecular dynamics simulation which is large enough to accurately represent the

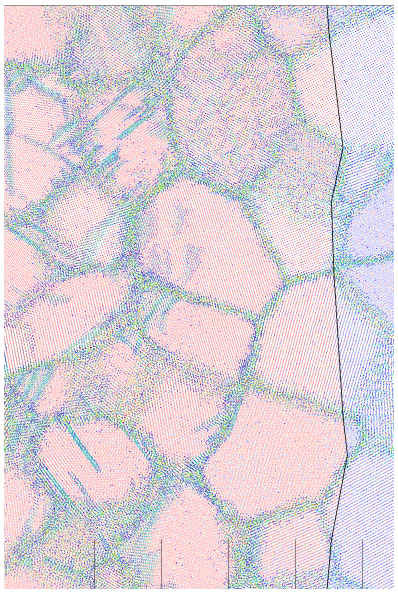

Figure 3.31: Shock in nanocrystal (boundary indicated by dashed line). The shock moves from left to right. Colour indicates the velocity in the shock direction. The shock front is highlighted where the particle velocity transitions from stationary (blue) to moving (red). Use of the centrosymmetry parameter enables grain boundaries (and stacking faults) to be shown.See animation F2.12 in the electronic appendix.]

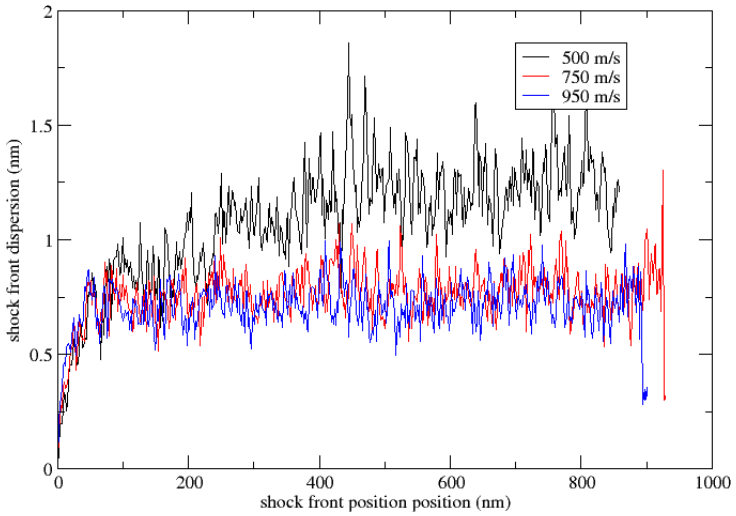


Figure 3.32: Standard deviation of shock front position as the front moves into the sample. Piston velocities are shown in the legend.

sizes of grains observed in experimental samples requires numbers of atoms which is well beyond current computing capability. The simulations shown here contain $>10^8$ atoms, and ∼6000 grains. Work is currently being undertaken to examine large grain sizes. However, as the grain size increases, which necessitates an increase in the simulation cell cross-section, the time to steady-state increases, and hence the simulation cell length increases as well. Therefore the number of atoms increases at least as the cube of the grain size.

### 3.2.4 Conclusions

The FCC to BCC transformation along the Bain path has been theoretically postulated for some time, and is observed under tightly controlled conditions experimentally but the observation of this effect is not common. In contrast, the difference in shock velocities due to grain orientation is well known,[81] and yet little experimental work has been carried out to examine in detail how this may affect the behaviour of polycrystalline materials.

The examples shown here highlight one of the difficulties which remain in using the MD method to simulate materials far from equilibrium. That is that the potentials used to describe the atomic interactions are required to be very robust, and accurately recreate subtle behaviours which are difficult to recreate in the necessarily small simulation cells such as are used in the development of those potentials. Therefore one needs to treat the observation of unusual behaviours seen, such as the Bain path relaxation, with some caution.

On the other hand, the observations of elastic and plastic behaviour as observed in the copper examples shown here, can help toward a more generalised understanding of shock response. Whilst this work may not quantitively recreate the experimental measurements, the veracity of the qualitative results will enable improved descriptions of the mesoscale behaviour anticipated in real applications.

Whilst single crystal simulations have demonstrated considerable value in furthering the understanding of the behaviour of metallic materials under shock loading, the work towards similar understanding in polycrystalline materials will require more compute resource than is currently commonly available.

# Chapter 4

# Particle Impact

## 4.1 Introduction

The study of impact phenomena lends itself to molecular dynamics because the timescales for the events of interest, for the size of problems that can be studied with modern computers fall within the bounds of what is currently feasible. The restriction here is related to the size of the target sample, which then restricts the size of the impacting projectile. This, in turn governs the real time over which the simulation is required to run.

In 1995 an opportunity arose to study the material ejected from the body of a comet due to its interaction with the solar wind. This phenomenon leads to the most well known part of the cometary behaviour; i.e. the development of its tail. The NASA project STARDUST[78] was led by Brownlee of the University of Washington and Tsou from the Jet Propulsion Laboratory. The principal aim was to intercept the tail of comet P/Wild 2 at a velocity slow enough that particles within the tail would be captured by aerogel material carried on board the spacecraft. A mechanism was developed which would return the aerogel samples to earth to enable detailed microanalysis of the particles. However, during the assembly of the aerogel tray a thin (100 micron) pure aluminium foil was used to ensure that the aerogel fit snugly into the sample tray. This meant that in addition to the aerogel there was metallic collecting material exposed to the cometary tail. Groups at LLNL and the Natural History Museum (NHM) in London have carried out detailed analysis of the exposed aluminium. As part of this analysis effort research is being carried out at Kent University where they are studying the relationship between particle characteristics (material, density, size, velocity) and crater characteristics (depth, width, morphology). As part of this study various groups have carried out simulations

using continuum finite element codes. Simulations with molecular dynamics have also been carried out to compare the results of the varying modelling methods.

The purpose of the simulations is to enable a better understanding of the interaction of space dust with metallic objects. This understanding will improve the veracity of continuum simulations, which are orders of magnitude cheaper computationally; it will improve the understanding of the response of metals to high velocity impact; and it will enable improved estimations of the damage done to spacecraft by space dust, thereby increasing their efficacy.

## 4.2 Background

Simulation of impacts using the molecular dynamic method has been carried out by many researchers, and for a very wide range of purposes including atomic absorption, desorption, ion implantation and chemistry. Further, the reaction of clusters themselves to bombardment has been studied in order to understand the behaviour of dust particles in space, sputtering of nanoparticles as part of the *secondary ion mass spectrometry* (SIMS) and *secondary neutral mass spectrometry* (SNMS) processes,[52,163] and to examine laser–matter interaction.[148]

The purpose of this work is specifically to simulate the interaction of large metallic particles impacting a metallic body.

Barghorn and Hilf[14] simulated the impact of gold clusters onto gold surfaces in order to understand desorption due to the sputtering process. In simulating the ion implantation process they describe the initial cluster velocity using a kinetic energy variable. Because the velocities were very high (30 $\mathrm{km\,s^{-1}}$), it was necessary for them to vary the timestep during the course of the simulation. They indicate that the timestep reduced from the early part of the run to later times by a factor of 20. In addition, their code allowed a double-timestepping method to be used. That is, the atoms making up the projectile, and the neighbours of those atoms, have their positions and velocities updated 10 times for each update of the bulk of the target. In this paper the boundary condition for the target is discussed. They opted for a thin bath with an added restoring force $F_{x,y,z} = -\alpha v^{\beta}_{x,y,z}$ where the parameters ($\alpha$,$\beta$) were fit to the critical damping in a one–dimensional chain.

In another study to understand the sputtering of gold, Colla and Urbassek[42] studied the behaviour of the damage cascade due to small gold clusters impacting a gold surface. They compared a change in cluster size from 1 to 4 atoms at a velocity of 125 $\mathrm{km\,s^{-1}}$, in order to examine the increase in sputter yield due to a change in cluster

size. The study also compared the effect of varying cluster size whilst maintaining the kinetic energy deposited at a constant value. This means that the impacting velocity of the cluster is reduced by a factor of $\sqrt{1/m}$ as the cluster mass is increased up to 12 atoms. This work has been extended by [5] who showed that the energy deposited per unit distance travelled into the target is a linear function of the initial projectile cluster kinetic energy.

Shapiro and Tombrello[138] showed that in the sputtering process, light ions are preferentially ejected over heavier ions. Childs, Shapiro and Tombrello[40] took this further and compared their results to experiments which examined the ionic species ejected when compounds were accelerated into gold targets. It should be noted that in these works the objective was to study the excitation of core electrons, and thus the subsequent chemistry, rather than the effects on the target material.

Raz and Levine[129] examined the behaviour of clusters of atoms impacting a hard wall. They examined the region where the cluster velocity is greater than 4 $\mathrm{km\,s^{-1}}$, as this was expected to be the velocity of interest when attempting to generate shock induced chemical reactions. They examined the thermal energy behaviour of the nanoclusters to show how the directed kinetic energy of the motion of the cluster body is converted into random thermal kinetic energy. Their setup consisted of a chain of nanoclusters directed at a rigid wall. This did not allow any exchange of energy with the target material. Furthermore, the motion of the clusters remained perpendicular to the wall, indicating that the interaction was poorly described. They attempted to correct this limitation by approximating the surface with hard cubes. This, however also showed no dissipation of energy into the surface.

Kholmurodov *et al*[92] were motivated by the deposition of material onto surfaces for the purpose of novel materials synthesis. They simulated the deposition of aluminium clusters onto an aluminium substrate, the aluminium atomic interactions being described by the Finnis-Sinclair potential. The system was small; the substrate consisted of 36000 atoms arranged into a block with a surface area of 30 $a_0$ by 30 $a_0$ (where $a_0$=4.0495Å) and the cluster consisted of 864 atoms arranged as a $6a_0$ cube. The velocities they studied were 0.5 – 5 $\mathrm{km\,s^{-1}}$ (which translates to 0.035 – 3.5 eV/atom). In order to control the outgoing shock, which emanates from the impact event, Kholmurodov *et al* use a Berendsen thermostat. In their case, the Berendsen thermostat was applied to all of the substrate atoms. This has the effect of connecting the substrate to a heat bath to extract excess heat generated by the impact. They show that for low energies (<0.15eV/atom, <1.04 $\mathrm{km\,s^{-1}}$) the substrate is to a large extent unaffected by the impact. They show that the cluster remains below

the melting point, its density increases by about 50% and the penetration depth is less than $2a_0$. They also show that the temperature in the substrate returns to its original value after approximately 3ps. Kholmurodov *et al* call this low energy behaviour soft landing. They describe two additional behaviours as droplet spreading and implantation, based on the cluster behaviour after impact. Only in implantation (E>3.5eV/atom, 5 $\mathrm{km\,s^{-1}}$) do they observe a temperature rise sufficient to cause melting. However, the effect of the thermostat on the substrate will severely reduce the plastic effects that may be seen at the lower impact energies. As I show below, the energy variations due to the passage of waves from the impact event are small. Whilst it is necessary to ensure that the substrate is connected to some energy control mechanism, by connecting all of the atoms to the heat bath, local excursions from the equilibrium temperature are greatly reduced. It is these local variations in thermal energy which enable the plastic effects that may be expected to occur to manifest themselves. Although the cluster is not thermostatted, the effect of controlling the thermal energy in the substrate is to present to the cluster a considerably more resistant body than might otherwise be there. So the cluster behaviour, then, is modified by the inaccurate substrate behaviour.

Yamaguchi and Gspann[157–159] saw the surface modification by cluster impact as their motivation. The impact of argon clusters on natural diamond has the effect of reducing the surface roughness, thus acting as a micromachining process. They studied the effects on diamond surfaces of the impact of Ar and $CO_2$ clusters at high energies (100keV/cluster, approx. 104eV/atom) to examine the surface erosion process. Unlike Kholmurodov *et al*,[92] Yamaguchi and Gspann surround the substrate with a thermostatted bath of atoms. The substrate is built as a hexagonal prism with the impacted surface containing the (111) plane. The substrate is approximately 12nm across. In order to reduce the computational cost, the thermostatted bath is built on only one side of the hexagonal substrate. The other sides of the substrate are connected to the thermostatted bath by a sophisticated use of periodic boundary conditions. There are two aspects of this work which should be noted. Firstly, the images of the impact sites shown in the paper exhibit a distinct asymmetry, both in the shape of the impacts and the resultant shock waves. Since the target diamond is set up symmetrically with respect to the direction of travel of the impacting cluster, then the likely candidate for producing these asymmetries is the one-sided way in which the thermostatted bath is created. Secondly, figure 9 in their paper shows clearly that the downward travelling shock is reflected from the base of the diamond substrate. This latter aspect results in a reduction in the depth of the impact crater,

which is seen in their figures. Clearly, then, although these authors have tried to deal with the simulation cell wall behaviour, their results show that their efforts are not fully effective.

The study of ion implanting into matter has been undertaken extensively by Ziegler *et al* since their early work[161] to the extent that there is now a web site[162] dedicated to the development of software which can be used to calculate the stopping of ions deposited at high velocity into substrates.

Ma and Yang[104] studied copper clusters impacting copper a substrate at impacting velocities ranging from 2 $\mathrm{km\,s^{-1}}$ to 10 $\mathrm{km\,s^{-1}}$. The main part of their study used a Lennard–Jones potential (see section 2.3.2) but they also carried out supporting simulations using an EAM potential. In their simulations only the highest velocity impacts produce craters; the other simulations show the crater being filled by molten material. That the material is molten is determined by examining the radial distribution function locally to the impact site. Furthermore, their simulations show a 'temperature measure' based on the mean kinetic energy. This measure indicates that except in the slowest case, the temperature of the entire substrate block is slightly above the melting temperature. A supporting calculation with a significantly larger number of atoms, however, indicates a substrate temperature well below the melting point. Although this point indicates that the main results of their calculations may be in error, this is not noted either in the text or in the conclusions. Additionally, their simulations utilise periodic boundary conditions, which will produce anomalous artifacts as the pressure pulse travels across the boundaries. Their simulation also utilises a timestep of 0.002 ps, which for the highest velocities will produce an error in the total energy (see table 4.2).

Germann[63] examined the damage behaviour in the impacting cluster itself, rather than the consequences to the target substrate. This was achieved by using a perfectly rigid wall of atoms, into which the projectile was driven. The wall consisted of atoms with the same potential interaction as the cluster material, but the atoms' positions were not updated during the integration step. Thus the wall is cold, but can be adhered to, or wetted in the case of liquid projectiles. Germann compared the behaviour of large clusters (51.2nm diameter, approx 5 million atoms) at initial temperatures of 300 K, 1000 K (solid projectile), 1500 K and 2000 K (liquid projectile). The velocities studied were between 500 $\mathrm{ms^{-1}}$ and 1100 $\mathrm{ms^{-1}}$ (a smaller projectile was simulated with a velocity of 2000 $\mathrm{ms^{-1}}$). The study examined two aspects of the behaviour – deformation of the cluster, where it was observed qualitatively that

the plastically deforming solid, particularly when hot, was similar to that of the liquid droplet, and breakup, including hydrodynamic jetting. Additionally there was a continuous loss of atoms from the deforming particle. This latter behaviour was described as a sublimation or evaporation process.

Part of the need for understanding the cratering process in the context of spacecraft operation lies in the reverse evaluation; for a given crater size, what is the size of particle which created it? This has been the central task of Kearsley *et al*[88–90] who have been studying the impact craters on the aluminium foils used in the STARDUST[78] mission. Their work has shown that simple linear relationships can be developed for projectile diameter to crater diameter. Clearly these curves differ between differing projectile materials, but from their work a logarithmic relationship has been developed between the projectile density and the projectile diameter to crater diameter ratio. The craters which have been examined from the STARDUST mission have a range of sizes, as well as a wide range of morphologies. An issue remains in that the electron microscopic analyses carried out on the STARDUST foil material has demonstrated the existence of impact craters of a size below that which can currently be produced in the laboratory. For instance, craters with a diameter of only 100 nm have been observed,[78] and it would be anticipated that craters of even smaller size exist within the sample material. Since one expects that the frequency of small impact events is very large, if difficult to detect, there is interest in determining if the linear behaviour observed for projectiles greater than a micron in diameter remains at very small sizes. Although the total mass collected during the STARDUST mission was very small ($\sim 3 \times 10^{-4}$ g) the numbers of craters is vast. For example, the extrapolation to a normalised areal density from impact clusters (that is, from a small region, the size distribution is given, and then normalised to units of numbers of impact craters per square metre of exposed foil material) for 1$\mu$m diameter craters varies from $\sim 5 \times 10^4 \mathrm{m}^{-2}$ to $\sim 10^7 \mathrm{m}^{-2}$. For 100 nm diameter craters, the extrapolated number density is estimated as $\sim 10^8 \mathrm{m}^{-2}$. It should be noted that for one particular crater cluster the equivalent values are $\sim 5 \times 10^9 \mathrm{m}^{-2}$ for 1$\mu$m diameter craters and $\sim 10^{11} \mathrm{m}^{-2}$ for 100nm craters. Now since the collector was approximately circular with a diameter of 41cm,[78] and approximately 15% of the area was aluminium foil,[30] then the area of the foil was approximately $0.02 \mathrm{m}^2$, and the expected number of small ($\sim$100nm) craters is of the order of $2 \times 10^6$, or for the high density cluster the extrapolated figure is $2 \times 10^9$. There is a wealth of information associated with these impact craters, but the effort required to extract that information is large. In order

to maximise the value of any assessment carried out some confidence is needed as to the nature of the dust particles which produced the craters.

Burchell and Price at Kent[33,34] have been calibrating the cratering process in order to develop models of that process for use in the analysis of the STARDUST craters. By using the velocity of impacts known to have occurred during the STARDUST mission they have been able to provide a best direct comparison between experiments and the NASA mission. Whereas the original work to calibrate the craters found a linear relation to the curve of crater diameter, $D_C$, to projectile diameter, $D_P$, and gave a consistent slope of $\sim$4.6,[87] more recent results show that for very small projectiles a much shallower relationship may be appropriate.[125]

## 4.3 Simulation Setup

Simulations were carried out of small spherical particles impacting a thin foil. The impacting velocity attributed to the STARDUST mission, 6.1 $\mathrm{km\,s^{-1}}$ (61 Å/ps) was used for the projectile cluster. For simplicity of setup, the same potential (material) was used for both the foil and the particle. For the same reason the copper potential which has been used for the majority of the shock studies in this thesis was also used here.

Many researchers have varied the timestep length during the simulation, so an investigation was undertaken to examine suitable parameters for these studies.

The LAMMPS code has the capability for freely varied timestep. The actual number used is calculated based on a maximum distance moved by any atom during the step. The code finds the maximum velocity and the maximum acceleration (=force/mass) within the simulation and then calculates the time required to move an atom by the user-specified distance based on those velocity and acceleration values. In order to test the usefulness of this capability within these simulations, a small simulation was set up, and the timestep at each calculational step printed out. The maximum distance set was 1% of the lattice spacing.

The output showed that there was little downward movement of the timestep after impact, but in fact the timestep was increased by this scheme towards 0.01 ps, a much larger value than is normally used in shock simulations. Since the issue being addressed is actually energy conservation, that aspect was examined separately. The same simulation was run, but at different fixed timestep values. For all runs except the first, there was a variation in the total energy output by the code. The total energy was observed to increase after impact, and then reduce to a plateau level.

| Projectile Diameter (nm) | No. of atoms | Kinetic Energy (eV) |
|---|---|---|
| 5 | 5425 | 66473.6 |
| 10 | 43923 | 538197.3 |
| 15 | 147347 | 1805472.2 |
| 20 | 349747 | 4285519.9 |

Table 4.1: Kinetic energy in the projectiles for the scaling study.

| $\Delta$t(ps) | $\Delta$E(eV) |
|---|---|
| 0.0001 | 0 |
| 0.001 | 1.0e-5 |
| 0.002 | 1.0e-5 |
| 0.003 | 1.9e-5 |
| 0.004 | 3.5e-5 |
| 0.005 | 1.2e-4 |
| 0.006 | 1.2e-4 |
| 0.007 | 1.8e-4 |

Table 4.2: Error in total energy as timestep is increased. The error can be seen to increase approximately as $\Delta t^2$, which fits with the order of the Verlet scheme used (see section 2.2.2).

The maximum difference between the starting total energy and that of some later time (along the energy plateau, approximately 20ps after the start of the simulation) during the simulation was recorded. The results are shown in table 4.2, and clearly indicate that for even reasonably large timesteps the error in the total energy is quite small.

The main reason for the difference in behaviour between my simulation and that of other researchers who have found it necessary to vary the timestep is due to the velocities involved. In comparison to either damage cascade work or sputtering simulations, the velocity of interception of the STARDUST – comet Wild 2, 6.1 $\mathrm{km\,s^{-1}}$, is very low. For purposes of comparison, table 4.1 shows the kinetic energy for the clusters used in these simulations. It can be seen, then, that the atomic kinetic energy of this simulation, at 12.25 eV/atom, is much lower than that of, for example, [14] at just under 1 keV/atom. This would lead to lower approach velocities and hence lower accelerations. It was concluded, then, that the standard timestep used for the shock simulations (0.001 ps/1.0 fs) is suitable for this work, and would be used throughout.

The study was begun with a simulation containing a particle of 4 nanometers diameter impacting a thin 4 nm foil. The simulation ran for 37ps. Since the foil

was very thin compared to the size of the projectile, it was not expected that the projectile would be stopped at this velocity. As expected, this simulation showed the particle passing through the foil and continuing its trajectory (see figure 4.1). The particle appeared molten, and the foil had a circular hole punched in it. The edges of the hole showed petalling in a similar fashion to that produced by a bullet or other projectile passing through a metal sheet. Furthermore, there were large numbers of smaller pieces of material ejected from the body. These ranged in size from tens of particles down to single atoms.

Figure 4.1: 4nm foil after impact by 4nm projectile.

The depth of the foil was subsequently increased in order to examine how big the foil needed to be. An increase in ten times the thickness prevented penetration, but subsequent visualisation indicated that the crater began to shrink, after it had reached a maximum depth of 7 nm (see figure 4.2). This behaviour is related to the dislocations which appear under the projectile impact site. Large numbers of partial dislocations are generated under the crater due to the deformation caused by the impact event. These partial dislocations bound thin stacking faults, which are readily observed (see fig 4.3). However, after some time the extent of the stacking faults was seen to diminish dramatically. This retreating behaviour accompanied the reduction in depth of the crater described above.

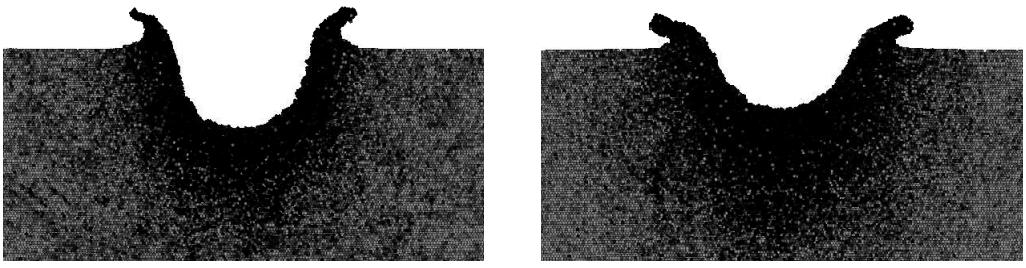

Figure 4.2: 15nm foil after impact by 4nm projectile.[See animation F3.1 in the electronic appendix.]

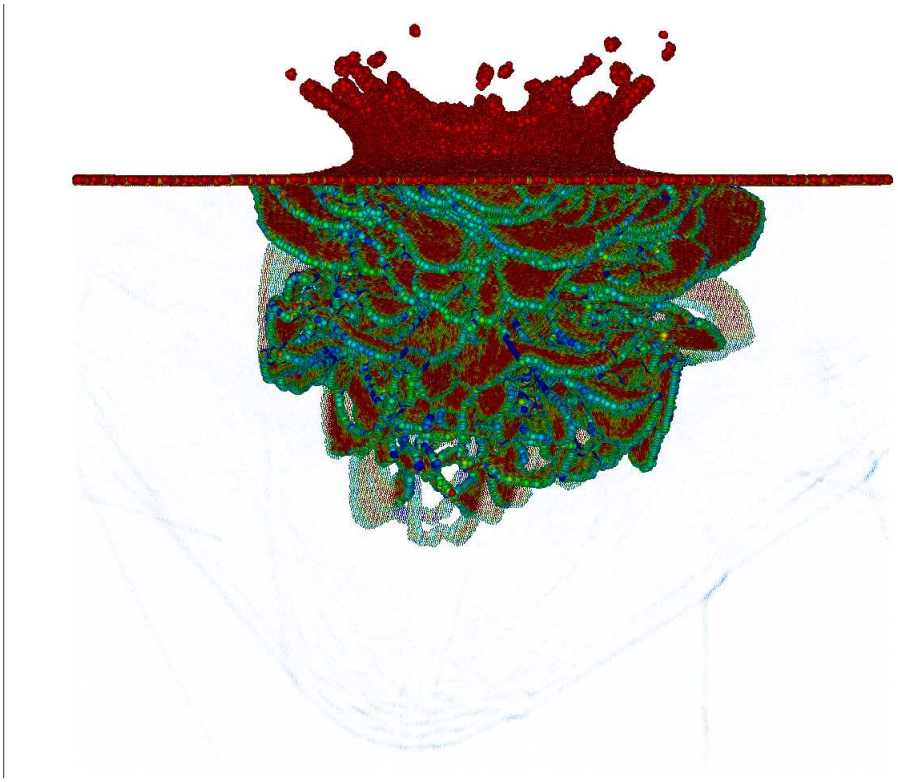

Figure 4.3: Stacking faults and partial dislocations under the impact site. Note also (pale blue) the shock front expanding away from the site.

A reason for this behaviour was the result of shock and release waves travelling through the body of the foil. Whereas shock waves are relatively simple to visualise by comparing velocities of the particles, release waves are more difficult to see due to the ramped nature of the profile. However, it was surmised that even though the wave is ramped, there is still a critical surface separating those particles under pressure and those particles that are close to ambient conditions. Both the compressed atoms and the fully released atoms have spent some time exchanging energy with their local neighbours. Thus the potential energy landscape in both of those regions will be relatively flat. However, where the material is being accelerated the atoms are being pushed higher up the potential well. In order to observe this, part of the release phase of the simulation was visualised using the potential energy as the grading variable. Whilst it was possible to discern the wave front, that front was not clear. This was because the local variations were small. The visualisation was repeated using the kinetic energy as the grading variable. Similarly, the front was unclear. Again, this was due to the small local fluctuations. What describes the front being observed was the local gradients of the energies. Unfortunately the point mesh in the visualisation data contained no connectivity information. That is, in the raw data there is no

indication of which particles are neighbours of which other particles. Consequently it is not possible to immediately describe the gradients of any variables.

However, the human brain is configured for optimal surveying of moving objects. Consequently, a movie would more readily exhibit subtle variations in the observed scene than would still images. In a movie containing several images all visualised the same way and taken over the later part of the simulation, it was quite clear that the initial shock wave was arriving at the bottom face of the foil and returning as a release wave. It was possible to observe the release wave causing the stacking faults to recombine returning the lattice to its original state. It was also observed that a similar behaviour was taking place due to interactions with the sides of the box. However, the size of this interaction was much smaller than for the interaction along the axis of the projectile motion. That is to say that the amplitude of the outgoing shock, and therefore the amplitude of the rarefaction, was lower laterally than vertically.

The incoming projectile causes a shock wave to travel out in all directions from the impact site. The velocity and magnitude of the shock is dependent on the crystallographic orientation, but nevertheless there is a shock wave. When the shock wave encounters the boundary of the problem, the resultant behaviour is dependent on that boundary. For most molecular dynamics studies, periodic boundaries are used. However, in this simulation such boundaries would cause the simulation to behave as if an identical projectile had arrived at the target surface at the same time, at a distance $L/2$ away, where $L$ is the width of the simulation box. That is, when an outgoing shock wave encounters the boundary, an incoming shock wave would appear on the opposite boundary. For the purposes of this work, that would be an undesirable effect adding complexity and obfuscating the results. Another boundary option is to have the boundaries either fixed, or shrink wrapped. In both of these cases there is no interaction of particles across the boundary. In the case of fixed boundaries the atom, being forced to cross the boundary, is lost to the problem. In the case of shrink wrapped boundaries, the particle is tracked as it moves away from its original lattice site, and the computational boundary is grown to include the new region of space encompassed by the problem. However, in both of these cases a release wave is set up, which then travels into the body of the problem, resulting in fictitious behaviour as described above.

It is thus necessary to set up localised damping at the boundaries. Other workers (e.g. [159]) have used thermostatted regions in order to produce this effect. An alternative approach has been developed by Moseler *et al.*[119] Their method considers the atoms as being in a chain joined by springs. A boundary layer of atoms is built

around the simulation cell in a similar fashion to a thermostatted bath. An integration scheme for the bath atoms has equations of motion which are modified depending on the motion of the neighbouring atoms within the main simulation cell. This enables coordinated (bulk) movement directed towards the main cell from the bath to be removed. Consequently a disturbance, for example a pressure pulse, would move from the cell into the bath region, but no reflection would be propagated. However, there is no adverse effect on the temperature (random motion) of the cell atoms due to the bath. This is achieved by separating out the low frequency from the high frequency motions of the atoms.

However, an option in the LAMMPS code is to use a simple viscosity parameter. This algorithm reduces the acceleration calculated from the gradient of the potential via the equation

$$F = -\Gamma v$$

where $v$ is the current velocity. The viscous force, $F$ is added to the calculated force thereby reducing the force felt by the affected atoms. This is similar to the method used by [14] described in section 4.2 above. One consequence of this is that kinetic energy is efficiently drained from the system, and the temperature of the entire foil drops dramatically, even though it is only a relatively small region over which the viscous algorithm is effected. The viscous region, then, acts as an efficient freezing bath. That freezing is not a large problem in this simulation, however. The average temperature of deep space is approximately 3K, whereas my simulation ran at between 30K and 10K.

## 4.4 Results

The time histories of the crater growth are shown in figure 4.4. In these figures three measurements are shown; the lowest position underneath the projectile, at $X = 0$ (i.e. the centreline of the simulation) (marked as *bottom*), the position of the top surface of the projectile, also at $X = 0$ (marked as *top*) and the width of the crater, at the level of the surface of the target (marked as *total width*). This latter position differs from the experimentally determined figures. In the work undertaken as part of the STARDUST recovery analysis,[87–90,125] the crater width is taken across the lip of the crater, at the maximal height of the material. For this work, such a measurement (particularly for the time histories as they are shown here) would have lead to a degree of subjectiveness and ambiguity. In this work, determining the level of the

target surface was trivial; experimentally such a determination would be excessively time consuming and complex.

For all measurements, the simulation cell was cut along the planes $Y = 0$ and $Y = -10$Å, so that a thin slice was apparent in the visualisation, from which the measurements were taken. From this it can be seen that the craters show some relaxation after reaching a maximum size. This reflects two aspects of the simulation. Firstly, the fact that the damping mechanism applied to the boundaries, in order to prevent shock wave reflection and reverberation, is not perfect. However, and secondly, one might expect some degree of relaxation since, for an infinite target, there will be a release wave generated at the impact site as the material locally returns to zero pressure.

Comparison of the four graphs here may help separate these effects to some degree. In this study, the target size was held fixed. Therefore the smallest projectile will show a behaviour closest to that with an infinite sized substrate. That is to say, for the 5 nm projectile, the extent of the damage zone into an infinite target would be the smallest. Therefore the degree to which the edge effects affect the impact zone will be least. So, whereas the measurements for the lowest points of the crater (*bottom* and *top*) show some rebound for all projectile sizes, it is only for the smallest, 5 nm, projectile that such behaviour is seen for the crater width. However, the 20 nm simulation shows the crater width continuing to rise at the end of the simulation time. Clearly the crater will not continue to expand indefinitely, indicating that the simulation time was insufficient to show the entire motion up to an equilibrium state. However, the 10 nm simulation shows some reverberation of the crater width. For an inifite sized substrate, no such reverberation would be possible, since there would be no edges from which the stress waves could be reflected.

Now in the 10 nm and 20 nm cases, the crater width increases to some maximum value and, the reverberations in the 10 nm case notwithstanding, remains at that level. So we may consider that there is a projectile size to target size effect in operation. From this we can conclude that two distinct motions dominate, depending on whether the measurement being considered is the crater lateral expansion, or the depth (excavation) of the crater. For the former, the release behaviour is minor, and the motion observed here is dominated by the reflections from the simulation cell boundaries. In contrast, the motion of the bottom of the crater shows the release behaviour from the shock. This is supported by the the 5 nm simulation. In this case, comparison of the *top* and *bottom* traces (difference shown in figure 4.5) shows the projectile material initially being compressed, and then expanding to some lower

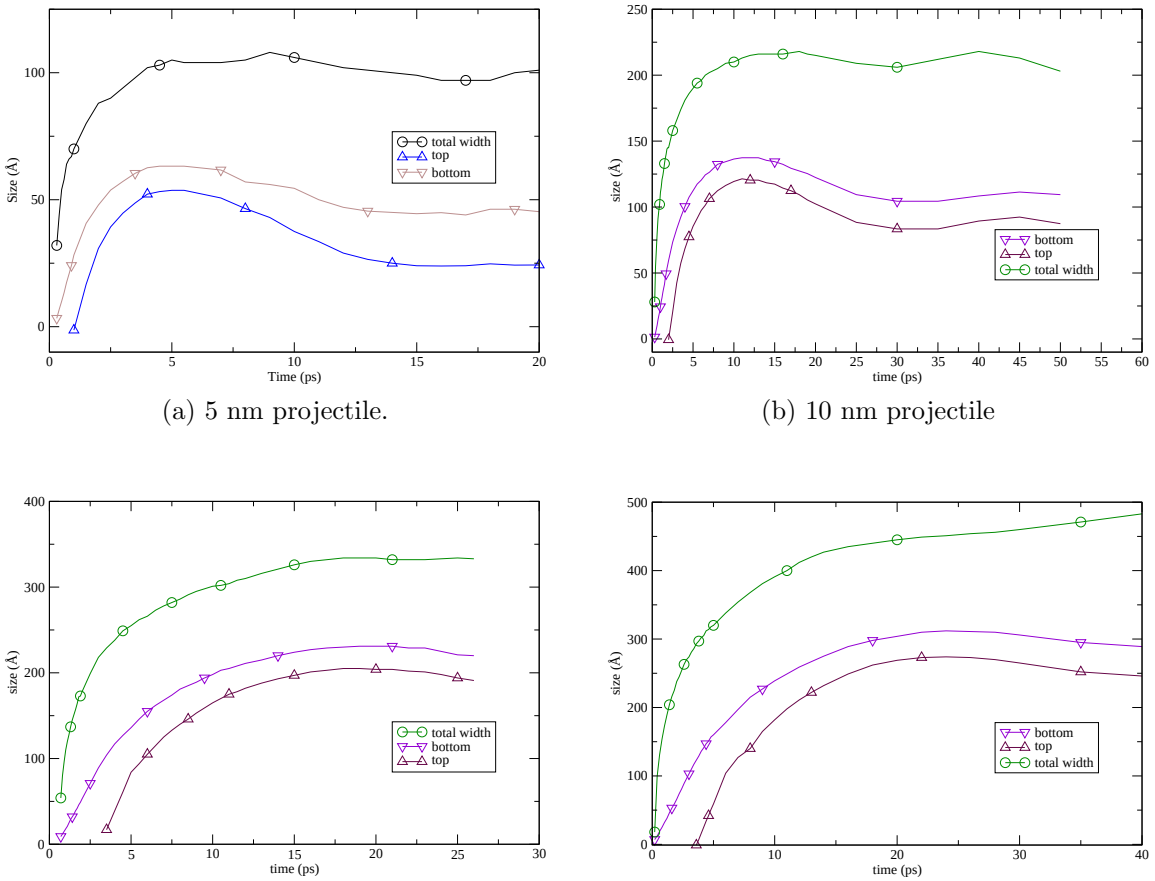


(a) 5 nm projectile.

(b) 10 nm projectile

(c) 15 nm projectile

(d) 20 nm projectile

Figure 4.4: Crater growth for a range of projectile sizes

pressure (and lower density) state. If this motion were the result of a wave returning from below, one might expect the trace of the *bottom* to show some movement upwards (hence to a lower value in figure 4.4a) ahead of a similar motion in the *top* trace. However, such fluctuation is not observed.

Part of this work was to compare these results with those of the Burchell *et al*.[87,125] Table 4.3 shows the crater widths (maximum value) for each of the simulations. This data can be fitted by the line

$$y = -1.7 + 2.314 \times x. \tag{4.1}$$

This line has a much lower slope than that demonstrated experimentally for larger projectiles.[87] However, recent work using very small projectiles shows a slope of 1.6 for projectiles less than 3 $\mu$m. The caveat to be noted is that, unlike the work of Burchell *et al*, the density of the projectiles simulated here is the same as the target substrate. Kearsley *et al*[89] shows a linear trend of crater depth to diameter ratio

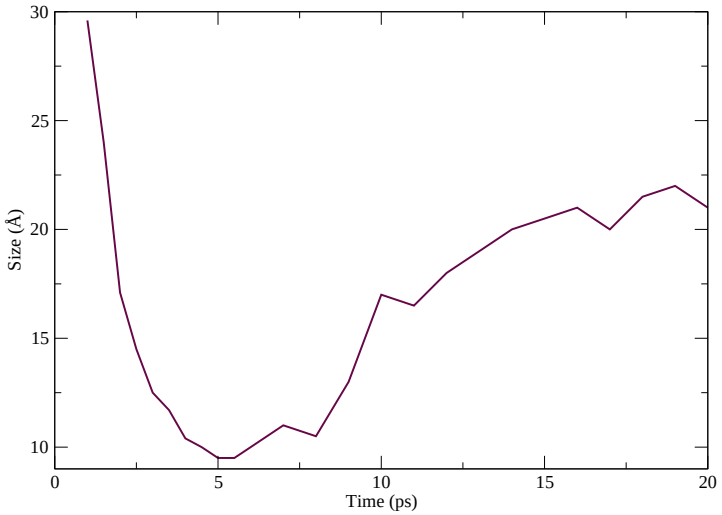


Figure 4.5: Difference between the *bottom* and *top* traces from figure 4.4a, showing the compression and subsequent expansion of the projectile material.

against projectile density, which shows that for more dense projectiles the crater is deeper than it is wide, whereas less dense projectiles produce shallower, more spherical craters. For the simulation data, comparison of the crater depth and diameter data shows a ratio of 0.64. From [89], this would fit with a projectile density of ∼5 g/cc. However, it should be noted that whilst for this work the projectiles have a density of 8.9 g/cc, which is nearly double that expected from this comparison, the target also has a density of 8.9 g/cc, which is more than 3 times the density of the targets used (aluminium – 2.7 g/cc) in both the experimental work and the STARDUST mission.

So one may expect that a different target material would exhibit a different relationship for the crater depth to diameter ratio against projectile density, and so one cannot directly compare the $^{D_P}/_{D_C}$ ratio shown here with that of Kearsley.[87]

Another point of note relates to the intercept found in equation 4.1. This value implies that for projectiles smaller than 0.735nm (approximately two lattice unit cells) the crater would have negative size. Clearly this is not going to be the case, and there are two possible descriptions of this behaviour. If it is considered that the crater width against projectile size is a linear function, clearly the function would be zero valued at zero projectile size. Now a fit to the data using a function of the form "$y = Ax$" yields a value for $A$ of 2.20067. This is surprisingly close to the slope of 2.314 found in equation 4.1. This is not surprising; they are both linear fits, and the intercept in equation 4.1 is not large. Furthermore, the correlation coefficients for the two fits are 0.9996842 and 0.9996840 suggesting that the two fits are as statistically significant as each other. However, the RMS error is 0.02% for equation 4.1 whereas

| Projectile Diameter (nm) | Crater Width |
|---|---|
| 5 | 10.2 |
| 10 | 21.1 |
| 15 | 32.7 |
| 20 | 44.9 |

Table 4.3: Crater width against projectile size.

that value is 0.05% for the line passing through zero crater width at zero projectile size.

However, the data for larger projectiles, given in [87], shows a larger slope than that observed here. Smaller projectiles again may show a yet smaller slope. This implies, then, that the data may follow a very shallow parabola. A fit to the data with a form "$y = a_0x + a_1x^2$" yields a curve which fits the data with a correlation coefficient of 0.999999. For this fit the RMS error is 0.00095%, or 1 part in $10^5$.

## 4.5 Conclusions

The need to identify the minerals which make up the body of comets within the solar system remains a current research topic. Improved analysis of the STARDUST mission is showing that the anticipated size distribution of the particulate material embedded in the icy matrix of comets such as Wild-2 may have an increased small fragment ratio than anticipated. This, then is highlighting the need for more work at the very fine scale examining the impact behaviour of ultra-small particles. This, then leads MD to appear at the boundary between what is possible computationally, and that accessible experimentally.

The work here has shown that the need to develop accurate potentials is of great importance in enabling this work to go forward. Futhermore, there remains a need to understand the behaviour of simulation boundaries and the transmission of energy through shock waves.

# Chapter 5

# General Discussion and Conclusions

## 5.1 Discussion

The work undertaken here makes use of a model scheme which was developed to study the behaviour of bulk material properties. The scheme itself (MD using EAM potentials) has been shown to successfully demonstrate not only the action of plasticity through the modelling of dislocations, stacking faults and twinning[56] but also more challenging aspects of material behaviour such as phase changes.[84] However in this work the modelling scheme has been used within a dynamic NEMD context to examine the microscopic behaviour of copper under shock loading. Such modelling has been shown previously[76] to be a valuable tool to aid understanding of shocks in condensed media. More recently the benefits of improved potentials have enabled this modelling to be successfully compared to experimental data.[27] Here the study has used the advantage of these improved potentials to investigate the mechanisms which occur under shock loading. By the use of sufficiently large samples, enabled by advances in computer resources, in which the atoms were thermalised to room temperature before the simulation was undertaken this work has demonstrated more clearly than previously the action of the elastic precursor ahead of the main plastic front, thus showing classical wave–splitting behaviour in $\langle 110 \rangle$ and $\langle 111 \rangle$ oriented single crystals. This behaviour has been taken further to show that NEMD simulations of shocks in copper match the empirically demonstrated relationship between pressure rise and rate of that rise for shocks.[142]

One of the most surprising behaviours is that exhibited by the $\langle 111 \rangle$ orientation. This point is illustrated in figure 5.1. For those curves describing shocks below the

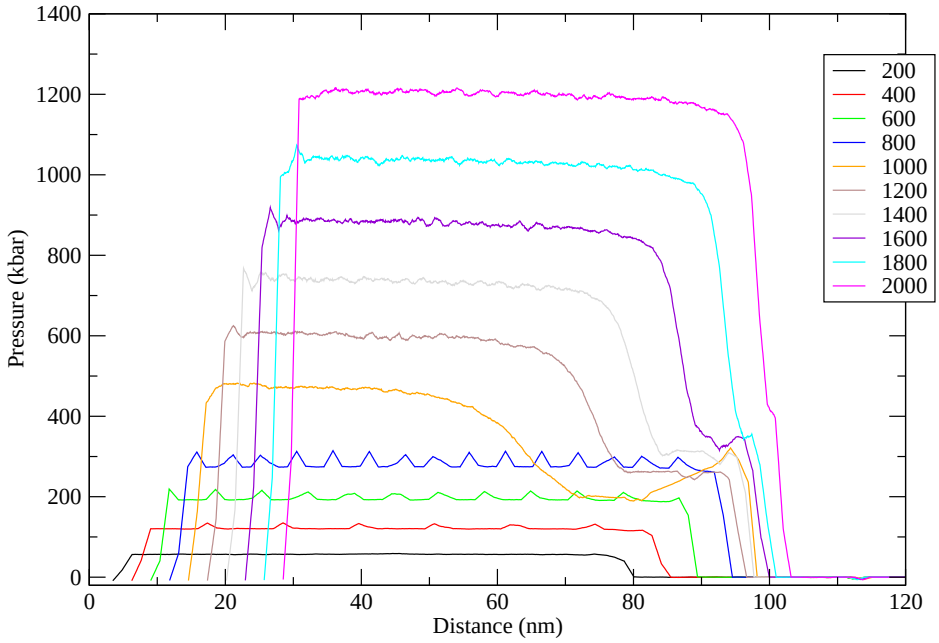


Figure 5.1: ⟨111⟩ simulation comparing pressure profiles for increasing piston velocities. Piston velocities are given in the legend. Snapshots taken at 14 ps from start of simulation. The transition from purely elastic to elastic–plastic behaviour is seen as the piston velocity is increased from 800 m s$^{-1}$ to 1000 m s$^{-1}$.

HEL, figure 5.1 shows an increasing elastic wavespeed with increasing shock amplitude. Consideration of the explanation of the HEL in section 2.1.2 suggests that this behaviour is a form of non-linear elasticity where the effective stiffness depends on the rate of application of the load. However, further examination of these results shows that closer consideration of the physical situation is needed. Whereas for experimental data the HEL is low, and the pressures experienced in purely elastic shocks are close to ambient, figure 5.1 shows that in the simulation this is not the case. Since the HEL is very high, significant pressures (ca. 30 GPa) are achieved in the purely elastic simulations. Now it might be expected from the shape of the potential function[a] that the elastic constants increase with increasing pressure. Figure 5.2 shows the variation in elastic constants with pressure for the potential used in these calculations.

It is possible to calculate the elastic wavespeed using the elastic constants. Equations for the speed of sound are usually given in terms of the experimentally measured elastic constants. Thus for the longitudinal wavespeed in polycrystalline material the

[a] At volumes below equilibrium the change in energy as the atomic nuclei approach each other is increasingly positive.

| | |
|---|---|
| $\langle 100 \rangle$ sim | $U_{el}^{100} = 4418.7 + 29.3 * P$ |
| eqn. 5.3a | $U_{el}^{100} = 4321.2 + 55.1 * P$ |
| $\langle 110 \rangle$ sim | $U_{el}^{110} = 5030.8 + 79.0 * P$ |
| eqn 5.3b | $U_{el}^{110} = 4952.0 + 60.2 * P$ |
| $\langle 111 \rangle$ sim | $U_{el}^{111} = 5317.1 + 41.1 * P$ |
| eqn 5.3c | $U_{el}^{111} = 5145.1 + 61.8 * P$ |
| $B$ (eqns 5.1 & 5.2) | $U_{el} = 323.2 + 33.675 * P$ |

Table 5.1: Comparison of the elastic wave speed against pressure derived by various methods.

relation is

$$U_{el} = \sqrt{\frac{B}{\rho}}. \tag{5.1}$$

where $B$ is the bulk modulus. This can be derived from the $C_{ij}$ using

$$B = \frac{1}{3}(C_{11} + 2C_{12}) \tag{5.2}$$

However, this calculation is based on the average properties of polycrystalline materials. It is also possible to calculate elastic wavespeeds in single crystals directly from the $C_{ij}$. From Meyers[110]

$$U_{el}^{100} = \sqrt{\frac{C_{11}}{\rho}} \tag{5.3a}$$

$$U_{el}^{110} = \sqrt{\frac{C_{11} + C_{12} + 2C_{44}}{2.\rho}} \tag{5.3b}$$

$$U_{el}^{111} = \sqrt{\frac{C_{11} + 2C_{12} + 4C_{44}}{3.\rho}} \tag{5.3c}$$

A comparison of the elastic-plastic behaviour of the three orientations is shown in figures 5.4, 5.5 and 5.6.

Figure 5.4 was created by taking snapshots at a series of uniformly spaced times from which particle velocity profiles are produced. By measuring the shock front position at a constant particle velocity for each snapshot the velocity of the front can be determined. Using a particle velocity slightly above zero the front measured is the elastic wave. In figure 5.4 these curves are denoted by the letter 'E'. In contrast, by using a particle velocity which is slightly above the HEL, the velocity of the plastic front in the weak shock can be ascertained. These curves are denoted 'P' in figure 5.4.

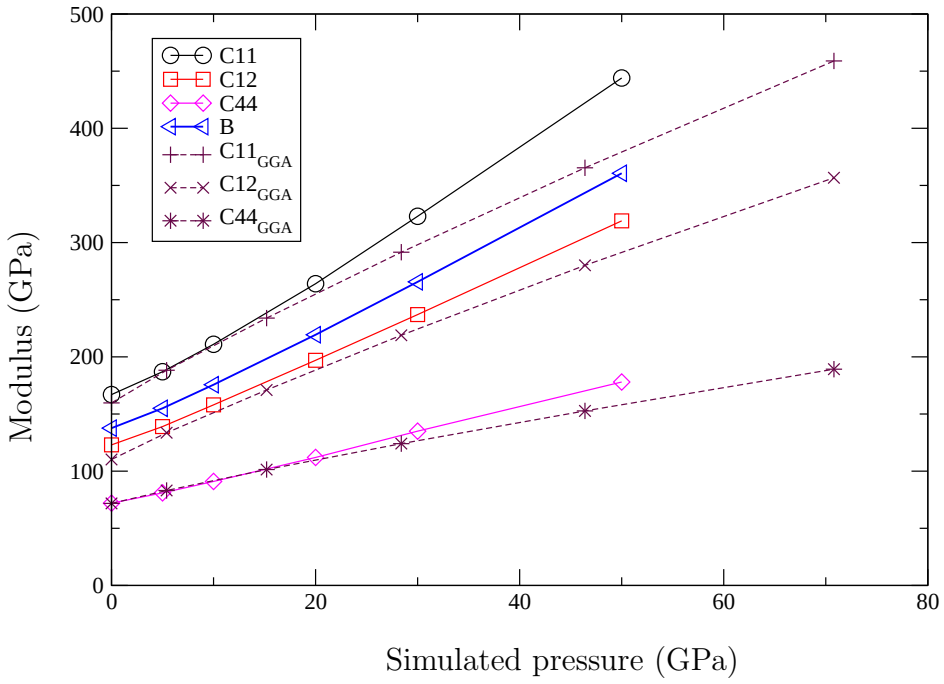


Figure 5.2: Variation of the elastic constants $C_{11}$, $C_{12}$ and $C_{44}$ with pressure. This data measured for samples at 300K. GGA values (calculated at 300K) from [101].

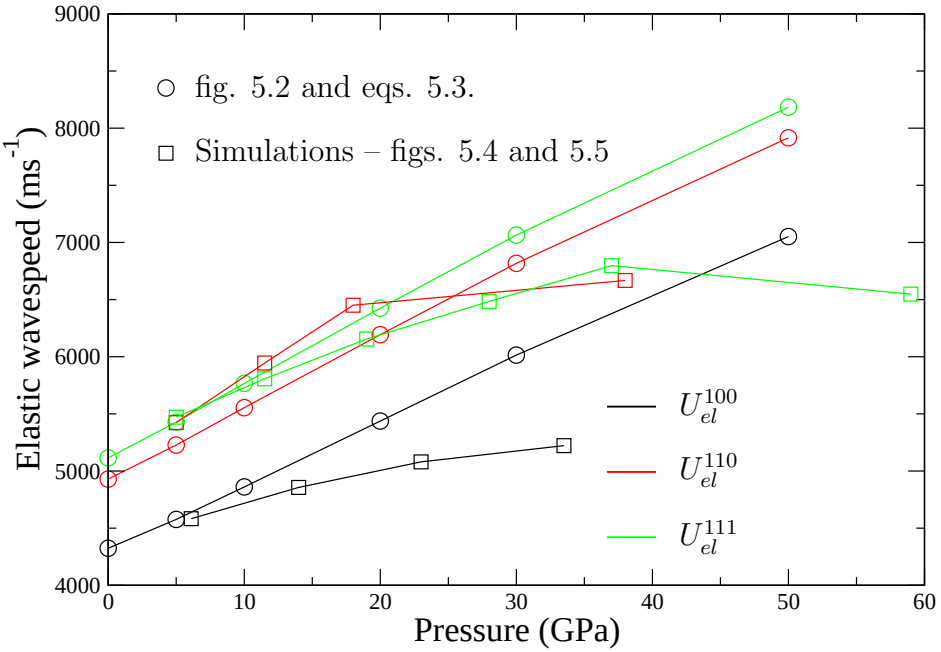


Figure 5.3: Variation of the elastic wavespeed with pressure. Comparison of the data derived from from equation 5.3 with that from simulations.

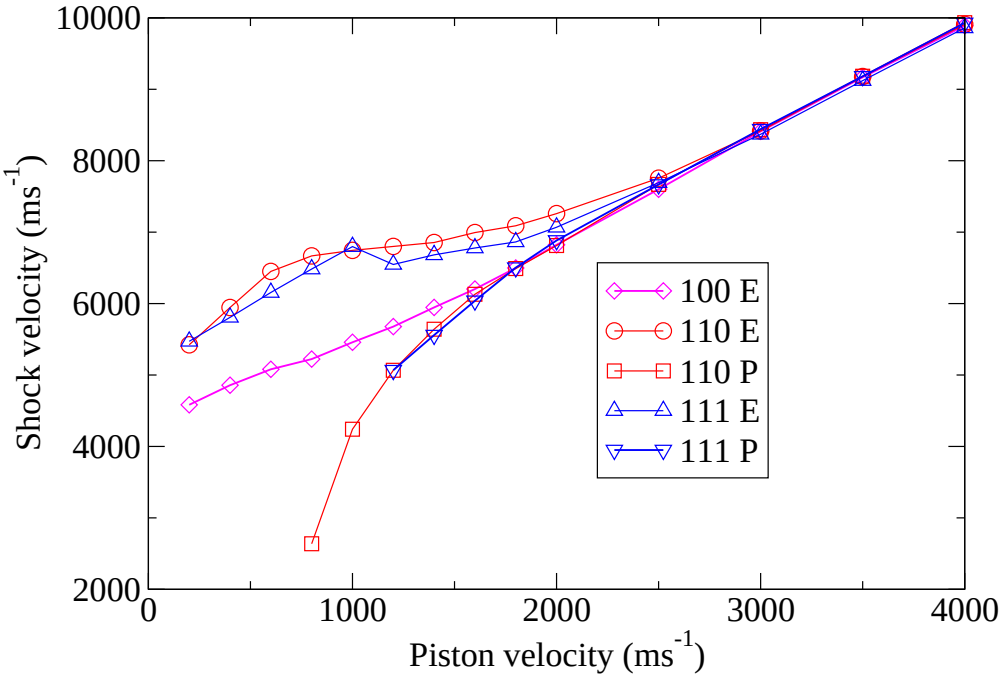


Figure 5.4: Comparison of the shock velocity – piston velocity curves for each of the three high symmetry orientations: ⟨100⟩, ⟨110⟩, ⟨111⟩.

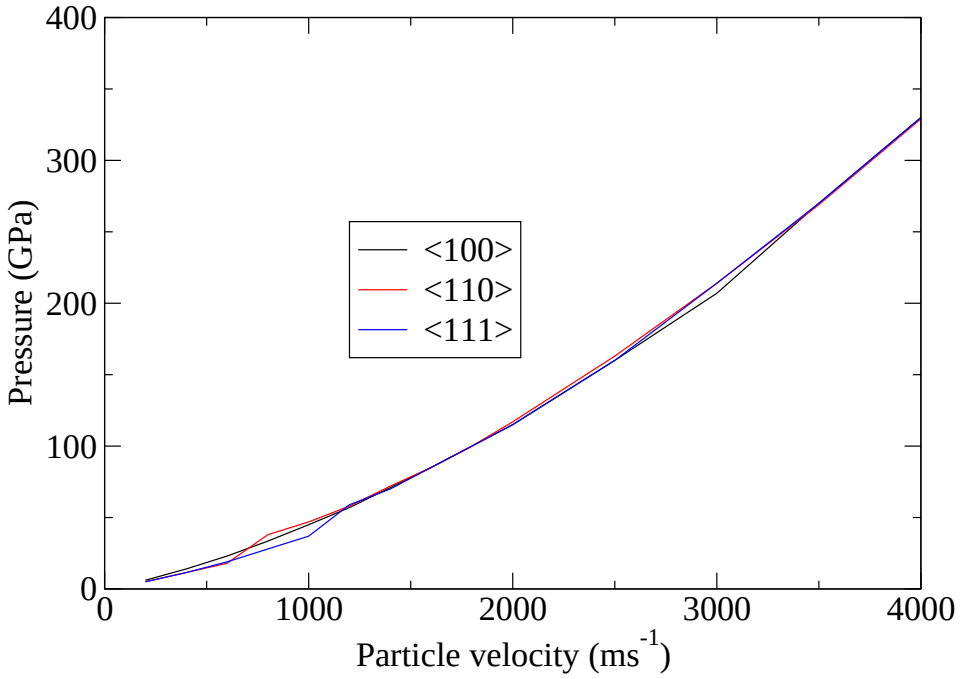


Figure 5.5: Hugoniots in the pressure–particle velocity plane for each of the three high symmetry orientations: ⟨100⟩, ⟨110⟩, ⟨111⟩.

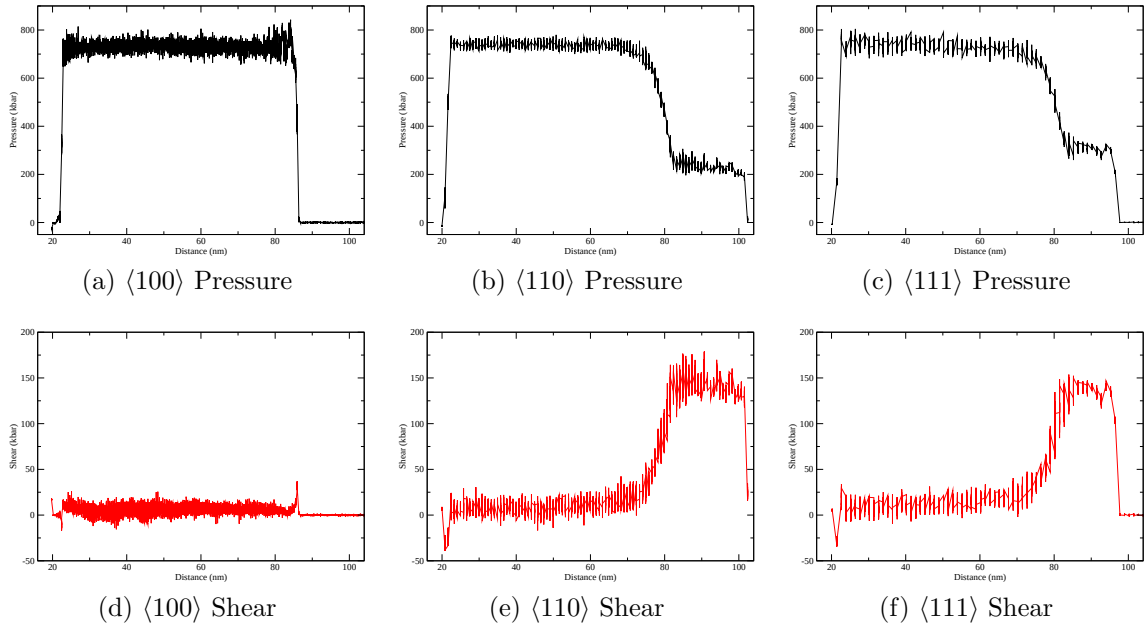


(a) ⟨100⟩ Pressure (b) ⟨110⟩ Pressure (c) ⟨111⟩ Pressure

(d) ⟨100⟩ Shear (e) ⟨110⟩ Shear (f) ⟨111⟩ Shear

Figure 5.6: Pressure and shear profiles in the three high symmetry directions. Piston velocity $1400\,\mathrm{m\,s^{-1}}$. Snapshots at 14ps.

In the strong shock regime the elastice wave is over–driven by the plastic front and hence the 'E' and 'P' curves are coincident.

Figure 5.4 contains a great deal of detail regarding the behaviours observed in this work. The difference in behaviour between the ⟨110⟩ and ⟨111⟩ orientations compared to the ⟨100⟩ orientations with respect to elastic–plastic transitions and wave splitting is clearly shown. Beyond that, the behaviour of each orientation is revealed. Therefore the curves need to be considered one by one. For consistence, the slope of an individual curve will be denoted by

$$\frac{\mathrm{d}U_s}{\mathrm{d}U_p}\Big|^{E|P}_{\mathrm{dir}}(U_p) \tag{5.4}$$

to indicate the slope of a curve from an orientation *dir* taken below the HEL ('E') or above ('P') at a particle velocity $U_p$.

Consider initially the behaviour of the ⟨110⟩ case. Taking the slope at $\frac{\mathrm{d}U_s}{\mathrm{d}U_p}\Big|^{E}_{110}(200)$, we can see that this curve is linear up to $U_p = 600\,\mathrm{m\,s^{-1}}$, after which the slope reduces towards zero. This is the point at which the HEL is approached, and there is no increase in the elastic wave velocity because there is no increase in the pressure or particle velocity within the elastically compressed region. It may be expected, then, that the slope between $\frac{\mathrm{d}U_s}{\mathrm{d}U_p}\Big|^{E}_{110}(600)$ and $\frac{\mathrm{d}U_s}{\mathrm{d}U_p}\Big|^{E}_{110}(2000)$ would remain at zero, at which point the plastic front would be expected to overtake the elastic wave, and the shock

would be over–driven. However it can be seen that the slope of the curve actually increases in this region, and the elastic front can be seen to be overtaken between $U_p = 2000\,\mathrm{m\,s^{-1}}$ and $U_p = 2500\,\mathrm{m\,s^{-1}}$.

In comparison, then, a consideration of the behaviour of the $\langle 111 \rangle$ elastic front shows some similarities to, as well as some differences from, the $\langle 110 \rangle$ elastic wave. Here we can see that the velocity of the elastic wave increases linearly up to the point at $U_p = 1000\,\mathrm{m\,s^{-1}}$. The slope of the curve between $U_p = 1000\,\mathrm{m\,s^{-1}}$ and $U_p = 1200\,\mathrm{m\,s^{-1}}$ is negative; the HEL at $U_p = 1200\,\mathrm{m\,s^{-1}}$ is lower than that at $U_p = 1000\,\mathrm{m\,s^{-1}}$. This is explained in section 3.1.5 as being due to overstress in the elastic wave, which is then reduced when dislocations are created. This behaviour can be seen in figure 5.1. In this figure the curve corresponding to $U_p = 1000\,\mathrm{m\,s^{-1}}$ (orange) shows a peak at the leading edge of the elastic wave, which then falls due to the onset of plasticity. It can be seen, however, that the amplitude of that peak (which governs the elastic wavespeed) is higher than the amplitude of the elastic wave for the curves corresponding to both $U_p = 1200\,\mathrm{m\,s^{-1}}$ and $U_p = 1400\,\mathrm{m\,s^{-1}}$. Figure 5.1 further shows the increase in amplitude of the elastic wave as the plastic front begins to overtake it and the shock becomes over–driven.

In the $\langle 110 \rangle$ and $\langle 111 \rangle$ cases the elastic wave is clearly much faster than the plastic front for the same piston velocity. Furthermore the slopes $\frac{\mathrm{d}U_s}{\mathrm{d}U_p}\big|^E_{110\,\&111}(400)$ is much higher than the slope of the curves in the over–driven state, $\frac{\mathrm{d}U_s}{\mathrm{d}U_p}\big|^E_{110\,\&111}(3000)$. Therefore, with increasing particle velocity, there must be a substantial change in the slopes of the wavefront velocity curves as the shock transitions from the underdriven to over–driven states. It is this period of stagnation, when the increase in wave velocity due to the increased particle velocity ceases, which allows the system to display the classic two-wave structure. In contrast, the $\langle 100 \rangle$ case does not show this behaviour clearly. Nonetheless, this behaviour does exist for the $\langle 100 \rangle$ case. The slope of the plastic front velocity, $\frac{\mathrm{d}U_s}{\mathrm{d}U_p}\big|^P_{100}(3000)$=1.5496 ($\mathrm{m\,s^{-1}}$ per $\mathrm{m\,s^{-1}}$) which gives an intercept ($U_s$ at $U_p = 0\,\mathrm{m\,s^{-1}}$) of $3726\,\mathrm{m\,s^{-1}}$. Now the shock velocity, $U_s$, for the slowest shock, $U_p = 200\,\mathrm{m\,s^{-1}}$ is $4582\,\mathrm{m\,s^{-1}}$ and the slope $\frac{\mathrm{d}U_s}{\mathrm{d}U_p}\big|^E_{100}(200)$ is 1.3686 ($\mathrm{m\,s^{-1}}$ per $\mathrm{m\,s^{-1}}$), implying an intercept of $4309\,\mathrm{m\,s^{-1}}$. So we can see that there is indeed a difference in the elastic and plastic front velocities. However, this difference much smaller than for both the $\langle 110 \rangle$ and $\langle 111 \rangle$ cases; since the slope of the $U_s$–$U_p$ curve, $\frac{\mathrm{d}U_s}{\mathrm{d}U_p}\big|^E_{100}(600)$, is already lower than that of the plastic front $\frac{\mathrm{d}U_s}{\mathrm{d}U_p}\big|^P_{100}(2000)$, there is no noticable change in slope required and the stagnation observed in the $\langle 110 \rangle$ and $\langle 111 \rangle$ cases is not seen for the $\langle 100 \rangle$ case.

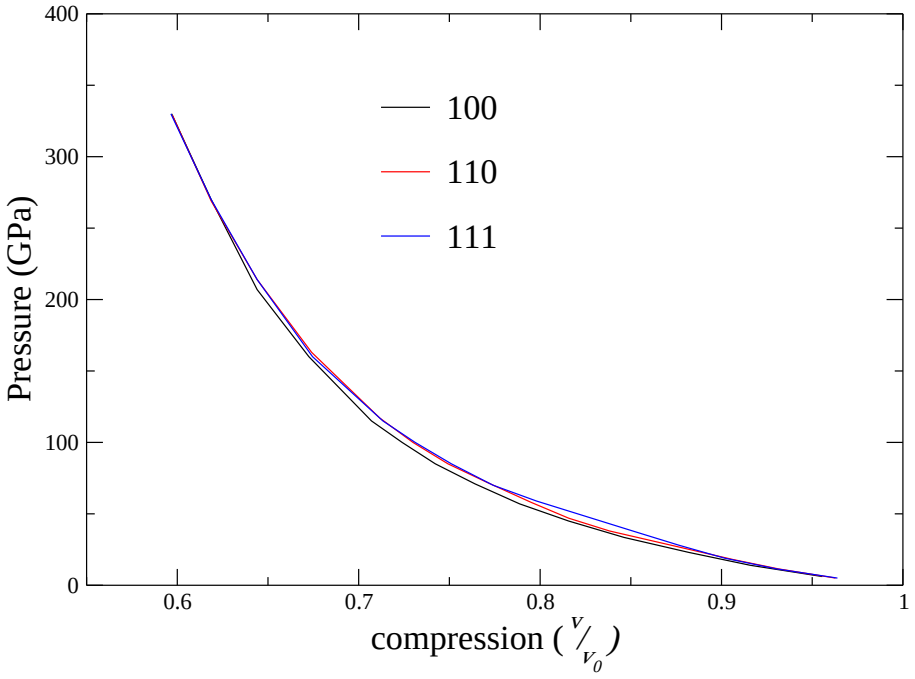


Figure 5.7: Hugoniots for the three high symmetry directions in the $P$-$v$ plane.

The phenomenon of the elastic wave being in a state of super-stress (observed in the ⟨111⟩ case) together with the rise in HEL (and hence wavespeed) as the piston velocity is increased towards the elastic wave being over–driven implies a time dependent behaviour in the initiation of plasticity and the development of the plastic front. What is interesting is to compare the three orientations with respect to this time dependency. Section 3.1.3 clearly shows that for the ⟨100⟩ case there is a significant time delay between the beginning of the shock simulation and the onset of plastic behaviour when the shock pressure is slightly higher than the HEL. Similarly, figure 3.10 in section 3.1.5 shows that for the ⟨111⟩ orientation there is a delay prior to the production of plasticity[b]. In contrast, the ⟨110⟩ case does not show this delay; even for shocks with $U_p$ slightly above the HEL, where the velocity of the shock front is very low (see figure 5.4, orange curve), plasticity develops quickly and the delay observed in the ⟨100⟩ and ⟨111⟩ is not seen.

Figure 5.5 shows the Hugoniot in the pressure–particle velocity plane. It can be seen that, apart from small regions at velocities near $U_p = 800\,\mathrm{m\,s^{-1}}$ and near $U_p = 3000\,\mathrm{m\,s^{-1}}$, the three curves are coincident. This point reflects two aspects of studies of shock behaviour. Firstly the plastic front velocities are almost coincident for the three orientations, which reflects the physics described by the Rankine-Hugoniot relations

[b]This time-delayed behaviour is readily seen in the electronic appendix.

(section 2.1) which are based in continuum conservation laws, giving identical starting conditions for the different orientations. Secondly figure 5.5 also reflects the fact that in this plane the Hugoniot curves are not particularly subtle; fairly dramatic differences in the $U_s$–$U_p$ are needed to produce a difference in the Hugoniot curve, even before practicalities and errors in experimental work are accounted for. Table 5.1 shows that large differences in the $U_s$–$U_p$ relationships do exist, but figure 5.4 shows that these differences exist only in the elastic regime.

A comparison of the three orientations using traces of the pressure and stress profiles is given in figure 5.6. The lack of an elastic precursor in the ⟨100⟩ direction, present in both the ⟨110⟩ and ⟨111⟩ directions, can be seen. Examination of the shear stress profiles reveals the reason for this difference. Whereas both the ⟨110⟩ and ⟨111⟩ show a high shear in the elastically compressed region, the ⟨100⟩ shows only a spike at the shock front. All three profiles show the shear stress falling to near zero behind the plastic front. From figure 5.4 it can be seen that the velocities of the plastic fronts are very similar for all three orientations. However, the velocities of the elastic waves are very different. It is the much higher elastic wave velocities seen in the ⟨110⟩ and ⟨111⟩ directions which enable the elastic wave to travel ahead of the plastic front, and hence form a precursor.

However, there are issues remaining within this modelling scheme. Although wavesplitting and the HEL have been demonstrated, the amplitude of the simulated HEL is considerably larger than that observed experimentally. Attempts to reduce the magnitude of the simulated HEL by including defects, and thus reducing the stress at which dislocations are spontaneously produced, have had only limited success[c]. It is anticipated that this is related to two, directly connected, issues which currently exist with this modelling method. These issues relate to the existing microstructure in the material being simulated. The first issue is that of the behaviour of perfect crystals; such samples do not exist in reality and hence this modelling necessarily displays some degree of artificiality. The second issue is that of an inability to initialise the simulation with a realistic defect microstructure.

Whereas the simulations here start with perfect crystals, and even the defected crystals have only isolated voids, in contrast, real metals, even the purest single crystals, contain a network of pre-existing dislocations. Therefore the shock front

[c]The behaviour of a shock in the ⟨111⟩ orientation with multiple voids can be seen in figure F1.9 in the electronic appendix. In this case, not only can the plastic front be seen to be characterised by the production of full dislocations (as opposed to stacking faults seen in the other high-symmetry orientations) but the overall dislocation density appears to be lower.

will, at all times, be passing over some material which has dislocations within it, acting as a continuous source of dislocation nucleation sites.

Now as there are no dislocations pre-existing in the simulated sample, we may compare the observed HEL to the ideal shear strength of the material. Discourses of the theoretical strength of a crystal are given in many textbooks. A classic description is given by Cottrell,[43] in which the critical shear stress is given by

$$\sigma = \frac{b}{a}\frac{G}{2\pi} \tag{5.5}$$

where $G$ is the shear modulus, $a$ is the separation of the planes of atoms, and $b$ is the separation of the atoms in the plane, in the direction of slip. Since $a \approx b$, then $\sigma$ is approximately $G/2\pi$. Further refinements, by consideration of more realistic interatomic potentials as well as stable configurations at intermediate positions (such as the BCC configuration {see section 3.2.2}) has reduced this estimation to approximately $G/30$.

Using the shear modulus $C_{44}$ from figure 5.2 gives, at $P = 0$, a value for $\sigma$ of 11.1 GPa. Alternatively the shear modulus relation

$$C' = \frac{C_{11} - C_{12}}{2} \tag{5.6}$$

can be used to give an approximation to the continuum mechanics shear modulus $G$. Now for this material equation 5.6 gives a value (at room pressure) of 23.5 GPa. This leads to an estimate for $\sigma$ in equation 5.5 of 3.74 GPa. Both from Bringa's calculation[27] ($P_{\mathrm{HEL}} = 32\,\mathrm{GPa}$) and from this work (from figure 5.6, $P^{110}_{\mathrm{HEL}} = 22\,\mathrm{GPa}$; $P^{111}_{\mathrm{HEL}} = 30\,\mathrm{GPa}$) it can be seen that the HEL calculated using this method is significantly higher even than the expected ideal shear stress.

However, it is not yet possible to recreate such a microstructure within a MD simulation. The reason for this lies in the nature of relaxed dislocations at low densities. Dislocations cause the lattice to be strained locally around them, thus setting up a strain field. This causes the dislocations to repel each other and become widely spaced.

In annealed, ultrahigh–purity single crystal copper the dislocation density can be as low as $10^2\,\mathrm{cm}^{-2}$.[160] Now, in a simulation cell which is considerably larger than those used in this work, it is possible using current computing resource to simulate a sample of material which is 400 nm (4x10$^{-5}$ cm) across. This sample has an area of 1.6x10$^{-9}$ cm$^2$, so the lowest dislocation density which can be simulated is 6.25x10$^8$ cm$^{-2}$, clearly far higher than that of the real single crystals being simulated.

The work shown here for bicrystals, and even more so for nanocrystalline samples makes this point about insufficient size even more acutely. The bicrystals may be

suitable to show the initial stages of the interaction processes, but their size prevents the interaction in a relaxed state being observed. Furthermore the examination of these behaviours in a low symmetry orientation exacerbates this issue due to the very large simulation cell required to produce lateral periodic boundaries.

Among the experimental issues related to producing large bicrystal discs one which is worthy of note is the possibility of recrystallisation. This problem is a possibility arising from the manufacturing process used to produce the samples. The experimental samples were made from large single copper crystals by slicing along predetermined angles so as to produce cylindrical crystals with the required lattice direction parallel to the cylinder axis. These cylinders were further sliced along the cylinder axis so as to create prisms with a semicircular cross-section. Pairs of prisms were matched up and joined so as to produce a complete cylinderwith a boundary across the diameter of the circular section and with one orientation on one side of the boundary and a different orientation on the other side of the boundary. In order to ensure that there was no material with a different density (e.g. void, air or glue) which may modify the shock, or otherwise interfere with the lateral movement of stress waves passing from one crystal into the other, the two halves were diffusion bonded together. The diffusion bonded cylinders were sliced normal to the cylinder axis to produce a series of discs which are the targets in a flyer plate shock experiment. The surfaces of the discs were examined in a scanning electron microscope to determine whether the pairs of crystals had remained intact or had, during processing, suffered some degree of recrystallisation which would negate the experiment. This procedure determined that for the end slices there was some small degree of recrystallisation along the boundary, for the remainder of the samples there was a negligible degree of recrystallisation. Certainly any observed recrystallisation is less than $5\,\mu$m wide, which is below the resolution of the line VISAR used in the dynamic experiments.

## 5.2 Conclusions

- The nature of shocks has been demonstrated to be such that the molecular dynamics method can be used to great advantage to gain insight into the processes operating at the atomic scale.

- The examination of single crystals shows that, despite the theory governing individual dislocation motion and the resultant deformation mechanisms being very well established, there is still much to be learned about how the multiplication and interaction of dislocations feed back into the strengthening which is

known to occur at the very high rates observed in shocks. Even though computational capacity is now at a level where it is believed that the simulation shows all of the behaviour that is expected from a much larger sample, the systems being simulated are not sufficient to allow the expected relaxation processes to continue to completion.

- A very large discrepancy remains between the amplitude of the elastic wave observed in these simulations and that of experiments. It is shown that the existence of defects within the crystal can account for at least some of this discrepancy. However, computational limitations not only prevent the creation of realistic sample sizes, but also prevent the simulation of realistic defect densities and microstructures. This computational limtation, then, means that it is not currently possible to recreate the low Hugoniot elastic limits observed experimentally.

- The inability of atomistic simulations to recreate experimental data notwithstanding, useful analysis of shock behaviour is demonstrated. This fortuity is used to examine the behaviour of bicrystals under shock loading. It is shown that the difference in shock speed, together with the difference in response of the two crystal orientations leads to an interaction which modifies the behaviour from that observed in single crystal simulations.

- Use is made of the ability of modern simulation methods to recreate salient features of dynamic processes to examine the behaviour of metallic substrates under high–speed impact from nanometer sized particles. Here the plasticity of the substrate is shown to be vital to ensuring that the simulation results are faithful to experiment, and hence to space science work. In order to capture this behavioour correctly, issues of substrate size and boundary behaviour are seen to be key.

## 5.3 Further Work

The value of this work is demonstrated by the applications in which this work has been of assistance (see Appendix E). Whereas for some of the papers presented in appendix E the modelling using MD is an aid to understanding of the results of experiments, paper E.1 uses MD directly to provide the main results for the paper. One aspect of the modelling of polycrystals which is noticeable here is the lack of a HEL seen in the profiles shown. This issue relates to the way in which nanocrystal

samples are created within a MD simulation, and also to the reversal of the well-known Hall-Petch effect which relates the strength of a material to its grain size. The issue is that not only are the grain boundaries relatively low density regions, in comparison ot the remaining part of the crystals, but since the grains are so small, the relative proportion of the material which is associated with the boundary is large. Now the relative low density of the grain boundary in these simulations causes this part of the sample to have very low strength, and deformation by grain boundary sliding occurs immediately upon arrival of the compression wave. In section 5.1 it was shown that for higher piston velocities (i.e. in the strong shock regime, when the plastic front has overdriven the elastic wave) the variation in shock velocity with particle velocity is the same for all orientations. Furthermore, since figure 5.5 shows that the variation of pressure with particle velocity is the same for all orientations, it may be expected that where there is a plastic front, but no elastic precursor, the simulation would show no dispersion. In the nanocrystal work, the material shows the particle velocity profile of an overdriven shock, but the dispersion expected of an elastic wave is observed. This shows that, although the precursor is not visible in the profiles, and the generation of dislocations is evident in the simulation (see figure 3.31 and animation F2.12), the elastic behaviour is still present. Furthermore, the animation (F2.12) clearly shows an elastically compressed region between the shock front and the region where dislocations are generated. The lack of a distinct elastic precursor in the profile, even though an elastically compressed region exists, shows that the manner in which the elastic compression occurs is not identical to that for the single crystal samples.

The general thrust of the work in this thesis is leading towards a physics based understanding of the metallurgical processes which take place during shock loading. Such a development is analogous to the early work on material strength, and takes those ideas further by including in the property–behaviour relationships the effects of high pressure and high rates of deformation and work. To this end, then, it can be seen that the current research into material behaviour using atomistic simulation techniques, such as MD, are somewhat nascent and have not yet reached the level of maturity required to contribute fully to the understanding of material response under dynamic loading conditions.

Within the shock response of the EAM model used here it has been shown in section 5.1 that the stress amplitudes at which plasticity occurs is unphysically high. Nevertheless paper E.2 shows that the increase in the amplitude of atomic motion caused by shock heating and plastic work is sufficient to allow the variation in the

Fourier response to be used to develop a diagnostic tool for temperature measurement. Furthermore, the reduction in amplitude due to compression, which in turn modifies the Debye temperature, is seen.

The development of experimental diagnostics is further aided by the use of MD in paper E.3. Here the use of Fourier analysis is used to determine the expected experimental output from the x-ray diffraction of shocked polycrystals. As with paper E.2, the fact that the pressure amplitudes are far higher than might be expected experimentally does not detract from the suitability of the use of MD in examination of the behaviour of the diagnostic tool.

The foregoing discussion indicates that much improvement is required both in the scale and the veracity of the simulations to move the analysis from being qualitative to being quantitative. Nevertheless, work is continuing to take the results shown here further. The study of the shock front broadening, and particularly the determination of its limiting value with increasing grain size will provide results which are of use to the wider community. The examination of low symmetry single crystals, with the lower dislocation densities and lower hardening rates, is providing an opportunity to examine in detail how the hardening behaviour continues behind the shock front.

It is very noticeable from this work that there is a need to repeat the impact study using a reliable potential interaction for aluminium. There is a great deal of interest in understanding the behaviours demonstrated in this work, but the translation of these results to those of the system of interest cannot be carried out with confidence. This concept can be taken further by the simulation of oxide materials for the impacting projectile. There is considerable experience of simulating isolated clusters of metal and silicon oxides. This expertise can be brought to bear in improving the modelling of fine–scale impacts. With the continuing improvement in compute capability the issues of size are becoming less of a hurdle to the use of MD in this type of endeavour. In contrast, the lack of suitable potentials is preventing workers from taking advantage of this advance.

# Appendix A

# Modified Embedded Atom Method

An extension to the EAM which considers the angular behaviour of the embedding function.[16]

The embedding function, $F(\rho)$ is given by

$$F(\rho) = AE_c \frac{\rho}{\rho_0} \ln \frac{\rho}{\rho_0} \qquad \text{(cf equation 2.58)}$$

where the parameter $A$ is arbitrary and $\rho_0$ is a density scaling parameter.

The electronic density, $\bar{\rho}$ is a function combining a set of partial electron densities. This is where the angular information is included in the model. Now the square of the electron density is given by a sum of the partial densities

$$\bar{\rho}^2 = \sum_{h=0}^{3} t^{(h)} \rho^{(h)2} \tag{A.1}$$

The differing contributions $(h)$ are associated with the symmetries attributed to s, p, d, f orbitals. The symmetry is included via use of Legendre polynomials. The various contributions are

$$\rho^{(0)} = \sum_j \rho^{a(0)}(r^j) \tag{A.2a}$$

$$(\rho^{(1)})^2 = \sum_\alpha \left[ \sum_j \rho^{a(1)}(r^j) \frac{r^j_\alpha}{r^j} \right]^2 \tag{A.2b}$$

$$(\rho^{(2)})^2 = \sum_{\alpha,\beta} \left[ \sum_j \rho^{a(2)}(r^j) \frac{r^j_\alpha r^j_\beta}{r^{j2}} \right]^2 - \frac{1}{3} \left[ \sum_j \rho^{a(2)}(r^j) \right]^2 \tag{A.2c}$$

$$(\rho^{(3)})^2 = \sum_{\alpha,\beta,\gamma} \left[ \sum_j \rho^{a(3)}(r^j) \frac{r^j_\alpha r^j_\beta r^j_\gamma}{r^{j3}} \right]^2 \tag{A.2d}$$

The $t^{(h)}$ in equation A.1 are given by

$$t^{(h)} = \sum_j t_j^{(h)} \frac{\rho_0^{a(0)}}{\rho^{(0)}}$$

The $\rho^{a(h)}$ terms are exponentially decreasing contributions

$$\rho^{a(h)}(r) = \rho_0^a \, e^{-\beta^{(h)}(\frac{r}{r_e - 1})}$$

This version of the MEAM scheme, however, does not reproduce the properties of some BCC metals correctly.[100] It should be noted that in the MEAM the neighbour atoms are assumed to be *first* neighbours. The effect of distance is then used to treat neighbours at a greater distance than the closest. In the ideal BCC structure there are eight closest atoms, but the next nearest atoms are only 15% further out, and can move to be at a similar distance due to thermal motion. The *second nearest–neighbour* MEAM (also known as "2NN–MEAM") scheme deals with this issue by adding a screening function. The screening for each neighbour, $j$, is given as a product of screening factors due to the remaining neighbours, $k$.

$$S_{ij} = \prod_{k \neq i,j} S_{ikj}$$

The factors, $S_{ikj}$ are based on an elliptical geometric construction. The ellipse passes through atoms $i$, $j$ and $k$, with the $x$ axis aligned along the $i$–$j$ vector. The equation for the ellipse is

$$x^2 + \left({}^1\!/_C\right) y^2 = \left({}^1\!/_2 r_{ij}\right)^2$$

where

$$C = \frac{2(X_{ik} + X_{kj}) - (X_{ik} - X_{kj})^2 - 1}{1 - (X_{ik} - X_{kj})^2}$$

and the factors $X$ are

$$X_{ik} = \left(\frac{r_{ik}}{r_{ij}}\right)^2 \qquad \text{and} \qquad X_{kj} = \left(\frac{r_{kj}}{r_{ij}}\right)^2$$

From this, the screening terms, $S_{ikj}$ are given by

$$S_{ikj} = f_c \left[\frac{(C - C_{min})}{(C_{max} - C_{min})}\right] \tag{A.3}$$

$C_{max}$ and $C_{min}$ are limiting values, and the cutoff function, $f_c$ is

$$f_c = \begin{cases} 1 & x \geq 1 \\ [1 - (1 - x)^4]^2 & 0 < x < 1 \\ 0 & x \leq 0 \end{cases}$$

Several workers (see for example [146]) have examined the relationships between the different angular-dependent schemes to explore the similarities and differences.

A comparison of some static properties related to melting has been assembled by Ryu and Cai.[132] They showed that although the MEAM scheme closely predicted the experimental melting points, the thermal expansion prediction was poor. They note, then, that a substantial improvement is gained for both FCC and BCC by reducing the parameter $C_{min}$ (equation A.3) substantially.

# Appendix B

# Mishin Copper Potential

The embedded atom method potential scheme developed by Mishin *et al.*[116]

Recall that the potential energy from the EAM scheme is given by

$$V(q) = \sum_i F_i(\bar{\rho}_i) + \frac{1}{2}\sum_i \sum_{j \neq i} \phi_{ij}(r_{ij}) \tag{B.1}$$

$$\begin{aligned} \phi(r_{ij}) = &[E_1 M(r, r_0^{(1)}, \alpha_1) + E_2 M(r, r_0^{(2)}, \alpha_2) + \delta] \\ &\times \Psi\left(\frac{r - r_c}{h}\right) - \sum_{n=1}^{3} H(r_s^{(n)} - r) S_n (r_s^{(n)} - r)^4 \end{aligned} \tag{B.2}$$

Here $M$ is a Morse exponential function

$$M(r, r_0, \alpha) = \exp[-2\alpha(r - r_0)] - 2\exp[-\alpha(r - r_0)] \tag{B.3}$$

and $H(x)$ is a unit step function. The function $\Psi(x)$ is a cutoff function where

$$\Psi(x) = \begin{cases} 0 & \text{if } x \geq 0 \\ \frac{x^4}{(1+x^4)} & \text{if } x < 0 \end{cases}. \tag{B.4}$$

Equation B.2 contains 15 fitting parameters

| | | |
|---|---|---|
| $E_1$ | (eV) | $2.01458\times10^{2}$ |
| $E_2$ | (eV) | $6.59288\times10^{-3}$ |
| $r_0^{(1)}$ | (Å) | 0.83591 |
| $r_0^{(2)}$ | (Å) | 4.46867 |
| $\alpha_1$ | ($Å^{-1}$) | 2.97758 |
| $\alpha_2$ | ($Å^{-1}$) | 1.54927 |
| $\delta$ | (Å) | $0.86225\times10^{-3}$ |
| $h$ | (Å) | 0.50037 |
| $r_c$ | (Å) | 5.50679 |
| $r_s^{(1)}$ | (Å) | 2.24000 |
| $r_s^{(2)}$ | (Å) | 1.80000 |
| $r_s^{(3)}$ | (Å) | 1.20000 |
| $S_1$ | ($eV/Å^4$) | 4.00000 |
| $S_2$ | ($eV/Å^4$) | 40.00000 |
| $S_3$ | ($eV/Å^4$) | $1.15000\times10^{3}$ |

The embedding function $f(\bar{\rho}_i)$ is given by either

$$F(\bar{\rho}) = f^{(0)} + \frac{1}{2}f^{(2)}(\bar{\rho}-1)^2 + \sum_{n=1}^{4} q_n(\bar{\rho}-1)^{n+2}$$

if $\bar{\rho} < 1$, or

$$F(\bar{\rho}) = \frac{f^{(0)} + \frac{1}{2}f^{(2)}(\bar{\rho}-1)^2 + q_1(\bar{\rho}-1)^3 + Q_1(\bar{\rho}-1)^4}{1 + Q_2(\bar{\rho}-1)^3} \tag{B.5}$$

if $\bar{\rho} > 1$.

The overall electronic density is given as a sum of the electronic density contributions from the other atoms in the system

$$\bar{\rho}_i = \sum_{j\neq i} \rho(r_{ij}). \tag{B.6}$$

The individual electronic density contributions are given by

$$\begin{aligned}\rho(r) = [\, a\exp(-\beta_1(r-r_0^{(3)})^2) + \exp(-\beta_1(r-r_0^{(4)}))\,] \\ \times \Psi\left(\frac{r-r_c}{h}\right)\end{aligned} \tag{B.7}$$

where the function $\Psi(x)$ is the cutoff function as before.

This latter set of functions (equations B.5 to B.7) then utilise a further 13 parameters.

| | | |
|---|---|---|
| $a$ | | 3.80362 |
| $r_0^{(3)}$ | (Å) | -2.119885 |
| $r_0^{(3)}$ | (Å) | -2.61984×$10^2$ |
| $\beta_1$ | (Å)$^{-2}$ | 0.17394 |
| $\beta_2$ | (Å)$^{-2}$ | 5.35661×$10^2$ |
| $f^{(0)}$ | (eV) | -2.28235 |
| $f^{(2)}$ | (eV) | 1.35535 |
| $q_1$ | (eV) | -1.27775 |
| $q_2$ | (eV) | -0.86074 |
| $q_3$ | (eV) | 1.78804 |
| $q_4$ | (eV) | 2.97571 |
| $Q_1$ | | 0.40000 |
| $Q_2$ | | 0.30000 |

It is noted in the paper describing this potential[116] that not all the parameters shown here are free parameters; the functions $\rho(r)$ are normalised to $\bar{\rho} = 1$ in the equilibrium fcc crystal,

$$\bar{\rho} = \sum_m N_m \rho_m = 1, \tag{B.8}$$

and the function $V(r)$ satisfies mechanical equilibrium of the fcc crystal at a lattice period $a_0$, the experimentally determined value, so that

$$\sum_m N - mR_m V'_m = 0. \tag{B.9}$$

In the equations B.8 and B.9, $V_m = V(R_m)$ and $\rho_m = \rho(R_m)$, where $R_m$ and $N_m$ are the radius and number of atoms at the $m$th coordination shell. From this, equations B.8 and B.9 can be solved for $a$ and $E_1$. Furthermore, the coefficient $f^{(0)}$ can be obtained from the cohesive energy, $E_0$,

$$f^{(0)} = E_0 - \frac{1}{2}\sum_m N_m V_m \tag{B.10}$$

and $f^{(2)}$ from the bulk modulus,$B$,

$$\frac{1}{2}\sum_m N_m V''_m R_m^2 + f^{(2)}\left(\sum_m N_m \rho'_m R_m\right) = 9B\Omega_0, \tag{B.11}$$

where $\Omega_0$ is the equilibrium volume. Finally, $q_1$ can be determined by setting $f(0) = 0$ (equation B.5). Hence there are overall 23 free fitting parameters, which are optimised following the methodology of [115].

# Appendix C

# Schmid Factors

In any crystal there are many ways in which atoms can be moved, one at a time, so as to enable the passage of a dislocation. However, the atomic movement which is most favoured is that which requires the smallest energy. Therefore the atoms themselves should move the smallest distance. This implies that the atomic movement will be in the direction of closest packing of atoms within the lattice. In a FCC lattice the atoms are packed in layers of atoms in a hexagonal arrangement. It can be seen, then, that there are 6 eqivalent directions of closest packing. Furthermore, by re-orienting the lattice, it can be seen that there are 4 planes which exhibit the close-packed hexagonal formation. This results in 24 crystallographically equivalent plane/direction pairs which can allow dislocations to move. These plane/direction pairs are known as *slip systems*.

In order to determine which slip system will operate under some particular loading arrangement, it is necessary to consider the shear force which is being applied to each system. Consider figure C.1. The slip system shown consists of slip in the direction $P$ in the plane $A$. The shear stress acting on this slip system is given by

$$\tau = \frac{\text{resolved force on plane}}{\text{area of slip plane}}. \tag{C.1}$$

Now the resolved force is

$$F_r = F\cos\Phi \tag{C.2}$$

and the area of the slip plane is given by

$$A = \frac{A_0}{\cos\Theta} \tag{C.3}$$

If we define the stress on the system as

$$\sigma = \frac{F}{A_0} \tag{C.4}$$

$F$ Load
$A$ Area of slip plane
$A_0$ Area of cylinder base
$P$ Slip direction
$N$ Normal to slip plane

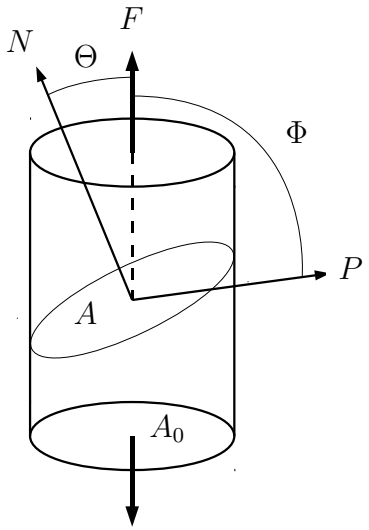


Figure C.1: Illustration of determination of shear stress.

then the shear stress on the slip system is

$$\tau = \sigma \cos\Theta \cos\Phi. \tag{C.5}$$

It has been found that for any material (i.e. for a given purity and dislocation density) the resolved stress, $\tau_c$, at which dislocations begin to move is a constant. This is Schmid's law. The quantity $\cos\Theta\cos\Phi$ is the *Schmid factor*, and the value of $\sigma$ when $\tau = \tau_c$ is the *yield stress*. For any crystal under stress the slip system which will be activated first (i.e. at lowest stress) is that system for which the Schmid factor is highest.

# Appendix D

# Plasticity 2005

## D.1 Atomistic simulations of shock generated dislocations in nickel

This work was centred around the need to understand how shock waves behave in polycrystalline metals. The study focussed on the effect on one crystal of there being a crystal of different orientation alongside; whether there was a frictional effect acting at the grain boundary, how crystal 'preshocking' – caused by the faster shock in the material of the lower shock speed – interfered with the shock behaviour of that lower shock speed crystal.

# ATOMISTIC SIMULATIONS OF SHOCK GENERATED DISLOCATIONS IN NICKEL

Nigel T. Park

Design Physics Department,
AWE Aldermaston, Reading, UK.
nigel.park@awe.co.uk

**ABSTRACT**- The time scales associated with molecular dynamics are very short, being of the order of a few to a few hundred picoseconds ($1E^{-12}$s up to $1E^{-10}$s). Consequently the strain rates simulated are above those observed experimentally, except in laser driven shock experiments. Simulations of shock flyer experiments in Ni show the generation of plastic deformation and the initiation and growth of voids in the spall process. I used NVE molecular dynamics with the MEAM potential scheme to observe a difference in the behaviour of crystals oriented with the [001] direction parallel to the shock direction, as opposed to a crystal with the [111] direction parallel to the shock direction.

**INTRODUCTION**: Molecular dynamics is a technique in which the Newtonian mechanics of the motion of individual atoms is tracked over time. This necessarily restricts both the numbers of atoms in the sample and the simulated time in order to make the computation practicable. This reduced time produces simulated conditions which are rarely seen in real world experience; such timescales are used experimentally only in the arena of shock physics. In the last 25 years, work has been carried out on different aspects of shock-crystal interaction. Holian and Straub [1979] considered the validity of the Rankine-Hugoniot conditions in MD shocks. Wagner et al. [1992] carried out simulations in two dimensions, in which a flyer plate was used to set up a stress pulse, leading to spallation. Kum [2003] investigated the orientation effects upon the passage of a shock front, as described by three different potentials.
Little work is available describing the interplay of shock waves and crystal boundaries. This is important to understand, as a polycrystalline material is made up of a very large number of small crystals, and so contains a significant number of such boundaries. This work investigates the interplay of shocks set up in two different crystals with a grain boundary normal to the shock direction.

**PROCEDURES, RESULTS AND DISCUSSION**: The simulations represent a standard gas-gun flyer test. For this, I created a simulation cell consisting of a slab of atoms, with a boundary along {y=0}. The region {y>0} contains a single crystal oriented with [001] parallel to the x-axis. The region {y<0} contains a crystal oriented with [111] parallel to the x-axis. The flyer has a thickness of 133 Å, into a sample of 464 Å. Both crystals are 1420 Å in the z direction and approximately 705 Å each in the y direction. All of the atoms are nickel, and the potential scheme is the modified embedded atom method (Lee and Baskes [2000]).

The two crystals were built with a 0.44 Å (~1/8 cell width) gap. The atoms were initialised with velocities from the Boltzmann distribution representing a temperature of 300ºK then allowed to thermalise for 20,000 timesteps, equivalent to 100 ps, under NVT conditions using a Nosé-Hoover thermostat. At this time, the computational cell had full periodic boundary conditions. During this equilibration time, the two crystals relax towards each other to form a grain boundary.

In order to create a flyer, all the atoms in the leftmost 133 Å have superimposed a velocity of 19.8 Å $ps^{-1}$ (=1.98 mm/μs). The periodic boundary along the x-axis is removed, and the timestep was reduced to 0.0001ps. The timestep reduction was required to overcome computational errors. The thermostat is also removed, so the simulation runs under NVE conditions.

Initially a shock can be seen in both crystals. The shock velocity in the [001] crystal is 4.75nm/ps (≡mm/μs), whereas the shock velocity in the [111] crystal is 8.5nm/ps. This compares well to the quoted value of 7.43nm/ps (Marsh [1980]), bearing in mind the quoted value is for polycrystalline material. Figs. 1 and 2 show the shocks in each crystal, represented by the {x} component of the velocity, averaged over the atoms in a small region in each crystal. The regions from which these data are obtained are in the centres of the crystals, and consequently are independent at the times shown.

Fig. 1 shows the shock position at early time. Here it is clearly seen that the shock in the [111] crystal is faster than that in the [001] crystal. It can also be seen that the [001] crystal behaves in the more traditional 'shock physics' manner; that is, the material in the shocked region all has the same velocity, which is half of the flyer velocity. This velocity persists to later times, see Fig. 2.

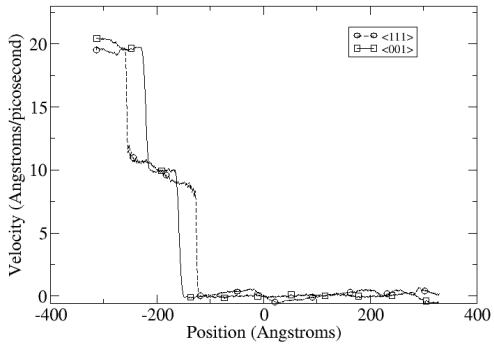


**Figure 1: 0.8ps**

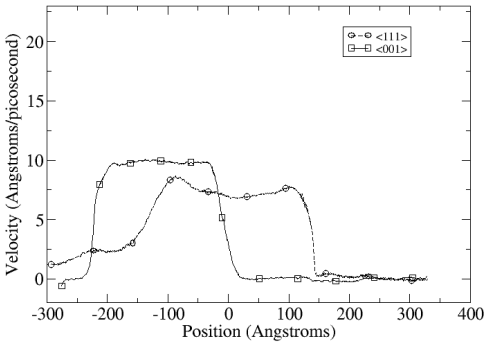


**Figure 2: 3.90ps**

**Velocity-position plots showing the shocks in both crystals.**

The [111] crystal, however appears to exhibit a two-wave structure due to the particle velocity in the shocked region not being half of the flyer velocity. This result is consistent with the Hugoniot elastic limit (HEL) having been exceeded in the [111] crystal. Visualisation of the atomic positions shows that indeed there is evidence of crystal damage in the [111] crystal behind the shock front, whereas no damage is seen in the [001] crystal.

Fig. 2 shows the shocks at some time later. The release wave in the [111] crystal, having arrived at the back surface first, has caused the entire shock pulses to be shifted relative to each other. Also note that the velocity rise in the [111] crystal has remained sharp, whereas that in the [001] crystal, being fully elastic and therefore below the sound speed, has begun to form a ramp.

The consequence of the one shock being ahead of the other is that a pulse is driven into the [001] crystal, normal to the shock direction. The grain boundary position is moved in the direction of this pulse. After the leading pulse has passed, the position reverses, and the grain boundary is moved back towards the [111] crystal. After both shocks have passed the grain boundary is no longer smooth, but exhibits a 'wavy' topology. The width of the grain boundary has increased from being almost smooth initially to include several atomic planes.

In the traditional 'shock-physics' paradigm, spall occurs on a single plane. This locus is where the rarefaction from the free surface of the sample, travelling back into that sample, meets the rarefaction at the rear of the shock pulse. In neither crystal seen here is the rarefaction sharp enough to produce this result. Whilst the [001] crystal spalls over a narrow region, the [111] crystal contains much more damage, and voids occur over a zone covering nearly one half of the thickness of the sample.

**CONCLUSIONS**: The difference in behaviour under shock of two orientations of FCC nickel is large enough for the shock waves to have an effect on neighbouring crystals. The shock velocities are radically different, resulting in a large difference in the positions of those fronts. The grain boundary between the crystals becomes perturbed following shock passage. The spall behaviour is more markedly different between these orientations, due to the differing levels of crystal damage created by similar shocks.

**REFERENCES**

Holian, B. L. & Straub, G. K. 1979, "Molecular dynamics of shock waves in three-dimensional solids. Transition from nonsteady to steady waves in perfect crystals and implications for the Rankine-Hugoniot conditions", Phys. Rev. Lett., **43**, 1598

Kum, O. 2003, "Orientation effects in shocked nickel single crystals via molecular dynamics", J. Appl. Phys., **93**, 3239.

Lee, B-J and Baskes M. I. 2000, "Second nearest-neighbor modified embedded-atom-method potential", Phys. Rev. B, **62**, 8564

Marsh, S. P. (ed.) 1980, "LASL Shock Hugoniot Data", p. 111, University of California Press, Berkeley, CA.

Wagner, N. J., Holian, B. L. and Voter, A. F. 1992, "Molecular-dynamics simulations of two-dimensional materials at high strain rates", Phys. Rev. A, **45**, 8457 .

# Appendix E

# Additional Papers

## E.1 The Atomistic Modeling of Wave Propagation in Nanocrystals

The work towards this paper arose from the need to understand shocks in Inertial Confinement Fusion (ICF) capsules.[120] It had been previously been determined that a variation in the arrival time of the shock at the inner surface of the ICF capsule would cause Rayleigh-Taylor instabilities to be set up in the interface, reducing the efficiency of the capsule.

The original calculations were carried out by Bringa and caro. This author's involvement concerned the discussion surrounding the 'two speed' model being used to predict a relationship between the observed shock front width and the microstructure of the material under investigation. The three authors of the paper discussed the ideas behind the model, and the resultant implications. This author's major input to that paper was in clarifying how the ideas were put across. In particular, figure 3 of that paper, which clarifies the connection between the width of the shock, as measured by the velocity profile averaged over the cross section of the sample (which would be measured experimentally by VISAR for instance), and the width of the fluctuations in the cross section, which would be the ones really leading to hydrodynamic instabilities.

# The Atomistic Modeling of Wave Propagation in Nanocrystals*

**E.M. Bringa, A. Caro, M. Victoria, and N. Park**

*This paper presents non-equilibrium molecular dynamics simulations of wave propagation in nanocrystals. The width of the traveling wave front increases with grain size, d, as $d^{1/2}$. This width also decreases with the pressure behind the front. When the results are extrapolated to micro-crystals, reasonable agreement with experimental data is obtained. In addition, this extrapolation agrees with models that only take into account the various velocities of propagation along different crystalline orientations without including grain boundary effects. The results indicate that, even at the nanoscale, the role of grain boundaries as scattering centers or as sources of plasticity does not increase significantly the width of the traveling wave.*

## INTRODUCTION

Nanocrystals have been extensively studied, both in experiments[1] and simulations,[2–4] for their numerous beneficial properties such as strength. In general, continuum-scale plasticity models only include polycrystalline effects by averaging over various crystalline directions to obtain some effective isotropic material.[5] There are several models that do include full polycrystalline anisotropy, but where grain boundaries (GB) are considered infinitesimally thin or not influencing the deformation of the material.[6] Few recent models have tried to incorporate the role of grain boundaries,[7,8] but the connection to atomic-scale processes has only recently begun to emerge.[9]

Many current experiments[1] and most atomistic simulations on nanocrystals[2–4] involve homogeneous deformation of the material (i.e., the whole system is subjected to the same deformation). However, there may be instances, especially at very high strain rates, where this would be no longer true;[10] a wave will travel through the material with deformed material behind the wave front. This article will focus on how the nanocrystalline structure can change the wave propagation due to polycrystalline effects. It is important to understand in detail the response of polycrystalline materials to wave propagation for a number of applications. For instance, the National Ignition Facility (NIF)[11] at Lawrence Livermore National Laboratory will require polycrystalline ignition targets where the wave front has to be extremely smooth to avoid Rayleigh-Taylor[12] instabilities caused by perturbations due to the grain structure. Such instabilities can grow, resulting in a final compression diminished below the desired value.

**A polycrystal introduces different wave velocities in each grain, with preferred wave propagation directions.**

Numerous studies, both experimental[13–16] and continuum modeling,[10,17–23] have been conducted on wave propagation in polycrystals, and samples with different grain size do show grain-size dependence in wave propagation.[13,16,18,21] However, models that include atomic-level information are lacking. Figure 1 shows a schematic of a wave traversing a polycrystal. In Figure 1a, the wave is crossing a single crystal and the wave front is "straight," since there are no perturbations (except for possible plasticity or phase transformations). A polycrystal introduces different wave velocities in each grain, with preferred wave propagation directions, as shown in Figure 1b. This fact alone would greatly enhance the wave front width if the difference between propagation velocities is not negligible. For instance, for many face-centered cubic (fcc) metals, the sound velocity along the fast direction can be 10–25% greater than the velocity along the slow direction.[17,18,24] Some models do include the role of anisotropy leading to refraction of the wave, for instance, by increasing the effective path it travels.[18] In addition to the polycrystal anisotropy, GB could play a role as scattering centers, or barriers to the wave transmission, with a fraction of the wave dissipated as indicated in Figure 1c. Finally, Figure 1d shows that GB can also act as sources of dislocations where the plastic deformation may change the width of the wave front. There are several calculations[17,18,21] estimating the effect sketched in Figure 1b, but no analytical or semi-analytical models predict shock width for a given grain size. Although there have been a few studies for single grain boundaries,[25,26] there are no studies regarding the effects sketched in Figure 1c and d in polycrystals. Based on Figure 1, the general expression of the width of the front, $\Delta z$, could be assumed to be the sum of (as a first approximation) independent contributions from Figure 1b–c:

$$\Delta z = \Delta z_{aniso} + \Delta z_{GBscatt} + \Delta z_{plastic} \quad (1)$$

An upper estimate of $\Delta z_{aniso}$ can be obtained from a two-dimensional (2-D) propagation case as follows. Imagine two rows of grains, one consisting only of grains where the velocity is slow and

the other where the velocity is fast. The spread $\Delta z$ of the front after a time t will be $\Delta v$ t, where $\Delta v$ is the velocity differential. For a sample of fixed length L, with grains of size d, $L/d = N_g$ is the mean number of traversed grains, and $t = L/\langle v \rangle$. Therefore,

$$\Delta z = (\Delta v/\langle v \rangle)\, d\, N_g = A_v\, d\, N_g \qquad (2)$$

where $(\Delta v/\langle v \rangle) = A_v$ is called the anisotropy factor. For a sample with many rows and grains of size d, with the same number of slow and fast grains randomly distributed, one would still expect a linear dependence of $\Delta z$ with the anisotropy factor. However, there will be a large number of rows where the number of slow and fast grains will be roughly the same, giving $\Delta z_{aniso} \sim 0$. Assuming a power law form for the grain size dependence, $d^{\alpha}$, this would give a dependence with $\alpha < 1$. The fact that the shock width increases with grain size has been experimentally observed for metals[13] and oxides.[16] Recent modeling[21] of this process for wave propagation in beryllium polycrystals gave $\alpha \sim 1/2$. Note that Equation 2 also predicts that a wave will continue widening with time or as it traverses more and more grains.

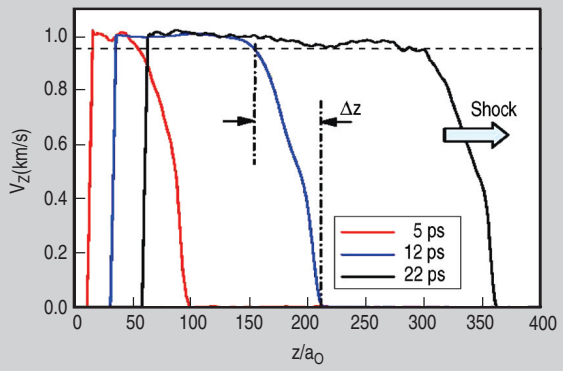


Figure 3. Three snapshots from an MD simulation for d = 20 nm and P = 47 GPa showing velocity profiles, averaged in slices one lattice parameter, $a_0$, thick, perpendicular to the shock propagation direction. The measurement of the width $\Delta z$ at t = 12 ps is indicated.

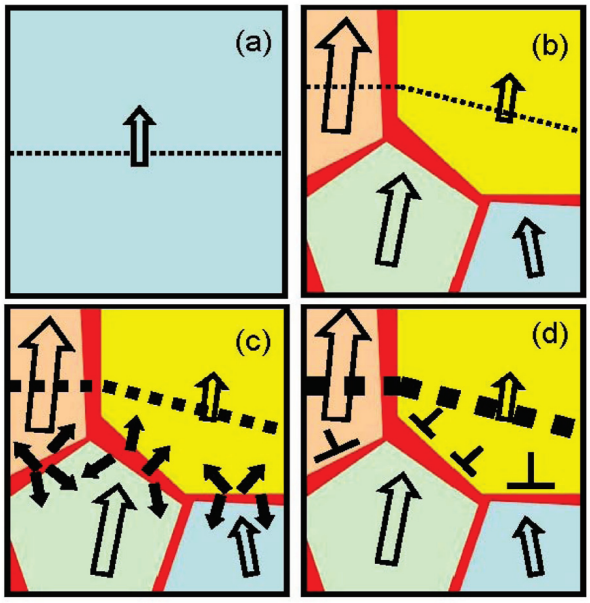


Figure 1. A schematic of wave propagation in a polycrystal. The dotted line indicates the wave front. (a) single crystal, (b–d) polycrystals showing: (b) anisotropy due to different crystalline orientations, (c) GB acting as scattering centers, and (d) GB enhancing plasticity induced by the wave front.

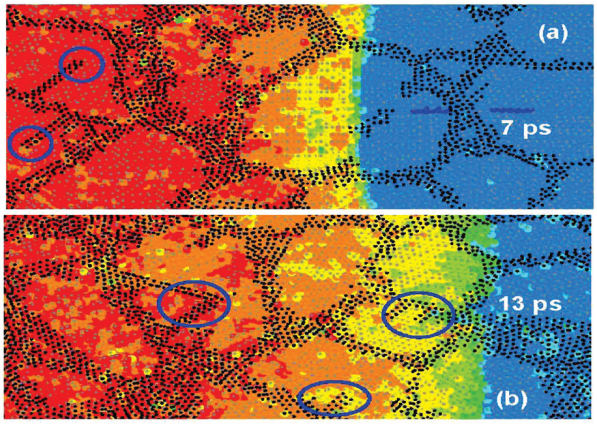


Figure 2. Snapshots of the MD simulation that show the wave front at two different times. Grain boundary atoms are overlapped as small black dots. d = 5 nm, P = 22 GPa, $U_p$ = 0.5 km/s and 10% strain. Atoms are colored according to their kinetic energy (red, high-moving at $U_p$; blue, low-unshocked). The upper frame shows a sharp front inside the grains, with some refraction due to orientation. Note that the energy levels track the GB, and that in frame (b) the front itself tracks the shape of one of the grains. Some of the stacking faults generated by the wave are marked with blue circles.

## ATOMISTIC SIMULATIONS

Typical GBs in real materials are only ~1 nm thick and are difficult to model using continuum models. In this study, the authors use the massively parallel code MDCASK[27] to carry out atomistic molecular dynamics (MD) simulations of embedded-atom method (EAM) copper samples.[27] Prismatic samples were built using the Voronoi construction with random texture.[3] Dislocation cores were identified using a centro-symmetry parameter filter.[29] The study focused on the propagation of waves moving faster than the speed of sound (i.e., shock waves). There are numerous MD simulations of shocks in single crystals,[24,30–32] but only a limited number on polycrystalline materials.[31–33] The authors have simulated samples with 0.5–64 million atoms, and average grain sizes of 5 nm, 10 nm, and 20 nm on 32–768 central processing units. Further analysis of these simulation results is in progress and will be published elsewhere.[33]

The samples had free surfaces along the shock wave direction and periodic boundary conditions in the transverse direction. The first few surface layers on one side were chosen as a piston. A step velocity function was applied to these piston atoms at the desired piston velocity, $U_p$, to create a traveling wave with velocity $U_s$.[24] The stress along the shock direction (the shock pressure) behind the

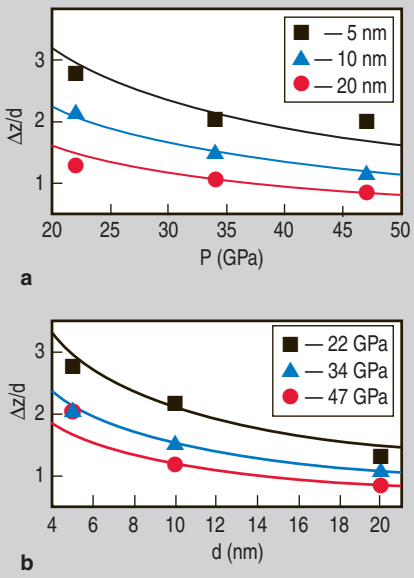


Figure 4. Front width, normalized to the grain size, versus (a) pressure and (b) grain size. Solid lines show the fitting from Equation 3. Width was measured when the wave front had traveled ~70 nm.

front is given by the Hugoniot equations[30] dealing with mass, momentum, and energy conservation at the front: $P_H = \rho_0 U_p U_s$. The strain behind the front is constant and given by $\varepsilon = U_p/U_s$. Assuming a linear Hugoniot relationship, $U_s = c_0 + s_1 U_p$. For copper, $c_0 = 4.0$ km/s and $s_1 = 1.5$.[24] The MD simulations[24] found that this equation is a reasonable approximation for this EAM potential, especially for strong shocks.

Figure 2 shows snapshots of a simulation with d ~ 5 nm and P = 22 GPa (strain is ~10%). Despite the small grain size, significant dislocation activity is observed, driven by the large applied stress. Partial dislocations are emitted from the GB and cross the grain leaving a stacking fault behind,[33] as in the previous homogeneous deformation simulations of larger grains.[2,3] Given the large level of plastic activity, one could expect strong influences at the shock front for the simulated cases, as suggested in Figure 1d. In addition, both frames of Figure 2 show refraction of the wave, as seen in Figure 1b.

Figure 3 shows several snapshots of the velocity profiles in one of the simulations. As the piston advances, the wave front advances, too, at a faster velocity. The piston drive is a step function, but the wave front develops a characteristic width, which is related to the gradient in kinetic energy (velocity) observed in Figure 2. A working definition of width is the distance between the edge of the front and the point where the velocity is 95% $U_p$, as shown in Figure 3. The profile in Figure 3 has been averaged perpendicularly to the propagation direction over about ten grains. However, the width of the wave can be identified along the shock direction with the width of the fluctuations normal to the direction of propagation. Close inspection of simulation snapshots, like those in Figure 2, shows that this identification is roughly valid.

Figure 4 shows the width, normalized to the grain size, versus pressure and grain size. A simple functional form has been adapted to fit the calculations in this work. For copper, $A_v \sim 0.25$ will depend on pressure only weakly in the interval studied and it is assumed constant. Assuming a power law behavior with grain size and pressure, the observed width can be fit using the following relationship:

$$\Delta z/d = C\, A_v\, (d/d_o)^{\alpha}\, (P/P_o)^{\beta} \qquad (3)$$

Setting $d_o = 10$ nm and $P_o = 47$ GPa, the data is fit to get $C \sim 5.4$, $\alpha \sim -1/2$, and $\beta \sim -3/4$. As the shock pressure increases plasticity also increases, but the overall result is a decrease in the width of the front, as seen in experiments and predicted by viscoplastic models.[34] This leads to a steep increase of the strain rate with pressure, as measured for strong, overdriven shocks. As mentioned previously, the $d^{1/2}$ grain size dependence is the same dependence that was recently found in simulations[21] of micro-scale polycrystalline beryllium which did not include GB effects, indicating that this dependence may be somewhat general and that the role of GBs may be relatively small for all cases. In fact, dislocation activity does not seem to significantly widen the relatively sharp front inside grains, as seen in Figure 2.

A continuum-level model has shown that the wave front width actually increases with time[17] (i.e., the irregularities in the front are enhanced as the wave traverses more grains). Experimental data, however, remains scarce and gives only marginal effects.[14,15] Figure 5 shows results for samples that are ~400 fcc cells (~150 nm) long. After a transient stage, a steady-state increase in width is reached, which can be modeled with a power law fit including the number of grains, as:

$$\Delta z/d = C\, A_v\, (d/d_o)^{-1/2}\, (P/P_o)^{-3/4}\, (N_g/N_{go})^{\gamma} \qquad (4)$$

with $N_{go} \sim 1$ for the 20 nm grains, with $\gamma \sim 1/5$. The length of the samples may be too small to carry out an appropriate fitting of this dependence. A fit to the continuum model results in Reference 15 gives $\gamma \sim 1/2$.

## WAVE PROPAGATION IN MICROMETER-SIZED GRAINS

From Figures 4 and 5, a simple analytical form can be obtained that is in good agreement with the simulation data. However, given the relatively small simulation data set and the narrow range of grain sizes and pressures accessible to atomistic simulations, it may not be valid to extrapolate these results to the micro-scale. Chhabildas and Asay[14] have measured an upper limit to the rise time

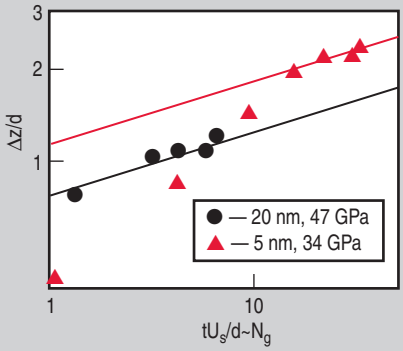


Figure 5. Evolution of the width with scaled time for two simulated cases showing the power law evolution that gives $\gamma = 1/5$.

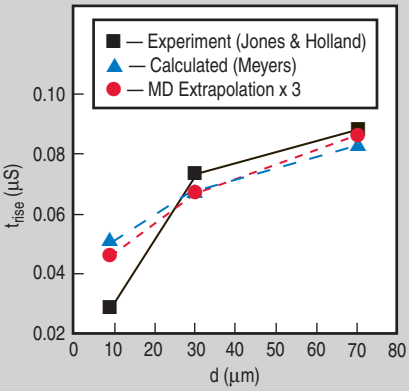


Figure 6. Experimental results[13] compared to the continuum level model by Meyers[18] and the extrapolation of MD results using Equation 4.

of shocks in copper targets with d ~ 5 μm at a few different pressures. They obtained times of 1.4–2.2 ns, close to their experimental resolution, while the model in this study gives times that are 15–25 times smaller. A worst-case scenario for the model would occur for grain sizes larger than 1 μm at low shock pressure, where the width is expected to be large. Figure 6 shows experimental data for the elastic wave in such a case. Calculations from a numerical model by Meyers,[18] which only includes anisotropies as in Figure 1b, without GB effects, are also shown. Extrapolation of the simulation data to the experimental conditions for a nickel disk of ~19 mm[13] is shown in Figure 6, using $A_v \sim 0.17$ for nickel in Equation 4 and $t_{rise} = \Delta z/U_s$. Results are obtained that are lower by a factor of ~3 than the experimental results and the continuum-level model. That these results are of the same order could be considered somewhat fortuitous, given the simple functional form used, the extrapolation from nano- to micro-scale, and the change of material from copper to nickel. However, the fact that the continuum model has the same behavior with grain size is likely indicating that the same basic governing principles are at play here. Since that model only considers the first term in Equation 1 (i.e., the anisotropy in the velocity of propagation of the wave for different grains), this term appears to dominate the development of the width of the wave front. In the simulations, this seems to be the case even for nanostructured materials where one would expect the other two terms in Equation 1 to contribute relatively more than in micrometer-sized materials. On the other hand, copper has a particularly high anisotropy factor, which could mask the role of the GB-related terms in developing the width of the front.

The results may be relevant to the design of NIF targets using micrometer-sized grains. Since anisotropy dominates the extent of the shock width, using targets with preferential texture, such as the candidate beryllium targets[21] ($A_v \sim 0.1$), would significantly reduce fluctuations at the shock front. The same effect would be achieved using a target with a polycrystalline material having small sound velocity anisotropies, as in the case of polycrystalline carbon ($A_v \sim 0$).[35] Future simulations of wave propagation in nanocrystals with hexagonal close packed and diamond crystalline structures, and with different values of the anisotropy parameter, are needed to assess the range of applicability of these findings which use fcc copper nanocrystals. Furthermore, a new generation of interferometry techniques[15,36,37] will allow for improved measurements of shock width, including the possible role of fluctuations.[36]

## CONCLUSION

The width of the wave is a function of grain size, pressure, and time. Simple analytical fits show the same scaling with grain size as models not including GB effects[21] (i.e., as $d^{1/2}$). In addition, extrapolation to micro-scale experiments[13] and models[18] shows reasonable agreement. The simulations suggest that the effect of GB on the width of the wave front is small compared to the effect of anisotropy from crystal to crystal. As a result, continuum-level models of wave propagation could provide front widths not significantly different from those in more computationally expensive atomistic simulations. Additional MD simulations in nanomaterials are needed to establish the soundness of this hypothesis, including materials with low anisotropy. These simulations would allow more accurate power-law fits and possibly a better understanding of the origin of the exponents governing shock width. Finally, despite all the limitations of atomistic simulations, these results clearly show that nanocrystalline NIF targets would guarantee small fluctuations in the shock front, decreasing the probability for unwelcome instabilities.[12]

## ACKNOWLEDGEMENT

*The authors would like to thank Alex Hamza for fruitful discussions. The work at Lawrence Livermore National Laboratory was performed under the auspices of the U.S. Department of Energy and Lawrence Livermore National Laboratory under contract No. W-7405-Eng-48, LDRD 04-ERD-021.*

## References

1. J.R. Weertman, *Nanostructured Materials: Processing Properties and Potential Applications*, ed. C.C. Koch (Norwich, NY: William Andrew, 2001), pp. pages.
2. J. Schiøtz and K.W. Jacobsen, *Science,* 301 (2003), p. 1357.
3. H. Van Swygenhoven et al., *Phys. Rev. B,* 60 (1999), p. 22.
4. V. Yamakov et al., *Nature Materials,* 1 (2002), p. 1.
5. M.A. Meyers and K.K. Chawla, *Mechanical Behavior of Materials* (New York: Prentice Hall, 1998).
6. R.A. Lebensohn and C.N. Tomé, *Acta Metall. Mater.,* 41 (1993), 2611.
7. H.H. Fu, D.J. Benson, and M.A. Meyers, *Acta Mater.,* 52 (2004), 4413.
8. B. Jiang and G.J. Weng, *J. Mech. Phys. Solids,* 52 (2004), p. 25.
9. A.C. Lund and C.A. Schuh, *Acta Mater.,* 53 (2005), 3193.
10. B. Remington et. al., *Met. Mat. Trans. A,* 35 (2004), p. 2587.
11. T.R. Dittrich et al., *Laser and Particle Beams,* 17 (1999), p. 217.
12. J.D. Colvin et al., *J. Appl. Phys.,* 93 (2003), p. 5287.
13. O.E. Jones and J.R. Holland, *Acta Metall.,* 16 (1968), p. 1037.
14. L. Chhabildas and J. Asay, *J. Appl. Phys.,* 50 (1979), p. 2749.
15. K.T. Gagahan et al., *Phys. Rev. Lett.,* 85 (2000), p. 3205.
16. N.K. Bourne et al., *Proc. Royal Soc. London A,* 446 (1994), p. 309.
17. M.A. Meyers and M.S. Carvalho, *Mat. Sci. Eng.,* 24 (1976), p. 131.
18. M.A. Meyers, *Mat. Sci. Eng.,* 30 (1977), p. 99.
19. D.J. Benson, *Wave Motion,* 21 (1995), p. 85.
20. K. Yano and Y. Horie, *Phys. Rev. B,* 59 (1999), p. 13672.
21. R.C. Cook, *Fusion Sci. Technol.,* 41 (2002), p. 155.
22. J.D. Clayton, *J. Mech. Phys. Sol.,* volume number (2004), p. beginning page number.
23. Z. Zhao, R. Radovitzky, and A. Cuitino, *Acta Mater.,* 52 (2004), p. 5791.
24. E.M. Bringa et al., *J. Appl. Phys.,* 96 (2004), p. 3793.
25. D.S. Ivanov et al., *Shock Compression of Condensed Matter-2003*, ed. M.D. Furnish, Y.M. Gupta, and J.W. Forbes (New York: APS, 2004), pp. 225–228.
26. P.K. Schelling, S.R. Phillpot, and P. Keblinski, *J. Appl. Phys.,* 95 (2004), p. 6082.
27. MDCASK: *http://www.llnl.gov/asci/purple/benchmarks/limited/mdcask/*
28. Y. Mishin et al., *Phys. Rev. B,* 63 (2001), p. 224106.
29. C.L. Kelchner, S.J. Plimpton, and J.C. Hamilton, *Phys. Rev. B,* 58 (1998), p. 11085.
30. L. Holian and P.S. Lomdahl, *Science,* 280 (1998), p. 2085.
31. K. Kadau et al., *Science,* 296 (2002), p. 1681.
32. F.A. Sapozhnikov, V.V. Dremov, and M.S. Smirnova, *J. Phys. IV France,* 110 (2003), p. 323.
33. E.M. Bringa et al., submitted to *Science* (2005).
34. A. Molinari and G. Ravichandran, *J. Appl. Phys.,* 95 (2004), p. 1718.
35. J.K. Krüger et al., *Diamond and Related Mat.,* 9 (2000), p. 123.
36. Yu.I. Mescheryakov, N.A. Mahutov, and S.A. Atroshenko, *J. Mech. Phys. Solids,* 42 (1994), p. 1435.
37. M. Hauer et al., *Thin Solid Films,* 453 (2004), p. 584.

*E.M. Bringa, A. Caro, and M. Victoria are with Lawrence Livermore National Laboratory in Livermore, California. N. Park is with Atomic Weapons Establishment in Berkshire, U.K.*

**For more information, contact E.M. Bringa, Lawrence Livermore National Laboratory, 7000 East Avenue, Livermore CA 94550, USA; (925) 423-5724; fax (925) 422-4665; e-mail ebringa@llnl.gov.**

## E.2 Molecular dynamics simulations of the Debye-Waller effect in shocked copper

This work is being undertaken as part of an experimental campaign, led by Justin Wark at Oxford University, to develop lattice–level diagnostic tools for shock driven experiments. One of the most pertinent questions relating to shock physics, and which is vital to connecting much macroscale continuum theory to experimental measurements is the determination of temperature in dynamically loaded systems (i.e. both shock compressed and ramp compressed samples).

In the room pressure field of crystallography it is known that the effect of temperature on x-ray diffraction can be accounted for through the Debye–Waller factor. This paper sets out the experimental possibility of using this knowledge, by examining the line broadening caused by increased thermal motion of the atoms, by which the measurement of temperature at these extreme conditions may be accomplished. However, two aspects need to be considered. Firstly, as the paper shows, the current experimental capability is only at the cusp of realising this goal, and difficulties remain to be solved. Secondly, some form of calibration, or estimate of precision rather, is needed. It has been shown that MD can be used in the simulation of shock experiments, coupled with Fourier analysis (see section E.3), to give an indication of expected experimental results.

Whereas Murphy carried out this analysis work as part of his own PhD thesis, the present author assisted by carrying out multi-million atom simulations which were used to reduce the errors produced by carrying out Fourier transforms on small datsets.

PHYSICAL REVIEW B **78**, 014109 (2008)

# Molecular dynamics simulations of the Debye-Waller effect in shocked copper

William J. Murphy,* Andrew Higginbotham, and Justin S. Wark
*Department of Physics, Clarendon Laboratory, University of Oxford, Parks Road, Oxford OX1 3PU, United Kingdom*

Nigel Park
*Material Modelling Group, AWE, Aldermaston, Reading, Berkshire RG7 4PR, United Kingdom*
(Received 31 March 2008; published 23 July 2008)

We present an analysis of the directionally dependent x-ray structure factors (and, hence, intensities) predicted by nonequilibrium molecular dynamics simulations of statically compressed and shocked single crystals of copper, and comment on the feasibility of using experimentally measured intensities to infer temperature information. We further consider the behavior of the diffracted intensity from isentropically compressed samples.

DOI: 10.1103/PhysRevB.78.014109 PACS number(s): 61.05.cp, 62.50.Ef, 64.30.Ef

## I. INTRODUCTION

The use of x-ray diffraction to interrogate the structure of shocked crystals on subnanosecond time scales is now a well-established technique, with recent experimental results providing some information on upper time limits necessary for plastic flow within various materials,[1] as well as on the underlying mechanisms of the widely studied shock-induced $\alpha$-$\epsilon$ transition in laser-compressed single crystals of iron.[2] In parallel with the development of short-time-scale shock and diffraction experiments, the prediction of the response of matter to shock compression by means of nonequilibrium molecular dynamics (NEMD) simulations has been a burgeoning field, with a similar concentration of interest in shock-induced plasticity[3,4] and phase transitions.[5,6] With the rapid increase in computing power and storage over recent years, the length and time scale of such simulations are now starting to become directly comparable with those of the laser shock-compression experiments. The simulation of crystals with spatial dimensions of a reasonable fraction of a micron for durations of hundreds of picoseconds are now quite feasible, if not entirely routine. This convergence of scales has understandably led to direct comparisons being made between the x-ray diffraction patterns predicted by the NEMD simulations and those directly observed in experiments. For example, Bringa *et al.*[7] recently used NEMD simulations to calculate the shift in both the Bragg (reflected) and Laue (transmitted) peaks in shock-compressed copper. Their work provided information on the time-dependent shape of the unit cell of a sample of shocked copper, which in turn offers insight into plastic flow. Hawreliak *et al.*[8] directly compared the diffraction patterns predicted by NEMD with the experimental data for the $\alpha$-$\epsilon$ transition in shocked iron, noting, among many other things, good agreement between the predicted x-ray linewidths in the $\epsilon$ phase and those seen experimentally—an observation which is consistent with the predicted mean size of two families of crystallites with orthogonal $c$ axes.

However, while diffraction patterns have been simulated by use of NEMD calculations, to date an analysis of them has largely concentrated on the position or width of the diffraction peaks, rather than explicitly their intensity. The intensity of diffracted radiation associated with a particular Bragg peak (i.e., set of Miller indices) relative to the intensity diffracted from an uncompressed sample will be a function of the local structure factor of the crystal, and this structure factor can be significantly altered by the action of shock compression of the crystal. In particular, the reflectivity will alter both due to the shock-induced temperature rise and the compression. This temperature rise will influence the intensity of a particular reflection owing to the well-known Debye-Waller effect[9] as the increase in temperature results in a larger rms displacement of a particular atom around its mean position. However, the Debye-Waller factor is also a function of the effective Debye temperature $\Theta$, and we note that under compression $\Theta$ will also change. For example, one might normally expect compression to steepen the potential, with a resultant increase in the effective Debye temperature, which will tend to reduce the rms displacement of the atoms. Such an increase in the effective Debye temperature would tend to increase the structure factor at finite temperatures; thus, the relative intensity of a particular Bragg reflection is not entirely trivial to calculate.

In this paper we present an initial analysis of NEMD calculations of the effect of shock compression on the expected intensities of Bragg reflections. We present the analysis in terms of effective Debye temperatures predicted by the NEMD for uniaxially compressed, hydrostatically compressed, and shock-compressed single crystals of copper, and compare these results with those predicted by analytic means. Given that the x-ray reflectivity is a function of temperature, we comment on the feasibility of using reflectivities as a temperature diagnostic of shocked crystals. Finally, as rapid isentropic compression is an area of great topical interest, we discuss the expected behavior of the relative x-ray intensities of crystals subject to such loading, noting that the x-ray reflectivity of higher diffraction orders can actually increase under these conditions.

## II. DEBYE-WALLER FACTOR

In the absence of phase transitions (which we do not consider here), the main factor that will alter the relative intensity of the angularly integrated x-rays within a given peak will be the Debye-Waller factor, which is a function of both

 

the temperature $T$ and the effective Debye temperature $\Theta$. The overall intensity of a particular reflection is a function of many factors, including the degree of perfection of the crystal. For a perfect crystal we must use dynamical diffraction theory, whereas for completely imperfect crystals the kinematic approximation must be used.[10] In each case, however, the influence of a shock is twofold: first, the positions of the peaks are altered, as the change in lattice spacing results in a change in Bragg angle. For small one-dimensional compressions, the change in the position of a particular peak is given by a simple differentiation of Bragg's law,

$$\Delta\theta = -\tan\theta\frac{\Delta(2d)}{2d}, \tag{1}$$

where $\theta$ is the Bragg angle associated with the plane of spacing $d$. For large compressions, we must recalculate the angular position of the peak from the full form of Bragg's law; but in any case such a calculation is trivial and finding the location of a particular reflection in the case where compression occurs along all three orthogonal directions (for example, as a crystal changes from elastic toward hydrostatic conditions under shock compression) is also not difficult.

The intensity of the peak, however, will depend on the structure factor. Within the Debye-Waller theory, for a reciprocal lattice vector $\mathbf{G}$, the structure factor $S_{\mathbf{G}}^{T}$ at a temperature $T$, is given by

$$S_{\mathbf{G}}^{T} = S_{\mathbf{G}}^{0}\exp(-M), \tag{2}$$

where $S_{\mathbf{G}}^{0}$ is the structure factor for the perfect, unheated lattice, which is the sum over atoms at positions $\mathbf{r}_i$ of the atomic form factors $f_i$ over all atoms in the unit cell,

$$S_{\mathbf{G}}^{0} = \sum_i f_i \exp(-i\mathbf{G}\cdot\mathbf{r}_i). \tag{3}$$

Note that for the compressions we consider here, there should be no change in the atomic form factor: we are not dealing with conditions such that pressure ionization occurs. The atomic form factor is, however, angularly dependent, and this should be taken into account when calculating real intensities. The temperature dependence enters into the factor $M$ in Eq. (2). In the kinematic limit the intensity $I$ of a particular reflection is proportional to the square of the structure factor, and thus,

$$I(T) = I(0)\exp(-2M), \tag{4}$$

where

$$2M = \frac{3h^2N_A|\mathbf{G}|^2}{mk_B\Theta}\left[\frac{T}{\Theta}\Phi\left(\frac{\Theta}{T}\right)+\frac{1}{4}\right], \tag{5}$$

and

$$\Phi(y) = \frac{1}{y}\int_0^y \frac{x}{e^x-1}dx. \tag{6}$$

$T$ is the temperature in kelvin, $h$ is Planck's constant, $N_A$ is Avogadro's number, $m$ is the atomic mass, and $k_B$ is Boltzmann's constant. For the sake of brevity, as we are only presenting the simple Debye theory for reasons of illustration, we have assumed an isotropic solid, which is also valid for a cubic system due to the manner in which the resolved displacement is summed. In an anisotropically compressed crystal, there will be a directional dependence.

In the normal Debye theory the function $\Phi(y)$ takes into account that the phonon modes in the crystal are populated according to Bose–Einstein statistics, and the factor of 1/4 in Eq. (5) takes into account zero-point motion. Clearly in classical NEMD calculations such as those we present here, this is not appropriate, and the vibrational modes present within the simulation obey Boltzmann statistics. In the simulations in this paper we calculate the effect of compression and temperature on Bragg reflections by calculating the Fourier transform of the atomic coordinates provided by the NEMD simulations. Integration in reciprocal space around particular Bragg reflections provides a relative measure of the x-ray structure factor for the reflection in question, and the variation of this integral with reciprocal lattice vector for a particular temperature can be used to deduce an effective Debye temperature. As the NEMD simulations are classical, when quoting an effective Debye temperature, it will be related to the exponential falloff in integrated intensity by

$$2M = \frac{3h^2N_A|\mathbf{G}|^2}{mk_B\Theta}\left[\frac{T}{\Theta}\right]. \tag{7}$$

## III. ANALYTIC CALCULATIONS

The main thrust of this paper is to use NEMD simulations as a tool to investigate how the intensity of x-rays diffracted by crystals is affected by temperature and compression. However, both as a comparison with NEMD simulations and as a tool in its own right, we can also use analytic models based on previously published forms of the Grüneisen parameter to predict the manner in which compression affects the Debye temperature. The Grüneisen parameter $\Gamma$ used in the Grüneisen equation of state is defined as

$$\Gamma(V) = -\frac{\partial\ln\Theta}{\partial\ln V}, \tag{8}$$

and thus,

$$\frac{\Theta}{\Theta_0} = \exp\left(-\int_{V_0}^{V}\frac{\Gamma(V)}{V}dV\right), \tag{9}$$

where $V$ is the volume.

We investigate four different forms of $\Gamma(V)$ for copper. The simplest model is to assume that $\Gamma/V$ is constant.[11,12] More generally, the Grüneisen parameter can be expressed as a power of the volume. Pandya *et al.*[13] used a theoretical model based in perturbation theory taking into account terms due to the atomic orbitals of the material. Ramakrishnan *et al.*[14] gave an empirical result based on measuring how the temperature of a sample is affected by adiabatic pressure changes. The compressions used in that study were low compared with the regime normally probed by shock experiments. These three models can be summarized as all being of the form

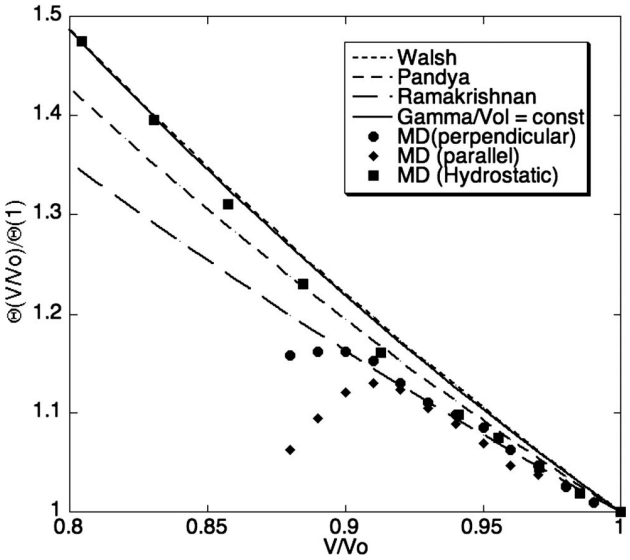


FIG. 1. Debye temperature as a function of compression calculated from MD and analytic models. The lines represent the analytic models from literature, and the points represent the results from MD simulations of the hydrostatic and uniaxial case (compressed along [001]). Results parallel and perpendicular to the compression direction are shown separately.

$$\Gamma(V) = \Gamma_0 \left( \frac{V}{V_o} \right)^q, \tag{10}$$

with the following values of $\Gamma_0$ and $q$ for copper: ($\Gamma_0 = 1.98$, $q = 1.0$),[11,12] ($\Gamma_0 = 1.93$, $q = 1.085$),[13] and ($\Gamma_0 = 2.008$, $q = 1.33$).[14]

The fourth model which we shall consider is that provided by Walsh *et al.*,[15] who used experimental Hugoniot data in conjunction with the Mie–Grüneisen equation of state to deduce a polynomial fit for the Grüneisen parameter as a function of volume,

$$\Gamma(V) = \Gamma_0 + A\left( \frac{V_o}{V} - 1 \right) + B\left( \frac{V_o}{V} - 1 \right)^2 + C\left( \frac{V_o}{V} - 1 \right)^3, \tag{11}$$

where for copper they found $\Gamma_0 = 2.04$, $A = -3.296$, $B = 10.493$, and $C = -19.264$. We note that Walsh *et al.*[15] performed experiments on long time scales compared with the NEMD calculations, and the Hugoniot elastic limit (HEL) of copper was small compared with the pressures of interest; thus, their Grüneisen parameter corresponds to that which one might expect for close to hydrostatic compression of the lattice.

The four models for the Grüneisen parameter are used to predict the Debye temperature as a function of hydrostatic compression. All four are plotted alongside the NEMD hydrostatic and uniaxial compression data in Fig. 1, and we discuss how they compare with NEMD predictions in Sec. IV.

## IV. MOLECULAR DYNAMICS CALCULATIONS

The intensity of x-rays scattered by a crystal (neglecting the effects of absorption and extinction) can be calculated from NEMD by taking the Fourier transform of the atomic coordinates at a particular moment in time. This gives the intensity in $k$ space, $I(\mathbf{k})$,

$$I(\mathbf{k}) = \left| \sum_j \exp(-i\mathbf{k} \cdot \mathbf{r}_j) \right|^2, \tag{12}$$

where now the sum is over all of the atomic positions in the simulation. For a particular experimental geometry, the overall structure factor associated with a given incident x-ray with wave vector $\mathbf{k}_0$ and a scattered x-ray with wave vector $\mathbf{k}_s$ can be found by using $\mathbf{k} = \mathbf{k}_0 - \mathbf{k}_s$. Note that Eq. (12) is a sum over specific coordinates; thus, we have not explicitly taken into account the dependence of the atomic form factor on scattering angle, but as this is tabulated[16] it can also be included in explicit intensity calculations if necessary. While fast Fourier transform techniques can do this Fourier transform over the whole of the meaningful region of $k$ space,[17] here we are only interested in the regions of intensity maxima surrounding specific Bragg reflections, and in this case it was computationally efficient to use a simple, rather than fast, Fourier transform. For all of the NEMD simulations presented here, the atomic coordinates were calculated using the MD code LAMMPS,[18] with the copper sample simulated using Mishin's EAM1 potential.[19]

### A. Debye temperature: Uncompressed sample

In the simple Debye theory the Debye temperature itself is independent of temperature. As a first test of the predictions of the NEMD simulations, we calculated the Fourier transform of the atomic positions of an uncompressed sample at different temperatures and calculated the Debye temperature from the predicted x-ray reflectivities (i.e., from the relative integrated intensity of the Bragg peaks in reciprocal space). A $60 \times 60 \times 60$ conventional cell sample of copper with lattice parameter $a = 3.615$ Å was thermalized for 10 ps with periodic boundary conditions at temperatures T = 300, 600, 900, and 1200 K.

According to Eq. (5) we expect that the logarithm of the integrated intensity is proportional to $(-|\mathbf{G}|^2 T/\Theta^2)$. Thus, in Fig. 2 we plot the logarithm of the integrated intensity of the Bragg peaks as a function of $|\mathbf{G}|^2$ for a variety of temperatures, and the gradient of this line provides the Debye temperature. From this (Fig. 2) a value for the Debye temperature was calculated (see Table I). The average agrees well with literature values, indicating the applicability of the Mishin potential. The calculated Debye temperature decreases slightly as the temperature of the sample is increased. This is possibly due to the atoms exploring further into the anharmonic region of the potential as the temperature is increased.

### B. Uniaxially compressed samples

To date NEMD simulations of the shock compression of single metal crystals predict elastic limits far higher than

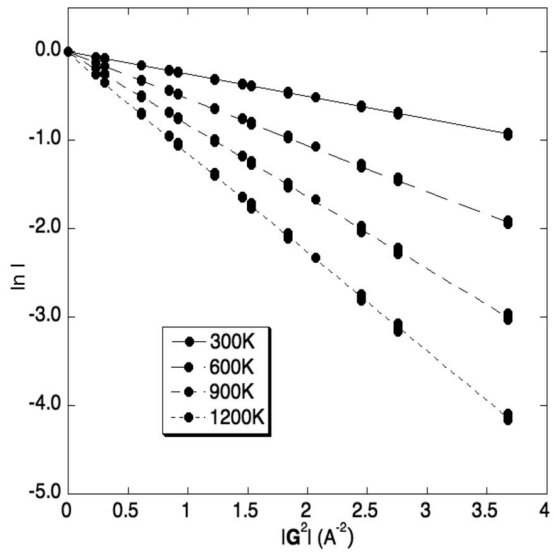


FIG. 2. MD simulations of the relative intensity of diffracted peaks as a function of reciprocal lattice vector for an uncompressed copper crystal.

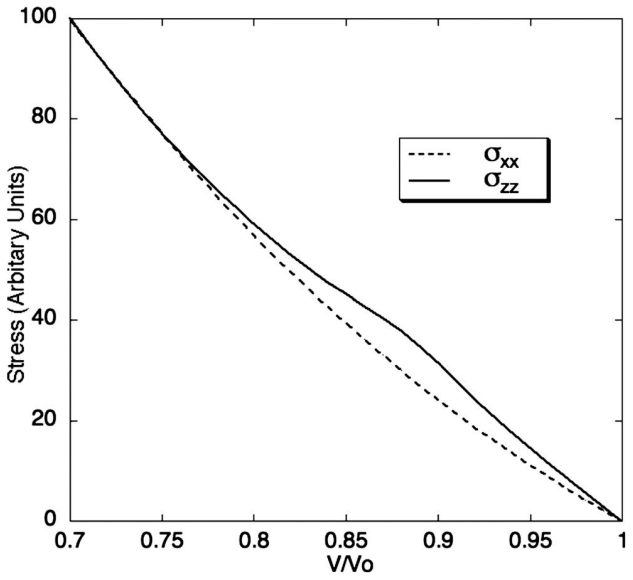


FIG. 3. Stress along the $x$ axis ($\sigma_{xx}$) and the $z$ axis ($\sigma_{zz}$) calculated from NEMD simulations of low-temperature Cu for compression along the [001] direction.

those seen in the majority of experiments. Indeed, the elastic limits are consistent with the theoretical limiting shear strength of a solid under compression and are typically up to 2 orders of magnitude higher than seen in long-time-scale (hundreds of nanoseconds) experiments. For example, in the work of Bringa *et al.*,[7] when a single crystal of copper simulated with the Mishin potential is shocked along the principal axis, completely elastic compression is seen up to compressions of order 15%, corresponding to pressures of order 350 kbar. While the addition of defects and a ramped pressure drive can somewhat reduce this value,[7] it is clear that at present NEMD simulations predict that very high elastic response can be observed on short time scales. We note also that for bcc crystals of iron, close to purely elastic response has been observed experimentally up to compressions of 6%,[20] in agreement with NEMD calculations.[21]

Thus, before simulating the change in intensities due to shock compression, in this section we consider how uniaxial elastic compression along a cube axis of a copper single crystal alters the calculated x-ray reflectivities. As in Sec. IV A, 864 000 atoms were taken, and for a variety of uniaxial compressions up to 12%, thermalized at 300 K. The crystal was compressed along the [001] axis, and the integrated reflectivities of Bragg spots in $k$ space were calculated for the reflections corresponding to directions both along and perpendicular to the compression axis. From the variation of reflectivity with the square of the reciprocal lattice vector, a Debye temperature was again calculated. The Debye temperatures for the directions parallel and perpendicular to the compression are shown in Fig. 1, where they have been normalized to the Debye temperature for the uncompressed case discussed above. We note that, as expected with a steepening of the potential under compression, the Debye temperature increases roughly linearly under compression.

TABLE I. The Debye temperature calculated from samples thermalized at different temperatures.

| $T/K$ | $\Theta/K$ |
|---|---|
| 300 | 322 |
| 600 | 321 |
| 900 | 316 |
| 1200 | 310 |
| Average | 317 |
| Literature | 315 |

It can be seen, however, that for compressions above about 9%, there is a radical change in the Debye temperatures. Above this point the Debye temperature reduces with compression along the compression direction, such that above 11% compression it is significantly lower in the compression direction than in the orthogonal direction. This is counterintuitive as one might expect that constraining the atoms in one direction would increase the effective Debye temperature for that direction.

This more complex behavior of the Debye temperatures is due to the effect of the Bain path. It is well known that uniaxial compression of a face-centered-cubic lattice along the [001] direction by a factor of $1/\sqrt{2}$ leads to a body-centered-cubic lattice, for which the shear stress must be zero. The stresses in the compression direction, $\sigma_{zz}$, and in the orthogonal direction, $\sigma_{xx}$, as a function of uniaxial compression along the $z$ direction are shown in Fig. 3. These results were determined for a $10\times10\times10$ conventional unit cell sample simulation compressed in a canonical ensemble at $5\times10^{-5}$ K to make temperature effects negligible and prevent shear relaxation by dislocations. As expected, the stresses are equal at the volume at which the lattice becomes body-centered-cubic. Between this point and zero compression, the stress in the compression direction is higher than that in the orthogonal direction, as expected. However, the

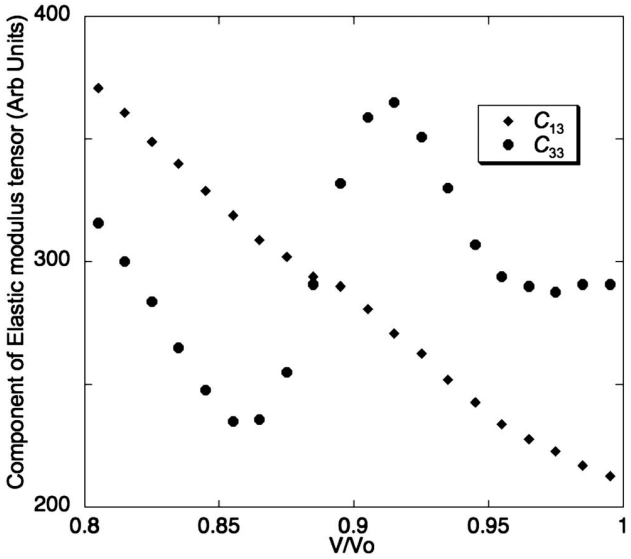


FIG. 4. $C_{11}$ and $C_{33}$ components of the elastic modulus tensor as a function of compression deduced from gradients of Fig. 3.

Mishin potential predicts that while the gradient of $\sigma_{xx}$ increases monotonically with compression along the $z$ direction, this is not the case for $\sigma_{zz}$. From these gradients we calculate the $C_{13}$ and $C_{33}$ components of the elastic modulus tensor. As cubic symmetry is lost on uniaxial compression, there are more than three independent terms in this tensor. In Fig. 4 we plot these elastic modulus terms as a function of uniaxial compression along $z$. It is evident that the maximum in the stiffness in the $z$ direction occurs at the same compression as the maximum in the Debye temperature deduced from the integration of the intensities in $k$ space.

### C. Hydrostatically compressed samples

At high shock compressions of face-centered-cubic perfect single crystals, NEMD simulations predict the homogeneous generation of defects at the shock front, the motion of which can alleviate the shear stress. This results in the lattice tending toward the hydrostatic state, although the strength of the material may support some residual shear stress and prevent it from becoming completely hydrostatic. It should be noted that this remains an area of active interest: the mechanism of defect generation and motion has been predicted to be a function of the direction of shock compression. Compression of single crystals along the [001] direction activates a partial dislocation resulting in a stacking fault; in contrast compression along the [111] direction results in full dislocations via two partial loops.[22] In any case, for perfect crystals the elastic limit is extremely high compared with values found experimentally on longer time scales. As noted in Sec. IV B, Bringa *et al.*[7] showed that pre-existing defects can reduce the effective elastic limit, although no simulation has yet been performed that reproduces the comparatively low elastic limits seen in long-time-scale experiments.

However, in any case the generation and motion of the defects acts so as to remove the shear stress, and the lattice which is initially tetragonal with a large aspect ratio under elastic compression tends more toward a compressed cube as the shear stress is released and the hydrostat approached.[23] It is thus of interest to use the NEMD simulations to calculate the effective x-ray Debye temperatures for hydrostatically compressed samples. These Debye temperatures, deduced by identical means to those outlined in Sec. IV A, are shown alongside analytically fitted Grüneisen parameters in Fig. 1. It can be seen that these more closely follow the higher compression Grüneisen parameter predictions, and reasonable agreement with the analytic model based on experimental data of Walsh *et al.*[15] is seen for larger compressions.

### D. Shock-compressed samples

Under shock compression we not only expect the Debye temperature to change, but we also expect a rise in temperature. We stress that as these simulations have been performed with shock compression of a perfect copper crystal along the [001] axis, stacking faults are not generated at the shock front until compressions in excess of 15%.

The simulated sample was a $30\times30\times130$ conventional cell crystal oriented with the principal axis along $x$, $y$, and $z$ with periodic boundary conditions in the $x$ and $y$ directions and shrink wrapped boundary in the $z$ direction. This was thermalized to 293 K to match the experimental parameters of Walsh *et al.*[15] To generate the shock all atoms within five lattice parameters of $z=0$ were fixed together and then driven as a unit into the crystal in the positive $z$ direction at the desired shock speed ($U_p$=108, 181, 362, 542, 651, 687, and 723 ms$^{-1}$). A $30\times30\times30$ conventional unit cell section situated 80 conventional cells behind the shock front when it reached the other end of the crystal was used to calculate the corresponding reciprocal space intensity.

We note that the samples considered here, which were initially thermalized to room temperature, predict an increase in the diffracted intensity for higher-order reflections for low shock compressions. Only once we reach compressions of between 7% and 10% do we start to observe a decrease in the diffracted intensity. Physically this corresponds to the constraining of the atoms by the increased steepness of the potential under compression being more important than any temperature rise associated with the compression. As the Hugoniot for a weak shock lies very close to the isentrope, we shall return to this point when we discuss isentropic compression in Sec. V.

The data of Walsh *et al.*[15] described in Sec. III can also be used to predict the change in intensity under shock compression, as Walsh *et al.* also used the experimental data to predict the temperature rise as a function of shock compression, as well as the compression-dependent Grüneisen parameter. The falloff in diffracted intensity as a function of the relative volume according to the data of Walsh *et al.* is shown for copper in Fig. 5, alongside the NEMD predictions. It can be seen that the model of Walsh *et al.* exhibits qualitatively the same response as the NEMD shock simulations.

Shocking the sample to a point above the Hugoniot elastic limit generated a large number of dislocations. These have the effect of broadening the peaks in reciprocal space, particularly the higher-order peaks (see Fig. 6). To calculate the

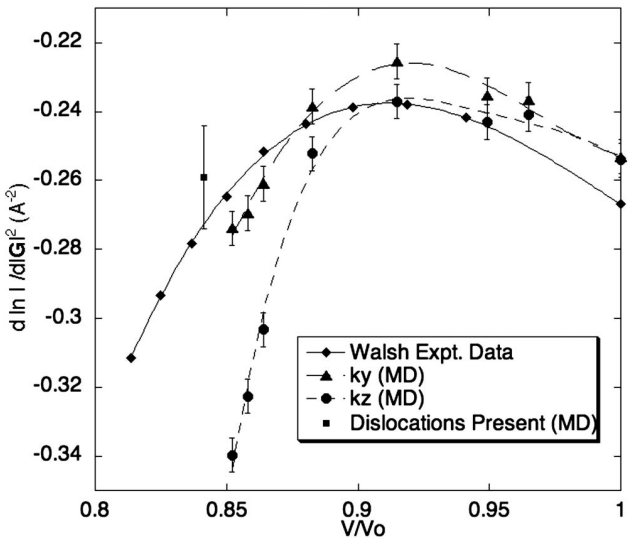


FIG. 5. Exponent of the Debye-Waller factor per reciprocal vector squared ($-2M/|\mathbf{G}|^2$) for copper shocked to $V/V_o$ times its original volume, calculated from MD simulations of single crystals shocked along the principle axis and from data of Walsh *et al.* (Ref. 15).

intensity in reciprocal space, a $1.9\times10^6$ atom block was taken from the shocked region and the Fourier transform of the atomic coordinates calculated. Integrating over the resultant Bragg peaks and subtracting the background gives a result close to the prediction based on the figures of Walsh *et al.*[15] (the data point labeled "Dislocations Present" in Fig. 5). Due to the relaxation of the shear stress by the generation and motion of the dislocations, there is no noticeable directional dependence in the Debye-Waller factor within the error bars.

### E. Strong-shock limit

In the strong-shock regime, where the velocity of the plastic wave exceeds that of the elastic wave it is usually found

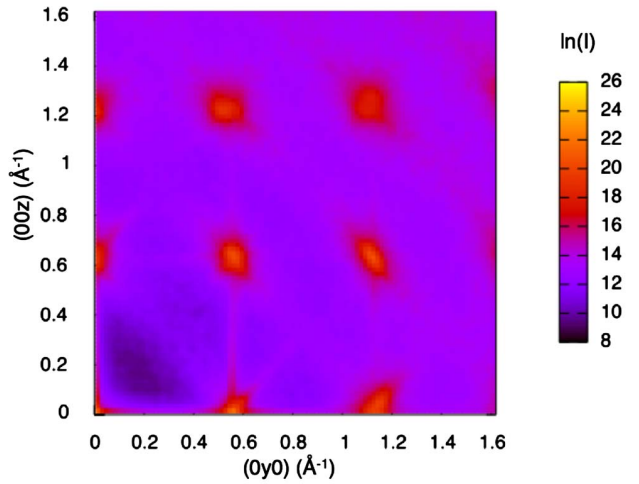


FIG. 6. (Color online) Intensity in the plane in $k$ space corresponding to the [100] plane intersecting with the origin for a MD simulation of a shock in the [001] direction to above the Hugoniot elastic limit (HEL).

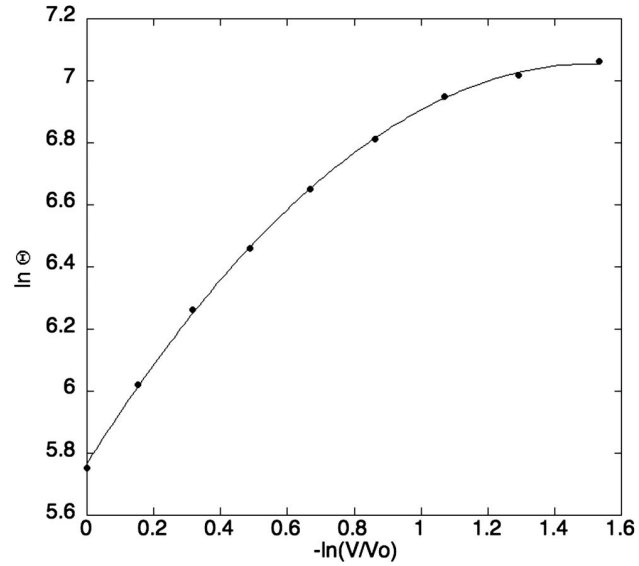


FIG. 7. Log-log plot of Debye temperature vs compression for MD simulated copper sample compressed hydrostatically fitted with a polynomial. The gradient gives the Grüneisen parameter.

that the shock speed $U_s$ is related to the particle velocity $U_p$ by

$$U_s = C_0 + s_1 U_p, \tag{13}$$

where $s_1$ is a constant and $C_0$ is close to the bulk sound speed. It can be shown that the Grüneisen parameter is a function of the volumetric compressive strain, $\epsilon=1-V/V_0$, and $s_1$, such that in the limit of $\epsilon=0$, $\Gamma=2s_1-1$.[23,24] Furthermore, the observation that $s_1$ is a constant for strong shocks implies that there is a limit to the compression,[25] $\epsilon=1/s_1$, and that at this limiting compression $\Gamma=2(s_1-1)$. Therefore at the limiting compression under shock conditions, the Grüneisen parameter is exactly 1 less than under ambient conditions.

In order to test how well the Debye temperatures deduced from the NEMD obey the above relations, we plotted $\Theta$ as a function of hydrostatic compression, as shown in Fig. 7. The atomic coordinates were generated by setting up an ideal $60\times60\times60$ conventional cell crystal already compressed by decreasing the lattice parameter and then thermalizing this to 300 K.

The data were fitted with a polynomial

$$\ln(\Theta) = A[-\ln(V/V_0)]^2 + B[-\ln(V/V_0)] + C, \tag{14}$$

which yielded the coefficients $A=-0.56\pm0.01$, $B=1.71\pm0.03$, and $C=5.76\pm0.02$. This upon differentiation yields

$$\Gamma = -\frac{d\ln(\Theta)}{d\ln(V/V_0)} = -2A\ln(V/V_0) + B. \tag{15}$$

Thus, for $\epsilon=0$, we deduce $\Gamma=1.71\pm0.03$, which we note is in reasonable agreement with the analytic Grüneisen coefficients discussed in Sec. III, and experiments give a value of $s_1=1.489$,[23] which implies $\Gamma=1.98$. This experimental value of $s_1$ implies a limiting compression of 0.67. If we solve Eq.

(15) for $\Gamma=0.71$, i.e., 1 less than the value under ambient conditions, we deduce a limiting compression of $0.59\pm0.03$, which is lower than the experimental figure, but it should be noted that this is a very high compression, and we would not necessarily expect the potential used in the NEMD to be valid at the high shock pressures necessary to asymptote toward this value.

## V. ISENTROPIC COMPRESSION

The possibility of compressing a crystal along an isentrope, via ramped compression, has attracted considerable attention in recent years,[26,27] as such a technique may allow the creation of solid state matter at compressions far in excess of those achievable in diamond anvil cells.

Given the growing interest in isentropic compression on short time scales and the stated desire by some workers to diagnose the lattice compressed in such a way via x-ray diffraction, it is clearly of relevance to explore how we would expect the Debye-Waller factor to behave under such conditions. In this section we show that very simple considerations indicate that for a sample compressed at finite temperature, we would actually expect an increase in the intensity of the higher-order diffraction peaks.

Let us consider a simple model of a solid, where we take the Grüneisen parameter to be constant. In such a model

$$\frac{\Theta}{\Theta_0}=\left(\frac{V}{V_0}\right)^{-\Gamma}, \tag{16}$$

and along an isentrope

$$\frac{T}{T_0}=\left(\frac{V}{V_0}\right)^{-\Gamma}. \tag{17}$$

If $\mathbf{G}_0$ is the reciprocal lattice vector of a particular reflection under ambient conditions, then $\mathbf{G}=\mathbf{G}_0(V/V_0)^{-1/3}$ for hydrostatic compression. Now the exponent in the Debye-Waller factor $M$ scales as

$$M\propto\frac{|\mathbf{G}|^2T}{\Theta^2}\propto\frac{|\mathbf{G}_0|^2T_0}{\Theta_0^2}\left(\frac{V}{V_0}\right)^{[\Gamma-2/3]}, \tag{18}$$

and thus

$$\frac{M}{M_0}=\left(\frac{V}{V_0}\right)^{[\Gamma-2/3]}. \tag{19}$$

Thus, as $\Gamma>2/3$, we find that $M$ decreases under compression, and as the intensity of a Bragg peak is proportional to $\exp(-2M)$ in the kinematic limit, at finite temperatures we expect an increase in diffracted intensity under isentropic compression.

The physical reason for this increase in reflectivity is that under isentropic compression the increase in the stiffness of the lattice is a more important effect than the temperature rise. For, although the thermal energy of an atom is increased, the rms amplitude of its vibration not only decreases in absolute terms, but, importantly for the intensity of diffracted radiation, actually decreases as a fraction of the lattice spacing even though the lattice is being compressed. For small compressions the shock adiabat lies close to the isentrope, and thus we would expect that for small shock compressions, starting at finite temperature, there is actually an increase in the reflectivity of higher-order reflections. For the case of copper here, only once the compression due to the shock exceeds ~10% does the increase in temperature start to dominate over the increased strength of the lattice and the structure factor start to decrease. This effect can also be seen in Fig. 5.

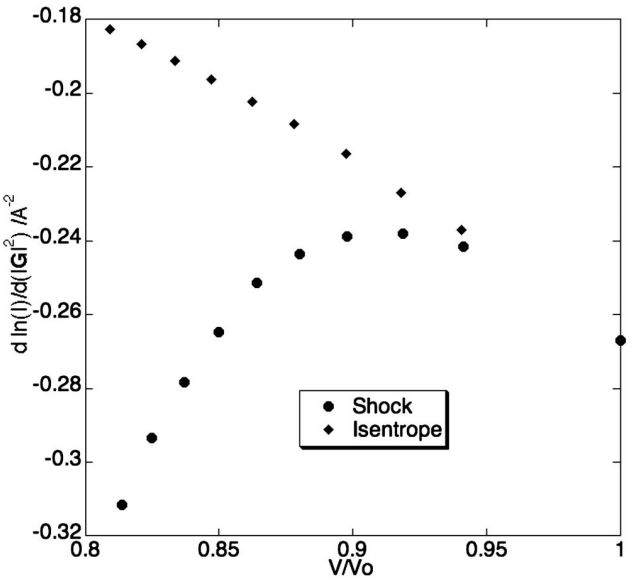


FIG. 8. Exponent of Debye-Waller factor per reciprocal vector squared for copper compressed via shock compression (circles) and isentropic compression (squares). Values are calculated from data of Walsh *et al.* (Ref. 15).

Walsh *et al.*[15] used a Mie–Grüneisen equation of state to calculate isentropic figures for temperature and compression. By using these, the Debye temperature can be calculated and the Debye-Waller factor deduced (see Fig. 8). These agree with our prediction that the intensity of the diffracted signal increases the more the material is compressed isentropically.

## VI. RELATION TO EXPERIMENTS

Given that x-ray diffraction experiments on picosecond and nanosecond time scales are currently being performed, it is useful to consider to what degree the effects discussed above may be observable experimentally. Our analysis has concentrated on the degree to which the Debye-Waller factor is altered by shock compression, insomuch that the temperature of the lattice changes, but so also does its effective Debye temperature. As the Debye-Waller factor $M$ is proportional to the square of the reciprocal lattice vector, it is evident that the effects will be most apparent for high-order reflections, which in turn require high-energy, short-wavelength x-rays in order to be observed.

In the field of laser-plasma interactions, where much of the work on time-resolved diffraction from shocked samples is being performed, x-rays of durations ranging from a few tens of picoseconds to several nanoseconds can be produced

by focusing high power optical radiation to intensities of order $10^{14}-10^{16}$ W cm$^{-2}$ onto solid targets. In such experiments, the x-rays are emitted from transitions within highly ionized atoms; and typically in the past the resonance line of helium-like ions has been used. Given the laser energies and intensities available with the systems that have been used for shock compression and diffraction experiments, the highest photon energies used to date correspond to the helium resonance line of copper at 8.4 keV (although it has been shown that this could be extended to the resonance line of He-like Ge).[28]

On the other hand, in the picosecond and subpicosecond regime, the huge intensities that can be produced $>10^{18}$ W cm$^{-2}$ induce the excitation and breaking of plasma waves, resulting in short bursts of energetic electrons penetrating the underlying target, producing a short burst of $K\alpha$ emission in an analogous manner to a conventional x-ray tube. It has been shown that such techniques can readily produce *K*-shell radiation up to 22 keV.[29] With such radiation sources, in principle at least, it should be possible to record reflections from copper crystals with Miller indices up to $\sqrt{h^2+k^2+l^2}$ of order 12. For an unshocked sample at room temperature, assuming a Debye temperature of 315 K, we would expect the intensity of such orders to be 2.8% of the (002) reflections (taking into account the dependence of the atomic form factor on scattering angle). If copper was shocked to 0.8 times its original volume, the ratio of the (579) to the (002) peak would be almost 2.5 times less than would be expected for the uncompressed sample at room temperature.

For the case of distinguishing between isentropic and shock compression the figures are even more promising. Consider copper compressed to 0.8 times its original volume. If it is compressed isentropically, the ratio of the (579) peak to the (002) peak will be more than ten times larger than if it is shocked to the same compression.

It is clear that the temperature affects the intensity of the diffraction patterns markedly. The problem lies in separating this effect from the compression effect. The compression itself can be measured readily from the peak shift but the limiting factor is deducing what effect this has on the Debye temperature.

## VII. SUMMARY

The effect of temperature on the diffraction pattern of a shocked sample has been investigated through the use of NEMD and also by examining empirical and theoretical fits to the Grüneisen parameter from literature values. These two approaches give qualitatively similar results. It is apparent that the temperature has a significant effect on the intensity of the diffracted peak. However the effect is complicated by the effect of compression. This means that the Debye-Waller factor gives the combined effect of the temperature and Debye temperature. In order to isolate the temperature, the Debye temperature must first be deduced and this requires an accurate form for the Grüneisen parameter. Even without this parameter, the combined effect gives a figure for $(T/\Theta^2)$ which in itself may be interesting.

## ACKNOWLEDGMENTS

The authors gratefully acknowledge financial support from a number of organizations. W.J.M. is grateful for support from AWE Aldermaston. A.H. has been generously supported by Daresbury Laboratory under the auspices of the NorthWest Science Fund.

*william.murphy@physics.ox.ac.uk

[1] K. Rosolankova, J. S. Wark, E. M. Bringa, and J. Hawreliak, J. Phys.: Condens. Matter **18**, 6749 (2006).
[2] D. H. Kalantar *et al.*, Phys. Rev. Lett. **95**, 075502 (2005).
[3] Y. M. Gupta, J. Appl. Phys. **48**, 5067 (1977).
[4] B. L. Holian and P. Lomdahl, Science **280**, 2085 (1998).
[5] K. Kadau, T. C. Germann, P. S. Lomdahl, and B. L. Holian, Science **296**, 1681 (2002).
[6] K. Kadau, T. C. Germann, P. S. Lomdahl, R. C. Albers, J. S. Wark, A. Higginbotham, and B. L. Holian, Phys. Rev. Lett. **98**, 135701 (2007).
[7] E. M. Bringa, K. Rosolankova, R. E. Rudd, B. A. Remington, J. S. Wark, M. Duchaineau, D. H. Kalantar, J. Hawreliak, and J. Belak, Nat. Mater. **5**, 805 (2006).
[8] J. Hawreliak *et al.*, Phys. Rev. B **74**, 184107 (2006).
[9] P. Debye, Ann. Phys. **43**, 49 (1914).
[10] W. H. Zachariasen, *Theory of X-Ray Diffraction in Crystals* (Dover, New York, 2004).
[11] Z. H. Fang and L. R. Chen, J. Phys.: Condens. Matter **6**, 6937 (1994).
[12] H. Schlosser, P. Vinet, and J. Ferrante, Phys. Rev. B **40**, 5929 (1989).
[13] C. V. Pandya, P. R. Vyas, T. C. Pandya, and V. B. Gohel, Bull. Mater. Sci. **25**, 63 (2002).
[14] J. Ramakrishnan, R. Boehler, G. H. Higgins, and G. C. Kennedy, J. Geophys. Res. **83**, 3535 (1978).
[15] J. M. Walsh, M. H. Rice, R. G. McQueen, and F. L. Yarger, Phys. Rev. **108**, 196 (1957).
[16] J. Ibers and W. C. Hamilton, *International Tables for X-Ray Crystallography* (Kynoch, Birmingham, UK, 1974), Vol. IV.
[17] G. Kimminau, B. Nagler, A. Higginbotham, W. Murphy, J. Wark, N. Park, J. Hawreliak, D. Kalantar, H. Lorenzana, and B. Remington, AIP Conf. Proc., Hawaii, 2007, Vol. 955, p. 1251.
[18] S. Plimpton, J. Comput. Phys. **117**, 1 (1995).
[19] Y. Mishin, M. J. Mehl, D. A. Papaconstantopoulos, A. F. Voter, and J. D. Kress, Phys. Rev. B **63**, 224106 (2001).
[20] D. H. Kalantar *et al.*, Rev. Sci. Instrum. **74**, 1929 (2003).
[21] K. Kadau, T. C. Germann, P. S. Lomdahl, and B. L. Holian, Phys. Rev. B **72**, 064120 (2005).
[22] T. C. Germann, B. L. Holian, P. S. Lomdahl, and R. Ravelo, Phys. Rev. Lett. **84**, 5351 (2000).
[23] E. M. Bringa, J. U. Cazamias, P. Erhart, J. Stölken, N. Tanushev, B. D. Wirth, R. E. Rudd, and M. J. Caturla, J. Appl. Phys. **96**, 3793 (2004).

[24] D. S. Drumheller, *Introduction to Wave Propagation in Nonlinear Fluids and Solids* (Cambridge University Press, Cambridge, 1998).
[25] M. A. Meyers, *Dynamic Behavior of Materials* (University of California, Berkeley, 1994).
[26] R. F. Smith, S. M. Pollaine, S. J. Moon, K. T. Lorenz, P. M. Celliers, J. H. Eggert, H. S. Park, and G. W. Collins, Phys. Plasmas **14**, 057105 (2007).
[27] D. B. Reisman, A. Toor, R. C. Cauble, C. A. Hall, J. R. Asay, M. D. Knudson, and M. D. Furnish, J. Appl. Phys. **89**, 1625 (2001).
[28] K. B. Fournier, M. Tobin, J. F. Poco, K. Bradley, S. B. Hansen, C. A. Coverdale, D. Beutler, M. Severson, E. A. Smith, and D. L. Reeder, J. Phys. IV **133**, 449 (2006).
[29] H. S. Park *et al.*, Phys. Plasmas **13**, 056309 (2006).

## E.3 Simulating picosecond x-ray diffraction from shocked crystals using post-processing molecular dynamics calculations

The group at Oxford, led by Justin Wark, has been studying shocks both experimentally and via MD simulation for some time. As part of that work, the use of Fourier analysis to simulate exerimental output has of late become invaluable. The main author of this paper examined how strength effects may become manifest within those results, and how one might go about extracting useful information suchn as dislocation densities.

The present author, having carried out many large (multi-million atom) simulations of nanocrystalline samples for the work presented here, was able to supply simulation output to the Oxford group. These datasets were then analysed by Kimminau in order to demonstrate the feasibility of the proposed experimental analysis.

IOP PUBLISHING JOURNAL OF PHYSICS: CONDENSED MATTER

J. Phys.: Condens. Matter **20** (2008) 505203 (8pp) doi:10.1088/0953-8984/20/50/505203

# Simulating picosecond x-ray diffraction from shocked crystals using post-processing molecular dynamics calculations

**Giles Kimminau[1], Bob Nagler[1], Andrew Higginbotham[1], William J Murphy[1], Nigel Park[2], James Hawreliak[3], Kai Kadau[4], Timothy C Germann[4], Eduardo M Bringa[5], Daniel H Kalantar[3], Hector E Lorenzana[3], Bruce A Remington[3] and Justin S Wark[1]**

[1] Department of Physics, Clarendon Laboratory, University of Oxford, Parks Road, Oxford OX1 3PU, UK
[2] AWE, Aldermaston, Reading RG7 4PR, UK
[3] Lawrence Livermore National Laboratory, Livermore, CA 94550, USA
[4] Los Alamos National Laboratory, Los Alamos, NM 87545, USA
[5] Institudo de Ciencias Basicas, Universidad Nacional de Cuyo, Mendoza CP 5500, Argentina

E-mail: giles.kimminau@physics.ox.ac.uk

Received 19 June 2008, in final form 6 October 2008
Published 7 November 2008
Online at stacks.iop.org/JPhysCM/20/505203

**Abstract**

Calculations of the patterns of x-ray diffraction from shocked crystals derived from the results of non-equilibrium molecular dynamics (NEMD) simulations are presented. The atomic coordinates predicted from the NEMD simulations combined with atomic form factors are used to generate a discrete distribution of electron density. A fast Fourier transform (FFT) of this distribution provides an image of the crystal in reciprocal space, which can be further processed to produce quantitative simulated data for direct comparison with experiments that employ picosecond x-ray diffraction from laser-irradiated crystalline targets.

(Some figures in this article are in colour only in the electronic version)

## 1. Introduction

Non-equilibrium molecular dynamics (NEMD) simulations have started to provide exceptional insights into the atomistic behaviour of materials under shock compression. A significant amount of effort has concentrated on the study of the elastic–plastic transition within both single and polycrystalline materials [1–4] as well as shock-induced polymorphic phase transitions [5–7]. In recent years, the impressive advances in computing power and storage space that have been made permit the size of such NEMD simulations to approach hundreds of millions (and in certain cases billions) of atoms, corresponding to samples of side-length approaching a micron, for simulated time-spans of up to hundreds of picoseconds [8, 9]. Given the vast amounts of data that can be generated by such simulations, a judicious choice of data-reduction and visualization systems is required in order to extract physical understanding from the raw data comprising the time-dependence of atomic coordinates. To date, most structural analysis has been limited to traditional short range methods such as obtaining radial distribution functions, centrosymmetry parameters [10] and coordination numbers.

However, simulations with these large spatial and temporal dimensions are starting to approach conditions found in experiments where matter, of thickness microns to several tens of microns, is shock compressed by high-power laser–matter interactions, and diagnosed by (amongst other techniques) *in situ* x-ray diffraction [11, 12]. These experiments have typically employed x-ray flashes of durations of several hundred picoseconds to a few nanoseconds, although picosecond resolution has been obtained by use of streak-

 

camera technology [13], and laser-plasma x-ray sources with durations of order 100 fs can now be produced routinely [14]. It is also expected that this field will benefit from the extremely bright femtosecond sources that will be afforded by future x-ray free-electron-laser technology [15].

As the NEMD simulations provide direct physical insight into the shock-deformation of materials at the lattice level, and the experimental and simulated time and length scales are converging, it is appropriate to make direct comparisons between the experimentally observed x-ray diffraction signals, and those predicted by the NEMD simulations. Indeed, such connections have started to be made: for example, Bringa and co-workers recently used NEMD simulations to calculate the shift in both the Bragg (reflected) and Laue (transmitted) peaks in shock compressed copper [8], which were directly related to the time-dependent shape of the unit cell, and via this provided information regarding the degree of plastic flow. Hawreliak *et al* directly compared the diffraction patterns predicted by NEMD with the experimental data for the $\alpha$–$\epsilon$ transition in shocked iron, noting, amongst many other things, good agreement between the predicted x-ray line widths in the $\epsilon$ phase and those seen experimentally—an observation which is consistent with the predicted mean size of two families of domains with orthogonal $c$-axes [12]. However, whilst simulated diffraction patterns have been presented, to date the procedure by which one can take the output of a NEMD simulation and produce quantitative predictions of what will be observed in an experiment has not been discussed in any detail. In this paper we present such an analysis, outlining how to post-process the NEMD data to efficiently produce diffraction patterns that can be directly compared with data obtained in commonly-employed experimental geometries.

## 2. Calculation of reciprocal space

Neglecting the effects of absorption, and in the kinematic approximation, when an x-ray of wavevector $\mathbf{k}_0$ is incident on a crystal, the intensity $I(\mathbf{k}_s)$ of the elastically scattered x-ray of wavevector $\mathbf{k}_s = \mathbf{k}_0 + \mathbf{q}$ is proportional to the modulus-squared of the Fourier component of the electron density of the lattice with reciprocal lattice vector $\mathbf{q}$. If, in a very simplified approach, we represent the atoms by point scatterers located at the spatial coordinates provided by the MD simulation, then the scattered intensity is given by

$$I(\mathbf{k}_s) \propto |F(\mathbf{q})|^2 \propto \left| \sum_{j=1}^{N} Z_j \exp(\mathrm{i}\mathbf{q} \cdot \mathbf{r}_j) \right|^2, \qquad (1)$$

where $Z_j$ is the atomic number of the $j$th atom, located at position $\mathbf{r}_j$, and the sum is over all $N$ atoms within the crystal. Whilst such a simple calculation can be of use in sampling specifically defined regions of reciprocal space which require the calculation of a very limited number of Fourier components (for example, a volume around a particular Bragg peak), it is inefficient when applied to calculations of the full range of reciprocal space due to the $O(N^2)$ computational operations required. Information about the full range of reciprocal space is potentially useful in many situations: for example to understand the polycrystalline response to shock compression, or to single crystal analysis where the large defect densities generated may give rise to significant scattering between the Bragg peaks.

Likewise performing an FT by this method is also sensible when the number of atoms is small. However, it is because the number of atoms in modern NEMD simulations is so large that this becomes prohibitive. While there is plenty of useful information to be gained from small scale equilibrium MD simulations, applications such as shock waves often require very large spatial and temporal dimensions in order not to hinder effects such as defect motion and to avoid reflection from the boundaries. In such NEMD simulations, the initial system, usually a perfect single crystal or a many grained polycrystal, is thermalized under equilibrium conditions before being deformed. As shock waves are assumed to be adiabatic there is no additional coupling of the atoms to a heat bath in NEMD.

In order to calculate reciprocal space from a large scale NEMD simulation we need a more efficient means of performing the Fourier transform than that given in equation (1). The method we employ is the fast Fourier transform (FFT) approach, the details of which are well known and will not be repeated here, save to recall that an FFT is an efficient method to compute a discrete Fourier transform (DFT) in $O(N \log_2 N)$ operations rather than $O(N^2)$. Whereas the summation used in the simple method of equation (1) exploited the fact that the position vectors of the atoms provided by the MD simulations could be used directly as delta functions, a DFT requires an evenly spaced sample array in real space, making it unsuitable. However, atomic coordinates from the MD actually represent the centres of atoms which have a spatially extended electron distribution. By associating an electron distribution with each atomic coordinate we can construct a discrete regular array of electron density upon which we can perform the FFT.

Calculations of spherically-symmetric electron distributions for the elements are available from a number of sources [16]. Certain very simple analytic forms exist which represent the distributions in real space as a sum of a finite number of Gaussian profiles [17]. The Fourier transform of these radial distributions, the atomic form factors, are also available based on a number of approximations, such as the Thomas–Fermi or Dirac–Fock methods [16], and we use such forms here for the quantitative calculation of diffraction patterns.

Once an electron distribution has been associated with each atomic coordinate, the level of real space sampling is determined by the range of interest in reciprocal space, with the number of samples per unit cell in real space determining the range of the transformation in reciprocal space. For example, if we wish to explore reciprocal space out to the fifth order (based on a conventional unit cell in real space) then we require a range of at least 10 reciprocal lattice vectors, corresponding to 10 samples per side of a conventional unit cell, i.e. $10^3$ over the conventional cell volume. On the other hand the resolution in reciprocal space is determined by the number of unit cells in the MD calculation, and hence the requirement for large MD

simulations if we wish to have high resolution in reciprocal space, and in the resultant calculated diffraction patterns.

Although we can use the physical electron distribution to calculate a realistic array of electron density, it is advantageous to exploit this method for greater efficiency. Difficulties arise because of the interplay between the width of the electron distribution in real space and the radial extent of the intensity of the Fourier components in reciprocal space. If the spatial profile is too narrow, the Fourier components in reciprocal space could still have significant amplitude at the edges of the chosen range of reciprocal space, resulting in the pattern being reflected back (as FFTs are periodic), or overlapping, which is known as aliasing. On the other hand, too wide a profile in real space for a chosen range of reciprocal space implies that the intensity of high orders in reciprocal space will be too weak, and information may be lost. In cases where we have selected a specific range of reciprocal space, we have found it useful to choose a Gaussian profile in real space such that the $4\sigma$ position of the Gaussian envelope (amplitude) in reciprocal space lies on the edge of the reciprocal space array. Thus we are no longer assigning a physical electron density, but are instead 'dressing' each atomic coordinate with a Gaussian which allows us optimal control.

The approach of 'dressing' each atomic coordinate works due to the relationship of a convolution in real space and multiplication in reciprocal space. The Fourier transform of the real space convolution of the atomic distribution function with a Gaussian electron density is just the product of the Fourier transforms of the atomic distribution function and the Gaussian profile. Therefore, the Fourier transform of the atomic distribution function with a physically realistic electron density function is just:

$$\mathcal{F}[\mathrm{ADF} \bigotimes \rho(r)] = \mathcal{F}[\mathrm{ADF} \bigotimes G(r)] \times \frac{\mathcal{F}[\rho(r)]}{\mathcal{F}[G(r)]}$$
$$= \mathcal{F}[\mathrm{ADF} \bigotimes G(r)] \times \frac{F(k)}{\widetilde{G}(k)}, \qquad (2)$$

where $\mathcal{F}$ is the Fourier transform operator, ADF is the atomic distribution function which is simply a delta function placed at each of atomic coordinates taken from MD, $\rho(r)$ is the electron density for one atom, $G(r)$ is the Gaussian profile of our choosing in real space and hence $\widetilde{G}(k)$ is the Fourier transform of it and $F(k)$ is the atomic form factor which is the Fourier transform of $\rho(r)$.

By exploiting the properties of Fourier transforms, using a non-physical radial electron density in this way for convenience does not compromise the physical validity of the calculation. By using a convenient Gaussian atomic electron density of know width, we avoid aliasing, and we are able to infer the FFT of the atomic distribution. After performing the FFT of the atomic distribution function convolved with the Gaussian profile we can then divide by the Fourier transform of the Gaussian profile (which we know analytically) to give us the FFT of the atomic distribution function. We then proceed to multiply by the atomic form factor which produces output equivalent to using the physically realistic electron density in the first place, as shown in equation (2).

It is evident that evaluating reciprocal space at high orders increases the size of the calculation significantly, but given the number of atoms involved, the FFT is still a more computationally efficient means of viewing reciprocal space compared with the normal FT, unless only a very small sub-set of reciprocal space is of interest. For example, calculating reciprocal space up to 5th order from several million atoms can be computed in a matter of minutes on a typical workstation. The main limitation of the FFT method is the memory usage which is around 4 GB per million unit cells if calculating reciprocal space up to 5th order at single precision. Large shared memory machines are particularly well suited to calculating FFTs of 10s or 100s of millions of atoms. The method also works on MPI (message passing interface) clusters, but with the disadvantage of requiring extra memory for the FFT transposes and node overhead. However, for analysis of MD simulations, it is often desirable to calculate reciprocal space with some spatial resolution, and, as such, the sample can be divided up into sections which can be calculated quickly on single nodes. Likewise on polycrystalline or highly defected samples where it may be necessary to gain information about the entire sample, the reciprocal peaks are often broad enough to allow a lower resolution, and hence the intensities of smaller FFTs can be summed.

## 3. Quantitative calculations

In section 4 we will show how we can post-process the representation of the crystal in reciprocal space to obtain simulated diffraction patterns for specific experimental geometries. This processing is reliant on the fact that the intensity of the scattered radiation is proportional to the square of the relevant Fourier component, as stated in equation (1).

Although the spatial scales of MD simulations are starting to converge, it is still generally the case that experiments use crystals of thickness between one and two orders of magnitude greater than the simulations. Furthermore, there could often be situations where due to constraints on computational resources it is desirable to perform a simulation that has a spatial scale significantly smaller than that used in an experiment, yet there is a requirement to have some predictive capability for the experimental intensity to compare with features in the simulations. Therefore, in order to have a means estimating what intensities might actually be found in an experiment, we need to associate each value of $|F(\mathbf{q})|^2$ in reciprocal space with a reflectivity that corresponds to that which may be expected in the experimental configuration.

Such an association can be made by noting that the efficiency of scattering from a single atom is known. If unpolarized x-rays of wavevector $\mathbf{k}_0$ are incident on a single atom, and are elastically scattered into wavevector $\mathbf{k}_\mathrm{s} = \mathbf{k}_0 + \mathbf{q}$, then the differential cross-section, $\mathrm{d}\sigma/\mathrm{d}\Omega$ is given by

$$\frac{\mathrm{d}\sigma}{\mathrm{d}\Omega} = r_\mathrm{e}^2 \frac{(1+\cos^2\theta)}{2} f^2(|\mathbf{q}|, Z), \qquad (3)$$

where $r_\mathrm{e}$ is the classical radius of an electron, $\theta$ is the angle of deflection and $f(|\mathbf{q}|, Z)$ is the atomic form factor for element $Z$, which is proportional to the Fourier transform of the spherically-symmetric electronic density distribution discussed

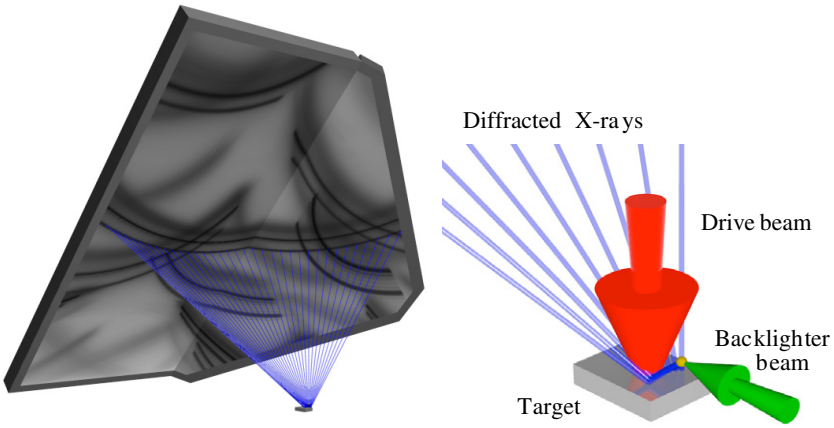


**Figure 1.** Experimental setup of single crystal diffraction from a diverging x-ray point source. For illustration the path of some x-rays of 1.85 Å diffracting from the (002) plane of Fe are shown.

in section 2. Let us consider the case where we have performed an NEMD simulation of a crystal which contains $N$ atoms,

$$\frac{\mathrm{d}\sigma}{\mathrm{d}\Omega} = r_\mathrm{e}^2 \frac{(1+\cos^2\theta)}{2} \left| \sum_{i=1}^{N} f_i(|\mathbf{q}|, Z) \mathrm{e}^{\mathrm{i}\,\mathbf{q}\cdot\mathbf{r}_j} \right|^2. \tag{4}$$

We note that if our system has only one type of atom the atomic form factor can be separated out

$$\frac{\mathrm{d}\sigma}{\mathrm{d}\Omega} = r_\mathrm{e}^2 \frac{(1+\cos^2\theta)}{2} f^2(|\mathbf{q}|, Z) \left| \sum_{i=1}^{N} \mathrm{e}^{\mathrm{i}\,\mathbf{q}\cdot\mathbf{r}_j} \right|^2, \tag{5}$$

and in this particular case we can easily remove the effect of the form factor after performing the FFT by deconvolution with the Gaussian in Fourier space associated with the form factor. Absolute intensities can be obtained by noting that as the electron density is real, the rms value of the electron density within the system is not a function of the correlations. This means that the integral of the intensity of Fourier components of the electron density over the whole of reciprocal space is a constant for a given number of atoms in a fixed volume. This is simply a form of Parseval's theorem which provides us with a means of normalizing the intensity of the components in reciprocal space, such that a given intensity density in reciprocal space corresponds to a quantitative measure of the scattered x-ray intensity.

This approach both neglects absorption within the crystal (and thus would not be valid for crystal thicknesses approaching or exceeding an absorption depth), and neglects the effect of extinction—that is to say re-scattering within the crystal. The proper handling of extinction effects require wave–wave interactions that are described by dynamical diffraction theory. The assumption of kinematic diffraction is likely to be valid for crystals containing large numbers of defects, or large strain gradients, as is the case in the shocked samples considered here. It may, however, not be a valid assumption for diffraction from large unshocked regions of the crystal if the sample has a high degree of perfection.

We can thus, using the above approach, calculate (within the approximations given) an absolute scattered x-ray fraction from the MD simulation. Furthermore, it is now simple to scale a calculated intensity. That is to say based on a simulation of a small system, we can infer the intensity that would be scattered in a larger system (as long as the path lengths of the scattered rays do not traverse distances greater than of order an absorption depth), as the intensity in this case is directly proportional to sample thickness. Of course, it may be that the physics of the MD simulation in question cannot be scaled linearly, but that is a separate matter from the diffraction calculation.

## 4. Experimental diffraction geometries

### *4.1. Single crystal diffraction*

One of the primary motivations for this work is to enable the comparison of the predictions of MD simulations with picosecond x-ray diffraction from laser-shocked crystals. Once the FFT has been performed, and we have the values for the intensities of the Fourier components $|F(\mathbf{q})|^2$ in reciprocal lattice space (and know how these can be translated into scattering cross-sections for an experimental sample), we can proceed to calculate the pattern observed experimentally. Our intent in this paper is to outline how such calculations are performed, and give example output alongside experimental results. We do not, however, go into detail concerning the physics that may be gleaned from these comparisons, leaving such discussions for future work dedicated to that specific purpose.

One of the most widely used experimental geometries for picosecond diffraction from shocked crystals has been the diverging beam geometry [18], described by Kalantar and co-workers [19] and explained in more detail in the appendix. In this geometry, shown schematically in figure 1, the output of a high-power ns optical laser is focused onto a thin foil, generating a highly ionized plasma which in turn emits a short pulse of quasi-monochromatic x-rays. The x-ray source is approximated as an isotropic point source for this simulation. Another laser beam is used to drive the shock wave in the crystal by ablating the front surface. The x-rays penetrate far

enough into the crystal to diffract from the regions both in front and behind the shock front and the resulting lines are recorded on the surrounding film packs.

To calculate the intensity incident on the film and hence the number of photons per pixel, we sample the film by ray-tracing back to the point source using the Laue formalism: $\mathbf{q} = \Delta\mathbf{k} = \mathbf{k}_s - \mathbf{k}_0$, where $\mathbf{k}_0$ is the incident wavevector, $\mathbf{k}_s$ the diffracted wavevector and $\mathbf{q}$ a vector in reciprocal space with known scattering intensity.

For each sample on the film, x-rays can arrive via any point on the crystal surface and as such the entire crystal needs to be well sampled for each film sample. We do this by dividing up our crystal in the surface plane into an array of sub crystals, each of which is illuminated by a collimated beam and hence corresponds to a single sample in reciprocal space per film sample. Obviously the sub-crystal must be small enough to be reasonably represented by a single reciprocal space sample which in turn can be found by linearly interpolating our FFT output and multiplying by the appropriate coefficients to calculate the cross-section. One advantage of sampling (as opposed to photon mapping) in both the film and crystal planes is that the sampling need not be uniform which can improve efficiency in certain situations.

As an example of this procedure we have simulated the diffraction from a single crystal of iron shocked along the [001] axis. The NEMD simulation was performed using the SPaSM code [20, 21] with the Voter–Chen potential [22]. A sample with dimensions 40.2 nm × 40.2 nm × 57.4 nm consisting of 8 million atoms were launched along the [001] direction at a velocity of 471 m s$^{-1}$ into a momentum mirror. Previous work using this potential have shown that at this particle velocity the iron undergoes a transition from the body-centred-cubic $\alpha$ phase into the hexagonal-close-packed $\epsilon$ phase. An image of the crystal after a simulation time of 8.46 ps is shown in figure 2, where the atoms are coloured according to coordination number. Here we can clearly see the 3 distinct sections consisting of the unshocked region coloured grey (right), the uniaxially compressed region in blue (middle) and the phase changed region in red (left). For further detail about the simulation one should refer to the original work [6].

Using the atomic coordinates provided by the MD simulation, the diffraction pattern was calculated according to the procedure described above. The reciprocal space was calculated by using a real space matrix of 1024 × 1024 × 1458 and hence requiring 6 GB of memory. This generated reciprocal space beyond 3.2 $\frac{2\pi}{a}$ which is the highest order experimentally accessible using Fe He-$\alpha$ x-rays at 1.85 Å. This contains 140 samples per reciprocal unit cell in the $x$ and $y$ directions and 187 in the $z$ direction corresponding to the number of unit cells in each dimension. We set the origin of our world coordinates to be the position of the x-ray point source and define the crystal to be in the $x$–$y$ plane, centred at (0,1.5, −1) mm. The crystal is 3 × 3 mm in extent with the crystallographic axis rotated by 13° around [001] to the world axis. In order to calculate the absolute intensities we assumed the crystal had a thickness of 10 $\mu$m as in the experiment. The film packs are then positioned 60 mm away with the normal along the [011] direction. The main rectangle is 130 mm in the [0$\bar{1}$1] direction and 65mm along [100]. The triangular pack (used in the experiments) is then positioned adjacent to this with the same extents but rotated inwards by 60°. Some minor rotations and offsets are then performed in order to fit the simulation to the exact experimental geometry. To produce this figure the film was sampled at 200 $\mu$m and the crystal surface at 50 $\mu$m resolution. Generating reciprocal space from an ASCII file containing atomic coordinates took 3 min and the tracing took 40 min on an 8-core Xeon Mac Pro. Lower quality but still meaningful figures can be traced in a fraction of the time.

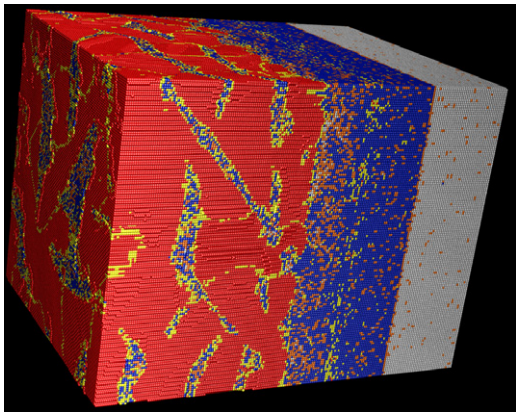

**Figure 2.** MD simulation of Fe shocked along [001] at 471 m s$^{-1}$. Atoms are coloured according to coordination number displaying the unshocked region coloured grey (right), the uniaxially compressed region in blue (middle) and the phase changed region in red (left). From [6]. Reprinted with permission from AAAS.

The simulated diffraction pattern is shown in figure 3 next to an example of experimental data taken on the Vulcan laser [23] under experimental conditions very similar to the work performed by Kalantar and co-workers [11]. The Fe single crystal was coated with 20 $\mu$m of parylene-N and driven with a 230 J pulse at 1053 nm and 6 ns duration. The x-ray source was generated with a 1ns pulse of approximately 150 J at 527 nm, delayed by 4.5 ns with respect to the drive pulse. On both the simulated and experimental diffraction patterns the 3 lines corresponding to unshocked, uniaxially compressed and phase changed lattice are clearly visible. This allows a direct comparison of NEMD simulations with experimental results. Even without detailed analysis we can clearly see that the strain in the uniaxially compressed region differs significantly between the NEMD simulation and the experiment from the position of the line while the unshocked and HCP lines either side match well. The line widths of the HCP features in the simulated and experimental data are comparable and the peak intensities are within an order of magnitude (after background subtraction) if we assume an x-ray conversion efficiency of $10^{-3}$ and sensitivity for Fujifilm MS type-image plate of around 100 photons per unit PSL per pixel [24]. Given that the image plate has a sensitivity of five orders of magnitude [25] and the images displayed are logarithmic, we conclude that the estimated absolute intensities that would be recorded are sufficiently accurate to aid in the design of experiments.

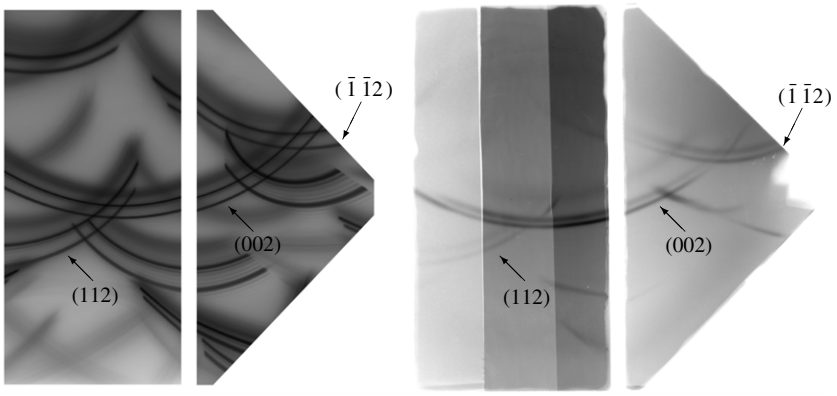


**Figure 3.** Simulated (left) and experimental (right) film recordings of x-rays diffracted from shock compressed iron. See the text for details. Both clearly show the unshocked, uniaxially compressed and phase changed lines. Miller indices for several reflections are indicated. The plotted intensity is logarithmic for the simulated diffraction with a range of 5 orders of magnitude with, a maximum number of photons per unit area of $3 \times 10^{-3}$ m$^{-2}$ of the total number emitted by the source in the helium alpha line.

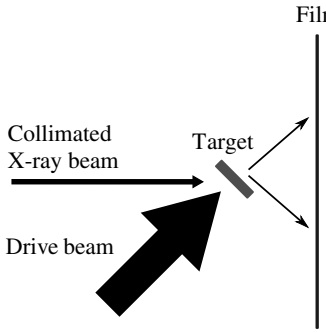


**Figure 4.** Polycrystalline experimental setup.

### *4.2. Polycrystalline diffraction*

Although many experiments involving picosecond diffraction from shocked materials have been performed with single crystals, it has recently been shown that single shot diffraction patterns can be obtained from polycrystalline samples using laser-plasma x-ray sources [26]. In this case, a collimated beam of quasi-monochromatic radiation, once more produced from the resonance lines of helium-like atoms, is incident on a foil of polycrystalline metal. In the experimental work of Hawreliak *et al*, the source to foil distance was 5 cm, and the diffracted x-rays were recorded on a cylindrical film pack co-axial with the incident x-rays. Here we simulate an experiment of similar dimensions, though we place a planar film pack behind the target in a normal Debye–Scherrer geometry, with similar target to film distances as those used in the experiment (conversion to a cylindrical film pack geometry provides no extra information). The geometry is shown in schematic form in figure 4.

In terms of the post-processing of the reciprocal space data, we note that in this case the direction of the incident beam is fixed, and its orientation with respect to the reciprocal space axes is simply determined by the angle $\psi$ which the surface normal of the foil makes to the incident beam. In this case the experimentally observed diffraction pattern is determined by the angle of the $\mathbf{k}_s$ vector as $\mathbf{k}_0$ is fixed in direction by the collimation and in magnitude by the monochromatic nature of the source. As a result, $\mathbf{k}_s$ traces out a shell in reciprocal space which touches the origin. This in turn intersects the shells of $\mathbf{G}_{hkl}$ of strong reflections, which are centred at the origin, resulting in a pattern of rings on film—the well-known Debye–Scherrer pattern.

In our calculations the crystal surface is placed at 45° to the collimated x-ray beam. This allows the shell that is traced out by $\mathbf{k}_s$ to intersect both the $x$–$y$ components (orthogonal to shock) and the $z$-components (shock direction) of the $\mathbf{G}_{hkl}$ shells and hence give an indication of the level of compression along different crystal axes.

As an example of this procedure we have simulated the diffraction from a polycrystal sample of Cu with x-rays of wavelength 1.48 Å. The NEMD simulation was performed using the LAMMPS package [27] using the Mishin EAM1 potential [28]. A sample with dimensions 72 nm × 72 nm × 72 nm consisting of 30 million atoms in approximately 3000 grains was used. The initial sample was created with the Atomeye utilities [29] before undergoing energy minimization by the conjugate gradient algorithm and thermalization at 300 K. A piston was set moving into the sample at 900 ms$^{-1}$ and the simulation was run for 15 ps to allow the shock wave to travel the full extent of the sample which compressed by approximately 20% volumetrically.

In order to compare diffracted intensities with those observed experimentally, it was assumed that the illuminated sample is a foil 25 $\mu$m thick and 1mm square. The diffraction was traced in the same manner as the single crystal case except that as the beam is collimated only one sample on the crystal is needed for every sample of the film. The target was placed 50 mm from an x-ray point source and the beam approximated as collimated. The 12 × 12 cm film was then placed 15mm from the sample. The FFT was performed using 8 processors and 32 GB of RAM on an SGI Altix 4700 in 26 min with the tracing taking seconds.

The diffraction patterns for both the unshocked (left) and shocked (right) foils are shown in figure 5. The maximum intensity observed is once more within an order of magnitude

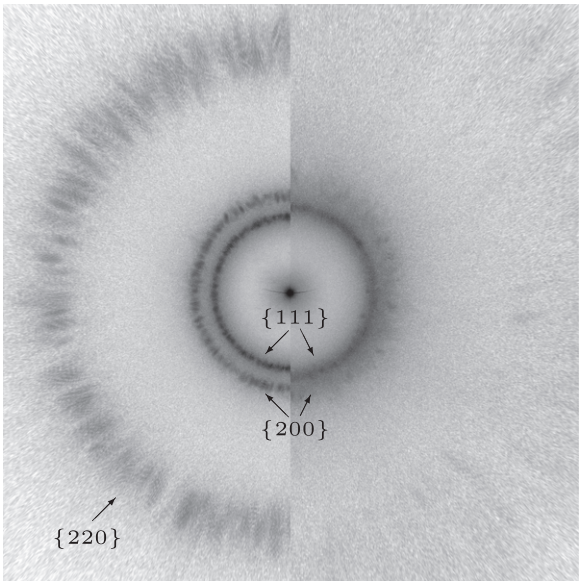


**Figure 5.** Simulated diffraction from polycrystalline Cu. The figure is split with the left side showing diffraction from the unshocked crystal and the right-hand side from the same crystal but shocked at 900 m $s^{-1}$. The plotted intensity is logarithmic with a range of 5 orders of magnitude with a maximum number of photons per unit area of $10^{-5}$ $m^{-2}$ of the total number emitted by the source in the helium alpha line. See the text for further details.

of those found in experiments. The expansion of the diffraction rings due to a compression of the lattice is clearly visible in the shocked sample.

## 5. Summary

We have presented calculations of the x-ray diffraction patterns from shocked crystals derived from the results of non-equilibrium molecular dynamics (NEMD) simulations. The atomic coordinates predicted by the NEMD simulations combined with atomic form factors are used to generate a discrete array of electron density. A fast Fourier transform (FFT) of this array provides an image of the crystal in reciprocal space, which can be further processed to produce simulated quantitative data for direct comparison with experiments that employ picosecond x-ray diffraction from laser-irradiated crystalline targets. Estimates of absolute intensities that may be observed in real experiments have been obtained from a knowledge of x-ray scattering cross-sections, and scaling the intensity scattered by the MD predictions accordingly. Good agreement is found between computed and experimental diffraction patterns, and the technique should be useful in both designing novel experiments, as well as in analysis of the signals obtained by using of picosecond diffraction from shocked crystals.

## Acknowledgments

The authors are grateful to a number of organizations for support. GK is grateful for partial support for this work from LLNL under subcontract No. B566832. BN is supported by the EU Marie-Curie RTN 'FLASH'. JH, DK, HL and BR work under the auspices of the US DOE by LLNL under Contract DE-AC52-07NA27344. HL and JH also received partial support from LDRD programme Project No. 06-SI-004 at LLNL. WJM is grateful for support from AWE Aldermaston. A.H. has been generously supported by Daresbury Laboratory under the auspices of the NorthWest Science Fund. KK and TG work under the auspices of the National Nuclear Security Administration of the US Department of Energy at Los Alamos National Laboratory under Contract No. DE-AC52-06NA25396. We also wish to thank P S Lomdahl and B L. Holian for valuable discussions. Simulations were performed on the QUEEG and ORAC machines at the Oxford Supercomputing Centre.

## Appendix. Experimental geometry

In the diverging beam geometry, shown schematically in figure 1, a short pulse of x-rays is generated by focussing the output of a high-power ns optical laser onto a thin foil. The laser intensities are such that a highly ionized plasma is formed, and copious x-rays are produced. Depending upon the element used, for laser intensities in the range of $10^{14}$–$10^{16}$ W $cm^{-2}$, a significant fraction of the radiation is emitted in the $n = 2 \rightarrow 1$ resonance line of the helium-like ion. These x-rays are quasi-monochromatic in that alongside the resonance line itself, which corresponds to the $1s2p\,^1P \rightarrow 1s^2\,^1S$ transition, in the plasma environment there is also significant emission in the intercombination line, $1s2p\,^3P \rightarrow 1s^2\,^1S$, as well as emission into dielectronic satellites. The fractional bandwidth of these transitions taken together is of order $5 \times 10^{-3}$. Typical conversion efficiencies from optical laser light into these lines is of order $10^{-2}$–$10^{-4}$ [30, 31], and typical source diameters are of order 100 $\mu$m.

The x-rays that are emitted from the hot plasma diverge into $4\pi$ steradians. Therefore, in order to maximize the information gleaned from diffracting from the shocked crystal, the x-ray source is placed close to the crystal (with typical source to crystal distances of order 1 mm), such that the shocked crystal subtends a relatively large solid angle to the x-ray source. The diameter of the region of the crystal which is shocked by the laser, determined largely by considerations of the laser energy, is typically of order 3 mm. X-rays diffracted from the shocked crystal are recorded on large area flat film packs placed several cm from the crystal, which are arranged to cover as large a solid angle as possible given the constraints imposed by experimental considerations such as the need to provide access for the optical laser beams. When the surface layer of thick crystals are shocked, the diffracted radiation is collected in the reflection geometry (so-called Bragg diffraction). Experiments with thin crystals, with thicknesses of order 10 $\mu$m, have also simultaneously allowed diffraction in transmission geometry (so-called Laue diffraction). The scattered x-rays are recorded on either x-ray film or image plates. The direct path between the x-ray source and film packs is obscured by highly absorbing beam blocks.

## References


[1] Gupta Y M 1977 Effect of crystal orientation on dynamic strength of LiF *J. Appl. Phys.* **48** 5067

[2] Holian B L and Lomdahl P S 1998 Plasticity induced by shock waves in nonequilibrium molecular-dynamics simulations *Science* **280** 2085

[3] Bringa E M 2004 Atomistic shock Hugoniot simulation of single-crystal copper *J. Appl. Phys.* **96** 3793

[4] Bringa E M, Caro A, Wang Y, Victoria M, McNaney J M, Remington B A, Smith R F, Torralva B R and Van Swygenhoven H 2005 Ultrahigh strength in nanocrystalline materials under shock loading *Science* **309** 1838–41

[5] Kadau K, Germann T C, Lomdahl P S and Holian B L 2005 Atomistic simulations of shock-induced transformations and their orientation dependence in bcc Fe single crystals *Phys. Rev.* B **72** 64120

[6] Kadau K, Germann T C, Lomdahl P S and Holian B L 2002 Microscopic view of structural phase transitions induced by shock waves *Science* **296** 1681–4

[7] Kadau K, Germann T C, Lomdahl P S, Albers R C, Wark J S, Higginbotham A and Holian B L 2007 Shock waves in polycrystalline iron *Phys. Rev. Lett.* **98** 135701

[8] Bringa E M, Rosolankova K, Rudd R E, Remington B A, Wark J S, Duchaineau M, Kalantar D H, Hawreliak J and Belak J 2006 Shock deformation of face-centred-cubic metals on subnanosecond timescales *Nat. Mater.* **5** 805–9

[9] Kadau K, Germann T C and Lomdahl P S 2006 Molecular dynamics comes of age:. 320 billion atom simulation on BlueGene/L *Int. J. Mod. Phys.* C **17** 1755–61

[10] Kelchner C L, Plimpton S J and Hamilton J C 1998 Dislocation nucleation and defect structure during surface indentation *Phys. Rev.* B **58** 11085–8

[11] Kalantar D H *et al* 2005 Direct observation of the $\alpha$–$\varepsilon$ transition in shock-compressed iron via nanosecond x-ray diffraction *Phys. Rev. Lett.* **95** 75502

[12] Hawreliak J *et al* 2006 An analysis of the x-ray diffraction signal for the $\alpha$–$\varepsilon$ transition in shock-compressed iron: simulation and experiment *Phys. Rev.* B **74** 17

[13] Wark J S, Riley D, Woolsey N C, Keihn G and Whitlock R R 1990 Direct measurements of compressive and tensile strain during shock breakout by use of subnanosecond x-ray diffraction *J. Appl. Phys.* **68** 4531

[14] Sokolowski-Tinten K, Blome C, Blums J, Cavalleri A, Dietrich C, Tarasevitch A, Uschmann I, Foerster E, Kammler M and Horn-von Hoegen M 2003 Femtosecond x-ray measurement of coherent lattice vibrations near the Lindemann stability limit *Nature* **422** 287–9

[15] Winick H 1995 The linac coherent light source (LCLS): a fourth-generation light source using the SLAC linac *J. Electron Spectrosc. Relat. Phenom.* **75** 1–8

[16] Cromer D T and Waber J T 1974 *International Tables for X-ray Crystallography* vol IV, Table 2.2 A (Birmingham: Kynoch Press) pp 99–101 (Present distributor Kluwer Academic, Dordrecht)

[17] Rez D, Rez P and Grant I 1994 Dirac–Fock calculations of x-ray scattering factors and contributions to the mean inner potential for electron scattering *Acta Crystallogr.* A **50** 481–97

[18] Wark J S, Whitlock R R, Hauer A, Swain J E and Solone P J 1987 Shock launching in silicon studied with use of pulsed x-ray diffraction *Phys. Rev.* B **35** 9391–4

[19] Kalantar D H 2003 Multiple film plane diagnostic for shocked lattice measurements (invited) *Rev. Sci. Instrum.* **74** 1929

[20] Lomdahl P S, Tamayo P, Gronbech-Jensen N and Beazley D M 1993 50 GFlops molecular dynamics on the Connection Machine-5 *Supercomputing'93 Proc.* pp 520–7

[21] Beazley D M and Lomdahl P S 1997 Controlling the data glut in large-scale molecular-dynamics simulations *Comput. Phys.* **11** 230–8

[22] Harrison R J, Voter A F and Chen S P 1988 *Atomistic Modeling of Materials: Beyond Pair Potentials* ed V Vitek and D J Srolovitz (New York: Plenum) pp 219–22

[23] Ross I, White M, Boon J, Craddock D, Damerell A, Day R, Gibson A, Gottfeldt P, Nicholas D and Reason C 1981 Vulcan–a versatile high-power glass laser for multiuser experiments *IEEE J. Quantum Electron.* **17** 1653–61

[24] Cookson D J 1998 Calculation of absolute intensities from x-ray imaging plates *J. Synchrotron Radiat.* **5** 1375–82

[25] Gales S G and Bentley C D 2004 Image plates as x-ray detectors in plasma physics experiments *Rev. Sci. Instrum.* **75** 4001

[26] Hawreliak J, Lorenzana H E, Remington B A, Lukezic S and Wark J S 2007 Nanosecond x-ray diffraction from polycrystalline and amorphous materials in a pinhole camera geometry suitable for laser shock compression experiments *Rev. Sci. Instrum.* **78** 083908

[27] Plimpton S 1993 Fast parallel algorithms for short-range molecular dynamics *Technical Report* SAND-91-1144, Sandia National Labs., Albuquerque, NM (United States) http://lammps.sandia.gov

[28] Mishin Y, Mehl M J, Papaconstantopoulos D A, Voter A F and Kress J D 2001 Structural stability and lattice defects in copper: *ab initio*, tight-binding, and embedded-atom calculations *Phys. Rev.* B **63** 224106

[29] Li J 2003 AtomEye: an efficient atomistic configuration viewer *Modelling Simul. Mater. Sci. Eng.* **11** 173–7

[30] Yaakobi B *et al* 1981 High x-ray conversion efficiency with target irradiation by a frequency tripled Nd:glass laser *Opt. Commun.* **38** 196–200

[31] Matthews D L *et al* 1983 Characterization of laser-produced plasma x-ray sources for use in x-ray radiography *J. Appl. Phys.* **54** 4260

# References


[1] T. J. Ahrens. *Methods of Experimental Physics*, volume 24, chapter Shock wave techniques for geophysics and planetary physics, pages 185–235. Academic Press, Orlando, 1987.

[2] M.P. Allen and D.J. Tildesley. *Computer Simulation of Liquids*. Oxford University Press, 1987.

[3] P. Ambrosi, W. Homeier, and Ch. Schwink. Measurement of dislocation density in [100]- and [111]- copper single crystals with high relative accuracy. *Scripta Metallurgica*, 14(3):325–329, 1980.

[4] Qi An, Sheng-Nian Luo, Li-Bo Han, Lianqing Zheng, and Oliver Tschauner. Melting of cu under hydrostatic and shock wave loading to high pressures. *Journal of Physics: Condensed Matter*, 20(9):095220 (8pp), 2008.

[5] Christian Anders and Herbert M. Urbassek. Nonlinear stopping of heavy clusters in matter: A case study. *Nuclear Instruments and Methods in Physics Research Section B: Beam Interactions with Materials and Atoms*, 258(2):497–500, 2007.

[6] Hans C. Andersen. Molecular dynamics simulations at constant pressure and/or temperature. *Journal of Chemical Physics*, 72(4):2384

[7] B. W Anderson, G. S Settles, J. D Miller, B. T Keane, and J. A. Gatto. High-speed imaging of shock-wave motion in aviation security research. In *54th Annual Meeting of the Division of Fluid Dynamics November 18 - 20, 2001 San Diego, California*. American Physical Society, 2001.

[8] Franz Aurenhammer. Voronoi diagrams—a survey of a fundamental geometric data structure. *ACM Computing Surveys*, 23(3):345–405, 1991.

[9] Edgar C. Bain. The nature of martensite. *Trans. Amer. Min. Met. Eng.*, pages 25–46, Feb 1924.

[10] Dennison Bancroft, Eric L. Peterson, and Stanley Minshall. Polymorphism of iron at high pressure. *Journal of Applied Physics*, 27(3):291, March 1956.

[11] C. Bradford Barber, David P. Dobkin, and Hannu Huhdanpaa. The quickhull algorithm for convex hulls. *ACM Transactions on Mathematical Software*, 22(4):469–483, 1996.

[12] J.L. Barber and K. Kadau. Shock-front broadening in polycrystalline materials. *Physical Review B*, 77:144106, 2008.

[13] Zoe H. Barber, editor. *Introduction to Materials Modelling.* Maney, 2005.

[14] K. Barghorn and E.R. Hilf. Low energy cluster impact simulated by molecular dynamics; angular distribution of sputtering yield and impact under various impact angles. *Nuclear Instruments and Methods in Physics Research Section B: Beam Interactions with Materials and Atoms*, 88(1-2):196–201, 1994.

[15] M.I. Baskes. Modified embedded-atom potentials for cubic materials and impurities. *Physical Review B*, 46(5):2727–2742, Aug 1992.

[16] M.I. Baskes. The modified embedded atom method. Sandia Report SAND94-8704.UC-411, Sandia National Laboratories, Albuquerque, New Mexico, Aug 1994.

[17] H. J. C. Berendsen, JPM Postma, WF Van Gunsteren, A Dinola, and JR Haak. Molecular-dynamics with coupling to an external bath. *Journal of Chemical Physics*, 81(8):3684–3690, 1984.

[18] Stephen D. Bond, Benedict J. Leimkuhler, and Brian B. Laird. The Nosé–Poincaré method for constant temperature molecular dynamics. *Journal of Computational Physics*, 151:114–134, 1999.

[19] F. E. Borgnis. Specific directions of longitudinal wave propagation in anisotropic media. *Phyical. Review*, 98(4):1000–1005, May 1955.

[20] M. Born and R. Oppenheimer. Zur quantentheorie der molekle (on the quantum theory of molecules). *Annalen der Physik*, 84:457–484, 1927.

[21] Max Born. On the stability of crystal lattices. i. *Mathematical Proceedings of the Cambridge Philosophical Society*, 36(02):160–172, 1940.

[22] Robert D Boyer, Ju Li, Shigenobu Ogata, and Sidney Yip. Analysis of shear deformations in Al and Cu: empirical potentials versus density functional theory. *Modelling and Simulation in Materials Science and Engineering*, 12(5):1017–1029, 2004.

[23] P. W. Bridgeman. Further rough compressions to 40,000 kg/cm$^2$, especially certain liquids. *Proceedings of the American Academy of Arts and Science*, 77:187, 1949.

[24] E. M. Bringa, A. Caro, Y. Wang, M. Victoria, J. M. McNaney, B. A. Remington, R. F. Smith, B. R. Torralva, and H. Van Swygenhoven. Ultrahigh strength in nanocrystalline materials under shock loading. *Science*, 309:1838–1841, 2005.

[25] E. M. Bringa, K. Rosolankova, R. E. Rudd, B. A. Remington, J. S. Wark, M. Duchaineau, D. H. Kalantar, J. Hawreliak, and J. Belak. Shock deformation of face-centred-cubic metals on subnanosecond timescales. *Nature Materials*, 5:805–809, 2006.

[26] E.M. Bringa, A. Caro, M. Victoria, and N. Park. Atomistic modelling of wave propagation in nanocrystals. *JOM*, 57(9):67–70, Sep 2005.

[27] E.M. Bringa, J.U. Cazamias, P.Erhart, J. Stölken, N. Tanushev, B.D. Wirth, R.E. Rudd, and M.J. Caturla. Atomistic shock Hugoniot simulation of single-crystal copper. *Journal of Applied Physics*, 96(7):3793–3799, Oct 2004.

[28] E.M. Bringa, B.D. Wirth, M.J. Caturla, J. St/"olken, and D. Kalantar. Metals far from equilibrium: From shocks to radiation damage. *Nuclear Instruments and Methods in Physics Research B*, 202:56–63, 2003.

[29] Witold Brostow, Mieczyslaw Chybicki, Robert Laskowski, and Jaroslaw Rybicki. Voronoi polyhedra and Delaunay simplexes in the structural analysis of molecular-dynamics-simulated materials. *Physical Review B*, 57(21):13448–13458, June 1998.

[30] Don Brownlee, Peter Tsou, Jerome Aleon, Conel M. O'D. Alexander, Tohru Araki, Sasa Bajt, Giuseppe A. Baratta, Ron Bastien, Phil Bland, Pierre

Bleuet, Janet Borg, John P. Bradley, Adrian Brearley, F. Brenker, Sean Brennan, John C. Bridges, Nigel D. Browning, John R. Brucato, E. Bullock, Mark J. Burchell, Henner Busemann, Anna Butterworth, Marc Chaussidon, Allan Cheuvront, Miaofang Chi, Mark J. Cintala, B. C. Clark, Simon J. Clemett, George Cody, Luigi Colangeli, George Cooper, Patrick Cordier, C. Daghlian, Zurong Dai, Louis D'Hendecourt, Zahia Djouadi, Gerardo Dominguez, Tom Duxbury, Jason P. Dworkin, Denton S. Ebel, Thanasis E. Economou, Sirine Fakra, Sam A. J. Fairey, Stewart Fallon, Gianluca Ferrini, T. Ferroir, Holger Fleckenstein, Christine Floss, George Flynn, Ian A. Franchi, Marc Fries, Z. Gainsforth, J.-P. Gallien, Matt Genge, Mary K. Gilles, Philipe Gillet, Jamie Gilmour, Daniel P. Glavin, Matthieu Gounelle, Monica M. Grady, Giles A. Graham, P. G. Grant, Simon F. Green, Faustine Grossemy, Lawrence Grossman, Jeffrey N. Grossman, Yunbin Guan, Kenji Hagiya, Ralph Harvey, Philipp Heck, Gregory F. Herzog, Peter Hoppe, Friedrich Horz, Joachim Huth, Ian D. Hutcheon, Konstantin Ignatyev, Hope Ishii, Motoo Ito, Damien Jacob, Chris Jacobsen, Stein Jacobsen, Steven Jones, David Joswiak, Amy Jurewicz, Anton T. Kearsley, Lindsay P. Keller, H. Khodja, A.L. David Kilcoyne, Jochen Kissel, Alexander Krot, Falko Langenhorst, Antonio Lanzirotti, Loan Le, Laurie A. Leshin, J. Leitner, L. Lemelle, Hugues Leroux, Ming-Chang Liu, K. Luening, Ian Lyon, Glen MacPherson, Matthew A. Marcus, Kuljeet Marhas, Bernard Marty, Graciela Matrajt, Kevin McKeegan, Anders Meibom, Vito Mennella, Keiko Messenger, Scott Messenger, Takashi Mikouchi, Smail Mostefaoui, Tomoki Nakamura, T. Nakano, M. Newville, Larry R. Nittler, Ichiro Ohnishi, Kazumasa Ohsumi, Kyoko Okudaira, Dimitri A. Papanastassiou, Russ Palma, Maria E. Palumbo, Robert O. Pepin, David Perkins, Murielle Perronnet, P. Pianetta, William Rao, Frans J. M. Rietmeijer, Francois Robert, D. Rost, Alessandra Rotundi, Robert Ryan, Scott A. Sandford, Craig S. Schwandt, Thomas H. See, Dennis Schlutter, J. Sheffield-Parker, Alexandre Simionovici, Steven Simon, I. Sitnitsky, Christopher J. Snead, Maegan K. Spencer, Frank J. Stadermann, Andrew Steele, Thomas Stephan, Rhonda Stroud, Jean Susini, S. R. Sutton, Y. Suzuki, Mitra Taheri, Susan Taylor, Nick Teslich, Kazu Tomeoka, Naotaka Tomioka, Alice Toppani, Josep M. Trigo-Rodriguez, David Troadec, Akira Tsuchiyama, Anthony J. Tuzzolino, Tolek Tyliszczak, K. Uesugi, Michael Velbel, Joe Vellenga, E. Vicenzi, L. Vincze, Jack Warren, Iris Weber, Mike Weisberg, Andrew J. Westphal, Sue Wirick, Diane Wooden, Brigitte Wopenka, Penelope Wozniakiewicz, Ian Wright, Hikaru Yabuta, Hajime Yano,

Edward D. Young, Richard N. Zare, Thomas Zega, Karen Ziegler, Laurent Zimmerman, Ernst Zinner, and Michael Zolensky. Comet 81P/Wild 2 Under a Microscope. *Science*, 314(5806):1711–1716, 2006.

[31] R. A. Buckingham. The classical equation of state of gaseous helium, neon and argon. *Proc. R. Soc. Lond. A*, 168:264–283, October 1938.

[32] V.V. Bulatov, O. Richmond, and M.V. Glazov. An atomistic dislocation mechanism of pressure-dependent plastic flow in aluminium. *Acta materiala*, 47(12):3507 – 3514, 1999.

[33] M J Burchell, M J Cole, J A M McDonnell, and J C Zarnecki. Hypervelocity impact studies using the 2 MV Van de Graaff accelerator and two-stage light gas gun of the University of Kent at Canterbury. *Measurement Science and Technology*, 10(1):41–50, January 1999.

[34] Mark J. Burchell and Neil G. Mackay. Crater ellipticity in hypervelocity impacts on metals. *Journal of Geophysical Research*, 103(E10):22,761–22,774, 1998.

[35] Buyang Cao, Eduardo M. Bringa, and Marc André Meyers. Shock compression of monocrystalline copper: Atomistic simulations. *Metallurgical and Materials Transactions A*, 38(11):26812688, 2007. Based on "Dynamic Behavior of Materials, TMS Annual Meeting, February 25March 1, 2007, Orlando, Florida.

[36] Fang Cao, Irene J. Beyerlein, Francis L. Addessio, Bulent H. Sencer, Carl P. Trujillo, Ellen K. Cerreta, and George T. Gray, III. Orientation dependence of shock-induced twinning and substructures in a copper bicrystal. *Acta Materialia*, 58:549–559, 2010.

[37] C.E. Carlton and P.J. Ferreira. What is behind the inverse hall-petch behavior in nanocrystalline materials. In E. LilleoddenP. BesserL. LevineA. Needleman, editor, *Size Effects in the Deformation of Materials Experiments and Modeling*, pages .0976–EE01–04, 2007.

[38] CEI. Ensight. Apex, North Carolina. http://www.ensight.com.

[39] M. Černý, R. Boyer, M. Šob, and S. Yip. Higher-energy structures and stability of Cu and Al crystals along displacive transformation paths. *Journal of Computer-Aided Materials Design*, 12(2):161–173, Jul 2005.

[40] A. M. Childs, M. H. Shapiro, and T. A. Tombrello. Simulation of kev clusters incident on gold targets. *Nuclear Instruments and Methods in Physics Research Section B: Beam Interactions with Materials and Atoms*, 143(3):298–305, 1998.

[41] Stefan W. Christensen and Noel W. Thomas. Structure characterization and predictability by Voronoi analysis. *Acta Crystallographica Section A*, 55(5):811–820, Sep 1999.

[42] Thomas J. Colla and Herbert M. Urbassek. Au sputtering by cluster bombardment: A molecular dynamics study. *Nuclear Instruments and Methods in Physics Research Section B: Beam Interactions with Materials and Atoms*, 164–165:687–696, 2000.

[43] A. H. Cottrell. *DISLOCATIONS AND PLASTIC FLOW IN CRYSTALS*. The International series of monographs on physics. Clarendon PressOxford, 1953.

[44] R. Courant and K.O. Friedrichs. *Supersonic Flow and Shock Waves*, volume 1 of *Pure and Applied Mathematics*. Interscience Publishers, 1948.

[45] L. P. Davila, P. Erhart, E. M. Bringa, M. A. Meyers, V. A. Lubarda, M. S. Schneider, R. Becker, and M. Kumar. Atomistic modeling of shock-induced void collapse in copper. *Applied Physics Letters*, 86(16):161902, 2005.

[46] Lee Davison and R. A. Graham. Shock compression of solids. *Physics Reports*, 55(4):255 – 379, 1979.

[47] Murray S. Daw and M. I. Baskes. Semiempirical, quantum mechanical calculation of hydrogen embrittlement in metals. *Physical Review Letters*, 50(17):1285 – 1288, Apr 1983.

[48] Murray S. Daw and M. I. Baskes. Embedded-atom method: Derivation and application to impurities, surfaces, and other defects in metals. *Physical Review B*, 29(12):6443–6453, Jun 1984.

[49] C.S. Deo, D.J. Srolovitz, W. Cai, and V.V. Bulatov. Stochastic simulation of dislocation glide in tantalum and ta-based alloys. *Journal of the Mechanics and Physics of Solids*, 53(6):1223–1247, 2005.

[50] Masao Doyama and Y. Kogure. Computer simulation of creation and motion of dislocations during plastic deformation in copper. *Materials Science and Engineering A*, 309-310:451–455, 2001.

[51] Vladimir Dremov and Eduardo Bringa. Molecular-dynamics simulation of highly-symmetric grain boundary shock interaction. In *14th APS Topical Conference on Shock Compression of Condensed Matter*. American Physical Society, 2005.

[52] Wolfgang Eckstein and Herbert M. Urbassek. Computer simulation of the sputtering process. In *Sputtering by Particle Bombardment*, volume 110 of *Topics in Applied Physics*, pages 21–31. Springer-Verlag, HEIDELBERGER PLATZ 3, D-14197 BERLIN, GERMANY, 2007.

[53] F. Ercolessi and J. B. Adams. Interatomic potentials from first-principles calculations: The force-matching method. *EPL (Europhysics Letters)*, 26(8):583–588, 1994.

[54] F. Ercolessi, M. Parrinello, and E. Tosatti. Simulation of gold in the glue model. *Philosophical Magazine A*, 58:213–226, 1988.

[55] Paul Erhart, Eduardo M. Bringa, Kai Kadau, Babak Sadigh, and Brian D. Wirth. Atomistic modeling of high pressure - high strain rate phenomena in aluminium. *Unpublished*, May 2005.

[56] F. Ernst, M. W. Finnis, D. Hofmann, T. Muschik, U. Schönberger, U. Wolf, and M. Methfessel. Theoretical prediction and direct observation of the 9r structure in ag. *Physical Review Letters*, 69(4):620–623, Jul 1992.

[57] Daniel Faken and Hannes Jónsson. Systematic analysis of local structure combined with 3D computer graphics. *Computational Materials Science*, 2:279–286, 1994.

[58] M. W. Finnis and J. E. Sinclair. A simple empirical n-body potential for transition metals. *Philosophical Magazine A*, 50(1):45–55, 1984.

[59] Mike Finnis. *Interatomic forces in condensed matter*. Oxford series on materials modelling. Oxford University Press, 2003.

[60] S.M. Foiles, M.I. Baskes, and M.S. Daw. Embedded-atom-method functions for the fcc metals Cu, Ag, Au, Ni, Pd, Pt, and their alloys. *Physical Review B*, 33(12):7983–7991, Jun 1986.

[61] W. E. Garner and J. E. Lennard-Jones. Molecular spectra and molecular structure. a general discussion. *Transactions of the Faraday Society*, 25:668, 1929.

[62] C. W. Gear. Numerical solution of ordinary differential equations at a remote terminal. In *Proceedings of the 1966 21st national conference*, pages 43–49. ACM, 1966.

[63] T.C. Germann. Large-scale molecular dynamics simulations of hyperthermal cluster impact. *International Journal of Impact Engineering*, 33(1-12):285 – 293, 2006. Hypervelocity Impact Proceedings of the 2005 Symposium.

[64] Timothy C. Germann, Brad Lee Holian, Peter S. Lomdahl, and Ramon Ravelo. Orientation dependence in molecular dynamics simulations of shocked single crystals. *Physical Review Letters*, 84(23):5351–5354, Jun 2000.

[65] Timothy C. Germann and Kai Kadau. Trillion-atom molecular dynamics becomes a reality. *International Journal of Modern Physics C*, 19(9):1315–1319, 2008.

[66] John J. Gilman. *Elastic-plastic impact (some persistent misconceptions)*, chapter 1, pages 3–9. In Staudhammer et al.,[139] 2001.

[67] Roy. W. Goranson, Dennison Bancroft, Blendin L. Burton, Theodore Blechar, Edwin E. Houston, Elisabeth F. Gittings, and Stanley A. Landeen. Dynamic determination of the compressibility of metals. *Journal of Applied Physics*, 26(12):1472, December 1955.

[68] O. Gülseren and R. E. Cohen. High-pressure thermoelasticity of body-centered-cubic tantalum. *Physical Review B*, 65:064103, 2002.

[69] H.R. Habibi. Atomic structure of the cu precipitates in two stages hardening in maraging steel. *Materials Letters*, 59(14-15):1824 – 1827, 2005.

[70] J.M. Haile. *Molecular Dynamics Simulation*. Wiley, 1997.

[71] George G. Hall. The Lennard-Jones paper of 1929 and the foundations of Molecular Orbital Theory. *Advances in Quantum Chemistry*, 22:1–6, 1991.

[72] S.C. Harvey, R.K.Z. Tan, and T.E. Cheatham. The flying ice cube: Velocity rescaling in molecular dynamics leads to violation of energy equipartition. *Journal of Computational Chemistry*, 19(7):726–40, 1998.

[73] R. Hill. A theory of the yielding and plastic flow of anisotropic metals. *Proceedings of the Royal Society of London A*, 193(1033):281–297, May 1948.

[74] B.L. Holian. Modeling shockwave deformation via molecular dynamics. Technical Report LA-UR-87-2367; CONF-870753-46, Los Alamos National Lab, 1987. American Physical Society topical conference on shockwaves in condensed matter, Monterey, CA, USA, 20 Jul 1987.

[75] Brad Lee Holian and Peter S. Lomdahl. Plasticity induced by shock waves in nonequilibrium molecular-dynamics simulation. *Science*, 280(LA-UR–97-4337; CONF-970707–):2085, 1998.

[76] Brad Lee Holian and Galen K. Straub. Molecular dynamics of shock waves in three-dimensional solids. Transition from nonsteady to steady waves in perfect crystals and implications for the Rankine-Hugoniot conditions. *Physical Review Letters*, 43(21):1598–1600, Nov 1979.

[77] William G. Hoover. Canonical dynamics: Equilibrium phase-space distributions. *Physical Review A*, 31(3):1695–1697, Mar 1985.

[78] Friedrich Hörz, Ron Bastien, Janet Borg, John P. Bradley, John C. Bridges, Donald E. Brownlee, Mark J. Burchell, Miaofang Chi, Mark J. Cintala, Zu Rong Dai, Zahia Djouadi, Gerardo Dominguez, Thanasis E. Economou, Sam A. J. Fairey, Christine Floss, Ian A. Franchi, Giles A. Graham, Simon F. Green, Philipp Heck, Peter Hoppe, Joachim Huth, Hope Ishii, Anton T. Kearsley, Jochen Kissel, Jan Leitner, Hugues Leroux, Kuljeet Marhas, Keiko Messenger, Craig S. Schwandt, Thomas H. See, Christopher Snead, Frank J. Stadermann, Thomas Stephan, Rhonda Stroud, Nick Teslich, Josep M. Trigo-Rodrguez, A. J. Tuzzolino, David Troadec, Peter Tsou, Jack Warren, Andrew Westphal, Penelope Wozniakiewicz, Ian Wright, and Ernst Zinner. Impact features on stardust: Implications for comet 81p/wild 2 dust. *Science*, pages 1716–1719, December 2006.

[79] H. Hugoniot. Propagation des mouvements dans les corps et spécialement dans les gaz parfaits. *Journal de lEcole Polytechnique*, 57:3–98, 1887.

[80] O. E. Jones. *Shock Wave Mechanics*, chapter 2, pages 33–55. In Rohde et al.,[130] 1973.

[81] O. E. Jones and J. D. Mote. Shock-induced dynamic yielding in copper single crystals. *Journal of Applied Physics*, 40(12):4920–4928, 1969.

[82] K. Kadau, T. C. Germann, P. S. Lomdahl, , and B. L. Holian. Microscopic view of structural phase transitions induced by shock waves. *Science*, 296:1681–1684, 2002.

[83] Kai Kadau, Timothy C. Germann, Peter S. Lomdahl, , and Brad Lee Holian. Atomistic simulations of shock-induced transformations and their orientation dependence in bcc fe single crystals. *Physical Review B*, 72:064120, 2005.

[84] Kai Kadau, Timothy C. Germann, Peter S. Lomdahl, Robert C. Albers, Justin S. Wark, Andrew Higginbotham, and Brad Lee Holian. Shock waves in polycrystalline iron. *Physical Review Letters*, 98:135701, 2007.

[85] S. Kajiwara, S. Ohno, K. Honma, and M. Uda. A new crystal structure of pure cobalt formed in ultrafine particles. *Philosophical Magazine Letters*, 55(5):215219, 1987.

[86] D. H. Kalantar, J. F. Belak, G.W. Collins, J. D. Colvin, H. M. Davies, J. H. Eggert, T. C. Germann, J. Hawreliak, B. L. Holian, K. Kadau, P. S. Lomdahl, H. E. Lorenzana, M. A. Meyers, K. Rosolankova, M. S. Schneider, J. Sheppard, J. S. Stolken, and J. S. Wark. Direct observation of the $\alpha - \epsilon$ transition in shock-compressed iron via nanosecond x-ray diffraction. *Physical Review Letters*, 95:075502, August 2005.

[87] A. T. Kearsley, M. J. Burchell, F. Hörz, M. J. Cole, and C. S. Schwandt. Laboratory simulation of impacts on aluminum foils of the stardust spacecraft: Calibration of dust particle size from comet wild-2. *Meteoritics and Planetary Science*, 41:167–180, feb 2006.

[88] A. T. Kearsley, G. A. Graham, M. J. Burchell, M. J. Cole, Z. R. Dai, N. Teslich, J. P. Bradley, R. Chater, P. A. Wozniakiewicz, J. Spratt, and G. Jones. Analytical scanning and transmission electron microscopy of laboratory impacts on stardust aluminum foils: Interpreting impact crater morphology and the composition of impact residues. *Meteoritics and Planetary Science*, 42:191–210, 2007.

[89] A.T. Kearsley, G.A. Graham, M.J. Burchell, M.J. Cole, P. Wozniakiewicz, N. Teslich, E. Bringa, F. Hörz, J. Blum, and T. Poppe. Micro-craters in aluminum foils: Implications for dust particles from comet Wild 2 on NASA's Stardust spacecraft. *International Journal of Impact Engineering*, 35(12):1616 – 1624, 2008.

[90] A.T. Kearsley, A.J. Westphal, M.J. Burchell, and M.E. Zolensky. Aluminium foils of the stardust interstellar collector; the challenge of recognising micrometer-sized impact craters made by interstellar grains. *Lunar and Planetary Science*, 39:1668, 2008.

[91] CL Kelchner, SJ Plimpton, and JC Hamilton. Dislocation nucleation and defect structure during surface indentation. *Physical Review B*, 58(17):11085–11088, NOV 1998.

[92] Kholmirzo Kholmurodov, Igor Puzynin, William Smith, Kenji Yasuoka, and Toshikazu Ebisuzaki. Md simulation of cluster-surface impacts for metallic phases: soft landing, droplet spreading and implantation. *Computer Physics Communications*, 141(1):1–16, 2001.

[93] S. Kim. Voronoi analysis of a soccer game. *Nonlinear Analysis: Modelling and Control*, 9(3):233–240, 2004.

[94] L. Koci, E. M. Bringa, D. S. Ivanov, J. Hawreliak, J. McNaney, A. Higginbotham, L. V. Zhigilei, A. B. Belonoshko, B. A. Remington, and R. Ahuja. Simulation of shock-induced melting of Ni using molecular dynamics coupled to a two-temperature model. *Physical Review B (Condensed Matter and Materials Physics)*, 74(1):012101, 2006.

[95] A. Ya. Krasovskii. Damping of elastic shock waves in iron caused by viscous damping of dislocations. *Strength of Materials*, 2(7):636–640, 07 1970.

[96] Alison Kubota, David B. Reisman, and Wilhelm G. Wolfer. Dynamic strength of metals in shock deformation. *Applied Physics Letters*, 88(24):241924, 2006.

[97] Oyeon Kum. Calculation of shock waves and temperatures of fcc single crystals (nickel) using large-scale molecular dynamics. In M. Laudon and B. Romanowicz, editors, *Nanotech 2003*, volume 2, pages 538–541, 2003.

[98] Oyeon Kum. Orientation effects in shocked nickel single crystals via molecular dynamics. *Journal of Applied Physics*, 93(6):3239–3247, Mar 2003.

[99] V. Senthil Kumar and V. Kumaran. Voronoi neighbor statistics of hard-discs and hard-spheres. *Journal of Chemical Physics*, 123(7):074502, August 2005.

[100] Byeong-Joo Lee and M. I. Baskes. Second nearest-neighbor modified embedded-atom-method potential. *Physical Review B*, 62(13):8564–8567, Oct 2000.

[101] Bai Li-Gang and Liu Jing. Equation of state and elastic constants of compressed fcc cu. *Chinese Physics Letters*, 27(3):036403, 2010.

[102] J J Lissauer. Planet formation. *Annual Review of Astronomy and Astrophysics*, 31:129–172, 1993.

[103] Alexander A. Lukyanov. Anisotropic materials behavior modeling under shock loading. *Journal of Applied Mechanics*, 76(6):061012, 2009.

[104] Xin-Ling Ma and Wei Yang. Supersonic wave propagation in cu under high speed cluster impact. *Nanotechnology*, 15(5):449–456, 2004.

[105] J.-B. Maillet, M. Mareschal, L. Soulard, R. Ravelo, P. S. Lomdahl, T. C. Germann, and B. L. Holian. Uniaxial hugoniostat: A method for atomistic simulations of shocked materials. *Physical Review E*, 63(1):016121, Dec 2000.

[106] Mikhail V. Medvedev and Abraham Loeb. Generation of magnetic fields in the relativistic shock of gamma ray burst sources. *The Astrophysical Journal*, 526:697–706, December 1999.

[107] Michael J. Mehl. Pressure dependence of the elastic moduli in aluminum-rich al-li compounds. *Physical Review B*, 47(5):2493—-2500, Feb 1993.

[108] J. Mei and J. W. Davenport. Free-energy calculations and the melting point of Al. *Physical Review B*, 46(1):21–25, Jul 1992.

[109] N. Metropolis, A.W. Rosenbluth, M.N. Rosenbluth, A.H. Teller, and E. Teller. Equation of state calculation by fast computing machines. *Journal of Chemical Physics*, 21:1087–1092, 1953.

[110] M.A. Meyers. A model for elastic precursor waves in the shock loading of polycrystalline metals. *Materials Science and Engineering*, 30:91–111, 1977.

[111] M.A. Meyers. *Dynamic Behavior of Materials*. Wiley-Interscience, 1994.

[112] M.A. Meyers, M.S. Schneider, B.K. Kad, V.A. Lubarda, F. Gregori, D.H. Kalantar, and B.A. Remington. Laser shock compression of copper monocrystals: Mechanisms for dislocation and void generation. *J. Phys. IV France*, 110:851–856, sep 2003.

[113] Diego Minciacchia, Roman M. Kassac, Claudia Del Tongoa, Raffaella Mariottic, and Marina Bentivoglioc. Voronoi-based spatial analysis reveals selective interneuron changes in the cortex of FALS mice. *Experimental Neurology*, 215(1):77–86, January 2009.

[114] Stanley Minshall. Properties of elastic and plastic waves determined by pin contactors and crystals. *Journal of Applied Physics*, 26(4):463, April 1955.

[115] Y. Mishin, D. Farkas, M. J. Mehl, and D. A. Papaconstantopoulos. Interatomic potentials for monoatomic metals from experimental data and ab initio calculations. *Phys. Rev. B*, 59(5):3393–3407, Feb 1999.

[116] Y. Mishin, M. J. Mehl, D. A. Papaconstantopoulos, A. F. Voter, and J. D. Kress. Structural stability and lattice defects in copper: Ab initio, tight-binding, and embedded-atom calculations. *Physical Review B*, 63:224106, May 2001.

[117] M. A. Mogilevskii. Structural changes in pure copper subjected to explosive loading. *Combustion, Explosion, and Shock Waves*, 6(2):197 –201, April 1970.

[118] Philip M. Morse. Diatomic molecules according to the wave mechanics. ii. vibrational levels. *Phys. Rev.*, 34:57–64, Jul 1929.

[119] Michael Moseler, Johannes Nordiek, and Hellmut Haberland. Reduction of the reflected pressure wave in the molecular-dynamics simulation of energetic particle-solid collisions. *Physical Review B*, 56(23):15439–15445, Dec 1997.

[120] Edward I. Moses. Ignition on the national ignition facility: a path towards inertial fusion energy. *Nuclear Fusion*, 49(10):104022 (9pp), 2009.

[121] Shichi Nosé. A molecular dynamics method for simulations in the canonical ensemble. *Molecular Physics*, 52(2):255–268, 1984.

[122] M. Ortiz. Multiscale modeling of shock-loaded materials. *APS Meeting Abstracts*, page K1001, jun 2001.

[123] M. Peach and J. S. Koehler. The forces exerted on dislocations and the stress fields produced by them. *Physical Review*, 80(3):436–439, Nov 1950.

[124] Steve Plimpton. Fast parallel algorithms for short-range molecular dynamics. *Journal of Computational Physics*, 117(1):1 – 19, 1995.

[125] M. C. Price, A. T. Kearsley, M. J. Burchell, F. Hörz, J. Borg, J. C. Bridges, M. J. Cole, C. Floss, G. Graham, S. F. Green, P. Hoppe, H. Leroux, K. K. Marhas, N. Park, R. Stroud, F. J. Stadermann, N. Telisch, and P. J. Wozniakiewicz. Comet 81p/wild 2: The size distribution of finer (sub-10$\mu$m) dust collected by the stardust spacecraft. *Meteoritics & Planetary Science*, 45(9):1409–1428, 2010.

[126] Xie Qian and Huang Meichun. Inverse lattice problem and Finnis-Sinclair model. *Chinese Physics Letters*, 12(4):221–224, 1995.

[127] W. J. Macquorn Rankine. On the thermodynamic theory of waves of finite longitudinal disturbance. *Philosophical Transactions of the Royal Society of London*, 160:277–288, January 1870.

[128] D.C. Rapaport. *The Art of Molecular Dynamics Simulation*. Cambridge University Press, second edition, 2004.

[129] T. Raz and R. D. Levine. On the shattering of clusters by surface impact heating. *The Journal of Chemical Physics*, 105(18):8097–8102, 1996.

[130] R.W. Rohde, B.M. Butcher, J.R. Holland, and C.H. Karnes, editors. *Metallurgical Effects at High Strain Rates*. Plenum Press, 1973.

[131] James H. Rose, John R. Smith, Francisco Guinea, and John Ferrante. Universal features of the equation of state of metals. *Physical Review B*, 29(6):2963–2969, Mar 1984.

[132] Seunghwa Ryu and Wei Cai. Comparison of thermal properties predicted by interatomic potential models. *Modelling and Simulation in Materials Science and Engineering*, 16(8):085005 (12pp), 2008.

[133] Manuel Salas. The curious events leading to the theory of shock waves. *Shock Waves*, 16(6):477–487, July 2007.

[134] Matthew S. Schneider, Bimal K. Kad, and Marc A. Meyers. In-situ x-ray diffraction from hohldraum-driven shock waves in solids. DOE Progress Report DE-FG03-98DP00212, University of California, San Diego, March 2003.

[135] M.S. Schneider, B.K. Kad, F. Gregori, D. Kalantar, B.A. Remington, and M.A. Meyers. Laser-induced shock compression of copper: Orientation and pressure

decay effects. *Metallurgical and Materials Transactions A*, 35(9):2633–2646, 2004.

[136] Nathan E. Schultz, Ahren W. Jasper, Divesh Bhatt, J. Ilja Siepmann, and Donald G. Truhlar. Aluminum nanoparticles: Accurate potential energy functions and physical properties. In Richard B. Ross and Sanat Mohanty, editors, *Multiscale Simulation Methods for Nanomaterials*, chapter 10. Wiley, Feb 2008.

[137] Peter Schwerdtfeger, Nicola Gaston, Robert P. Krawczyk, Ralf Tonner, and Gloria E. Moyano. Extension of the Lennard-Jones potential: Theoretical investigations into rare-gas clusters and crystal lattices of He, Ne, Ar, and Kr using many-body interaction expansions. *Physical Review B*, 73(6):064112, 2006.

[138] M. H. Shapiro and T. A. Tombrello. Simulation of core excitation during cluster impacts. *Physical Review Letters*, 68(10):1613–1615, Mar 1992.

[139] Karl P. Staudhammer, Lawrence E. Murr, and Marc . Meyers, editors. *Fundamental Issues and Applications of Shock-Wave and High-Strain-Rate Phenomena*. Elsevier, 2001.

[140] Frank H. Stillinger and Thomas A. Weber. Computer simulation of local order in condensed phases of silicon. *Physical Review B*, 31(8):5262–5271, Apr 1985.

[141] A. P. Sutton and J. Chen. Long-range Finnis-Sinclair potentials. *Philosophical Magazine Letters*, 61(3):139–146, 1990.

[142] J.W. Swegle and D.E. Grady. Shock viscosity and the prediction of shock wave rise times. *Journal of Applied Physics*, 58(2):692–701, Jul 1985.

[143] H. Van Swygenhoven, M. Spaczer, A. Caro, and D. Farkas. Competing plastic deformation mechanisms in nanophase metals. *Physical Review B*, 60(1):22 – 25, July 1999.

[144] Masaharu Tanemura, Tohru Ogawa, and Naofumi Ogita. A new algorithm for three-dimensional Voronoi tesselation. *Journal of Computational Physics*, 51:191–207, 1983.

[145] Andrew Taylor, Mike Dunne, Steve Bennington, Stuart Ansell, Ian Gardner, Peter Norreys, Tim Broome, David Findlay, and Richard Nelmes. A route to the brightest possible neutron source? *Science*, 315(5815):1092–1095, 2007.

[146] B. J. Thijsse. Relationship between the modied embedded-atom method and Stillinger-Weber potentials in calculating the structure of silicon. *Physical Review B*, 65:195207, 2002.

[147] Blas P. Uberuaga and Arthur F. Voter. Accelerated molecular dynamics methods. In KE Sickafus, EA Kotomin, and BP Uberuaga, editors, *Radiation Effects in Solids*, volume 235 of *NATO Science Series, Series II: Mathematics, Physics and Chemistry*, pages 25–43, PO Box 17, 3300 AA Dordrecht, Netherlands, 2004. Springer. Conference of the NATO Advanced Study Institute on Radiation Effects in Solids, Erice, Italy, July 17–29, 2004.

[148] Herbert M. Urbassek, Christian Anders, Luis Sandoval, and Arun K. Upadhyay. Ultrafast laser irradiation vs cluster ion impact: Molecular-dynamics comparison of materials processes in highly energized solids - art. no. 700507. In CR Phipps, editor, *High-Power Laser Ablation VII, PTS 1-2*, volume 7005 of *Proceedings of the Society of Photo-Optical Instrumentation Engineers (SPIE)*, page 507. SPIE; Photon Associates, LLC; European Off Aerosp Res & Dev (United Kingdom), SPIE, 2008. Conference on High-Power Laser Ablation VII, Taos, NM, APR 20-27, 2008.

[149] Benjamin W. van de Waal. Can the Lennard-Jones solid be expected to be fcc? *Physical Review Letters*, 67(23):3263–3266, Dec 1991.

[150] Loup Verlet. Computer "experiments" on classical fluids. I. Thermodynamical properties of Lennard-Jones molecules. *Physical Review*, 159(1):98–103, Jul 1967.

[151] J. M. Walsh. *Bulletin of the Amercan Physical Society*, 29:28, 1954.

[152] Guofeng Wang, A. Strachan, T. Cagin, and W.A. III Goddard. Atomistic simulation of kinks for 1/2a< 111 > screw dislocation in Ta. In V. Bulatov, L. Colombo, F. Cleri, L.J. Lewis, and N. Mousseau, editors, *Advances in Materials Theory and Modeling - Bridging Over Multiple-Length and Time Scales.*, pages AA7.30.1 – AA7.30.6. Materials Research Society, 2001. San Francisco, CA, USA 16-20 April 2001.

[153] Jinghan Wang, Ju Li, Sidney Yip, Simon Phillpot, and Dieter Wolf. Mechanical instabilities of homogeneous crystals. *Physical Review B*, 52(17):12627–12635, Nov 1995.

[154] Grethe Winther. Effect of grain orientation dependent microstructures on flow stress anisotropy modelling. *Scripta Materialia*, 52(10):995–1000, May 2005.

[155] Wolfram Research, Inc. Mathematica. Champaign Illinois, 2008. http://www.wolfram.com/products/mathematica/index.html.

[156] D.S. Xu, R. Yang, J. Li, J.P. Chang, H. Wang, D. Li, and S. Yip. Atomistic simulation of the influence of pressure on dislocation nucleation in bcc Mo. *Computational Materials Science*, 36(1-2):60 – 64, May 2006.

[157] Y Yamaguchi and J Gspann. Large-scale molecular dynamics simulations of high energy cluster impact on diamond surface. *EUROPEAN PHYSICAL JOURNAL D*, 16(1–3):103–106, SEP 2001. 10th International Symposium on Small Particles and Inorganic Clusters (ISSPIC 10), ATLANTA, GA, OCT 11-15, 2000.

[158] Y Yamaguchi and J Gspann. Large-scale molecular dynamics simulations of cluster impact and erosion processes on a diamond surface. *Physical Review B*, 66(15):155408, OCT 15 2002.

[159] Y Yamaguchi and J Gspann. Large-scale molecular dynamics simulations of highly accelerated cluster impact on diamond surface. *Microsystem Technologies*, 9(1–2):109–112, NOV 2002.

[160] F. W. Young and J. R. Savage. Growth of copper crystals of low dislocation density. *Journal of Applied Physics*, 35:1917, 1964.

[161] J. F. Ziegler, Biersack J. P, and U. Littmark. *The Stopping and Range of Ions in Solids*, volume 1 of *Stopping and Ranges of Ions in Matter*. Pergamon Press, New York, 1984.

[162] James F. Ziegler. Particle interactions with matter. http://www.srim.org/. site accessed 07 Oct 2010.

[163] Steffen Zimmermann and Herbert M. Urbassek. Sputtering of nanoparticles: Molecular dynamics study of au impact on 20 nm sized au nanoparticles. *International Journal of Mass Spectrometry*, 272(1):91–97, APR 15 2008.

[164] Jonas A. Zukas and William P. Walters, editors. *Explosive Effects and Applications*. High-Pressure Shock Compression of Condensed Matter. Springer-Verlag, 1998.